

**UNIVERSITAT  
JAUME•I**

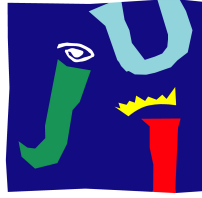
# Elastic, Electrostatic and Magnetic Properties in Colloidal Quantum Wells

Doctoral Thesis  
**Jordi Llusar Camarelles**

**Thesis Director:** Dr. Juan Ignacio Climente Plasencia

**June 2022**





**UNIVERSITAT  
JAUME·I**

## **Doctoral Programme in Sciences**

Universitat Jaume I Doctoral School

# **Elastic, Electrostatic and Magnetic Properties in Colloidal Quantum Wells**

**Report submitted by Jordi Llusar Camarelles in order to be eligible  
for a doctoral degree awarded by the Universitat Jaume I**

A handwritten signature in black ink, consisting of several loops and a long horizontal stroke extending to the right.

Doctoral Student

**Jordi Llusar Camarelles**

Thesis Director

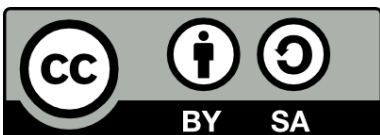
**Juan Ignacio Climente Plasencia**

**Castelló de la Plana, June 2022**



**Funding sources:**

- Participation in MICINN: CTQ2017-83781-P project.
- Participation in UJI-B2017-59 project
- Participation in UJI-B2021-06 project.



License Creative Commons:  
**Attribution – ShareAlike**



## Thesis by compendium of publications:

1. Jordi Llusar, Josep Planelles, and Juan I. Climente. **Strain in Lattice-Mismatched CdSe-Based Core/Shell Nanoplatelets.** *J. Phys. Chem. C* DOI: <https://doi.org/10.1021/acs.jpcc.9b06577> Impact Factor 2020: 4.126 (Q2) SJR 2020: 1.401.
2. Jordi Llusar and Juan I. Climente. **Nature and Control of Shakeup Processes in Colloidal Nanoplatelets.** *ACS Photonics* DOI: <https://doi.org/10.1021/acsp Photonics.0c01160> Impact Factor 2020: 7.529 (Q1) SJR 2020: 2.735.
3. Jordi Llusar and Juan I. Climente. **Changing Spin and Orbital Ground State Symmetries in Colloidal Nanoplatelets with Magnetic Fields.** *Phys. Status Solidi B* DOI: <https://doi.org/10.1002/pssb.202200081> Impact Factor 2020: 1.71 (Q3) SJR 2020: 0.510.
4. Jordi Llusar and Juan I. Climente. **Highly Charged Excitons and Biexcitons in Type-II Core/Crown Colloidal Nanoplatelets.** *J. Phys. Chem. C* DOI: <https://doi.org/10.1021/acs.jpcc.2c00827> Impact Factor 2020: 4.126 (Q2) SJR 2020: 1.401.
5. Jordi Llusar and Juan I. Climente. **Shell Filling and Paramagnetism in Few Electron Colloidal Nanoplatelets.** *XX* DOI: XX Impact Factor 2020: XX (QX) SJR 2020: XX. (*under review*)

“This Thesis has been accepted by the co-authors of the publications listed above that have waved the right to present them as a part of another PhD thesis”

## Publications not included in this Thesis:

1. Ivo Tanghe, Jordi Llusar, Juan I. Climente, Alex Barker, Giuseppe Paterò, Francesco Scotognella, Anatolii Polovitsyn, Ali Hossain Khan, Zeger Hens, Dries Van Thourhout, Pieter Geiregat, and Iwan Moreels. **Role of Thermally Occupied Hole States in Room-Temperature Broadband Gain in CdSe/CdS Giant-Shell Nanocrystals.** *XX* DOI: XX Impact Factor 2020: XX (QX) SJR 2020: XX. (*under review*)





# Contents

<b>Acknowledgements</b>	<b>i</b>
<b>Abstract</b>	<b>ii</b>
<b>Resum</b>	<b>iv</b>
<b>Acronyms</b>	<b>ix</b>
<b>1 Introduction</b>	<b>1</b>
1.1 Colloidal nanocrystals and nanoplatelets . . . . .	1
1.2 Modelling of colloidal nanoplatelets . . . . .	12
1.3 Elastic properties . . . . .	17
1.4 Electrostatic properties . . . . .	20
1.5 Magnetic properties . . . . .	22
<b>2 Publications</b>	<b>26</b>
2.1 Strain in Lattice-Mismatched Nanoplatelets . . . . .	26
2.2 Nature and Control of Shakeup Processes . . . . .	63
2.3 Highly Charged Excitons and Biexcitons in Nanoplatelets . . . . .	107
2.4 Shell Filling and Spontaneous Magnetism in Nanoplatelets . . . . .	136
2.5 Changing Symmetries in Nanoplatelets . . . . .	151
<b>3 Conclusions</b>	<b>164</b>
<b>Bibliography</b>	<b>167</b>
<b>Appendices</b>	<b>186</b>
A Coauthors Authorization . . . . .	A1
B Training Activities . . . . .	B1
C Curriculum Vitae . . . . .	C1

# Acknowledgements

I would like to thank the Química Quàntica (QQ) group of the Universitat Jaume I for accepting me to carry out my dissertation. Although this group is made up of a modest number of researchers, they compensate for it with a large amount of knowledge and passion for science.

I express my special thanks to my supervisor, Dr. Juan I. Climente (Nacho), whose ability and knowledge were pure gold for my learning process. Most of the things I know, not only during this dissertation but also along my chemistry degree, are because of him. Personally, his dedication and deftness to teach me during all these past years and especially his guidance during this doctoral program were priceless. Undoubtedly, I can be sure that Nacho can be considered for me, let's say, as my academic father.

I also thank my tutor, Prof. Dr. Josep Planelles. It goes without saying that he is like the tribal shaman or the oracle of the QQ Group. His years of experience and his physical intuition make him, without a doubt, the cornerstone of this wonderful group. His advice was unvaluable.

Of course, I would like to thank David (in a few months Dr. David Macias). He was a great colleague and is naturally a greater person. From him, I take his calm in stressful situations.

In addition, I strongly thank my parents for helping me financially support this doctorate. Unfortunately, in Spain, governments apparently do not have much interest in science. This fact affects a large number of outstanding potential researchers who, due to different factors, are unable to pay for resources, dissemination of their results, or even worse, for doctorate enrolment.

Finally, I would like to thank my partner Mical from the bottom of my heart for being fully supportive of me when all of these ups and downs that involve a doctorate programme arose. Thanks to her I could get away from that workaholic instinct, which should be shut off in some cases to preserve good mental health.

# Abstract

Metal chalcogenide colloidal nanoplatelets (NPLs) have received increasing interest since their very first synthetic route was proposed in 2008. Unlike previous types of colloidal nanocrystals (quantum dots, rods, tetrapods), NPLs present excellent size (thickness) homogeneity which translates into extremely narrow fluorescence linewidths ( $\sim 35$  meV in 4.5 monolayer CdSe NPLs). This feature provides better colour purity for applications in lasers, lighting, and displays. In addition to promising technological prospects, NPLs also exhibit characteristic optoelectronic properties of fundamental interest. These arise from the quasi-two-dimensional (2D) geometry, combined with the severe dielectric confinement imposed by the organic ligands surrounding the inorganic semiconductor. Large exciton binding energies (100 to 300 meV), suppressed Auger recombination, and (allegedly) giant oscillator strength are examples of such phenomena.

The goal of this Ph.D. dissertation is to provide a better understanding of the photophysics of CdSe NPLs and CdSe-based hetero-NPLs through theoretical modelling of the electronic structure. We consider homo- and heterostructured NPLs, and build adapted  $\mathbf{k} \cdot \mathbf{p}$  Hamiltonians for such systems (including many-body interactions through Configuration Interaction (CI) techniques). The models are then used to analyse the influence of several relevant physical factors whose role has not been clarified in the literature. The gained understanding allows us to provide interpretation for different reported experimental observations, as well as to propose new paradigms of exploitation to further expand the functionalities of NPLs.

Specifically, in this dissertation:

- (1) We provide the first study on the impact of lattice-mismatch strain in core/shell NPLs (CdSe/ $XY$ , with  $X=\text{Zn,Cd}$  and  $Y=\text{S,Te}$ ). We clarify the relative contributions of tunnelling and strain to the determination of emission redshift observed in experiments with CdSe/ZnS NPLs, propose structural designs to mitigate it, and reveal the origin of the bending observed in thick-shell NPLs.
- (2) We analyse the role of radiative Auger (shake-up) processes in NPLs. We show that these are much stronger than in quantum wells and dots and

hence susceptible to explain the low-energy satellite observed in the photoluminescence spectra of individual CdSe NPLs. These processes are, however, rapidly quenched upon shell growth, because the weaker dielectric confinement reduces Coulomb interactions. This challenges the interpretation provided in recent experiments, which invoked shake-up processes to explain the multi-peaked emission of CdSe/CdS NPLs.

- (3) We propose going beyond the usual photocharging regime (producing neutral excitons) and filling in NPLs with a few interacting carriers of the same sign (fermions). Strong Coulomb repulsions (stimulated by quasi-2D confinement and dielectric mismatch), in combination with weak lateral confinement, lead to a regime of severe correlations. Then many properties of interest are observed. These range from violations of Hund's rules in shell filling to large chromic shifts (over 100 meV) in the emission spectrum when neutral excitons are charged with excess electrons or holes.
- (4) We present strategies to modulate the ground state spin and orbital symmetry in NPLs, by means of external magnetic fields. These rely on the anomalously large exchange interactions (favouring high-spin states) and on the doubly-connected topology of core/crown NPLs, which enables the building-up of Aharonov-Bohm (AB) effects.

All in all, the body of theoretical work presented in this PhD helps to elucidate the role of different physical factors affecting metal chalcogenide NPLs, which can be exploited for rational engineering of their optoelectronic properties.

# Resum

Les nanolàmines col·loïdals (nanoplatelets, NPLs) basades en calcogenurs metàl·lics han rebut un interès creixent des que es va proposar la seua primera ruta sintètica en 2008. A diferència d'altres tipus de nanocristalls col·loïdals (punts quàntics, varetes, tetràpodes), les NPLs presenten una homogeneïtat de grandàries (espessor) excel·lent que es tradueix en una fluorescència amb amplàries de línia estretes ( $\sim 35$  meV en 4.5 monocapes de NPLs de CdSe). Aquesta característica aporta una millor puresa espectral que pot ser aprofitada per a làsers, il·luminació i pantalles. A banda de la perspectiva fascinant de cara al futur en quant a aplicacions tecnològiques, les NPLs exhibeixen propietats optoelectròniques característiques d'interès fonamental. Aquestes sorgeixen de la geometria quasi-bidimensional (2D), combinada amb el confinament dielèctric majúscul imposat pels lligams orgànics que envolten al semiconductor inorgànic. Les grans energies d'enllaç excitòniques (100 – 300 meV), les esmortides recombinacions d'Auger i (presumptament) la gran força de l'oscil·lador són alguns exemples d'aquests fenòmens optoelectrònics.

L'objectiu del present treball de doctorat és oferir una millor comprensió de la fotofísica de les NPLs de CdSe com també d'aquelles heteroestructures basades en CdSe. Aquesta millor comprensió es duu a terme mitjançant el modelatge teòric de l'estructura electrònica. Considerem NPLs homo- i heteroestructurades, i construïm Hamiltonians  $\mathbf{k} \cdot \mathbf{p}$  adaptats per a aquests sistemes (incloent-hi interaccions multi-cos mitjançant tècniques d'Interacció de Configuracions - Configuration Interaction, CI -). Aleshores, els models s'utilitzen per analitzar l'influència de diversos factors físics el rol dels quals no ha estat aclarit en la literatura. La comprensió adquirida ens permet aportar interpretacions a diferents observacions experimentals reportades, així com proposar nous paradigmes d'aprofitament per tal d'expandir més enllà les funcionalitats de les NPLs.

Específicament, en aquest doctorat:

- (1) Aportem el primer estudi sobre l'impacte que té la pressió originada per la disparitat de cel·la en les NPLs nucli/escorsa (CdSe/XY, amb X=Zn,Cd i Y=S,Te). Aclarim les contribucions relatives de l'efecte túnel i de la pressió en determinar el corrent al roig dels pics d'emissió observats en

experiments amb NPLs CdSe/ZnS, proposem dissenys estructurals per tal d'atenuar aquest corrent, i desvetllem l'origen de l'encorbament observat en NPLs amb escorses grosses.

- (2) Examinem el rol dels processos d'Auger radiatius (shake-up) en NPLs. Mostrem que aquests processos són considerablement més forts que els que ocorren en pous i punts quàntics i per tant, són susceptibles d'explicar el satèl·lit de baixa energia vist als espectres de fotoluminescència en NPLs de CdSe individuals. Aquests processos són, però, ràpidament amortits en fer créixer l'escorsa, perquè l'afebliment del confinament dielèctric redueix les interaccions de Coulomb. Açò, contrasta i, per tant, obliga a revisar la interpretació aportada en experiments recents, que fan ús dels processos shake-up per explicar l'emissió multi-pic en NPLs de CdSe/CdS.
- (3) Proposem anar més enllà de l'habitual règim de fotocàrrega (que preodueix excitons neutres) i emplenar les NPLs amb uns quants portadors amb mateix signe que interactuen entre ells (fermions). Les fortes repulsions de Coulomb (estimulades pel confinament quasi-2D i el contrast dielèctric), en combinació amb el confinament lateral feble, dóna lloc a un règim d'alta correlació. Llavors, s'observen moltes propietats d'interès. Aquestes van des de violacions de les regles de Hund en omplir orbitals (shells) fins a grans desplaçaments cròmics (més de 100 meV) en l'espectre d'emissió quan es carreguen excitons neutres amb un excés d'electrons o forats.
- (4) Presentem estratègies per modular les simetries orbitals i d'espín en NPLs, mitjançant camps magnètics externs. Aquestes estratègies es basen en les, anòmales, grans interaccions de bescanvi (afavorint als estats d'espín alt) i la doblement connexa topologia de les NPLs nucli/corona que indueixen el desenvolupament d'efectes Aharonov-Bohm (AB).

En definitiva, el cos de treball teòric presentat en aquest doctorat ajuda a esbrinar el paper de diferents factors físics que afecten les NPLs de calcogenurs metàl·lics, que poden ser aprofitades per fer un disseny raonable de les seues propietats optoelectròniques.

*To my family and  
my significant other.*

*„Wer es einmal so weit gebracht hat,  
daß er nicht mehr irrt,  
der hat auch zu arbeiten aufgehört.“  
–Max Planck*

# List of Tables

1.1	Comparison of some properties between CdSe-based QDs and NPLs (zincblende) . . . . .	9
1.2	Lattice parameters corresponding to different materials. Lattice misfit experienced by different heterostructures of interest . . . . .	18



# List of Figures

1.1	Electron excitation and absorption process. Exciton formation and electron-hole recombination. Emission process. . . . .	2
1.2	Quantum confinement effect on the spacing of energy levels in quantum dots. Sketch of the kinetic, potential and total energy as a function of the one-dimensional box size $a$ . . . . .	3
1.3	TEM images. Quantum dot, nanorods and nanoplatelets . . . . .	6
1.4	Sketch of a transition from an exciton vacuum state to an exciton $i$ -th state. . . . .	8
1.5	Illustration of core-shell and core-crown systems. Band alignments in heterostructures. . . . .	10
1.6	Simple sketch of a heterostructure. Offset potential in a heterostructure. . . . .	13
1.7	Two-dimensional in-plane representation of an exciton inside a NPL without dielectric confinement and in presence of dielectric confinement between inorganic and organic media. . . . .	20
1.8	Different kind of excitonic species in nanostructures. . . . .	21
1.9	Illustration of a magnetic field flux piercing the orbit of a charged carrier; ground state oscillations as a function of an applied magnetic field $\mathbf{B}$ : Quantum ring and type-II quantum disk. . . . .	23

# Acronyms

$\sigma$  Absorption cross-section

**AB** Aharonov-Bohm

$E_{gap}$  Band gap energy

$E_b^{XX}$  Biexciton binding energy

$\tau_{XX}$  Biexciton decay lifetime

**cQD** Colloidal Quantum Dot

$E_c$  Conduction band energy

**CI** Configuration Interaction

**CC** Core-crown

**CO** Core-only

**CS** Core-shell

$e^-$  Electron

$V_{e-h}$  Electron-hole Coulomb interaction

$\lambda_{emi}$  Emission wavelength

**EFA** Envelope Function Approach

**eQD** Epitaxial Quantum Dot

$E_b^X$  Exciton binding energy

$\tau_X$  Exciton decay lifetime

**FRET** Förster Resonant Energy Transfer

**FWHM** Full Width at Half Maximum

**GOST** Giant Oscillator Strength Transition

**HH** Heavy hole  
 $h^+$  Hole  
**LH** Light hole  
**LED** Light-Emitting Diode  
**ML** Monolayer  
**NC** Nanocrystal  
**NPL** Nanoplatelet  
**NR** Nanorod  
**OA** Oleic acid  
**1B** One-band  
**1D** One-dimensional  
**oAB** Optical Aharonov-Bohm  
**OLED** Organic Light-Emitting Diode  
**PL** Photoluminescence  
**PLQY( $\Phi$ )** Photoluminescence Quantum Yield  
 $\gamma_B$  Photon  
 $E_{\lambda(abs)}$  Photon energy absorbed  
 $E_{\lambda(emi)}$  Photon energy emitted  
**QD** Quantum Dot  
**QD-LED** Quantum Dot Light-Emitting Diode  
**QW** Quantum well  
**QQ** Química Quàntica  
**RT** Room temperature  
**SU** Shakeup  
 $V_i$  Single i-particle potential  
 $kT$  Thermal energy  
**3D** Three-dimensional

**TEM** Transmission Electron Microscopy

**2D** Two-dimensional

$E_v$  Valence band energy

**0D** Zero-dimensional

**ZB** Zinblende

# Chapter 1

## Introduction

### 1.1 Colloidal nanocrystals and nanoplatelets

Almost 40 years ago, solid state researchers began to realise how different the electronic properties of semiconductor quantum dots (QDs) are with respect to those made with the same material but in large volumes. [1] By quantum dimensions, it could be understood that the dimensions of a semiconductor, along given space directions, are shorter than the de Broglie wavelength along those same directions. Within this quantum framework the particle behaviour (mainly electrons) which was ruled by classical physics becomes quantised. It opens, then, a wide variety of possibilities where electronic, optical, magnetic, and other properties can be modified simply by tuning the QD size, composition, and shape. [2, 3, 4]

In most semiconductor materials (Si, Ge, GaAs, InAs, CdSe, CdTe, etc.), electrons display effective masses lower than those seen in free electrons. The resulting de Broglie wavelength,  $\lambda = h/p$  with  $p = m^*v$  (here  $h$  is the Planck constant,  $p$  the linear momentum,  $v$  and  $m^*$  the speed and effective mass of an electron confined within a semiconductor material), is located in a range of 10 – 100 nm. Therefore, a semiconductor starts to behave like a QD when the aforementioned three space directions are below these de Broglie wavelengths. Because of the discrete distribution of their energy levels, QDs are known as artificial atoms. [5, 6]

As in voluminous semiconductors (bulk), the QDs optics is given by, mainly, the formation and annihilation of a quasiparticle named **exciton**. The formation and annihilation of an exciton generally occur in the following manner. When a photon  $\gamma$ , with energy  $E_{\gamma(abs)}$  equal or greater than the band gap energy  $E_{gap}$  of a semiconductor, is absorbed, an electron  $e^-$  situated in the valence band  $E_v$  promotes to the conduction band  $E_c$  leaving a hole,  $h^+$ , behind. This is illustrated in Fig. 1.1 for a resonance excitation case (Fig. 1.1, (1)). Then, this electron in the conduction band remains bound to the hole in the valence band, forming a pair due to the Coulomb interaction existent between each other  $V_{e-h}$ , this is known as

exciton (Fig. 1.1, ②). Eventually, the electron relaxes radiatively by recombining with the hole that was left in the valence band and therefore emits a photon with an energy  $E_{\gamma(emi)}$  which is equal to the band gap energy  $E_{gap}$  (Fig. 1.1, ③). [7]

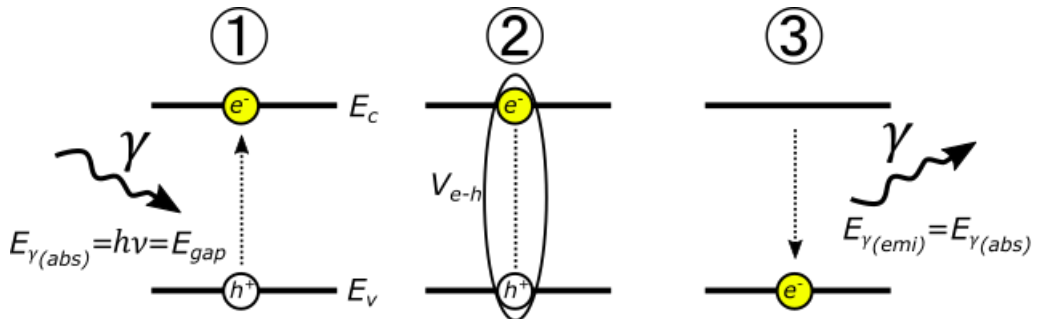


**Figure 1.1:** Electron excitation and absorption process (left); exciton formation (centre); electron-hole recombination and emission process (right).

Compared with the bulk, the QD spatial confinement involves a modification of the energy levels distribution or spacing, in both the conduction and valence bands. Consequently, if the energy levels distribution in both bands is modified, the difference between them is also modified, that is, the energy separation between the bottommost of the conduction band and the topmost of the valence band (or band gap energy). [8, 9, 10] This energy difference can be easily visualized (Fig. 1.2a) when applying a 1-band (1B)  $\mathbf{k} \cdot \mathbf{p}$  Hamiltonian [11], for electrons and holes, to the particle-in-a-box problem with infinite potential walls  $V(x) = \infty$  (inside the box  $V(x) = 0$ )

$$\hat{H}_{(1B)} = \frac{\mathbf{p}^2}{2\mu} - \frac{e^2}{\kappa r} + V(x) \quad , \quad (1.1)$$

where the kinetic energy autovalue is

$$E_n = \frac{n^2 \hbar^2}{2\mu a^2} \quad , \quad (1.2)$$

with  $\hbar$  being the reduced Planck constant,  $\mu$  the exciton reduced mass,  $a$  the box length,  $\kappa$  the Coulomb constant,  $e$  the free electron charge, and  $n$  stands for energy levels  $n = 1, 2, 3, \dots$ . This increase in the kinetic energy of electrons and holes, which changes as  $a^{-2}$ , competes with the greater Coulomb attraction between holes and electrons when confining. However, this Coulomb term scales up according to  $a^{-1}$ . Therefore, in highly confined systems, the kinetic energy term  $a^{-2}$  predominates over the Coulomb one  $a^{-1}$  (Fig. 1.2b). [12] In excitons, the electron and hole are similar to the hydrogen atom. Hence, the effective Bohr radius is defined as

$$a_B^* = \frac{4\pi\epsilon_0\epsilon_r\hbar^2}{\mu e^2} \xrightarrow{\text{a.u.}^1} a_B^* = \frac{\epsilon_r}{\mu} . \quad (1.3)$$

Here  $\epsilon_0$  and  $\epsilon_r$  are the vacuum and relative electric permittivity, respectively. This effective Bohr radius indicates the size limit whereby the quantum confinement effects start to predominate over the Coulomb effects. Since quantum confinement is a variable that increases as the kinetic energy increases (the system becomes more energetic) and the Coulomb interaction existent between the electron and the hole (exciton) is attractive (the system yields stabilization), in QDs with  $a < a_B^*$ , optical spectra present a blueshift effect as the sizes of these QDs become smaller. The QDs optical gap sensitivity to their dimensions allows one to tune the absorption and emission wavelengths without changing their material composition. This has enormous practical implications for optical and optoelectronic devices.

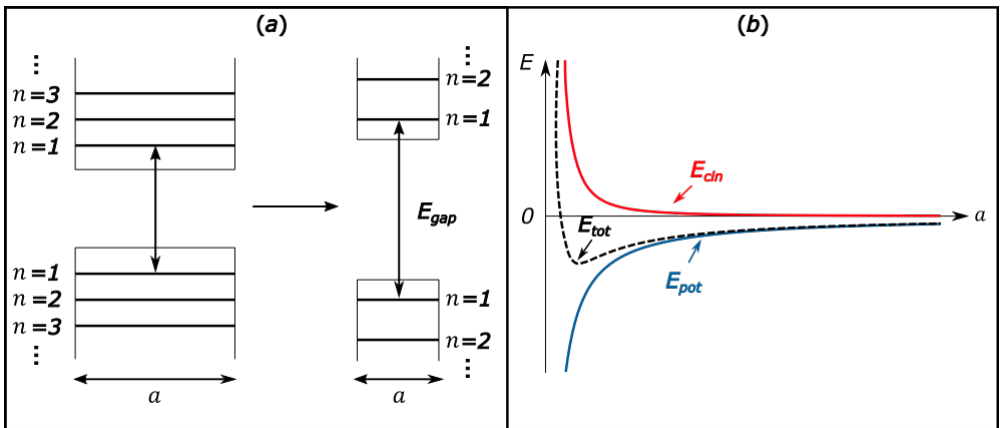


**Figure 1.2:** (a) Quantum confinement effect on energy levels spacing in QDs. Large QD (left) and small QD (right). (b) Sketch of the kinetic – quantum confinement – (red solid line), potential (blue solid line), and total energy (black dashed line) as a function of the 1D box size  $a$ . Notice the energetic threshold led by the Coulomb or spatial confinement terms predominance. In the excitons case, this energetic threshold is similar to the Bohr radius.

In addition to size, QD photophysics is also sensitive to other factors such as QD material composition or shape. Depending on the material, different band gap energies are obtained, as well as different  $\epsilon_r$  and  $\mu$ , which determine the Bohr radius. Furthermore, the QD shape is important in terms of fluorescence. The confinement anisotropy allows us to conjugate strong and weak confinement effects along different directions, which gives rise to a particular electronic density of states outside the strictly, zero-, one-, two- or three-dimensional limits. This

<sup>1</sup>a.u. means 'atomic units'.

confinement anisotropy allows one to design objects that benefit simultaneously from quantum and classical properties leading to hybrid structures of (quantum) dots, wires, and wells. [13, 14, 15, 16]

Shape-controlled QDs have been synthesized by means of, for instance, deposition methods such as vapour deposition, [17] molecular beam epitaxy, [18] lithography [19], or wet-chemical methods [20] (colloids). It is worth highlighting two of the most commonly used routes when synthesizing QDs: on the one hand, the epitaxial synthesis [21, 22] and on the other hand, the colloidal one. [23, 24, 25] The main differences are: [26, 27] i) *type of synthesis*; in epitaxial synthesis a solid substrate is required where phase vapour reagents are deposited on it (heterogeneous reaction), while in colloidal synthesis are used, simply, reagents which are soluble with either aqueous or organic solvents. Colloidal synthesis is carried out in solution (homogeneous reaction); ii) *QD self-assembly*; in epitaxial synthesis, self-assembly is based on lattice mismatch, where both substrate and growing material lattice parameters are required to be alike (but not identical). Because of this lattice mismatch between substrate and the thin-layer liquid precursor deposited on it, tiny drops or islands (QDs) are produced spontaneously to minimize their elastic energy. This growing mechanism is known as the *Stranski-Krastanov* growing mode. [28] Therefore, in epitaxial synthesis, QDs are rearranged by strain effects. However, in colloidal synthesis, organic or aqueous molecules (ligands) rearrange the system thermodynamically to achieve the desired geometry. Because of this control on system geometry, QDs showing higher homogeneity and reproducibility are generally easier to obtain; [29] iii) *QD size*; QDs synthesized by epitaxial routes (eQDs) used to have sizes  $> 10$  nm laterally, while those QDs synthesized by colloidal routes (cQDs) can reach, along all directions, sizes  $< 10$  nm. [26] This variety of sizes leads to important differences in terms of quantum confinement when one route is applied or the other. Another distinguishing aspect to consider would be the Coulomb interactions present between each carrier located inside of the QDs. These carriers experience Coulomb effects that become amplified in cQDs when the QD (inorganic) and the external medium (organic) present a dielectric mismatch. This dielectric mismatch occurs because carriers in these colloidal systems are placed closer to the QD-external medium interface than that in the eQD case; iv) *synthesis conditions*; while very specific conditions are required in epitaxial synthesis, such as ultrahigh vacuum conditions and reagent evaporation with high purity materials, in colloidal synthesis, there is no special condition to be fulfilled to carry this synthesis out. Therefore, economically, this latter route turns out to be more attractive; [26] v) *QD optics*; colloidal synthesis allows the control of size and shape in an accurate and reproducible way. This gives rise to high monodispersity, spectral purity, and photoluminescence quantum yield (PLQY). Moreover, the stronger confinement in colloidal systems results in exciton binding energies ( $E_b^X$ ) above thermal energy  $kT$  even at room temperature (RT). Thus, devices such as those based on the mid- and long-wave infrared spectrum [30] can take advantage of the excellent optics of excitons against non-



bound electrons and holes.

In view of all these features present in the colloidal route, one can understand the intensive efforts made on the synthesis, comprehension, and, subsequently, use of cQDs. In fact, over the last years, the transition from laboratories to the commercial market of this cQD technology has been produced as an active means for LED screens and devices. As an example, QD-LEDs have already been seen as a substitute for organic LED (OLED) devices, since they present higher performance. [31] In addition, television displays based on cQDs are expected to be low-cost, bendable, rollable, and hangable (like posters). [32]

To go deeper into colloidal systems, it is convenient to summarize how a colloidal nanocrystal is formed. There are required: [13] i) *precursors* that provide the atoms that will promote the nanocrystals growing; ii) *ligands* that are responsible for providing stability against the environment, controlling size and shape of nanoparticles; iii) *solvent* that provides a homogeneous reaction medium that makes the precursors soluble and, therefore, yields stability to the final product, a nanocrystal.

The importance of ligands in colloidal synthesis must be particularly emphasized<sup>2</sup>. The ligands in the colloidal synthesis can control the size and shape of QDs, simply by tuning the surface free energy and the growth kinetics of the QD, [33, 34, 35, 36] leading, thus, to isotropic or anisotropic QDs at will. [6, 37, 38] By means of ligand engineering a distinct number of physics associated with semiconductor dimensionality can arise. That is, semiconductors can be obtained where their carriers (electrons, holes, etc.) are confined quantumly within the three space dimensions (3D), yet they are not able to freely move along any dimension (QD, 0D, Fig. 1.3a). Furthermore, those semiconductors with their carriers confined quantumly within two space dimensions (2D) and freely moving along one single dimension (nanorod - NR -, 1D, Fig. 1.3b). Or those where their carriers experience quantum confinement along one spacial dimension (1D) and have free movement over a plane in the coordinate space (nanoplatelet - NPL -, 2D, Fig. 1.3c), among others.

With respect to the dimensionality of the colloidal semiconductor, diverse genuine elastic, electrostatic, optical, electronic, and magnetic properties can be achieved. Next, the latter properties will be explored, making special mention of 2D Cd-chalcogenide-based NPLs, which are the main goal of this thesis.

NPLs are nanostructured semiconductors with ultrathin thickness controlled by atomic precision. They are reminiscent of epitaxial quantum wells which revolutionized solid-state physics at the end of the twentieth century, [41, 42] but with

---

<sup>2</sup>From here on, if otherwise is said, cQD is stated as a QD to simplify notation.

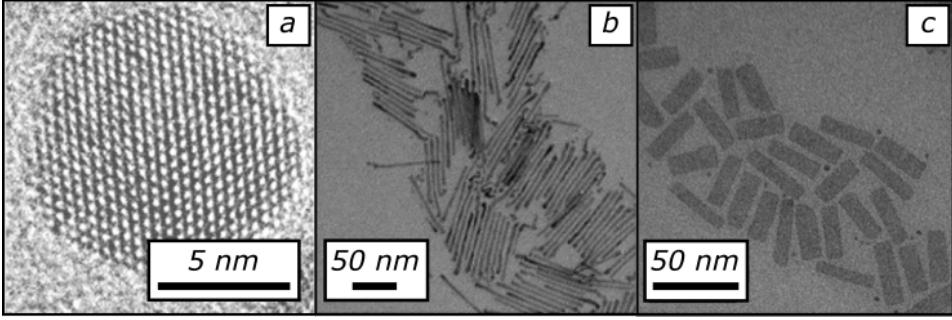


**Figure 1.3:** TEM images. (a) QD. Adapted from reference [12]. Copyright © 2021 American Chemical Society. (b) NRs. Adapted from reference [39]. Copyright © 2018 American Chemical Society. (c) NPLs. Adapted from reference [40]. Copyright © 2013 American Chemical Society.

some particularities such as:

1. Controllable lateral confinement between a few and tens of nanometres. [43, 44] This confers, to NPLs, adjustable spectra, from quasi-continuous spectra to a merely discrete one. Then, NPLs are considered quasi-2D systems. [42, 45, 46]
2. Strong dielectric contrast between organic medium and NPL. [47, 48, 49]
3. Possibility of developing heterostructures in-plane. [50, 51, 52, 53]

Due to all of these particular features, research on NPLs has been intense and prolific over the past decade. Some of the most noteworthy properties in NPLs, hitherto observed, are mentioned.

Firstly, as a consequence of this synthesis control of NPLs layer by layer, NPLs do not show inhomogeneous broadening problems [13, 54] (single and ensemble optical spectra of NPLs, normally, overlap between each other [55]). This results in narrow broadband emissions (FWHM  $\sim 7$  nm in CdSe [13]) in contrast to those observed in QDs (FWHM  $\sim 30$  nm in CdSe [27]). Additionally, because of this homogeneity and meticulousness between various sizes of NPLs, a fast Förster resonant energy transfer (FRET) [56] is observed in contrast to that seen in a bunch of QDs. On account of this, their emission energy tends to redshift (donor *atom* emission) with relation to their absorption energy (acceptor *atom* absorption). [57]

Secondly, because NPLs are quasi-2D systems, their effective Bohr radii are situated between two boundaries: the bulk effective Bohr radius (upper limit), which is equivalent to the 3D Bohr radius – equation (1.3) –

$$a_B^* = (a_B)_{3D} \ , \quad (1.4)$$

and the 2D effective Bohr radius (lower limit), which is equivalent to half of the 3D Bohr radius (or equal to the 2D Bohr radius), [47, 58]

$$a_B^* = (a_B)_{3D}/2 = (a_B)_{2D} . \quad (1.5)$$

It is straightforward to see that the Bohr radius of the quasi-2D system is smaller than that present in the 3D one but greater than (or similar to) that of pure 2D systems, as long as dielectric effects are considered

$$(a_B)_{2D} \lesssim (a_B)_{quasi-2D} < (a_B)_{3D} . \quad (1.6)$$

From the 3D and 2D boundaries in equation (1.6) different conclusions can be extracted:

1. When considering the hydrogen-atom Bohr formula, the  $N$ -dimensional exciton binding energy  $(E_b^X)_{ND}$  associated with this Bohr formula is

$$(E_b^X)_{ND} = \frac{\hbar^2}{2\mu(a_B)_{ND}^2} . \quad (1.7)$$

Furthermore, if equation (1.5) is considered and inserted into equation (1.7), one can conclude that the relation existent between the 3D and 2D exciton binding energy is  $(E_b^X)_{2D} = 4(E_b^X)_{3D}$  [45] or simply

$$(E_b^X)_{2D} > (E_b^X)_{3D} . \quad (1.8)$$

Therefore, relation (1.8) implies that excitons in NPLs are strongly bound even at RT, despite the absence of strong lateral confinement.

2. Due to the combination of the reduced Bohr radius with the extended lateral dimensions, another observed feature in NPLs is that the electric dipole moment matrix element for excitonic state transitions which take place from a vacuum state  $|0\rangle$  to a given state  $|i\rangle_X$  - between the valence and conduction bands (Fig. 1.4) - is described by the following proportionality [59]

$$(\langle 0 | \boldsymbol{\mu} | i \rangle_X)^{ND} \propto \left( \frac{L}{(a_B)_{ND}} \right)^N , \quad (1.9)$$

where  $N$  represents the nanostructure dimensionality and  $L$  is the length along the weak confinement direction. The proportionality in equation (1.9) can be rewritten in 2D in the following way: [47]

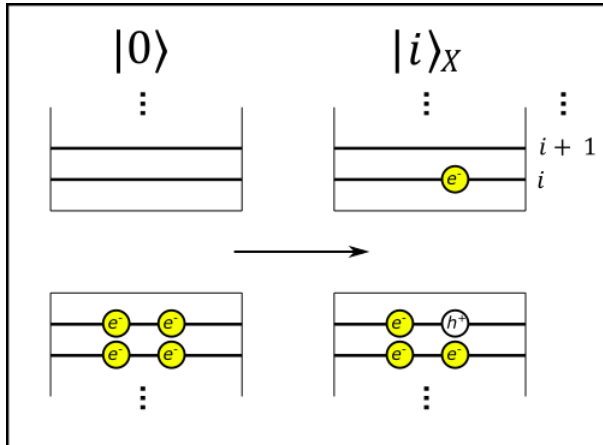


**Figure 1.4:** Sketch of a transition from an exciton vacuum state to an exciton  $i$ -th one.

$$(\langle 0 | \boldsymbol{\mu} | i \rangle_X)^{2D} \propto \left( \frac{L}{(a_B)_{2D}} \right)^2 \equiv \frac{L_x L_y}{((a_B)_{2D})^2} . \quad (1.10)$$

3. Since in expression (1.10) the 2D Bohr radius is much smaller than the lateral dimensions  $(a_B)_{2D} \ll L_x L_y$ , the term  $(\langle 0 | \boldsymbol{\mu} | i \rangle_X)^{2D}$  turns out to be increased in NPLs. Furthermore, the term  $(\langle 0 | \boldsymbol{\mu} | i \rangle_X)^{2D}$  is proportional to the oscillator strength. Thus, this proportionality in NPLs gives rise to a greater oscillator strength than in QDs. This effect is known as *Giant Oscillator Strength Transition* (GOST) and it affects linear [45] as non-linear [59] optics in NPLs. However, it must be said that the exciton localization over partial regions of the NPL, with an area inferior to that of  $L_x L_y$ , often represents practical limitations on the GOST in experimental samples. [60]

Another consequence, owing to the fact that the lateral dimensions in NPLs are much larger than those dimensions that the diameter of a QD can achieve, is that NPLs can obtain higher *absorption cross-sections*  $\sigma$ . [61] Then this results in lower *lasing thresholds* [62] when trying to reach stimulation regimes in generating lasers and, in turn, in higher *optical gains*. [63]

The superior optical properties displayed by CdSe NPLs in a wide variety of aspects (summed up in Table. 1.1 by comparison with their QD counterparts) made NPLs one of the most studied objects since their suggested synthesis in 2008 by the two-person team Ithurria-Dubertret. [64] A NPL that is made up of a single material and acts as an optically active core also finds itself simultaneously exposed to both external medium inconveniences (e.g., having an impact on the surface of the NPL that turns out photo-oxidized [65] or forming traps due to the desorption of ligands [66]) and superficial structural defects during its synthesis that consequently affect the PLQY of the NPL and stability. [67, 68] In the case

of QDs, most of the problems that arise from the surface or external medium can be prevented by adopting the strategy of coating the core material with another inorganic material, which has a band gap greater than that of the coated material (that is, forming a potential energy barrier). [69, 70, 71, 72]

Property	CdSe QD	Refs.	CdSe NPL	Refs.
$\Phi$ (PLQY)	$\sim 0.1(\lambda_{emi} = 545\text{nm})$ (RT)	[55]	$\sim 0.4(\lambda_{emi} = 551\text{nm})$ (RT)	[55]
FWHM (nm)	$\sim 30$	[27] [29] [55]	$\sim 7$	[13]
FRET (ns)	0.12-1	[57] [73] [74]	$\sim 0.006-0.023$	[56]
$a_B$ (nm)	4.9	[75] [76]	1.89	[45] <sup>3</sup>
	5.4	[77]	1.2-2	[77]
$E_b^X$ (meV)	$\sim 40$ ( $d = 3\text{nm}$ )	[78]	$\sim 100-200$	[79]
			193 (5ML $\sim 1.5\text{nm}$ )	[49]
			132 (5ML)	[48]
			130-175	[80]
$E_b^{XX}$ (meV)	14 ( $d = 7\text{nm}$ ) <sup>4</sup> 33 ( $d = 3.6\text{nm}$ ) 12 ( $d = 2.2\text{nm}$ )	[81]	30 (5ML)	[48]
	19-26 ( $d = 4.6\text{nm}$ )	[82]		
$\tau_X$ (ns)	23 ( $d = 2.3\text{nm}$ ) (RT)	[83]	$\sim 0.44$ (5ML) (RT)	[48]
	25-35 ( $d = 2 - 4\text{nm}$ ) (RT)	[84] [85]		
$\tau_{XX}$ (ns)	0.006-0.1 ( $d = 2.2 - 7\text{nm}$ ) (RT)	[81]	$\sim 0.12$ (5ML) (RT)	[48]
	0.17 ( $d = 4.6\text{nm}$ ) (RT)	[82]		
Dipole moment (D)	5-15	[60]	15-23	[60]
$\sigma \times 10^{-12}$ (cm <sup>2</sup> )	$\sim 0.016$ ( $d = 6\text{nm}$ )	[86]	$\sim 2(L_x L_y = 57.2 \text{ nm}^2)$	[87]
Lasing threshold ( $\mu\text{J} \cdot \text{cm}^{-2}$ )	$\sim 100-1000$ ( $d = 2 - 6\text{nm}$ )	[88]	$\sim 6$ (5ML)	[48]

**Table 1.1:** Comparison of some properties between CdSe-based QDs and NPLs (zincblende).

<sup>3</sup>Calculated Bohr radius from definitions (1.3) and (1.5)  $(a_B)_{3D}/2 = (a_B)_{2D} \Rightarrow (a_B)_{2D} = 2\varepsilon_r/\mu$ , using the values found in reference [45] supplementary information:  $m_e = 0.13m_0$ ,  $m_{hh} = 0.9m_0$  and  $\varepsilon_r = 8.3$ .

<sup>4</sup>The trend is reversed for small QDs because in a strong quantum confinement regime, electron-electron and hole-hole interactions overcome exciton-exciton interactions. Consequently, both excitons turn out unbound, since the binding energy between each other results weakened.

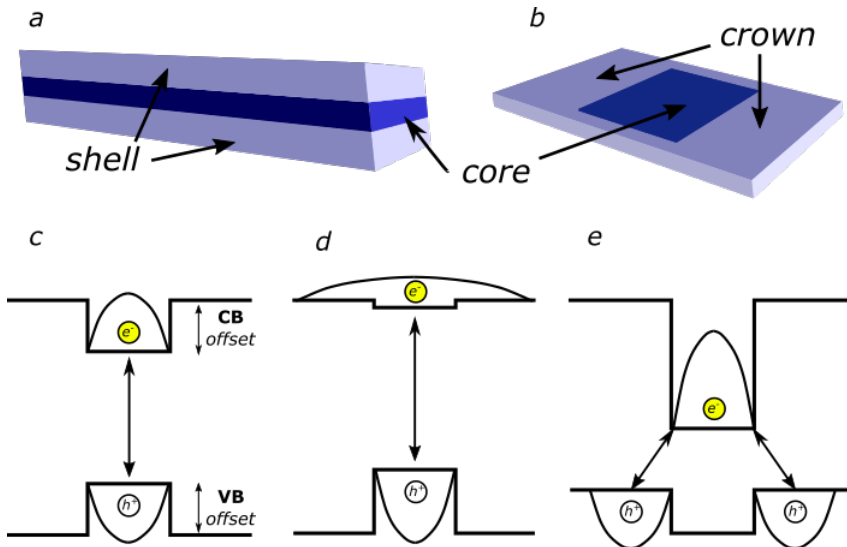


**Figure 1.5:** (Superior part) (a) core-shell and (b) core-crown NPLs. (Inferior part) band alignments in heterostructures. (c) Type-I, (d) quasi-Type-II and (e) Type-II.

Analogously to QDs, a similar strategy is adopted for NPLs. On the one hand, there are core-shell NPLs (CS, Fig. 1.5a). [65, 68] These heterostructures place their carriers inside or near the core, that is, far from the surface. This distance between carriers and the surface produces a probability of decreasing the number of trap states that affect the fluorescence efficiency and the environmental factors that influence the emission intensity (e.g., a higher energy threshold when reducing/oxidizing a given surface or greater stability against the formation of defects [28]). This leads to, at RT, quantum yields two times greater ( $\Phi = 0.8$ ) than those seen in a single NPL - core-only, CO - (Table 1.1). [89] It must be said that, as a consequence of increasing the thickness of the NPL, an energetic redshift can be observed with respect to that of a CO NPL due to the relaxation of the confinement energy experienced by the exciton. [90]

On the other hand, core-crown NPLs (CC, Fig. 1.5b) are heterostructures that consist of coating a CO NPL laterally forming, as it claims its name, a crown. [90, 91] This lateral growth around CdSe NPLs provides the possibility of tuning and controlling the optoelectronic properties of the CC NPL while keeping its thickness intact. As a consequence of fixing the NPL thickness, every single absorption energy from both materials comprising the CC NPL remains at the same position as it would be in a CO NPL formed by their constituents. Alternatively, the CC NPL emission energy, which depends on the material used for forming its crown, can coincide with the lower absorption energy (almost negligible Stokes shift due to a direct band gap recombination, Fig. 1.5c,d) or appear redshifted with relation to it (evident Stokes shift caused by an indirect band gap recombination, Fig. 1.5e). [52, 90] In addition, it must be remarked that when lateral dimensions are increased in certain band alignments, the absorption cross-section

increases notably.

Currently, there are available synthesis routes that allow one to form CS as CC structures with combinations of metallic chalcogenides ( $CdX/MY$ ) which give rise to different types of carrier distribution (Fig. 1.5c,d,e). The most frequent combinations are as follows: [13, 65, 90, 92]

- $CdSe/ZnS$  (type-I): [93] the electrons and holes formed in this heterostructure are both confined within the coated material (CdSe core) leaving the coating material (ZnS shell) empty (Fig. 1.5c). This kind of heterostructure is known to have a direct band gap. Consequently, it has so far possessed one of the highest quantum yields among heterostructures ( $\Phi \sim 1$ ). [89, 90, 94, 95, 96] The origin of such an elevated quantum yield is twofold: i) the high overlap between electrons and holes which results in fast radiative recombinations; ii) the effective passivation of the CdSe core which suppresses superficial traps acting as non-radiative recombination channels.
- $CdSe/CdS$  (quasi-type-I): [50, 95] holes are confined like in a type-I heterostructure, whereas electrons can delocalize over the whole heterostructure (Fig. 1.5d), since they have a low offset between core and shell/crown in the conduction band. [97] The electron-hole overlap in this kind of heterostructure is lower than in type-I ones. Furthermore, electrons can suffer from superficial effects. In the particular case of CC NPLs, note that the optics of the formed exciton turns into a type-I-system-like behaviour, since the confined hole pulls the delocalized electron towards it. This pulling happens because the weak lateral confinement in the core, experienced by the electron, cannot compensate the Coulomb interaction that the source (hole) exerts on it. [50]
- $CdSe/CdTe$  (type-II): [92, 98] electrons are placed within the CdSe domain. Otherwise, the holes are spread over the CdTe region (Fig. 1.5e) placing their electronic density as much in the top as in the bottom parts of the shell (or around the core, that is, inside the crown). Slow radiative recombinations as a result of spatial separation between carriers, whose overlap is relatively poor, are characteristic of these heterostructures. [92] Moreover, in contrast to what happens in type-I heterostructures, transitions take place through an indirect band gap. These transitions show up not in the visible spectrum but in the infrared one, below the CdSe and CdTe band gap energy. [52]

From the good optoelectronic properties and versatility that offer CdSe-based NPLs, these ones are suggested as building blocks in applications such as lasing, [48, 62] LEDs, [99, 100] ratiometric sensors, [101] photodetectors, [102] piezo-electronics, [103], and so forth.

Theoretical models are required to capture the main physical factors that determine the NPL behaviour. These theoretical models allow us to understand the features of these NPLs and predict situations of interest.

## 1.2 Modelling of colloidal nanoplatelets

Different computational methods have been explored to model the electronic structure of NPLs in an efficient and precise manner. On the one hand, there are methods which model the NPL electronic structure by means of *ab initio* techniques. [104, 105] On the other hand, there are those semi-empirical methods that are used the most: the atomistic and continuum ones. Atomistic models (*such as Tight-Binding, pseudo-potentials, etc.*) account for every single atom that forms a NPL, and thus, they are more appropriate when studying alloys, [106] extremely thin monolayers [107] or ligand effects on the surface of a NPL, [108, 109], for instance. Occasionally, these methods have been used to study NPLs, [110] but, in general, they are computationally expensive and often impractical. This is due to the large but finite lateral extension, consisting of tens of nanometres, present in this kind of nanostructure. Therefore, it turns out to be worthwhile to use other more efficient methods, such as the continuum ones. These latter methods are based on the approach that a semiconductor can be visualized as a continuum medium, just as its name indicates. In particular, the effective mass model, also known as the  $\mathbf{k} \cdot \mathbf{p}$  method, [11, 111] allows one to know at an arbitrary Brillouin zone point (for instance, at the  $\Gamma$  point in ZB semiconductors like CdSe-based NPLs) the excitons energy, PL spectrum characteristics, etc., by means of a reduced set of parameters, which can be obtained directly from the corresponding bulk properties. [47, 112, 113, 114] The power of this method when studying Cd-chalcogenide-based nanostructures lies in the fact that these materials show their excitonic transitions around this aforementioned symmetry zone. [115] In view of this fact, the  $\mathbf{k} \cdot \mathbf{p}$  method is ideal for dealing with these systems. [80, 116, 117]

In the first place, to derive this method, it must be considered the Bloch theorem. [11, 111, 118, 119, 120, 121] This theorem states that the electron wavefunction in a crystal, which has periodic potential  $V(\mathbf{r} + \mathbf{a}) = V(\mathbf{r})$ , with  $\mathbf{a}$  standing for the lattice parameter, can be written as

$$\Psi_{n\mathbf{k}}(\mathbf{r}) = e^{i\mathbf{k}\cdot\mathbf{r}}u_{n\mathbf{k}}(\mathbf{r}) . \quad (1.11)$$

Here,  $\mathbf{k}$  is the wavevector (quantum number of translational symmetry) and  $n$  denotes different bands of the crystal. In the equation (1.11),  $u_{n\mathbf{k}}(\mathbf{r})$  are cell-periodic functions which have translational symmetry  $u_{n\mathbf{k}}(\mathbf{r} + \mathbf{a}) = u_{n\mathbf{k}}(\mathbf{r})$ . The exponential term  $e^{i\mathbf{k}\cdot\mathbf{r}}$  are plane waves, slowly varying over the crystal. Wavefunctions of the form (1.11) satisfy the periodicity condition  $\Psi_{n\mathbf{k}}(\mathbf{r} + \mathbf{a}) = \Psi_{n\mathbf{k}}(\mathbf{r})$ :

$$\Psi_{n\mathbf{k}}(\mathbf{r} + \mathbf{a}) = e^{i\mathbf{k}\cdot\mathbf{a}}\Psi_{n\mathbf{k}}(\mathbf{r}) , \quad (1.12)$$



so that any function satisfying equation (1.12) can be written in the form of equation (1.11). Furthermore, any function of the form of equation (1.11) satisfies equation (1.12). [121]

However, when heterostructures are studied, the translational symmetry is lifted in the direction in which the heterostructure is grown. In these cases, the  $\mathbf{k} \cdot \mathbf{p}$  method must be aided by the *Envelope Function Approach* (EFA). [11, 111, 120, 121] This approach assumes that, in both materials: (i) the lattice constants are similar; (ii) there is absence of defects in the interface between them; (iii) their crystalline structure is the same. A simple example is given below.

Let a heterostructure B–A–B be like that in Fig. 1.6a, where the translational symmetry has been truncated along the  $z$  direction. Otherwise, the  $x$ - and  $y$ -directions conserve this symmetry. The wavefunction corresponding to this heterostructure can be written as

$$\Psi(\mathbf{r}) = \sum_l \underbrace{e^{ik_x x} e^{ik_y y} \chi_l(z)}_{f_l(\mathbf{r})} u_{l,\mathbf{k}}(\mathbf{r}), \quad (1.13)$$

where one function changes very slowly  $f_l(\mathbf{r})$  (envelope part) and the other, a Bloch function  $u_{l,\mathbf{k}}(\mathbf{r})$ , varies very quickly (periodic function). Note that  $\chi_l(z)$  is an envelope function along the  $z$  direction and is initially unknown. The summation over  $l$  runs over as many (band) edges as are included in the analysis.

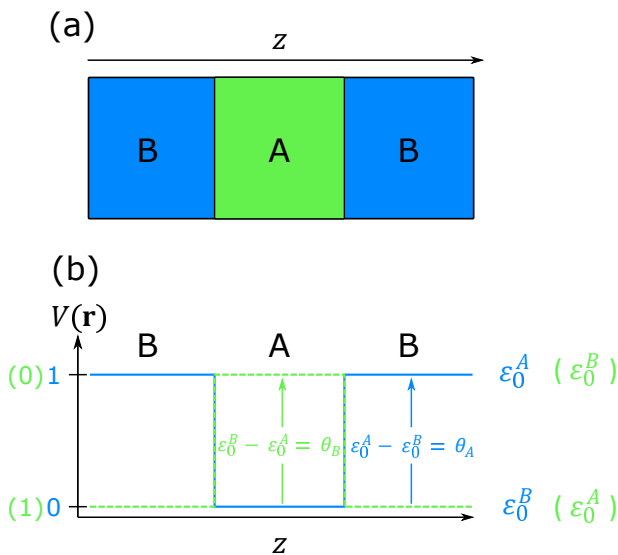


**Figure 1.6:** (a) Simple sketch of an heterostructure. (b) Offset potential in an heterostructure. Green(blue) colour stands for material A(B).

Then, two assumptions must be made with relation to the wavefunctions be-

longing to the materials A and B: [11]

- (i) **Assumption 1:** within each material the wavefunction is expanded on the periodic parts of the Bloch functions of the considered edges

$$\Psi(\mathbf{r}) = \sum_l f_l^{(A)}(\mathbf{r}) u_{l,\mathbf{k}}^{(A)}(\mathbf{r}) , \quad (1.14)$$

if  $\mathbf{r}$  corresponds to the A material and,

$$\Psi(\mathbf{r}) = \sum_l f_l^{(B)}(\mathbf{r}) u_{l,\mathbf{k}}^{(B)}(\mathbf{r}) , \quad (1.15)$$

if  $\mathbf{r}$  corresponds to the B material.

- (ii) **Assumption 2:** the periodic parts of the Bloch functions are assumed to be the same in each material which constitutes the heterostructure:

$$u_{l,\mathbf{k}}^{(A)}(\mathbf{r}) \equiv u_{l,\mathbf{k}}^{(B)}(\mathbf{r}) \equiv u_{l,\mathbf{k}}(\mathbf{r}) . \quad (1.16)$$

Therefore, the heterostructure wavefunction can be written as

$$\Psi(\mathbf{r}) = \sum_l f_l^{(A,B)}(\mathbf{r}) u_{l,\mathbf{k}}(\mathbf{r}) . \quad (1.17)$$

Additionally, the Schrödinger equation for an electron in this heterostructure would be

$$\hat{H}^{(A,B)}(\mathbf{r}) u_{l,\mathbf{k}}(\mathbf{r}) = \varepsilon_l^{(A,B)} u_{l,\mathbf{k}}(\mathbf{r}) , \quad (1.18)$$

with, on the one hand,  $\hat{H}^{(A,B)}$ ,

$$\hat{H}^{(A,B)}(\mathbf{r}) = -\frac{\hbar^2}{2m} \nabla^2(\mathbf{r}) + V_A(\mathbf{r})\theta_A + V_B(\mathbf{r})\theta_B , \quad (1.19)$$

where the first term is the kinetic energy,  $V_A$  and  $V_B$  are the potential energies with their corresponding Heaviside functions  $\theta_A$  and  $\theta_B$  which are related to the material A or B, respectively; and on the other hand,  $\varepsilon_l^A(\varepsilon_l^B)$  is the  $l$ -band edge energy in material A (B), as shown in Fig. 1.6b. In equation (1.19), the potential energy and Heaviside terms take under consideration the confinement potential effects felt by electrons depending on the material they are located and modify, consequently, this Hamiltonian equation in the following manner:

$$\hat{H}^{(A,B)}(\mathbf{r}) = \begin{cases} -\frac{\hbar^2}{2m} \nabla^2(\mathbf{r}) + V_A(\mathbf{r}), & \text{if } \mathbf{r} \in A \implies \theta_A = 1 \wedge \theta_B = 0 \\ -\frac{\hbar^2}{2m} \nabla^2(\mathbf{r}) + V_B(\mathbf{r}), & \text{if } \mathbf{r} \in B \implies \theta_A = 0 \wedge \theta_B = 1 \end{cases} . \quad (1.20)$$

Here, taking into account Fig. 1.6b,  $V_A(V_B)$  can be visualized as  $\varepsilon_0^A(\varepsilon_0^B)$  and, for instance, in the case where  $V_A = 0$ ,  $V_B$  yields

$$V_B(\mathbf{r}) = \varepsilon_0^B - \varepsilon_0^A . \quad (1.21)$$

Thus, equation (1.21) is what is known as the *band offset potential* ( $V^{bo}$ ). Notice that this value is distinct for different bands  $l$  of the crystal.

The role of the EFA is to incorporate the confinement potential [122] in heterostructures taking into account all the considerations described above. Therefore, by combining EFA with the  $\mathbf{k} \cdot \mathbf{p}$  method, heterostructures can be correctly described.

Particularly, to investigate photophysical properties in NPLs it is often enough to consider one band Hamiltonians. That is, Hamiltonian (1.19) is projected on equation (1.17) but restricting  $l$  to a single band, either the conduction band ( $\Gamma_6$ ) for electrons or the *heavy hole* valence band ( $\Gamma_8$ ) – HH band – for holes<sup>5</sup>:

$$\hat{H} = \sum_{i=1}^{N_e} \hat{h}_e + \sum_{i=1}^{N_h} \hat{h}_h + \sum_{i=1}^{N_e} \sum_{j=1}^{N_h} V_c(\mathbf{r}_{e,i}, \mathbf{r}_{h,j}) + \frac{1}{2} \sum_{k=e,h} \left[ \sum_{i=1, j \neq i}^{N_k} V_c(\mathbf{r}_{k,i}, \mathbf{r}_{k,j}) \right], \quad (1.22)$$

where  $N_e$  ( $N_h$ ) is the number of electrons (holes). The  $V_c$  terms consider Coulomb interactions and  $\hat{h}_e$  ( $\hat{h}_h$ ) is the electron (hole) single-particle Hamiltonian that corresponds to:

$$\hat{h}_i = \sum_{i=e,h} \left( \frac{\mathbf{p}_i^2}{2m_i^*} + V_i \right). \quad (1.23)$$

Here,  $\mathbf{p}_i = (p_{i,x}, p_{i,y}, p_{i,z})$  is the three-dimensional momentum operator and  $m_i^*$  the effective mass of the (quasi) particle  $i$ . On the other hand, the single-particle potential term  $V_i$  in equation (1.23) can admit all kinds of interactions between charge carriers and the environment (e.g., the potential barrier or offset felt by electrons or holes when being placed in a given material or another,  $V_{(e,h)}^{bo}$ ). Or, the dielectric confinement effects that experience electrons and holes with their image charges,  $V_{(e,h)}^{self}$ , among other terms. A particularly fruitful strategy in the study of QDs has been the gradual inclusion of an increasing number of single-particle potential terms in equation (1.23). [124, 125, 126, 127, 128] Compared to experiments, this allows one to pinpoint the physical factors that are responsible for the observed behaviour. The interpretation of experiments is often reached with lower computational cost and more intuitive insight than with sophisticated

---

<sup>5</sup>The use of only the HH band in modelling NPLs, in contrast to QDs [123], is motivated by the high anisotropy of NPLs along the thickness direction that pushes the *light hole* band away from the HH one. This splitting, in CdSe, is about  $\sim 140$ – $180$  meV. [45]

Hamiltonians that simultaneously include all the possibly relevant terms.

In recent years, the Quantum Chemistry (QQ) Group of the Universitat Jaume I (<http://quimicaquantica.uji.es/>) has focused on developing  $\mathbf{k} \cdot \mathbf{p}$ -EFA models to study the electronic structure of NPLs. The goal is to properly determine and include the relevant terms that make NPLs different from related nanostructures, previously investigated with  $\mathbf{k} \cdot \mathbf{p}$  models, such as epitaxial QWs or nanocrystal QDs. Three features are critical in this regard: (i) *a weak but finite lateral confinement* of a few tens of nm; (ii) *the possibility of developing radial heterostructures* (CC NPLs) – apart from CS NPLs –; (iii) *the strong dielectric confinement* due to their ultrathin thickness and the dielectric contrast between NPL and external medium, which amplifies both repulsions and attractions between carriers.

The above-mentioned features make carrier-carrier interactions especially challenging to model. The finite lateral confinement forbids the use of Jacobi coordinates, which is employed in QWs to simplify the mathematical formulation of many-body interactions. Also, the strong dielectric confinement enhances Coulomb interactions within the NPL. Along with the weak confinement, this leads to a severe correlation regime where the standard methodology used in QDs, such as perturbative approaches [129] or configuration interaction techniques [130], may fall short. [131]

In 2017, the QQ Group developed its first model based on effective mass Hamiltonians for excitons within homo- or heterostructured NPLs. [47] The Hamiltonian introduced excitonic interactions successfully by using a hybrid variational function between that of a QW and that of a QD, which avoids the possible lack of convergence, [47]

$$\Psi_X = \frac{1}{N} \Phi_e \Phi_h e^{-\frac{\mathbf{r}_{\parallel,e-h}}{a_B^*}}. \quad (1.24)$$

In this wavefunction,  $N$  is the normalization factor,  $\Phi_e$  and  $\Phi_h$  are the single-band electron and hole particle-in-the-box states, respectively. The exponential term is an in-plane Slater correlation factor, where  $\mathbf{r}_{\parallel,e-h}$  represent the relative in-plane coordinates between electron and hole; and recall from equation (1.3) that  $a_B^*$  is the effective Bohr radius. By optimizing  $a_B^*$ , [47] equation (1.24) is able to capture the in-plane strong correlation effects between electron and hole (using the exponential term) and the quantum confinement existing in-plane and out-of-plane (through the product of  $\Phi_e \Phi_h$ ).

The main goal of this Ph.D. project is to investigate the fundamentals of optoelectronic and magnetic properties of a wide variety of many-body species in heterostructured CS and CC NPLs based on CdSe. To do so, we build on the reference [47] model and add several extensions to address NPLs of current

practical interest, mainly for CS and CC heterostructured NPLs. To this end, we will introduce  $V_i$  terms in equation (1.22) that were not yet considered in our previous works and are expected to be relevant. These include the influence of strain through deformation potentials; or the impact of point charges (acting as surface electrostatic impurities) through point charge electrostatic potentials, by solving Poisson equation. Apart from the  $V_i$  terms, the consequences of applying external magnetic fields are considered as well. In general, we intend to study and explain, in heterostructured NPLs, the impact of **elastic**, **electrostatic**, and **magnetic** phenomena on different excitonic species. To this end, we will rewrite equation (1.22) in the following manner:

$$\hat{H} = \hat{H}^{conf} + \hat{H}^{strain} + \hat{H}^{elect} + \hat{H}^B . \quad (1.25)$$

Here,  $\hat{H}^{conf}$  gathers the terms of the Hamiltonian that describe spatial quantum confinement effects. Then it is given by equation (1.23) with  $V_i = V_i^{bo}$ . Additionally,  $\hat{H}^{strain}$  accounts for elastic effects,  $\hat{H}^{elect}$  for electrostatic interactions, and  $\hat{H}^B$  for magnetic effects. Explicit expressions for the latter terms are given below.

### 1.3 Elastic properties

The NPLs crystal lattice experiences deviations with respect to the bulk one. Basically, this deviation is due to two types of crystal defects: *surface* [132, 133, 134] and *interface defects*. [65, 128, 135]

The former gives rise to lattice deformations induced by organic ligands, which are used to passivate chemically dangling bonds of surface atoms. Furthermore, they are responsible for effects such as (i) modification of the crystal structure (e.g., from zincblende to tetragonal [133] or pseudotetragonal<sup>6</sup> [136]) or (ii) loss of plate form (e.g., formation of nanoscrolls [40, 137, 138]).

The latter (*interface defects*) arise in heterostructures because of the different lattice parameters between materials. This elastic property will be one of the objectives of study in this thesis, see **Chapter 2, § 2.1**.

The formation of heterostructures involves strain phenomena. [128, 135, 139, 140] The different lattice parameters between the *core* and the *shell/crown* materials (Table 1.2a) lead to compressive and tensile forces inside the heterostructured system due to the lattice misfit (Table 1.2b). This lattice misfit has been exploited successfully for the application of low-threshold current density lasers in epitaxial QWs, for example. [128, 141, 142] More recently, strain engineering has also gained weight within the nanocrystal community. The first atomic layers around the heterojunction undergo significant deformations to reduce the misfit,

---

<sup>6</sup>The NPL in-plane (lateral dimensions) lattice parameter is 1% smaller than the out-of-plane (thickness) one.

which give rise to deviations with respect to the electronic structure of the same materials in bulk. Some of the resulting effects reported so far are changes in the expected band alignment [135], the appearance of built-in piezoelectric fields [125], or the stabilization of otherwise unstable crystal phases. [143]

(a)

$a$ ( $\text{\AA}$ ) <sup>6</sup>	Material
6.08	CdSe
5.42	ZnS
5.83	CdS
6.48	CdTe

(b)

Lattice misfit <sup>7</sup>	CdSe/ZnS	CdSe/CdS	CdSe/CdTe
$f = \left  \frac{a_2 - a_1}{a_1} \right  \times 100$	$\sim 11\%$	$\sim 4\%$	$\sim 6.5\%$

**Table 1.2:** (a) Lattice parameters corresponding to different materials. (b) Lattice misfit experienced by different heterostructures of interest.

To model these strain phenomena in NPLs, the position-dependent strain tensor  $\epsilon$  must be calculated by the elastic energy minimization. This minimization on the elastic energy is carried out through a continuum and linear elasticity model. [145] The influence of the resulting strain on the electronic structure of electrons and holes is then defined through a single-particle potential  $V_i = V_{(e,h)}^{strain}$  in equation (1.23). Then, within the deformation potential theory, up to first order in  $\epsilon$  and second order in  $k$ , [146] the following general form of the strain terms in a  $k \cdot p$  Hamiltonian can be used [121]

$$\hat{H}^{strain} = \mathbf{D}^\epsilon \cdot \epsilon - \frac{\mathbf{k}\epsilon\mathbf{k}}{m_0} - 2\frac{\mathbf{k}\epsilon\mathbf{p}}{m_0}, \quad (1.26)$$

where  $\epsilon$  and  $\mathbf{D}^\epsilon$  are the strain and deformation potential tensors, respectively;

<sup>6</sup>Lattice parameter values, in  $\text{\AA}$ , taken from reference [139].

<sup>7</sup>Equation taken from reference [144]. The terms  $a_{i=1,2}$  stand for the lattice parameters of the core (1) and the shell/crown (2).

$m_0$  is the free electron mass;  $\mathbf{k}$  and  $\mathbf{p}$  are the momentum operators acting on the envelope and Bloch functions, respectively. The corresponding second and third terms in equation (1.26) describe the change in kinetic energy and the band coupling strength due to strain. Both terms are generally neglected when studying epitaxial quantum wells, since they are expected to be much smaller than the terms containing only  $\epsilon$ . [121] It is not obvious, however, if the second term can also be neglected in NPLs because the extreme quantum confinement makes the kinetic energy very sensitive to small deformations along the thickness direction. [133] The third term is straightforwardly neglected because the HH and LH bands are energetically well separated from each other. [45] The strong confinement, considered in the second term of equation (1.26), can be relevant through the  $k_z$  component of the envelope momentum. When  $\hat{H}^{strain}$  is projected on the Bloch function of the conduction band, equation (1.26) yields  $V_e^{strain} = V_e^{strain,dp} + V_e^{strain,pz}$  with [121]

$$V_e^{strain,dp} = a_c(\epsilon_{xx} + \epsilon_{yy} + \epsilon_{zz}) \quad (1.27)$$

and

$$V_e^{strain,pz} = -\frac{k_z \epsilon_{zz} k_z}{m_{e,z}^*}. \quad (1.28)$$

Here,  $a_c$  is a material-dependent deformation potential coefficient;  $k_z = -i\hbar d/dz$ ; and  $m_{e,z}^*$  is the electron effective mass along the  $z$  axis, which stands for the NPL thickness direction. Notice that the last term of equation (1.26) has vanished in  $V_e^{strain}$  since the operator  $p$  has odd parity under inversion and, as a consequence, changes even Bloch functions to odd ones and vice-versa. Similarly, when  $\hat{H}^{strain}$  is projected on the Bloch function of the heavy hole valence band, equation (1.26) leads to  $V_h^{strain} = V_h^{strain,dp} + V_h^{strain,pz}$  where

$$V_h^{strain,dp} = \left(a_v + \frac{b}{2}\right)(\epsilon_{xx} + \epsilon_{yy}) + (a_v - b)\epsilon_{zz} \quad (1.29)$$

and

$$V_h^{strain,pz} = -\frac{k_z \epsilon_{zz} k_z}{m_{h,z}^*}. \quad (1.30)$$

Here  $a_v$  and  $b$  are the deformation potential coefficients and  $m_{h,z}^*$  the hole effective mass along the thickness direction. Piezoelectric terms, which may be relevant in wurtzite NCs, [16, 127, 128] are neglected when studying zincblende CdSe-based hetero-NPLs because their high symmetric crystal phases make piezoelectric potentials influence on electron and hole ground states poorly. [147]

Because lattice mismatch strain is inherent in all types of heterostructured NPLs (CS and CC), one of the goals of this Ph.D. dissertation is to implement equations (1.27)–(1.30) into Hamiltonian (1.22) and elucidate what the influence of strain is in these systems. This is addressed in **Chapter 2, § 2.1**.

## 1.4 Electrostatic properties

The dielectric mismatch effect between colloidal semiconductors (NPLs, QDs, NRs, etc.) and the external medium turns out to be an important electrostatic property to be taken into consideration. [47, 148, 149, 150, 151] For example, in a cubic CdSe-based semiconductor at RT and low (high) frequency electric fields, its relative dielectric constant  $\epsilon_0$  ( $\epsilon_\infty$ ), along all directions of space, is around 9 (6). [152] On the contrary, a typical ligand, as it is the oleic acid (OA), under the same conditions as stated above for CdSe, its relative dielectric constant ranges from 2 to 3. [80] This difference between the relative dielectric constants of a semiconductor and its external medium leads to what is known as dielectric confinement. This dielectric confinement implies a modulation of Coulomb interactions between charges that, within a semiconductor, become stronger when effectively reducing the dielectric screening of the system (Fig. 1.7). [47, 49, 80]

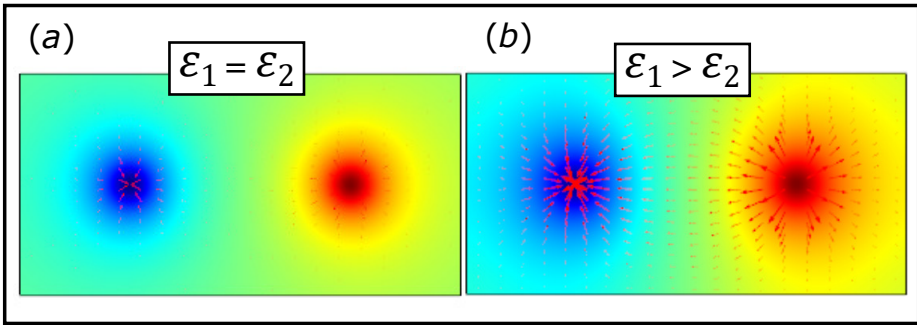


**Figure 1.7:** Two-dimensional in-plane representation of an exciton inside a NPL (a) without dielectric confinement and (b) in the presence of dielectric confinement between inorganic medium  $\epsilon_1$  and organic one  $\epsilon_2$ . Superficial colours on the NPL surface represent, qualitatively, the electric potential from positive (red) to negative (blue) charge and the superficial arrows represent the direction and magnitude of the electric field force.

With the objective of quantifying this dielectric confinement, it is often convenient (and physically intuitive) to face the problem like that of charges inside a homogeneous dielectric medium. In this manner, the effects coming from the different polarizability are considered by means of an induced superficial charge. [153, 154, 155] This superficial charge has a twofold effect, when  $\epsilon_1 > \epsilon_2$  (Fig. 1.7b), it intensifies the direct interactions between distinct particles, but also between each particle with the superficial image charge that each real particle generates<sup>8</sup>. The latter effect must be corrected since it makes no physical sense. To do so, a term called self-energy  $V_{(e,h)}^{self}$  is plugged into the single-particle Hamiltonian (1.23). Similarly,  $V_{pot}(\mathbf{r}_e, \mathbf{r}_h)$ , which is the polarized Coulomb interaction between the electron and hole. This term would be established in the general Hamiltonian (1.22). In the case of an exciton, a dielectric Hamiltonian

<sup>8</sup>When  $\epsilon_1 = \epsilon_2$  all the interactions are weakened (Fig. 1.7a).



containing these terms can be written as<sup>9</sup>

$$\hat{H}^{diel} = \sum_{k=e,h} \left[ \sum_{i=1}^{N_k} V_i^{self}(\mathbf{r}_i) \right] + \sum_{i=1}^{N_e} \sum_{j=1}^{N_h} V_{pol}(\mathbf{r}_{e,i}, \mathbf{r}_{h,j}) . \quad (1.31)$$

Both  $V_i^{self}$  and  $V_{pol}$  are responsible for the dielectric confinement modulation. For the case of  $\varepsilon_1 > \varepsilon_2$ ,  $V_{(e,h)}^{self}$  increases the system energy ( $> 0$ ) while  $V_{pol}(\mathbf{r}_e, \mathbf{r}_h)$  decreases it ( $< 0$ ). [156]

In strongly confined spherical QDs,  $V_i^{self}$  and  $V_{pol}$  cancel each other approximately. [148] In NRs, due to anisotropy, cancellation is less efficient, with  $V_i^{self}$  having greater influence than  $V_{pol}$ . This, once their longitudinal quantum confinement saturates, has led to energy blueshifts of up to 50 meV. [150] For NPLs, because of the combination of their ultrathin thickness and extreme anisotropy, the attraction of the electron and hole image charges partially compensates for the dominant repulsive effect of single-particle self-energies. [140] As a consequence, NPLs give rise to a whole gamut of energy blueshift values from  $\sim 25 - 50$  meV. [43, 47, 157] These values are the balance between lateral confinement and electron-hole interaction. For the case of self-energy terms, without considering lateral confinement, the energy blueshift can reach up to a few hundreds of meV. [47, 112] This conspicuous amplification of electrostatic interactions between carriers inside a NPL makes it essential to consider the dielectric confinement when studying this type of nanostructure.

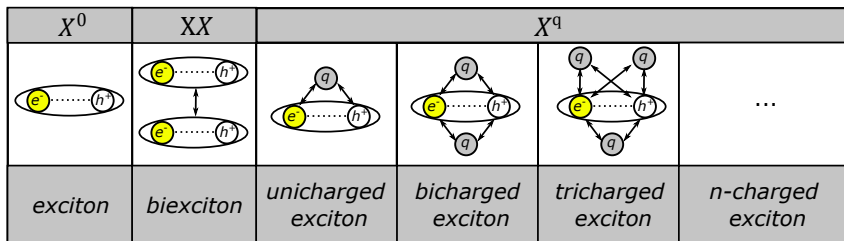


**Figure 1.8:** Different kind of excitonic species in nanostructures. The superscript  $q$  represent sign and number of spectator charges. When  $q$  is negative (positive) implies insertion of electrons (holes).

This change in interactions amplifies not only excitonic interactions – between electron and hole ground states, which are the most frequently encountered species in experiments – but also those interactions between (i) *a recombinant exciton and possible spectator charges*, which can form multicharged species (Fig. 1.8 –  $X^q$  species –) and, as shown in **Chapter 2 § 2.2**, can give rise to

<sup>9</sup>In reference [156] can be found explicitly  $V_{(e,h)}^{self}$  and  $V_{pol}$  terms for a dielectric quantum well.

*shake-up* processes<sup>10</sup>, for instance. [158, 159, 160] These processes, among others [114, 161, 157, 162] can contribute to a broadening of the emission band in CO and CS NPLs; [160, 163] (ii) or *within biexciton complexes* (Fig. 1.8 – **XX species** –), which are also of interest for applications in low-threshold lasing, [48] energy harvesting [164] and quantum cascade emission of photon pairs. [165] These biexciton complexes are formed, quite the opposite for excitons, when NPLs are exposed to high excitation power pumps. [166] At the same time, the above-mentioned change in interactions may lead to a different behaviour in NPLs, with respect to other nanostructures, in terms of charge injection [167, 168, 169] or multicharged species optics. [128, 170, 171, 172] Therefore, both (charge injection and multicharged species optics) are explored in this thesis, see **Chapter 2 § 2.3 and 2.4** along with the role that have shakeup processes in spectra linewidth broadening mediated by point charge electrostatic potentials  $V_{(e,h)}^{imp}$  inserted into the single-particle potential term  $V_i$  in equation (1.23), which modify electron and hole wavefunctions, see **Chapter 2 § 2.2**.

The terms accounting for electrostatic interactions in the Hamiltonian read

$$\hat{H}^{elect} = \hat{H}^{coul} + \hat{H}^{diel} + V_{(e,h)}^{imp}, \quad (1.32)$$

where the bare Coulomb interaction is given by

$$\hat{H}^{coul} = \sum_{i=1}^{N_e} \sum_{j=1}^{N_h} V_c(\mathbf{r}_{e,i}, \mathbf{r}_{h,j}) + \frac{1}{2} \sum_{k=e,h} \left[ \sum_{i=1, j \neq i}^{N_k} V_c(\mathbf{r}_{k,i}, \mathbf{r}_{k,j}) \right]. \quad (1.33)$$

That is, the interaction in a homogeneous dielectric environment.

## 1.5 Magnetic properties

The application of magnetic fields on nanocrystals has been used exhaustively in elucidating the fine structure of excitons in diverse semiconductor systems. [12, 173, 174, 175, 176]

Under external magnetic fields, excitons, which were optically active (bright excitons), may turn into optically inactive (dark excitons). This modification in the optical activity of excitons is due to the hybridization of their energy states. [173, 177, 178, 179, 180]

Beyond the interaction of the magnetic field with the exciton fine structure, there are other manifestations of magnetic effects that have been barely explored to date. One such effect is the **Aharonov-Bohm** (AB) phenomenon. [183] This

---

<sup>10</sup>It is a partly radiative Auger process, where an e-h pair recombines radiatively, giving part of its energy to an spectator charge (extra electron or hole). This spectator charge, consequently, promotes towards an excited state (this excitation happens in-plane).

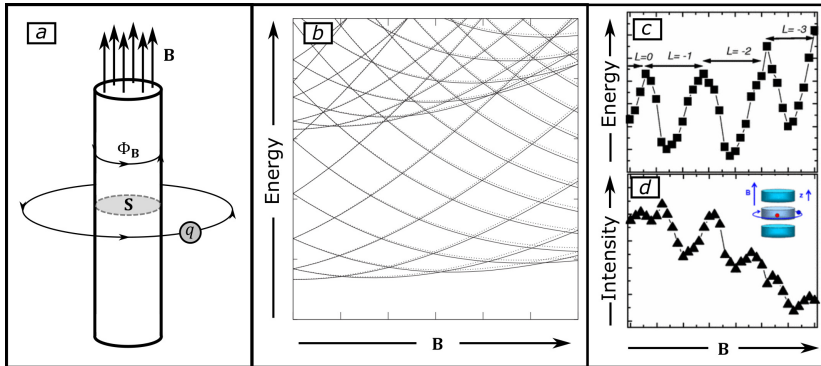


**Figure 1.9:** (a) Illustration of a magnetic field flux piercing the orbit of a charged carrier; (b,c,d) ground state oscillations as a function of an applied magnetic field  $\mathbf{B}$ : (b) Quantum ring. Adapted from the reference [181]. Copyright © 2005 IOP Publishing. (c,d) Type-II quantum disk. Adapted from the reference [182]. Copyright © 2008 American Physical Society.

phenomenon consists of the action that a potential vector exerts on quantum-mechanical particles in systems with doubly-connected topology. That is: a charge  $q$  orbiting around a doubly-connected region with non-zero magnetic flux ( $\Phi_{\mathbf{B}} = \int \mathbf{B} \cdot d\mathbf{S} \neq 0$ , Fig. 1.9a) acquires a Peierls phase, which turns out to be a periodic function of the magnetic flux  $\Phi_{\mathbf{B}}$ ,  $g = f(\Phi_{\mathbf{B}})$ , where its period is given by a quantum of magnetic flux  $\hbar/e$ . Remarkably, this occurs even if the magnetic field is zero in the region of the charge. It is the vector potential that affects this particle. [184]

A specific consequence of this phenomenon, which takes place in some nanostructures, is the so-called optical AB effect (oAB). [182, 185] This effect arises in doubly-connected structures if the electron and hole that form an exciton have a different mean radius. The magnetic flux (and the ensuing Berry phase) acquired by each carrier in the presence of an external field is then different. With increasing magnetic flux, the electron and hole ground state start changing their symmetry (that is, the so-called AB oscillations), but they do so at a different pace. At some values of the external field, the two carriers have different orbital symmetry. The optical transition across the band gap is then forbidden by selection rules. Thus, the external field emerges as a handy knob for turning on and off the optical recombination in the nanostructure. The question arises whether colloidal NCs, which are already implemented in optical display technologies, may also benefit from this effect. We address this question in type-II CC NPLs, where the doubly-connected topology of the crown [see Fig. 1.5b] enables one of the carriers to undergo AB oscillations.

Another important magnetic effect to consider is the formation of magnetic phases in nanostructures, as it could be paramagnetism. For example, by controlling the surface chemistry [159, 186] or charge [187, 188], in CdSe-based QDs,

paramagnetic centres can arise as the source of magnetism in these systems. Furthermore, the pronounced exchange interactions between electrons and holes, in these QDs, turn out to be an important feature in the way of obtaining magnetic ordering. [189] These exchange interactions, in NPLs, such as CO and CC, may be particularly relevant and may also become increased due to the strong quantum and dielectric confinement, in the out-of-plane direction, combined with the weak lateral confinement, over the in-plane directions, seen in these types of nanostructures. In a typical CdSe-based CO NPL with large lateral dimensions: first, the energy spacing between ground and first excited states is about 10 meV [92, 112, 190] and secondly, when applying magnetic fields perpendicularly to the NPL plane, considerable diamagnetic shifts are enabled through the radial part of the first term in equations (1.34) and (1.35). The mean squared radius,  $x^2 + y^2$  in both equation 1.34 and 1.35, increases with the lateral dimensions of the NPL, leading to significant diamagnetic shifts. As a consequence, these NPLs can give rise, with the application of attainable external magnetic fields, to paramagnetism mediated by dangling bonds [177, 191] – which have paramagnetic surface spins – or doping. [192, 193] Then, effects of paramagnetism in NPLs, when applying external magnetic fields, may result worthy of exploration.

In this thesis, then, it has been investigated as well, in type-II CC NPLs, whether the AB effect occurs and whether magnetic phases are formed when external magnetic fields are applied through systems containing multiple injected charges; see Chapter 2 § 2.5. To carry out our calculations regarding the magnetic effects pointed out above, for NPLs, axial magnetic fields are used<sup>11</sup>. For the case of 1-band electrons (spin  $\uparrow$  or spin  $\downarrow$ ) and using a potential vector with symmetric gauge  $\mathbf{A} = \frac{B_z}{2}(-y, x, 0)$ , which provides an out-of-plane magnetic field  $\mathbf{B} = \nabla \times \mathbf{A} = (0, 0, B_z)$ , the following magnetic Hamiltonian  $\hat{H}_e^B$  can be used:

$$\hat{H}_e^B = \sum_{i=1}^{N_e} \left( \frac{B_z^2}{8m_{\perp,e}^*} (x^2 + y^2) + \frac{B_z}{2m_{\perp,e}^*} (x\hat{p}_y - y\hat{p}_x) + g_e \mu_B B_z \sigma_z \right), \quad (1.34)$$

where  $B_z$  is the axial magnetic field,  $m_{\perp,e}^*$  the in-plane electron effective mass,  $g_e$  the electron gyromagnetic constant,  $\mu_B$  the Bohr magneton,  $x$  and  $y$  are the in-plane coordinates,  $\hat{p}_x$  and  $\hat{p}_y$  the in-plane momentum operator components and  $\sigma_z$  is the Pauli matrix in the direction  $z$ . In the case of holes, it must be taken into consideration that, in 1-band models, electron and hole dispersion energies are considered, qualitatively, as mirror images of each other. [194] Then, the hole magnetic Hamiltonian would be

---

<sup>11</sup>The use of axial magnetic fields in NPLs is motivated by the fact that carriers can move more freely over all the extended lateral dimensions, affecting to a greater extent the Bohr radius of excitons, or other formed species. [77]

$$\hat{H}_h^B = \sum_{i=1}^{N_h} \left( -\frac{B_z^2}{8m_{\perp,h}^*} (x^2 + y^2) - \frac{B_z}{2m_{\perp,h}^*} (x\hat{p}_y - y\hat{p}_x) - 3g_h\mu_B B_z \sigma_z \right). \quad (1.35)$$

Note that in equation (1.35), in contrast with equation (1.34): (i) the signs between terms change from additions to subtractions and (ii) the extra 3 in the Zeeman(last) term, which is given by the heavy hole pseudospin  $\pm 3/2$ .

Equations (1.34) and (1.35) can be rewritten to account for many-body systems and set them in  $\hat{H}^B$  leading to

$$\hat{H}^B = \sum_{k=e,h} \left[ \sum_{i=1}^{N_k} \hat{H}_{k,i}^B \right]. \quad (1.36)$$

To bring together all the effects seen so far (elastic, electrostatic, and magnetic effects) in the same Hamiltonian, it can be written from equations (1.23), (1.25), (1.26), (1.32), and (1.36), the following expression

$$\hat{H} = \frac{1}{2} \left( \sum_{i=1}^{N_e} \left[ \frac{\mathbf{p}_{e,i}^2}{m_{e,i}^*} + 2\hat{H}_{e,i}^B \right] + \sum_{j=1}^{N_h} \left[ \frac{\mathbf{p}_{h,j}^2}{m_{h,j}^*} + 2\hat{H}_{h,j}^B \right] + \sum_{k=e,h} \left[ \sum_{i=1, j \neq i}^{N_k} V_c(\mathbf{r}_{k,i}, \mathbf{r}_{k,j}) \right] \right) + \sum_{i=1}^{N_e} \sum_{j=1}^{N_h} (V_{e,i} + V_{h,j} + V_c(\mathbf{r}_{e,i}, \mathbf{r}_{h,j}) + V_{pol}(\mathbf{r}_{e,i}, \mathbf{r}_{h,j})) , \quad (1.37)$$

where the single-particle potential terms can be expanded as

$$V_{e,i} = V_{e,i}^{bo} + V_{e,i}^{self} + V_{e,i}^{strain,dp} + V_{e,i}^{strain,pz} + V_e^{imp} \quad (1.38)$$

$$V_{h,j} = V_{h,j}^{bo} + V_{h,j}^{self} + V_{h,j}^{strain,dp} + V_{h,j}^{strain,pz} + V_h^{imp} . \quad (1.39)$$

Then, manipulating equations (1.37) along with (1.38) and (1.39), in this doctoral programme, different studies have been carried out on phenomena of interest, mainly in NPLs, within the  $k \cdot p$ -**EFA** method, leading to a collection of published articles and the elaboration of this thesis.

# Chapter 2

## Publications

### 2.1 Strain in Lattice-Mismatched Nanoplatelets

”Strain in Lattice-Mismatched CdSe-Based Core/Shell Nanoplatelets.”

Jordi Llusar, Josep Planelles, and Juan I. Climente.

*J. Phys. Chem. C* **2019** *123* (34), 21299-21306

DOI: <https://doi.org/10.1021/acs.jpcc.9b06577>

#### Abstract:

We investigate the role of stress arising between core and shell materials in colloidal CdSe/X hetero-nanoplatelets (X = ZnS, CdS, CdTe). The resulting strain distribution is calculated within the linear elastic regime and also its influence on the electronic structure with  $k \cdot p$  theory. We show that strain shifts the energy of electrons and that of holes by several tens of millielectronvolts (meV). In structures with type I band alignment, the two shifts have opposite signs and the net effect on the exciton emission energy is small, but both these add up in type II systems. The strain response in colloidal nanoplatelets (NPLs) is found to exhibit some differences as compared to that of epitaxial quantum wells, including a sizable influence of lateral dimensions below 10 nm and a potentially relevant effect of coupled strain–momentum terms of the Hamiltonian. We further show that an asymmetric shell covering leads to bending of the nanoplatelet and tilted potential profiles along the strong confinement direction, analogous to a built-in electric field. We propose overcoating CdSe/CdS NPLs with an outer ZnS shell as a method to mitigate the tunneling-induced red shift of emission via strain engineering.

# **Strain in lattice mismatched CdSe-based core/shell nanoplatelets**

Jordi Llusar, Josep Planelles, and Juan I. Climente\*

*Departament de Química Física i Analítica, Universitat Jaume I, E-12080, Castelló de la  
Plana, Spain*

E-mail: [climente@uji.es](mailto:climente@uji.es)

## Abstract

We investigate the role of the stress arising between core and shell materials in colloidal CdSe/X hetero-nanoplatelets (X=ZnS,CdS,CdTe). The resulting strain distribution is calculated within the linear elastic regime, and its influence on the electronic structure with k-p theory. We show that strain shifts the energy of electrons and that of holes by several tens of meV. In structures with type-I band alignment the two shifts have opposite signs and the net effect on the exciton emission energy is small, but in type-II systems they add up. The strain response in colloidal NPLs is found to exhibit some differences as compared to that of epitaxial quantum wells, including sizable influence of lateral dimensions below 10 nm and potentially relevant effect of coupled strain-momentum terms of the Hamiltonian. We further show that asymmetric shell covering leads to bending of the nanoplatelet and tilted potential profiles along the strong confinement direction, analogous to a built-in electric field. We propose overcoating CdSe/CdS NPLs with an outer ZnS shell as a method to mitigate tunneling-induced redshift of emission via strain engineering.



# Introduction

In the last decade, quasi-two-dimensional colloidal metal chalcogenide semiconductors –often referred to as nanoplatelets (NPLs)– have emerged as an alternative to quantum dots for a variety of optoelectronic applications.<sup>1</sup> Many properties of interest have been reported, often related to their 2D dimensionality. Thus, precisely controllable quantum confinement in one direction enables narrow emission linewidths and reduced Auger recombination rates. At the same time, the large in-plane area grants large absorption cross-sections and giant oscillator strength through exciton correlation.<sup>1–4</sup>

The large surface-to-volume ratio of NPLs makes them highly sensitive to the environment.<sup>5,6</sup> Attempts have been made to passivate the surface of CdSe NPLs by growing either core/crown heterostructures<sup>7,8</sup> or core/shell ones,<sup>9–12,15</sup> which have succeeded in improving the emission quantum yield and stability. However, the addition of shell materials has a profound impact on the electronic structure too. As compared to core-only CdSe NPLs, CdSe/ZnS hetero-NPLs display redshifts of up to 300-400 meV and CdSe/CdS ones up to 500 meV.<sup>12–14,16,17</sup> The origin of such a large redshift has been discussed in the literature. Some studies suggest it simply arises from carrier tunneling into the shell, which relaxes quantum confinement.<sup>13,14,17</sup> Others claim instead that tunneling in CdSe/ZnS is hindered by the large band-offset (around 1 eV) and suggest the decrease in dielectric confinement upon shell growth provides an additional, non-negligible contribution to the redshift.<sup>12</sup> On the other hand, CdSe has significant lattice mismatch with both CdS (4%) and ZnS (12%). Therefore, strain is also expected to play a role. Achtstein et al. calculated the effect of linear elastic strain on the exciton energy of CdSe/CdS NPLs, and concluded it gives a moderate blueshift of the exciton energy.<sup>17</sup> By contrast, Luo et al. grew CdSe/ZnS NPLs for solar cell devices and inferred from photoluminescence and open current voltage measurements that strain was producing a redshift, and possibly type-II band alignment.<sup>18</sup> In this context, a thorough study of the influence of elastic strain in lattice mismatched hetero-NPLs is on demand.

In free-standing colloidal hetero-nanocrystals, strain engineering has proved to be a powerful tool to modulate exciton energy and wave function, with direct implications on the optoelectronic response.<sup>19–21</sup> Likewise, in epitaxial quantum wells, strain engineering of the band structure has been key to reducing lasing threshold and optimizing laser performance.<sup>22</sup> Since core/shell NPLs are the colloidal analogous of epitaxial quantum wells, the question arises of whether strain can also give rise to significant changes of the electronic structure, and whether they take place in the same way as in epitaxial quantum wells. In this work, we address such questions for lattice mismatched hetero-NPLs.

We study core/shell NPLs with binary CdSe/X composition (X=CdS, ZnS, CdTe). The strain is calculated within linear elastic theory, and the effect of the resulting deformation potential on excitons is computed with effective mass Hamiltonians fully including electronic correlation effects, which are critical in these structures owing to the weak lateral spatial confinement and strong dielectric mismatch.<sup>26,27</sup> We find that the strain response of colloidal NPLs is reminiscent of that epitaxial quantum wells, albeit with some qualitative differences. The finite lateral size of the NPL influences the strain value in the core for dimensions below  $\sim 10$  nm. Also, coupled strain-momentum terms of the Hamiltonian, which are negligible in epitaxial systems, have a moderate impact on the exciton energy (up to tens of meV) due to the stronger quantum confinement of colloidal structures. In CdSe/CdS and CdSe/ZnS NPLs, the compressive strain inside the core blueshifts and redshifts electron and hole energies, respectively. For neutral excitons, the two effects tend to compensate and the energetic imprint of strain is weak. The effect is stronger for excitons in type-II CdSe/CdTe NPLs, as the electron stays in the tensiled core but the hole migrates into the compressed shell, so that the two carriers redshift. In all cases, however, the strain effect on the emission energy is found to be secondary as compared to tunneling into the shell. We propose the use of ternary structures, such CdSe/CdS/ZnS NPLs, as a means of decoupling tunneling and strain effects. Interestingly, we show that a slightly asymmetric shell covering –different number of shell monolayers (MLs) on top and bottom sides of the core– can explain the

bending of NPLs observed in recent experiments with CdSe/ZnS NPLs.<sup>12</sup>

## Methods

Strain maps are calculated by minimizing the elastic energy in the anisotropic continuous mechanical model.<sup>28</sup> The boundary conditions are zero normal stress for the free surface.<sup>29</sup> The strain tensor elements  $\epsilon_{ij}(\mathbf{r})$  is obtained using the multiphysics mode of Comsol 4.2 software. Exciton states are calculated following Ref.,<sup>26</sup> but adding strain-induced potential terms. Thus, excitons are described by the Hamiltonian:

$$H^X = H^e + H^h + V^{e-h} + E_{\Gamma}^{gap}, \quad (1)$$

where  $E_{\Gamma}^{gap}$  is the bulk band gap of CdSe at the  $\Gamma$  point,  $V^{e-h}$  is the electron-hole Coulomb attraction including dielectric mismatch enhancement, and  $H^j$  are the single-particle Hamiltonians for electron ( $j = e$ ) and hole ( $j = h$ ). These are 3D single-band k-p Hamiltonians of the form  $H^j = H_{kin}^j + V^j$ , where  $H_{kin}^j$  is the kinetic energy term and  $V^j$  the single-particle potential. The latter can be split into several terms:

$$V^j = V_{bo}^j + V_{self}^j + V_{strain}^j. \quad (2)$$

where  $V_{bo}^j$  is the spatial confining potential defined by the (bulk) band offsets between CdSe and the shell material,  $V_{self}^j$  the self-interaction potential due to the inhomogeneous dielectric environment, and  $V_{strain}^j$  the strain-induced potential. Within deformation potential theory, up to first order in  $\epsilon$  and second in  $k$ , the general form of the strain terms in a k-p Hamiltonian is:<sup>22</sup>

$$H_{strain} = \mathbf{D}^{\epsilon} \cdot \boldsymbol{\epsilon} - \frac{\mathbf{k}\boldsymbol{\epsilon}\mathbf{k}}{m_0} - 2 \frac{\mathbf{k}\boldsymbol{\epsilon}\mathbf{p}}{m_0}. \quad (3)$$

Here,  $\boldsymbol{\epsilon}$  and  $\mathbf{D}^{\epsilon}$  the strain and deformation potential tensors,  $m_0$  the free electron mass,  $\mathbf{k}$  the momentum operator acting on the envelope function and  $\mathbf{p}$  that acting on the (microscopic)

Bloch function. The second term in Eq. (3) describes the change in the kinetic energy due to the strain, and it is generally neglected in the study of epitaxial quantum wells because it is expected to be smaller than terms containing  $\varepsilon$  alone.<sup>22</sup> However, we keep the  $k_z$  component because the strong confinement of colloidal NPLs along [001] suggests it can become relevant, as we confirm in the next section. When projected on the conduction band (CB) Bloch function, Eq. (3) gives rise to  $V_{strain}^e = V_{strain}^{dp,e} + V_{strain}^{pz,e}$ , with:

$$V_{strain}^{dp,e} = a_c (\varepsilon_{xx} + \varepsilon_{yy} + \varepsilon_{zz}), \quad (4)$$

and

$$V_{strain}^{pz,e} = -\frac{k_z \varepsilon_{zz} k_z}{m_{e,z}^*}, \quad (5)$$

Here  $a_c$  is a material dependent deformation potential coefficient,  $k_z = -i\hbar d/dz$  and  $m_{e,z}^*$  the electron effective mass along  $z$ . Notice the last term of Eq. (3) vanishes in  $V_{strain}^e$  because  $\mathbf{p}$  has odd parity. Likewise, when projected on the valence band (VB) heavy hole Bloch function, Eq. (3) gives  $V_{strain}^h = V_{strain}^{dp,h} + V_{strain}^{pz,h}$ , with:

$$V_{strain}^{dp,h} = \left(a_v + \frac{b}{2}\right) (\varepsilon_{xx} + \varepsilon_{yy}) + (a_v - b)\varepsilon_{zz}, \quad (6)$$

and

$$V_{strain}^{pz,h} = -\frac{k_z \varepsilon_{zz} k_z}{m_{h,z}^*}, \quad (7)$$

where  $a_v$  and  $b$  are deformation potential coefficients, and  $m_{h,z}^*$  the hole effective mass along  $z$ . As we shall see below, strain is roughly constant around the center of the NPL plane, where most of the charge density is located. For this reason, it is a good approximation to describe  $V_{strain}^e$  and  $V_{strain}^h$  simply as functions of  $z$ , taken along the axis orthogonal to the NPL plane. Piezoelectric terms are neglected in this study because they are negligible in CdSe-based hetero-NPLs with cubic crystal structure.<sup>17</sup>

Hamiltonian (1) is solved variationally by optimizing the effective exciton Bohr radius.<sup>26</sup>

Material parameters used in the calculation are given in the Supporting Information.

## Results and discussion

Our goal is to study the strain distribution in core/shell NPLs and its influence on the electronic structure. We first analyze in detail the prototypical case of CdSe core surrounded by a shell of CdS, ZnS or CdTe. The shell is symmetric on top and bottom. Next, we analyze the effect of having asymmetric shell coating, and show that this deviation from ideality can explain a few features observed in recent experiments. Last, building on the behavior observed in previous sections, we briefly address the case of ternary NPLs, to illustrate the potential of strain engineering in such systems.

### Symmetric core/shell NPLs

Finite and controllable lateral confinement is a distinct feature of colloidal NPLs as compared to epitaxial quantum wells. We then start by studying if it has a significant effect on the strain experienced inside the platelet. We consider CdSe/CdS NPLs with 4.5 ML CdSe core and 5 ML shell thickness, and calculate the hydrostatic strain,  $\varepsilon_{hyd} = \varepsilon_{xx} + \varepsilon_{yy} + \varepsilon_{zz}$ , for the three different lateral dimensions shown in Figure 1(a-c).

In general,  $\varepsilon_{hyd}$  is compressive in the CdSe core and tensile in the CdS shell (Fig. S1). Because the ground state charge density is mostly localized inside the core, it is worth inspecting this region in detail. The corresponding values of  $\varepsilon_{hyd}$  on the mid-height  $xy$  plane of the core are plotted in Figure 1(d-f), and a cross-section comparing the strain in all three structures along the  $x$  semi-axis is shown in Figure 1(g). The general behavior is as follows. A flat area of compressive strain ( $\varepsilon_{hyd} < 0$ ) is formed around the center of the NPL, which extends towards the sides. About 5 nm before reaching the border, the strain becomes slightly more compressive and in the close vicinity of the border ( $< 1$  nm), it switches to tensile ( $\varepsilon_{hyd} > 0$ ). The compressive character is because of the larger lattice constant of the

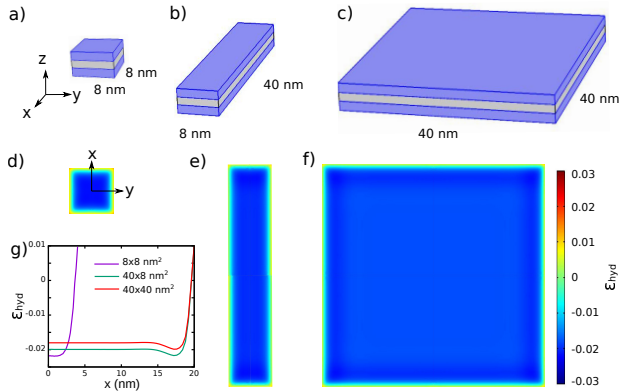


Figure 1: Effect of the lateral sides on strain. (a-c) Schematic of core-shell NPLs with different lateral dimensions. The CdSe core has 4.5 ML and the CdS shell 5 ML thickness. (d-f) Corresponding values of hydrostatic strain over the  $xy$  plane at mid-height of the core. (g) Hydrostatic strain cross-section along the  $x$  semi-axis for different lateral dimensions. A flat area of compressive strain is formed around the center, with deviations in the vicinity ( $\sim 5$  nm) of the borders. NPLs with smaller lateral dimensions are more compressed.

CdSe core, which needs to shrink to reduce lattice mismatch with the CdS shell. The tensile character near the borders, instead, is a compensation for the central contraction, which is facilitated by the absence of forces acting on the lateral sides.

Since the strain potential felt by electrons is  $V_{strain}^e = a_c \epsilon_{hyd}$ , with  $a_c = -2$  eV for CdSe, the increase in compressive character near the borders gives rise to a small potential barrier, while the sudden switch to tensile strain yields a narrow potential well near the borders. These effects modify the effective size of the NPL because quantum confinement in the plane is very weak, but the ground state wave function is only slightly perturbed and stays around the center of the core (Fig. S2). In the center of the core, strain is also affected by lateral confinement, as  $\epsilon_{hyd}$  grows stronger with decreasing dimensions  $\sim 20\%$  increase from  $40 \times 40$  nm<sup>2</sup> to  $8 \times 8$  nm<sup>2</sup>, see Fig. 1(g). This will blueshift the electron energy through  $V_{strain}^e$  by a several meV. It is worth noting that this magnitude is comparable to that of lateral quantum confinement itself,<sup>26,30</sup> and provides a source of linewidth broadening in ensembles of core/shell NPLs.

In what follows, we focus on NPLs with  $40 \times 8$  nm<sup>2</sup> sides, which is close to the experi-

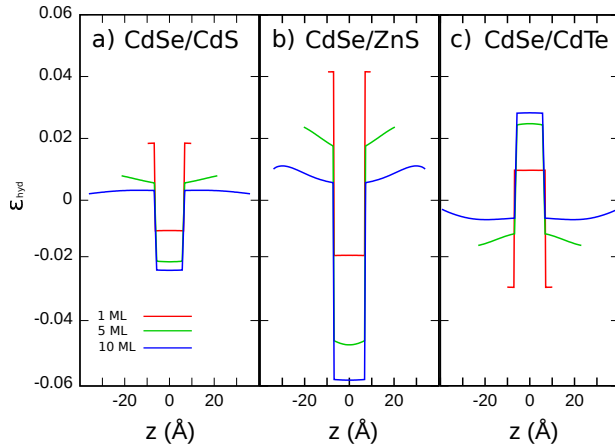


Figure 2: Effect of shell thickness and composition on the hydrostatic strain. (a) CdSe/CdS NPL. (b) CdSe/ZnS NPL. (c) CdSe/CdTe NPL. The strain is taken along the  $z$  axis, passing through the NPL center, normal to the its surface.

mental dimensions of recent works.<sup>12,13</sup> In Figure 2 we study the effect of shell thickness and composition on  $\varepsilon_{hyd}$  along the  $z$  axis. For CdSe/CdS and CdSe/ZnS, the strain is compressive in the core and tensile in the shell, while the opposite occurs for CdSe/CdTe because the lattice constant of the CdTe shell is larger than that of the CdSe core. In all cases, the core (shell) becomes more (less) strained with increasing shell thickness. This is because the thicker material forces the thinner one to endure most of the deformation. The net compressive (CdS, ZnS shells) or tensile (CdTe shell) character of  $\varepsilon_{hyd}$  in the core is given by  $\varepsilon_{xx} + \varepsilon_{yy}$ . Since the interface between core and shell lies on the  $xy$  plane, the magnitude of this term is larger than that of  $\varepsilon_{zz}$ , which has opposite sign as expected from the Poisson ratio (see Figure S3). This is precisely the opposite behavior to that of core/shell nanorods.<sup>29</sup> In the center of the NPL, we find the ratio between lateral contraction and vertical expansion –or vice-versa– closely follows the biaxial strain expression for cubic crystals,  $\varepsilon_{zz} = -2c_{12}/c_{11} \varepsilon_{xx}$ , as in epitaxial quantum wells.<sup>22</sup>

From the diagonal elements of the strain tensor one can infer the strain-induced deformation potential,  $V_{strain}^{dp,e}$  and  $V_{strain}^{dp,h}$ , which we plot in Figure 3. The figure shows that, inside compressed cores, a shift of the CB bottom to higher energies takes place, which saturates

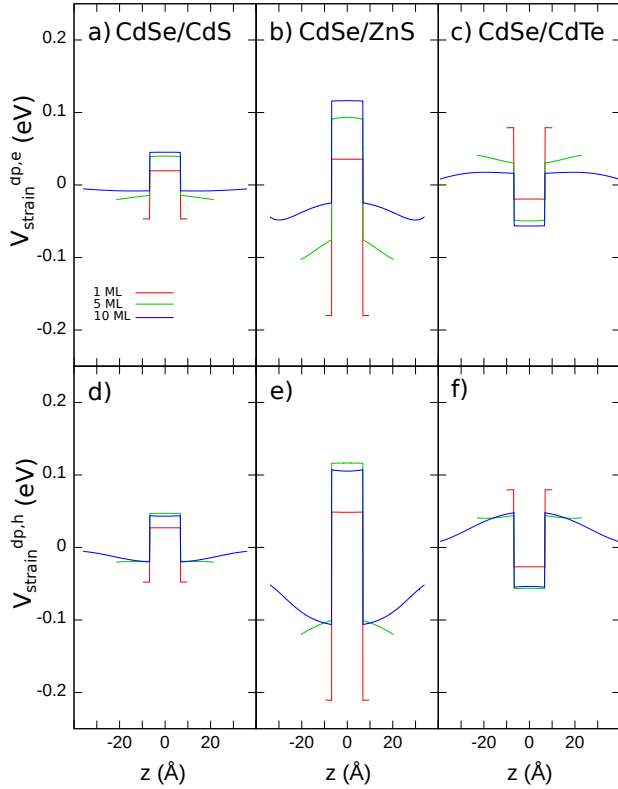


Figure 3: Effect of shell thickness and composition on the deformation potential for CB (top panels) and VB (bottom panels). (a,d) CdSe/CdS NPL. (b,e) CdSe/ZnS NPL. (c,f) CdSe/CdTe NPL.

at about 50 meV (CdSe/CdS, Fig. 3(a)) and 120 meV (CdSe/ZnS, Fig. 3(b)). Conversely, when the core is under tensile strain (CdSe/CdTe), the CB shifts to lower energies (down to -60 meV, Fig. 3(c)). This modifies the band offsets seen by electrons, providing energetic corrections which have been overlooked in previous simulations of hetero-NPLs disregarding strain.<sup>12–14,26</sup> The good agreement between theory and experiments in such works is because for holes the behavior is similar to that of electrons. As shown in Fig. 3(d-f), strain also shifts the VB top towards higher (lower) energies when the core is compressed (expanded).<sup>31</sup> Even the magnitude of the shift is comparable, despite the anisotropic nature of  $V_{strain}^{dp,h}$ . Then, the shift of electrons and holes partially compensates, and the exciton emission energy is not



expected to change drastically.

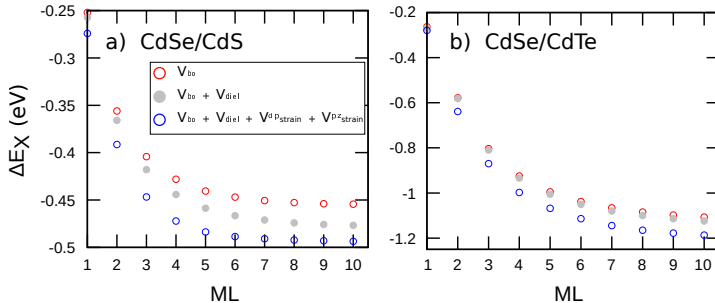


Figure 4: Exciton energy as a function of the shell thickness in (a) CdSe/CdS and (b) CdSe/CdTe NPLs. Red circles show results considering tunneling only. Grey dots include dielectric effects too. Blue circles further add strain effects. All energies are referred to that of the exciton in core-only CdSe NPL.

To better visualize and understand the role of strain on the exciton ground state, we calculate its energy from  $H^X$ , with full inclusion of in-plane Coulomb interaction, for different shell natures. First, we focus on the case of CdSe/CdS NPLs. Fig. 4(a) shows the exciton energy shift in CdSe NPLs with  $n$  MLs of CdS shell on each side, as compared to the core-only CdSe NPL. Red circles show the case where dielectric confinement ( $V_{self}^j$ , polarization of  $V^{e-h}$ ) and strain terms ( $V_{strain}^j$ ) are neglected. The exciton is then found to redshift by 454 meV upon shell growth, due to electron leaking into CdS. The inclusion of dielectric confinement terms gives rise to an additional redshift of up to 23 meV (grey dots). This effect was noticed in Ref.<sup>12</sup> and is a consequence of the suppression of self-interaction potential energy. Further including strain terms provides yet an extra 17 meV redshift (blue circles). As anticipated above, the energetic effect of strain is relatively small, owing to the compensation of electron and hole shifts. We note that a previous theoretical study indicated that strain in CdSe/CdS NPLs gives rise to a blueshift instead.<sup>17</sup> This is due to the different parameters used for deformation potential and elastic constants, as there is enough dispersion in the literature to change the net sign of strain energy perturbation (see discussion in SI). In any case, for all set of parameters we find that in CdSe/CdS NPLs strain is secondary term (few tens of meV) as compared to tunneling (hundreds of meV).

Next we consider the case of CdSe/CdTe NPLs. As can be seen in Fig. 4(b) –cf. blue circles and grey dots–, here strain produces an exciton energy redshift up to 63 meV, almost 4 times larger than in CdSe/CdS. This is because of the type-II band alignment, which places the electron inside the tensiled CdSe core and the hole inside the compressed CdTe shell. Then, both carriers redshift and there is no cancellation. However, the strain effect is still but a perturbation to the confinement energy set by the staggered band-offset (red dots in the figure).

In CdSe/ZnS NPLs, photoluminescence experiments have shown shell growth leads to a large redshift (300-400 meV, for 4.5 ML cores).<sup>12,14</sup> Because the band-offset between CdSe and ZnS is around 1 eV, tunneling is expected to be less important than with CdS or CdTe shells. By contrast, the lattice mismatch is large (over 10%). For this reason, some studies have suggested strain may play a chief role in determining the redshift, and may even lead to a type-II band alignment.<sup>18</sup> To clarify the influence of strain in these structures, in Figure 5 we plot the exciton energy as a function of the ZnS shell thickness. The result is similar to that of CdSe/CdS, with a large redshift whose main contribution (320 meV) comes from tunneling. Strain provides a redshift of about 34 meV, which is 1.5 times larger than the dielectric confinement suppression proposed in Ref.<sup>12</sup> All in all, the redshift is mostly due to tunneling plus strain, with no need to invoke indirect excitons, as the band alignment stays type-I –see Fig. 3–. Further, we note that strain builds up gradually with increasing shell thickness. Consequently, in Fig. 5 the energy splitting between strained (blue circles) and unstrained (red circles) exciton shifts increases from 1 to 5 ML. Therefore, the large redshift (up to 200 meV) reported by photoluminescence and atomistic studies upon growth of the first ML of shell<sup>16,17,32,33</sup> must be associated primarily with the reduced spatial confinement, with a minor contribution from strain.

The blue circles in Figure 5 indicate that the fully strained exciton should have minimum energy between 4-5 MLs of ZnS. The origin of this inflection point is as follows. With increasing strain, the electron energy blueshifts and that of the hole redshifts, due to changes

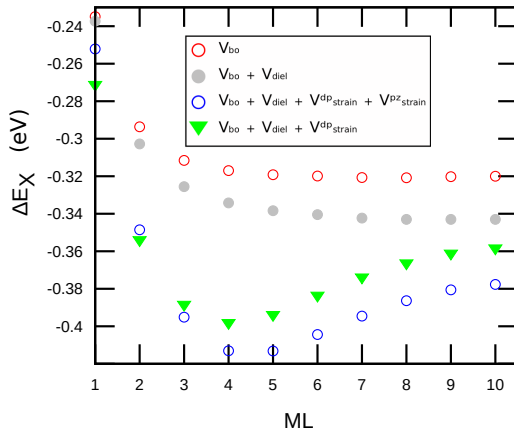


Figure 5: Exciton energy as a function of the shell thickness in CdSe/ZnS. Energies are referred to that of the exciton in core-only CdSe NPL. Strain has a stronger contribution to the overall redshift than in CdSe/CdS. A sizable part of the redshift is due to the relaxed quantum confinement when the CdSe core expands vertically,  $V_{pz,e} + V_{pz,h}$ .  $V_{diel}$  stands for dielectric effects ( $V_{self}$  and polarization of  $V^{e-h}$ ).

in the deformation potential reported in Fig. 3(b) and (e). For 1-5 ML, the hole redshift dominates over the electron blueshift. With increasing shell thickness, however, vertical expansion of the core becomes more difficult. Then,  $\varepsilon_{zz}$  saturates around 4-5 ML. Since the hole redshift is mostly given by  $(a_v - b)\varepsilon_{zz}$ , from this distance on the electron blueshift takes over. We have tested that the minimum is robust to different sets of material parameters and interface alloying effects. However, it has not been observed in available experiments so far, where exciton emission energy decreases monotonically.<sup>12,14</sup> A possible interpretation of the experimental results is given in the next section.

To close the study of symmetric core/shell NPLs, we note that a recent study about the influence of surface ligands on CdSe NPL emission has suggested that the strain induced by ligands is responsible for large exciton redshifts of up to 250 meV.<sup>23</sup> The underlying idea is that the compressive in-plane stress gives rise to transversal expansion, which in turn reduces the extreme quantum confinement. While our continuum mechanical model is not suitable for the study of molecular ligands, we investigate if a similar effect can be expected in strained core/shell structures. The reduced quantum confinement due to transversal

expansion should be captured by coupled momentum-strain operators,  $V_{strain}^{pz,e}$  and  $V_{strain}^{pz,h}$  in Eqs. (5) and (7). Green triangles in Fig. 5 show the energy of strained excitons neglecting  $V_{strain}^{pz}$  terms, while blue circles show the fully strained system. The comparison reveals that the strain-induced expansion of the core gives rise to a redshift of about 20 meV, comparable to the contribution of deformation potential terms,  $V_{strain}^{dp}$ . This is one order of magnitude smaller than the redshift suggested for ligand-induced strain,<sup>23</sup> but clearly larger than in epitaxial quantum wells, where these terms are systematically neglected arguing they are much weaker than (linear-in- $\varepsilon$ ) deformation potential terms. The different behavior arises from quantum confinement in colloidal NPLs being much stronger than in epitaxial wells, with higher potential barriers –set by the ligands– and often thinner dimensions.<sup>3,24</sup>

## Asymmetric core/shell NPLs

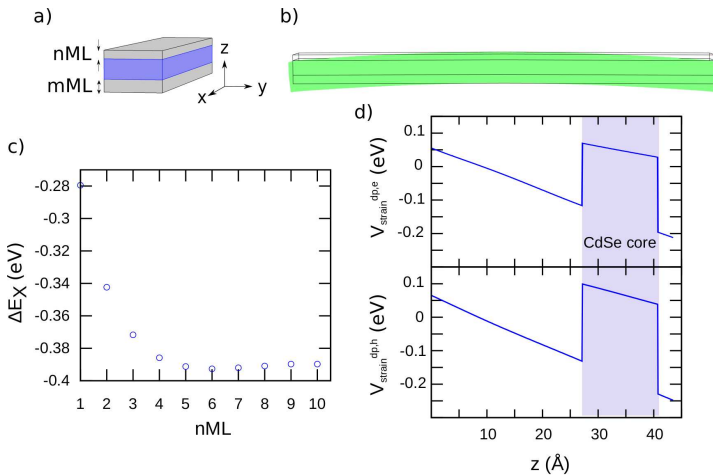


Figure 6: CdSe/ZnS NPLs with asymmetric shell distribution. (a) Schematic of the structure. Different number of shell MLs  $n$  and  $m$  are considered. (b) Total displacement of the NPL upon strain relaxation in a NPL with  $n = 5$  and  $m = 6$ . Notice the bending on the sides. (c) Exciton energy shift as a function of shell thickness.  $m = n + 1$ . The energy decreases monotonically and stabilizes around 5 MLs, in agreement with experiments. (d) Deformation potential for electrons and holes in a NPLs with  $n = 1$  and  $m = 10$ . The asymmetric shell gives rise to a small tilting of the potential.

The growth of shells around a core NPL is susceptible of small accidental or intentional asymmetries. We then consider a CdSe/ZnS NPL with  $n$  and  $m$  ZnS MLs on the top and bottom sides of the core, respectively –see schematic in Fig. 6(a)–. Interestingly, in such a structure a single ML difference between  $n$  and  $m$  suffices to give rise to bent hetero-NPLs, owing to the unbalanced strain on top and bottom sides. An example is plotted in Fig. 6(b). The presence of bending is in fact consistent with high-angle annular dark-field scanning transmission electron microscope images of thick shell CdSe/ZnS NPLs.<sup>12</sup> We have tested that the bending does not modify the electron and hole wave function localization significantly, as they stay near the center. Yet, it has a clear impact on the emission energy. In Fig. 6(c) we plot the exciton shift with respect to the core-only NPL with increasing shell thickness, keeping one extra ML for the bottom shell ( $m = n + 1$ ). Unlike in the symmetric case, the shift now decreases monotonically, in agreement with the experiments in Refs.<sup>12,14</sup> Both the bending and the smooth redshift support the hypothesis that CdSe/ZnS hetero-NPLs may have slightly asymmetric shell. It is worth noting that the asymmetric strain also induces band tilting through  $V_{strain}^{dp}$  terms. This is illustrated in Fig. 6(d). In Ref.,<sup>18</sup> CdSe NPLs deposited on a porous TiO<sub>2</sub> film were overcoated with ZnS. This synthetic procedure may lead to severe shell asymmetry. In principle, the asymmetry and the resulting band tilting –which acts as an built-in electric field, and increases with the difference between  $m$  and  $n$ – may explain the type-II band alignment inferred from the experiments. However, we find that even for large differences between  $m$  and  $n$ , the field is only of 35 meV/nm. Considering the strong confinement in the  $z$  direction, it is not enough to separate electrons from holes.

## Core/shell/shell NPLs

As mentioned before, the use of CdS shells to passivate the CdSe NPL surface can improve the emission quantum yields and stability. However, it necessarily implies a redshift of the emission wavelength due to the reduced quantum confinement, dielectric and strain effects

discussed in previous sections. This is sometimes an undesired side effect, as one may want to preserve high emission energy. In this section we propose a means of partially mitigating the redshift, by exploiting the different sensitivity of CB and VB deformation potential to the shell thickness, which we noticed in the analysis of Fig. 5. The idea is to design a ternary NPL, where the CdSe/CdS NPL is overcoated with ZnS, as plotted in Fig. 7(a). Fig. 7(b) shows the exciton energy shift upon ZnS coating. If the thickness of the CdS shell is small (2 MLs, left panel), the effect of ZnS is producing a small additional redshift ( $\Delta E_X < 0$ ), since it facilitates tunneling as compared to organic ligands. However, as CdS grows thicker (5 MLs, right panel), tunneling effects saturate and one observes strain effects only. Then, ZnS starts blueshifting the exciton energy ( $\Delta E_X > 0$ ). For thick ZnS shells, the blueshift can reach around 60 meV. This is in contrast with the behavior of binary (core/shell) CdSe/ZnS NPLs reported in Fig. 5, where the main effect of ZnS is to redshift.

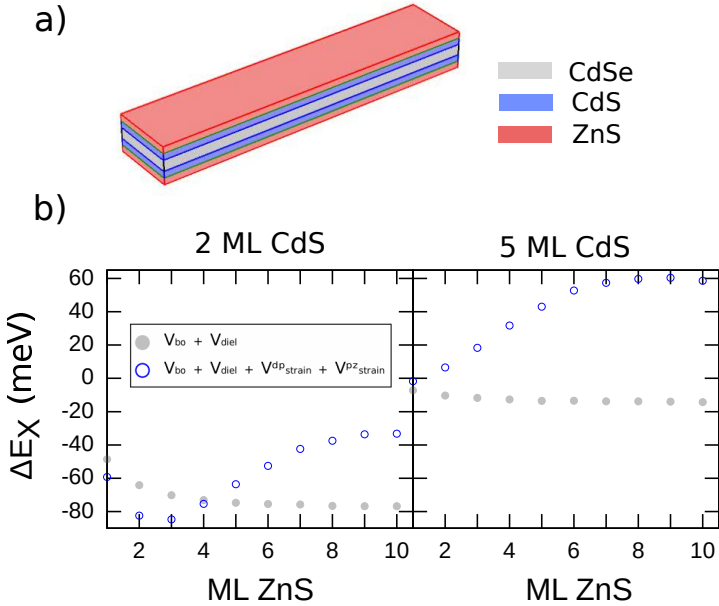


Figure 7: (a) Schematic of the core/shell/shell NPL under study. (b) Exciton energy shift as a function of the number of MLs of ZnS surrounding CdSe/CdS NPL. Left: CdS has 2 ML thickness. Right: CdS has 5 ML thickness. Energies are referred to that of CdSe/CdS NPL. The strain induced by the outer ZnS shell can give rise to a blueshift of tens of meV.

The origin of the strain induced blueshift when adding ZnS is reminiscent of that observed in Fig. 5 beyond 5 MLs. Since ZnS has smaller lattice constant than CdSe and CdS, it further compresses the core in the in-plane direction ( $\varepsilon_{xx} + \varepsilon_{yy}$ ). However, its bonds are stiff, so that vertical expansion  $\varepsilon_{zz}$  is inhibited with increasing ZnS thickness (see Fig. S4). The compensation between electron blueshift and hole redshift is then quenched, as the latter arises from  $(a_v - b)\varepsilon_{zz}$ , see Eq. (6). The blueshift induced by ZnS in Fig. 7(b) may be underestimated, because the value of  $a_c$  we have chosen for CdSe is among the smallest proposed in the literature. Photoluminescence experiments with these structures may provide direct measures of the strain induced blueshift, and prove the operating principle, which can then be transferred to other materials. We stress that observing a blueshift would additionally confirm that core/shell/shell structures enable separate engineering of tunneling and strain effects.

## Conclusions

In summary, we have investigated theoretically the role of linear elastic strain in core/shell NPLs based on CdSe. The main findings are: (i) the finite lateral size of NPLs influences the strain value up to 5 nm away from the borders; (ii) coupled strain-momentum terms of the strain Hamiltonian, which are generally neglected in epitaxial quantum wells, can be comparable to deformation potential terms in strongly strained NPLs (e.g. CdSe/ZnS), owing to the stronger quantum confinement of colloidal structures; (iii) the energetic influence of strain is larger in type-II systems (e.g. CdSe/CdTe) than in type-I ones (CdSe/CdS, CdSe/ZnS) because in the latter electrons and holes have opposite response to strain. In any case, the energetic influence reaches several tens of meV at most. This is secondary as compared to tunneling, which remains as the main responsible for exciton redshift even in CdSe/ZnS NPLs. (iv) single-ML asymmetry in the shell growth can explain the NPL bending and smooth exciton energy decay vs. shell thickness in Ref.<sup>12</sup> (v) the use of ternary

(core/shell/shell) NPLs enables separate engineering of tunneling and strain, opening a route to partially compensate for the large redshift obtained when passivating CdSe cores with a single shell.

## Acknowledgement

Support from MINECO project CTQ2017-83781-P and UJI project B2017-59 is acknowledged.

**Supporting Information Available:** Further details of material parameters and additional calculations on the electron and hole wave function in-plane distribution, strain tensor components ( $\varepsilon_{xx} + \varepsilon_{yy}$  vs  $\varepsilon_{zz}$ ) in binary (core/shell) and ternary (core/shell/shell) NPLs, as well as ensuing CB and VB potentials.

## References

- (1) Kovalenko M.; Manna L.; Cabot A.; Hens Z.; Talapin D.V.; Kagan Ch.R.; Klimov V.I.; Rogach A.L.; Reiss P.; Milliron D.J.; *et al.* Prospects of Nanoscience with Nanocrystals. *ACS Nano* **2015**, *9*, 1012-1057.
- (2) E. Lhuillier, S. Pedetti, S. Ithurria, B. Nadal, H. Heuclin, B. Dubertret. Two-Dimensional Colloidal Metal Chalcogenides Semiconductors: Synthesis, Spectroscopy, and Applications. *Acc. Chem. Res.* **2015**, *48*, 22 - 30
- (3) S. Ithurria, M. D. Tessier, B. Mahler, R. P. S. M. Lobo, B. Dubertret and Al. L. Efros, Colloidal nanoplatelets with two-dimensional electronic structure. *Nature Materials* **2011**, *10*, 936-941.
- (4) J. Planelles, A. W. Achtstein, R. Scott, N. Owschimikow, U. Woggon, and J. I. Cl-



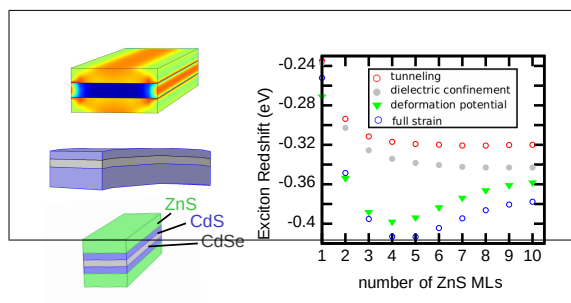
- mente. Tuning Intraband and Interband Transition Rates via Excitonic Correlation in Low-Dimensional Semiconductors. *ACS Photonics* **2018**, *5* (9), 3680-3688
- (5) M. Lorenzon, S. Christodoulou, G. Vaccaro, J. Pedrini, F. Meinardi, I. Moreels, and S. Brovelli. Reversed oxygen sensing using colloidal quantum wells towards highly emissive photoresponsive varnishes. *Nature Communications* **2015**, *6*, 6434
- (6) S. Singh, R. Tomar, S. ten Brinck, J. de Roo, P. Geiregat, J. C. Martins, I. Infante and Z. Hens. Colloidal CdSe Nanoplatelets, A Model for Surface Chemistry/Optoelectronic Property Relations in Semiconductor Nanocrystals. *J. Am. Chem. Soc.* **2018**, *140*, 13292-13300
- (7) A. Prudnikau, A. Chuvilin and M. Artemyev. CdSe–CdS Nanoheteroplatelets with Efficient Photoexcitation of Central CdSe Region through Epitaxially Grown CdS Wings. *J. Am. Chem. Soc.* **2013**, *135*, 14476-14479
- (8) M. D. Tessier, P. Spinicelli, D. Dupont, G. Patriarche, S. Ithurria and B. Dubertret. Efficient Exciton Concentrators Built from Colloidal Core/Crown CdSe/CdS Semiconductor Nanoplatelets. *Nano Lett.* **2014**, *14*, 207-213
- (9) B. Mahler, B. Nadal, C. Bouet, G. Patriarche and B. Dubertret. Core/Shell Colloidal Semiconductor Nanoplatelets. *J. Am. Chem. Soc.* **2012**, *134*, 18591-18598
- (10) M. D. Tessier, B. Mahler, B. Nadal, H. Heuclin, S. Pedetti and B. Dubertret. Spectroscopy of Colloidal Semiconductor Core/Shell Nanoplatelets with High Quantum Yield. *Nano Lett.* **2013**, *13*, 3321-3328
- (11) A. A. Rossinelli, A. Riedinger, P. Marqués-Gallego, P. N. Knüsel, F. V. A. and D. J. Norris. *Chem. Commun.* **2017**, *53*, 9938-9941
- (12) A. Polovitsyn, Z. Dang, J. L. Movilla, B. Martín-García, A. H. Khan, G. H. V. Bertrand,

- R. Brescia and I. Moreels. Synthesis of Air-Stable CdSe/ZnS Core–Shell Nanoplatelets with Tunable Emission Wavelength. *Chem. Mater.* **2017**, *29*, 5671-5680
- (13) H. Cruguel, C. Livache, B. Martinez, S. Pedetti, D. Pierucci, E. Izquierdo, M. Dufour, S. Ithurria, H. Aubin, A. Ouerghi, E. Lacaze, M. G. Silly, B. Dubertret, and E. Lhuillier. Electronic structure of CdSe–ZnS 2D nanoplatelets *Appl. Phys. Lett* **2017**, 152103
- (14) S. Shendre, S. Delikanli, M. Li, D. Dede, Z. Pan, S. Tung Ha, Y. Hsing Fu, P. L. Hernández-Martínez, J. Yu, O. Erdem, A. I. Kuznetsov, C. Dang, T. Chien Sum and H. Volkan Demir. Ultrahigh-efficiency aqueous flat nanocrystals of CdSe/CdS@Cd<sub>1-x</sub>Zn<sub>x</sub>S colloidal core/crown@alloyed-shell quantum wells *Nanoscale* **2019**, *11*, 301-310
- (15) Y. Altintas, U. Quliyeva, K. Gungor, O. Erdem, Y. Kelestemur, E. Mutlugun, M. V. Kovalenko, H. Volkan Demir. Highly Stable, Near-Unity Efficiency Atomically Flat Semiconductor Nanocrystals of CdSe/ZnS Hetero-Nanoplatelets Enabled by ZnS-Shell Hot-Injection Growth. *Small* **2019**, *15*, 1804854
- (16) C. Meerbach, R. Tietze, S. Voigt, V. Sayevich, V. M. Dzhagan, S. C. Erwin, Z. Dang, O. Selyshchev, K. Schneider, D. R. T. Zahn, V. Lesnyak, A. Eychmüller. Brightly Luminescent Core/Shell Nanoplatelets with Continuously Tunable Optical Properties. *Adv. Optical Mater.* **2019**, *7*, 1801478
- (17) A. W. Achtstein, O. Marquardt, R. Scott, M. Ibrahim, T. Riedl, A. V. Prudnikau, A. Antanovich, N. Owschimikow, J. K. N. Lindner, M. Artemyev and U. Woggon. Impact of Shell Growth on Recombination Dynamics and Exciton–Phonon Interaction in CdSe–CdS Core–Shell Nanoplatelets. *ACS Nano* **2018**, *12*, 9476-9483
- (18) S. Luo, M. Kazes, H. Lin and D. Oron. Strain-Induced Type II Band Alignment Control in CdSe Nanoplatelet/ZnS-Sensitized Solar Cells. *J. Phys. Chem. C* **2017**, *121*, 11136-11143

- (19) A. M. Smith, A. M. Mohs and S. Nie. Tuning the optical and electronic properties of colloidal nanocrystals by lattice strain. *Nature Nanotechnology* **2009**, *4*, 56–63
- (20) S. Christodoulou, F. Rajadell, A. Casu, G. Vaccaro, J. Q. Grim, A. Genovese, L. Manna, J. I. Climente, F. Meinardi, G. Rainò, T. Stöferle, R. F. Mahrt, J. Planelles, S. Brovelli, I. Moreels. Band structure engineering via piezoelectric fields in strained anisotropic CdSe/CdS nanocrystals. *Nat Commun.* **2015**, *6*, 7905
- (21) C. Segarra, J. I. Climente, A. Polovitsyn, F. Rajadell, I. Moreels and J. Planelles. Piezoelectric Control of the Exciton Wave Function in Colloidal CdSe/CdS Nanocrystals. *J. Phys. Chem. Lett.* **2016**, *7*, 2182-2188
- (22) John P. Loehr Physics of Strained Quantum Well Lasers. *Springer US* **1998**
- (23) A. Antanovich, A. W. Acthstein, A. Matsukovich, A. Prudnikau, P. Bhaskar, V. Gurin, M. Molinari and M. Artemyev. A strain-induced exciton transition energy shift in CdSe nanoplatelets: the impact of an organic ligand shell. *Nanoscale* **2017**, *9*, 18042-18053
- (24) S. Christodoulou, J. I. Climente, J. Planelles, R. Brescia, M. Prato, B. Martin-Garcia, A. Hossain Khan and I. Moreels, Chloride-Induced Thickness Control in CdSe Nanoplatelets. *Nano Letters* **2018**, *18*, 6248-6254.
- (25) M. Dufour, J. Qu, C. Greboval, C. Méthivier, E. Lhuillier, S. Ithurria. Halide Ligands To Release Strain in Cadmium Chalcogenide Nanoplatelets and Achieve High Brightness. *ACS Nano.* **2019**, *13*, 5326-5334
- (26) F. Rajadell, J. I. Climente, and J. Planelles. Excitons in core-only, core-shell and core-crown CdSe nanoplatelets: Interplay between in-plane electron-hole correlation, spatial confinement, and dielectric confinement. *Phys. Rev. B* **2017**, *96*, 035307
- (27) M. Richter. Nanoplatelets as material system between strong confinement and weak confinement. *Phys. Rev. Materials* **2017**, *1*, 016001

- (28) M. Tadić, F. M. Peeters, K. L. Janssens, M. Korkusiński and P. Hawrylak. Strain and band edges in single and coupled cylindrical InAs/GaAs and InP/InGaP self-assembled quantum dots. *J. Appl. Phys.* **2002**, *92*, 5819
- (29) F. Rajadell, M. Royo, and J. Planelles. Strain in free standing CdSe/CdS core-shell nanorods. *J. Appl. Phys.* **2012**, *111*, 014303
- (30) G. H. V. Bertrand, A. Polovitsyn, S. Christodoulou, A. H. Khan and I. Moreels. Shape control of zincblende CdSe nanoplatelets. *Chem. Commun.* **2016**, *52*, 11975
- (31) For light holes, the sign of the deformation potential is opposite to that of heavy holes. Therefore, core/shell strain splits heavy and light holes energetically in all the structures we study.
- (32) B. M. Saidzhonov, V. F. Kozlovsky, V. B. Zaytsev, R. B. Vasiliev. Ultrathin CdSe/CdS and CdSe/ZnS core-shell nanoplatelets: The impact of the shell material on the structure and optical properties. *Journal of Luminescence* **2019**, *209*, 170-178.
- (33) A. Szemjonov, T. Pauporté, S. Ithurria, B. Dubertret, I. Ciofini and F. Labat. Combined Computational and Experimental Study of CdSeS/ZnS Nanoplatelets: Structural, Vibrational, and Electronic Aspects of Core–Shell Interface Formation. *Langmuir* **2018**, *34*, 13828-13836

# Graphical TOC Entry



# **Supporting Information for “Strain in Lattice Mismatched CdSe-Based Core/Shell Nanoplatelets”**

Jordi Llusar, Josep Planelles, and Juan I. Climente\*

*Departament de Química Física i Analítica, Universitat Jaume I, E-12080, Castelló de la  
Plana, Spain*

E-mail: [climente@uji.es](mailto:climente@uji.es)

## Material parameters

Below we summarize the material parameters used in the calculations. They all refer to cubic crystal phase. While most parameters are taken from Ref.,<sup>1</sup> in the table we provide more specific citations –often within that source–. When a sequence of references is provided for the same parameter, they refer to CdSe, ZnS, CdS and CdTe, respectively. In the table,  $m_0$  is the free electron mass and  $\varepsilon_0$  the vacuum permittivity.

Description	Symbol	CdSe	ZnS	CdS	CdTe	Units	Ref.
Elastic modulus tensor	$C_{11}$	70.7	74.2	97.8	53.5	GPa	Refs. <sup>4567</sup>
Elastic modulus tensor	$C_{12}$	51.6	56.7	59.7	36.5	GPa	Refs. <sup>4567</sup>
Elastic modulus tensor	$C_{44}$	26.5	50.5	30.6	19.9	GPa	Refs. <sup>4567</sup>
Dielectric constant	$\varepsilon$	9.6	8.43	8.43	8.43	$\varepsilon_0$	Ref. <sup>8</sup>
Lattice constant	$a$	6.077	5.4102	5.825	6.48	Å	Refs. <sup>9101112</sup>
Effective electron mass ( $\perp$ )	$m_{e,z}^*$	0.11	0.20	0.14	0.09	$m_0$	Refs. <sup>13141516</sup>
Effective hole mass ( $\perp$ )	$m_{h,z}^*$	0.33	0.96	0.39	0.51	$m_0$	Ref. <sup>17</sup>
Effective electron mass ( $\parallel$ )	$m_{e,p}^*$	0.11	0.11	0.11	0.11	$m_0$	Refs. <sup>13141516</sup>
Effective hole mass ( $\parallel$ )	$m_{h,p}^*$	0.15	0.30	0.20	0.19	$m_0$	Ref. <sup>17</sup>
Luttinger parameter	$\gamma_1$	2.04	2.54	4.11	4.14	$\frac{1}{m_0}$	Refs. <sup>18192021</sup>
Luttinger parameter	$\gamma_2$	0.58	0.75	0.77	1.09	$\frac{1}{m_0}$	Refs. <sup>18192021</sup>
CB Deformation potential	$a_c$	-2	-4.33	-2.54	-2.81	eV	Ref. <sup>22</sup>
VB Deformation potential	$a_v$	0.9	0.83	0.40	0.81	eV	Ref. <sup>23</sup>
VB Deformation potential	$b$	-0.8	-1.1	-1.05	-1	eV	Refs. <sup>242526</sup>

**Table S1: Material parameters used in the calculations.**

The effective mass of electrons and holes in the ligands region is taken as a fitting parameter to match the order of magnitude of exciton shifts observed in experiments.<sup>2,3</sup> This is achieved with  $m_e^{*,out} = m_h^{*,out} = 0.25 m_0$ . A relative dielectric constant of 2 and confining

potential of 4 eV is taken outside the NC to account for the dielectric environment. The finite confining potential at the NPL/ligand barrier allows us not to overestimate quantum confinement.<sup>27</sup> At the same time, it prevents the use of a single analytical formula, such as that we employed in Ref.,<sup>28</sup> to determine the self-energy and exciton Coulomb integral. Instead, we use different analytical formulae for every region (inside/outside the NPL), following Ref.<sup>29</sup> We note that in order to avoid the self-energy singularity at the dielectric interface, a blurring parameter  $\delta = a/2$  is introduced in self-energy terms (see Eqs. (2.14) and (2.15) in Ref.<sup>29</sup>), where  $a$  is the lattice parameter of the inorganic material in contact with the outer environment.

## Band offsets

All values are derived from calculations in Ref.<sup>30</sup>

Band Offsets (eV)		
Conduction Band Offset (CBO)		
CdSe/ZnS	CdSe/CdS	CdSe/CdTe
1.05	0.48	0.53
Valence Band Offset (VBO)		
CdSe/ZnS	CdSe/CdS	CdSe/CdTe
0.99	0.24	-0.69

It is worth noting that there is significant dispersion of the band-offset values reported in the literature, cf. for instance Ref.<sup>31</sup> with current values. We have chosen all data from the same reference for consistency, but using different values proposed in different studies for each material would likely allow one to better fit experimental energies.



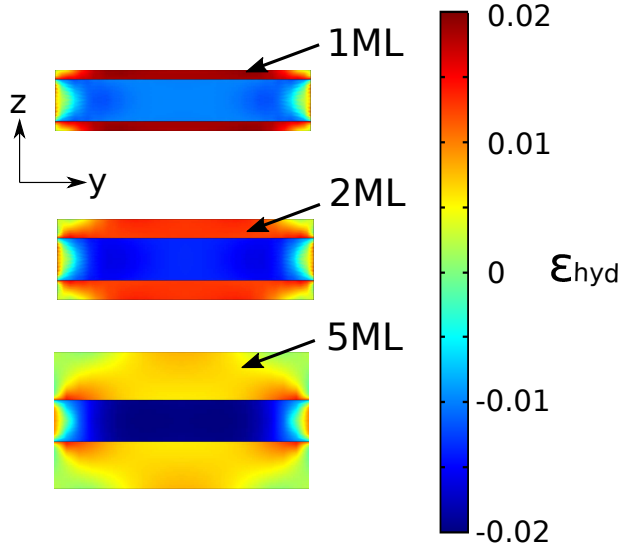


Figure S1: Hydrostatic strain in CdSe/CdS NPL with increasing shell thickness. The CdSe core has 4.5 ML thickness and  $40 \times 8$  nm lateral dimensions. The strain is represented on a transversal cross-section, coincidental with the  $yz$  plane.

## Additional calculations

Figure S1 shows  $\varepsilon_{hyd}$  in a transversal cross-section of CdSe/CdS NPLs with increasing shell thickness. The strain is compressive in the core and tensile in the shell. For thin shells, much of the strain accumulates in the shell. For thick ones, it starts accumulating in the core instead. The influence of the lateral sides extends a few nm inside the NPL.

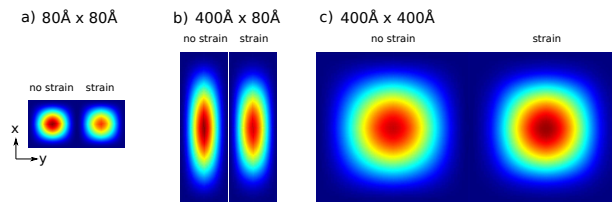


Figure S2: Electron ground state charge density in the NPLs analyzed in Fig. 1 of the main text. Left/right panels represent strained/unstrained cases. The plot is taken on the  $xy$  plane, across the middle of the core.

Figure S2 shows the electron ground state charge density in CdSe/CdS NPLs neglecting

(left) or including (right) strain terms of the Hamiltonian,  $V_{strain}^{dp}$  and  $V_{strain}^{pz}$ . For small ( $8 \times 8$  nm<sup>2</sup>) and mid-sized ( $40 \times 8$  nm<sup>2</sup>) NPLs, the charge density slightly spreads. For larger NPLs ( $40 \times 40$  nm<sup>2</sup>), the charge slightly concentrates. These are consequences of the strain-induced potential wells and barriers forming near the lateral borders, as described in Figure 1(d-g) of the main text. In all cases, the change is only moderate and most of the carrier density stays in the center of the NPL.

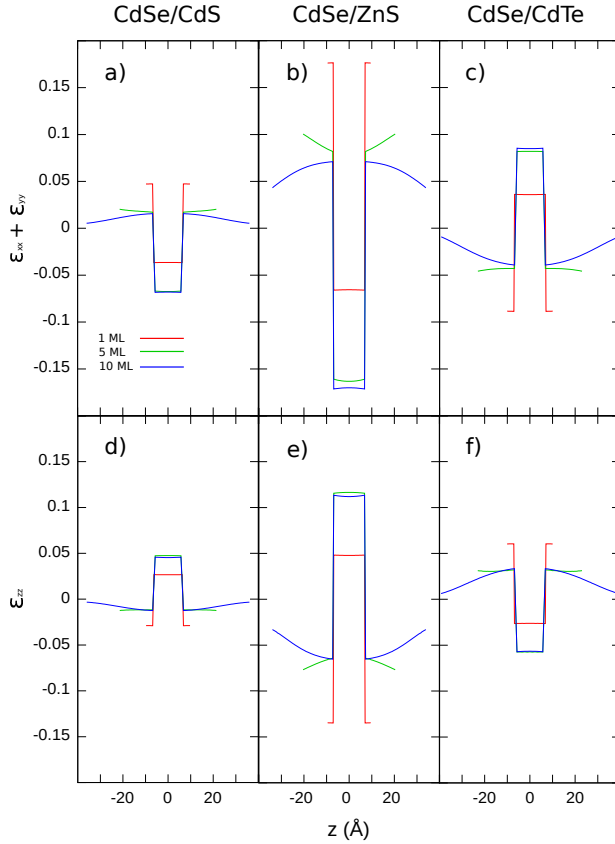


Figure S3: Strain tensor in-plane ( $\epsilon_{xx} + \epsilon_{yy}$ ) and out-of-plane ( $\epsilon_{zz}$ ) diagonal components, taken along the  $z$  axis, orthogonal to the NPL surface. Different shell materials and thicknesses are considered.

Figure S3 shows the in-plane and out-of-plane diagonal components of the strain tensor along the  $z$  axis of the NPL. For CdSe/CdS and CdSe/ZnS, the core experiences lateral

compression ( $\varepsilon_{xx} + \varepsilon_{yy} < 0$ ) and vertical expansion ( $\varepsilon_{zz} > 0$ ). The strain doubles from CdSe/CdS to CdSe/ZnS, owing to the larger lattice mismatch (4% vs 12%). The strain inside the core increases as the shell becomes thicker, and saturates between 5 and 10 MLs.

It is worth pointing out that  $\varepsilon_{zz}$  saturates slightly faster than  $\varepsilon_{xx} + \varepsilon_{yy}$ , because the increasing shell thickness makes vertical deformation more difficult. This has direct implications in the VB strain potential terms. The hole deformation potential is given by  $V_{strain}^{dp,h} = (a_v + \frac{b}{2})(\varepsilon_{xx} + \varepsilon_{yy}) + (a_v - b)\varepsilon_{zz}$ . In the core,  $(a_v - b) > (a_v + b/2)$  (see CdSe parameters in Table S1). Then  $\varepsilon_{zz}$  is chiefly responsible for the changes in the VB potential profile. Since  $\varepsilon_{zz} > 0$ , this gives rise to a redshift of hole states. As discussed in the article, in type-I structures this redshift compensates energetically for the blueshift of the electron, which is set by  $V_{strain}^{dp,e} = a_c\varepsilon_{hyd}$  instead. When  $\varepsilon_{zz}$  saturates, however,  $(a_v + b/2)(\varepsilon_{xx} + \varepsilon_{yy})$  gains weight and the hole redshift is less pronounced. Then, the compensation between  $V_{dp,h}$  and  $V_{strain}^{dp,e}$  starts failing. This can be seen e.g. when comparing panels (b) and (e) of Figure 3 in the main text. As the shell thickness increases (1 ML, 5 MLs, 10 MLs), the bottom of the CB in the core gradually shifts upwards. By contrast, the top of the VB first shifts upwards (from 1 to 5 ML,  $\varepsilon_{zz}$  dominates  $V_{strain}^{dp,h}$ ) but then shifts downwards (from 5 to 10 ML). This is responsible for the inflection point observed in the strained exciton energy in Figure 5 of the paper.

A similar situation arises in ternary (core/shell/shell) CdSe/CdS/ZnS NPLs. As can be seen in Figure S4(a-c), with increasing number of ZnS MLs  $\varepsilon_{hyd}$  becomes more compressive inside the core. The lateral compression ( $\varepsilon_{xx} + \varepsilon_{yy}$ ) also increases, Fig. S4(d-f). However, the vertical expansion ( $\varepsilon_{zz}$ ) is hindered by thick and stiff shells. Consequently, it increases from 1 to 5 ML of ZnS, but decreases from 5 to 10 MLs, see Fig. S4(g). The implication on the deformation potential of electrons and holes is plotted in Fig. S5. In the core, the bottom of the CB shifts upwards as ZnS thickness increases. By contrast, the top of the VB first shows a small shifts upwards (1-5 MLs of ZnS) and then downwards (5-10 MLs). The overall influence on the exciton energy is then given mainly by  $V_{strain}^{dp,e}$ .

## Sign of strain induced exciton energy shift

In Figures 4 and 5 of the paper, we show that strain induces a redshift of the exciton energy. In the case of CdSe/CdS NPLs, this is contrast with previous simulations, which estimated a blueshift instead using k-p theory as well.<sup>32</sup> The sign of the shift is largely given by the difference  $\Delta_{strain} = V_{strain}^{dp,e} - V_{strain}^{dp,h}$ . Coupled strain-momentum terms provide additional redshift, but they have secondary weight in CdSe/CdS structures because strain is moderate. From Eqs. (5) and (6) in the main text, considering  $\varepsilon_{xx} \approx \varepsilon_{yy}$  and the biaxial strain ratio between  $\varepsilon_{zz}$  and  $\varepsilon_{xx}$ , we obtain:

$$\Delta_{strain} = \varepsilon_{xx} 2 \left[ a_c - \left( a_v + \frac{b}{2} \right) - \frac{c_{12}}{c_{11}} (a_c - (a_v - b)) \right], \quad (1)$$

where one should take the strain and material parameters of the region where the carriers (electron and hole) are placed. In CdSe/CdS, both carriers are inside the compressed core, so that  $\varepsilon_{xx}$  is negative. However, there is sufficient dispersion in the deformation potential and elastic constant parameters reported in the literature as to change the sign of the term between square brackets. For the CdSe values in Table S1,  $\Delta_{strain} < 0$ , while for those in Ref.<sup>32</sup> (see supporting information therein),  $\Delta_{strain} > 0$ . We have chosen deformation potential values from Ref.,<sup>22</sup> which are calculated from ab initio models without assumptions on the reference energy level. To our knowledge, this is state of the art calculation of deformation potentials. On the other hand, Ref.<sup>32</sup> takes the deformation potentials from Ref.<sup>33</sup> The latter is a computational simulation of the electronic structure of pure (unstrained) CdSe and CdS NPLs, which simply lists deformation potential values without citing its source. The elastic coefficients in both our work and in Ref.<sup>32</sup> are taken from atomistic calculations, which show differences of  $\sim 15\%$ . This degree of uncertainty suffices to prevent a definite prediction on the sign of the strain influence. Nonetheless, one should realise this uncertainty is precisely a consequence of one of the central messages we convey: in type-I NPLs, the compensation between electron and hole trends makes the exciton shift small (few tens of

meV at most). It is precisely this compensation that enables fluctuations of the energy shift around zero, with the exact sign depending on the material parameters.

## References

- (1) Sadao, A. *Handbook of Physical Properties of Semiconductors*; Kluwert Academic Group, 2004.
- (2) S. Shendre, S. Delikanli, M. Li, D. Dede, Z. Pan, S. Tung Ha, Y. Hsing Fu, P. L. Hernandez-Martinez, J. Yu, O. Erdem, A. I. Kuznetsov, C. Dang, T. Chien Sum and H. Volkan Demir. Ultrahigh-efficiency aqueous flat nanocrystals of CdSe/CdS@Cd<sub>1-x</sub>Zn<sub>x</sub>S colloidal core/crown@alloyed-shell quantum wells *Nanoscale* **2019**, *11*, 301-310
- (3) A. Polovitsyn, Z. Dang, J. L. Movilla, B. Martn-Garca, A. H. Khan, G. H. V. Bertrand, R. Brescia and I. Moreels. Synthesis of Air-Stable CdSe/ZnS CoreShell Nanoplatelets with Tunable Emission Wavelength. *Chem. Mater.* **2017**, *29*, 5671-5680
- (4) J.J. Tan, Y. Cheng, W. J. Zhu, Q.Q. Gou. Elastic and Thermodynamic Properties of CdSe from First-Principles Calculations. *Communications in Theoretical Physics* **2008**, *50*, 220.
- (5) C. Bocchi, A. Catellani, F. Germini, L. Nasi, J. K. Morrod, K. A. Prior, and G. Calestani. Metastable zinc-blende MgS structure: Combined experimental and theoretical study. *Phys. Rev. B* **2009**, *79*, 235310.
- (6) E. Deligoz, K. Colakoglu, Y. Ciftci. Elastic, electronic, and lattice dynamical properties of CdS, CdSe, and CdTe. *Physica B: Condensed Matter* **2006**, *373*, 124-130.
- (7) H. J. McSkimm, D. G. Thomas. Elastic Moduli of Cadmium Telluride. *J. Appl. Phys.* **1962**, *33*, 56-59.

- (8) The dielectric constant of cubic CdSe and CdS (as well for ZnS and CdTe) is reported as the geometric average of the hexagonal  $\varepsilon_{\perp}$  and  $\varepsilon_z$  dielectric constants, see e.g.<sup>1</sup>
- (9) N. Samarth, H. Luo, J. K. Furdyna, S. B. Qadri, Y. R. Lee, A. K. Ramdas, and N. Otsuka, *Appl. Phys. Lett.* **54**, 2680 (1989).  
Cited in Ref.<sup>1</sup> p. 312.
- (10) J. C. Jamieson and H. H. Demarest, Jr., *J. Phys. Chem. Solids* **41**, 1980, 963. Cited in Ref.<sup>1</sup> p. 124.
- (11) W. R. Cook, Jr., *J. Am. Ceram. Soc.* **51**, 1968, 518.  
Cited in Ref.<sup>1</sup> p. 256.
- (12) D. J. Williams, *EMIS Datareviews Series* **10**, 1994, 399.  
Cited in Ref.<sup>1</sup> p. 360.
- (13) R. Dalven, *Phys. Status Solidi B* **48**, 1971, K23.  
Cited in Ref.<sup>1</sup> p. 322.
- (14) Y. Imanaka, N. Miura, *Phys. Rev. B* **50**, 1994, 14065.  
Cited in Ref.<sup>1</sup> p. 142.
- (15) R. Dalven, *Phys. Status Solidi B* **48**, 1971, K23.  
Cited in Ref.<sup>1</sup> p. 265.
- (16) M. Helm, W. Knap, W. Seidenbusch, R. Lassnig, E. Gornik, R. Triboulet, and L. L. Taylor, *Solid State Commun.* **53**, 1985, 547.  
Cited in Ref.<sup>1</sup> p. 383.
- (17) Effective hole masses obtained from  $m_{h,z}^* = \frac{1}{\gamma_1 - 2\gamma_2} m_{h,p}^* = \frac{1}{\gamma_1 + \gamma_2}$
- (18) D. J. Norris, M. G. Bawendi M. G. Measurement and assignment of the size-dependent optical spectrum in CdSe quantum dots. *Phys. Rev. B.: Condens. Matter* **53**, 1996, 16338-16346.

- (19) P. Lawaetz, *Phys. Rev. B* **4**, 1971, 3460.  
Cited in Ref.<sup>1</sup> p. 142.
- (20) Luttinger parameters of c-CdS were estimated from a plot of  $E_0$  versus  $\gamma_i$  for some cubic group-IV, III-V, and II-VI semiconductors in Ref.<sup>1</sup> p.266.
- (21) T. Friedrich, J. Kraus, G. Schaack, and W. O. G. Schmitt, *J. Phys.: Condens. Matter* **6**, 1994, 4307.  
Cited in Ref.<sup>1</sup> p. 384.
- (22) Yong-Hua Li, X. G. Gong, and Su-Huai Wei. Ab initio all-electron calculation of absolute volume deformation potentials of IV-IV, III-V, and II-VI semiconductors: The chemical trends. *Phys. Rev. B* **73**, 2006, 245206.
- (23) H. J. Lozykowski and V. K. Shastri, *J. Appl. Phys.* **69**, 1991, 3235.  
Cited in Ref.<sup>1</sup> p. 324.
- (24)  $\Gamma$  - valence band deformation potential  $b$  taken from a table as a mean value in Ref.,<sup>1</sup> pag 144.
- (25) R. Said, A. Qteish, and N. Meskini, *J. Phys.: Condens. Matter* **10**, 1998, 8703.
- (26)  $\Gamma$  - valence band deformation potential  $b$  taken from a table as a mean value in Ref.,<sup>1</sup> pag 386.
- (27) S. Christodoulou, J.I. Climente, J. Planelles, R. Brescia, M. Prato, B. Martin-Garcia, A.H. Khan, and I. Moreels, Chloride-Induced Thickness Control in CdSe Nanoplatelets. *Nano Letters* **18**, 2018, 6248-6254.
- (28) F. Rajadell, J. I. Climente, and J. Planelles. Excitons in core-only, core-shell and core-crown CdSe nanoplatelets: Interplay between in-plane electron-hole correlation, spatial confinement, and dielectric confinement. *Phys. Rev. B* **96**, 2017, 035307.

- (29) M. Kumagai, T. Takagahara, Excitonic and nonlinear-optical properties of dielectric quantum-well structures. *Phys. Rev. B* **40**, 1989, 12359.
- (30) Yong-Hua Li, Aron Walsh, Shiyu Chen, Wan-Jian Yin, Ji-Hui Yang, Jingbo Li, Juarez L. F. Da Silva, X. G. Gong, and Su-Huai Wei. Revised ab initio natural band offsets of all group IV, II-VI, and III-V semiconductors. *Appl. Phys. Lett.* **94**, 2009, 212109.
- (31) S.H. Wei, S.B. Zhang, and A. Zunger, First-principles calculation of band offsets, optical bowings, and defects in CdS, CdSe, CdTe and their alloys. *J. Appl. Phys.* **87**, 2000, 1304.
- (32) A. W. Achtstein, O. Marquardt, R. Scott, M. Ibrahim, T. Riedl, A. V. Prudnikau, A. Antanovich, N. Owschimikow, J. K. N. Lindner, M. Artemyev and U. Woggon. Impact of Shell Growth on Recombination Dynamics and ExcitonPhonon Interaction in CdSeCdS CoreShell Nanoplatelets. *ACS Nano* **2018**, 12, 9476-9483
- (33) S. Bose, Z. Song, W.J. Fan, and D.H. Zhang, Effect of lateral size and thickness on the electronic structure and optical properties of quasi two-dimensional CdSe and CdS nanoplatelets, *J. Appl. Phys.* **2016**, 119, 143107.



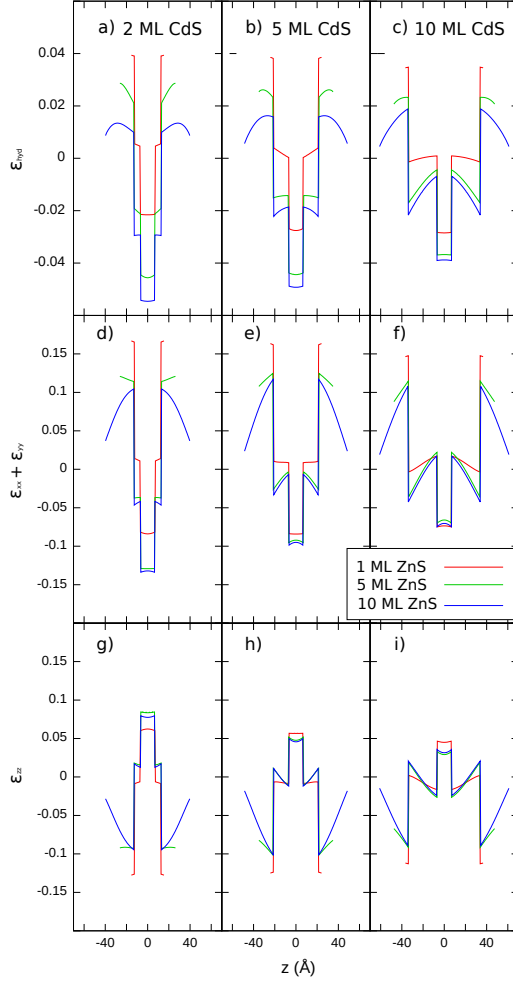


Figure S4: Hydrostatic strain ( $\epsilon_{hyd} = \epsilon_{xx} + \epsilon_{yy} + \epsilon_{zz}$ ), and separate in-plane ( $\epsilon_{xx} + \epsilon_{yy}$ ) and out-of-plane ( $\epsilon_{zz}$ ) components, taken along the  $z$  axis of a CdSe/CdS/ZnS NPL. Different thicknesses of the inner shell (CdS) and outer shell (ZnS) materials are considered.

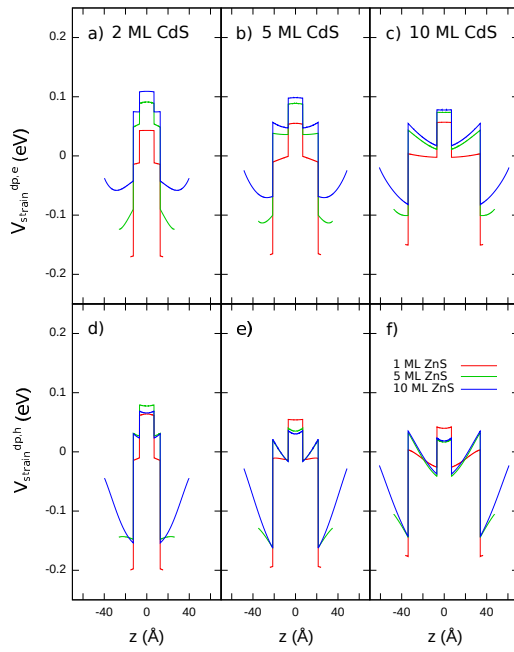


Figure S5: Electron (top) and hole (bottom) deformation potential profile, taken along the  $z$  axis of a CdSe/CdS/ZnS NPL. Different thicknesses of the inner shell (CdS) and outer shell (ZnS) materials are considered.

## 2.2 Nature and Control of Shakeup Processes

”Nature and Control of Shakeup Processes in Colloidal Nanoplatelets.”

Jordi Llusar and Juan I. Climente.

*ACS Photonics* **2020** 7 (11), 3086-3095

DOI: <https://doi.org/10.1021/acsp Photonics.0c01160>

### Abstract:

Recent experiments suggest that the photoluminescence line width of CdSe nanoplatelets (NPLs) and core/shell CdSe/CdS NPLs may be broadened by the presence of shakeup (SU) lines from negatively charged trions. We carry out a theoretical analysis, based on effective mass and configuration interaction (CI) simulations, to identify the physical conditions that enable such processes. We confirm that trions in colloidal NPLs are susceptible of presenting SU lines up to 1 order of magnitude stronger than in epitaxial quantum wells, stimulated by dielectric confinement. For these processes to take place, trions must be weakly bound to off-centered charge traps, which relax symmetry selection rules. Charges on the lateral sidewalls are particularly efficient to this end. Our simulations display a single strong SU replica in most instances, which agrees well with experiments on CdSe NPLs, but suggests that the multip peaked emission reported for core/shell CdSe/CdS NPLs must involve other factors beyond SU processes. We propose emission from a metastable spin triplet trion state may be responsible. Understanding the origin of SU processes may open paths to rational design of NPLs with narrower line width.

# Nature and Control of Shakeup Processes in Colloidal Nanoplatelets

Jordi Llusar and Juan I. Climente\*

*Departament de Química Física i Analítica, Universitat Jaume I, E-12080, Castelló de la Plana, Spain*

E-mail: [climente@uji.es](mailto:climente@uji.es)

## Abstract

Recent experiments suggest that the photoluminescence line width of CdSe nanoplatelets (NPLs) and core/shell CdSe/CdS NPLs may be broadened by the presence of shakeup (SU) lines from negatively charged trions. We carry out a theoretical analysis, based on effective mass and configuration interaction (CI) simulations, to identify the physical conditions that enable such processes. We confirm that trions in colloidal NPLs are susceptible of presenting SU lines up to one order of magnitude stronger than in epitaxial quantum wells, stimulated by dielectric confinement. For these processes to take place, trions must be weakly bound to off-centered charge traps, which relax symmetry selection rules. Charges on the lateral sidewalls are particularly efficient to this end. Our simulations display a single strong SU replica in most instances, which agrees well with experiments on CdSe NPLs, but suggests that the multi-peaked emission reported for core/shell CdSe/CdS NPLs must involve other factors beyond SU processes. We propose emission from a metastable spin triplet trion state may be responsible. Understanding the origin of SU processes may open paths to rational design of NPLs with narrower line width.

## Keywords

trion emission, radiative Auger, heterostructure, impurities, CI method

Colloidal metal chalcogenide NPLs offer well defined advantages over their quantum dot and rod counterparts as semiconductor building blocks for optical applications.<sup>1-4</sup> Some of the most distinctive features are order-of-magnitude shorter radiative lifetimes, which result from the strong exciton binding energies in quasi-2D systems (Giant Oscillator Strength effect),<sup>5,6</sup> and precisely controlled thickness of the nanostructure,<sup>7-10</sup> which largely suppresses the emission broadening due to size dispersion usually observed in dots. These properties give rise to bright and narrow emission lines, which are of interest for displays, lighting and lasers.<sup>3,4</sup>

Unfortunately, ligand passivation of NPL surface dangling bonds is usually incomplete because of labile binding and steric hindrance between ligands. This can translate into significant non-radiative losses.<sup>11</sup> To overcome this problem, core-only NPLs are sometimes replaced by core/shell or core/crown heterostructures, where some facets of the core material are coated with a higher band gap inorganic material.<sup>1</sup> Typical heterostructures are CdSe/CdS,<sup>12-14</sup> CdSe/CdTe,<sup>15,16</sup> CdSe/ZnS<sup>17,18</sup> and their alloys.<sup>19,20</sup> These heterostructures succeed in isolating the photogenerated carriers, which remain in and around the core, from the NPL surfaces, thus translating into enhanced fluorescence quantum efficiency and photostability.<sup>1,4,21</sup> The heterostructure growth has however a negative side effect, namely the systematic broadening of the emission line width, e.g. from  $\sim 35 - 40$  meV in CdSe NPLs to  $\sim 60 - 80$  meV in core/shell CdSe/CdS NPLs.<sup>12,22</sup> Line width broadening in such NPLs was initially ascribed to the presence of local traps induced upon shell coating.<sup>12</sup> Graded interface composition was then used to narrow the line width down to  $\sim 55$  meV,<sup>19,20</sup> but this figure is still larger than in core-only NPLs, which suggests that interface defects are not the only source of broadening.

To shed light into this problem, Antolinez and co-workers recently investigated the origin of the fluorescence line width broadening in core/shell CdSe/CdS NPLs by means of

single-particle spectroscopy.<sup>23</sup> They observed that individual NPLs present a series of 2 to 4 narrow peaks split from each other by  $\sim 10$  meV. Altogether, the peaks fit well the asymmetric line shape of ensemble NPLs at cryogenic temperatures.<sup>12</sup> A similar feature was soon after reported in core-only CdSe NPLs, although in this case only two peaks were measured.<sup>24</sup> Having ruled out more conventional mechanisms, such as exciton-phonon interaction or spectral diffusion, the nature of the additional peaks was tentatively ascribed to SU processes of negative trions ( $X^-$ ). These are partly radiative Auger processes, whereby an electron-hole pair recombines radiatively but transfers part of its energy to the remaining electron by exciting it into a higher single-electron level (in-plane excitation). They have been previously reported in epitaxial quantum wells<sup>25–28</sup> and self-assembled quantum dots<sup>29</sup> under the magnetic fields, corresponding to inter-Landau level excitations of the excess carrier.<sup>30</sup> More recently, SU peaks have been clearly revealed in the magneto-photoluminescence of electrically charged InGaAs and GaAs quantum dots.<sup>31</sup> By contrast, they do not seem to appear in type-II core/crown NPLs.<sup>32</sup> In this context, clarifying the role of SU processes in the emission of colloidal NPLs is a desirable step to better understand and control the emission line width of NPLs, which would be advantageous for optical applications.

In this work, we analyze the possible occurrence of SU processes in colloidal CdSe-based NPLs from a theoretical perspective. The goal is to determine which physical conditions enable these processes. To this end we use effective mass models and full CI simulations, which provide an intuitive description of the underlying physics. We shall confirm that one intense SU replica can be expected for negative trions ( $X^-$ ) in both core-only and core/shell NPLs, corresponding to the excitation of the remaining electron into a higher orbital with the same symmetry as the ground state. For this to take place, the trion must be weakly bound to an off-centered acceptor charge. The role of the charge is to lower the system symmetry, thus relaxing selection rules, and to stimulate electron-electron repulsion (quench electron-hole attraction) in the ground orbital. By doing so, SU peaks can reach intensities exceeding 10% of the fundamental (band edge, fully radiative) transition. This is one order of magnitude

higher than in epitaxial quantum wells, which can be rationalized from the stronger Coulomb interactions in NPLs, which result from the pronounced dielectric confinement, and from the presence of lateral sidewalls, which are prone to surface traps. Analogous conclusions hold for positive trions. We discuss connections with experiments in the literature and propose potential strategies to suppress these processes.

## Results

We analyze the emission spectra of trions in core-only and core/shell NPLs. Negative trions are studied unless otherwise noted, as it is the most frequently reported species in these structures,<sup>23,24,33,34</sup> but the conclusions do not depend on the sign of the charged exciton (see Fig. S2 in the Supporting Information, SI). Once the general behavior of SU processes in these systems is understood, we discuss how our conclusions fit the interpretation of different experimental observations and the practical implications of our findings.

### Core-only NPLs

We start by studying core-only CdSe NPLs. The NPLs are chosen to have 4.5 monolayer (ML) thickness and a lateral size of  $20 \times 20 \text{ nm}^2$ , for similarity to the core dimensions of Ref.<sup>23</sup> They have a pronounced dielectric mismatch with the organic environment, which we model with  $\epsilon_{in} = 6$  and  $\epsilon_{out} = 2$  as the dielectric constants inside and outside the NPL, unless otherwise stated.<sup>35,36</sup> The presence of few-meV spectral jumps in photoluminescence experiments<sup>23</sup> suggests that the trion is subject to the influence of carriers temporarily trapped on the surface.<sup>22,37</sup> To model this phenomenon, a fractional point charge is placed on the surface, with charge  $Q = eQ_X$  ( $|Q_X| \leq 1$  and  $e$  is the full electron charge). The fractional value of  $Q_X$  accounts for the screening of trapped charges (e.g. a hole) by the trap defect itself (e.g. a surface dangling bond).<sup>38</sup> Two scenarios are considered: a charge centered on the top facet ( $Q_{top}$ ) and an off-centered charge, located along the edge of a

lateral facet ( $Q_{edge}$ ). The latter setup is suggested by studies showing that edge and vertex atoms in CdSe structures have weaker binding to oleate ligands.<sup>39</sup> The two systems are represented in Figure 1a and 1b. The corresponding emission spectra are shown in Fig. 1c and 1d. The figure reveals a number of important observations. (i) In the absence of surface charge ( $Q_X = 0$ , thick lines), only the fundamental transition shows up, with no sizable SU replica. (ii) Charges on the top facet induce SU peaks (see arrow in Fig. 1c), but their strength is two orders of magnitude smaller than that of the fundamental transition (main line). This is similar to the case of epitaxial quantum wells.<sup>25-28</sup> (iii) Stronger SU replica are however obtained for charges located on the lateral sidewall, provided the charge is attractive (acceptor charge) and binding to the trion is moderately weak, see Fig. 1d. For  $Q_{edge} = 0.4$  (marked with a star in the figure), the SU peak reaches  $\sim 25\%$  of the main peak height. This ratio is about 20 times higher than in epitaxial quantum wells, and it holds despite the Giant Oscillator Strength enhancing the band edge recombination,<sup>5-7,36</sup> which suggests that SU satellites also benefit from this phenomenon. For  $Q_{edge} > 0.4$ , however, the SU peak intensity is lowered again and the energy splitting (redshift) with respect to the main line increases. Second and third SU lines are built for strong surface charges (see inset in Fig. 1d at  $Q_{edge} = 0.7$ ), but their magnitude is negligible. We have also explored different locations of the charge, obtaining intermediate results between those shown in Fig. 1 (see Fig. S3 in SI). These results point out the potentially significant role of lateral sidewalls, which are characteristic feature of colloidal quantum wells as compared to epitaxial ones, in obtaining high SU peaks.

To gain understanding on the origin of strong SU peaks when trions bind to lateral surface acceptors, beyond the full numerical calculation of Fig. 1, in Fig. 2a and 2b we compare sketches of the SU processes, in the absence and presence of an attractive edge charge. Within effective mass theory, the conduction band and valence band energy levels of (non-interacting) electrons and holes can be described as particle-in-the-box states, with quantum numbers  $(n_x, n_y, n_z)$ . It is useful however to label the states by their symmetry



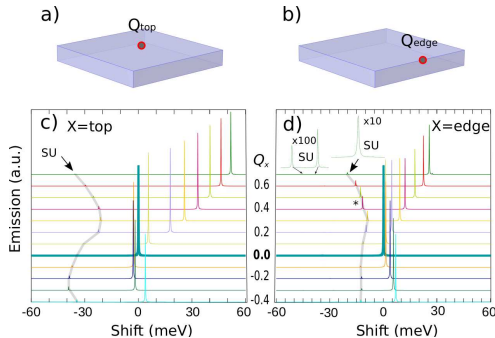


Figure 1: (a,b) Schematics of core-only NPLs with different location of the surface charge. (c,d) Corresponding  $X^-$  emission spectrum for charge strength  $Q = Q_X e$ . The arrows point at the SU satellites (shaded lines are guides to the eyes). The highest SU peak is observed for off-centered acceptor charges weakly bound to the trion ( $Q_{edge} = 0.4$ , marked with a star in (d)). The spectra are normalized to the intensity of the fundamental transition at  $Q_X = 0$ , and offset vertically for clarity. The insets for  $Q_{edge} = 0.7$  in (d) show amplified SU peaks.

(irreducible representation). When  $Q_{edge} = 0$ , because the NPL has squared shape, the point group is  $D_{4h}$ . When  $Q_{edge} \neq 0$ , the electrostatic potential yields a symmetry descent to  $C_s$ . As a consequence, degeneracies are lifted and additional states with the same symmetry as the ground orbital ( $A'$ ) are obtained. This is important because after electron-hole recombination, the excess electron can only be excited to an orbital with the same symmetry as the initial one (as shown by the vertical arrows in Fig. 2a and 2b). Therefore, lowering the system symmetry opens new channels for SU processes. Furthermore, these can involve low-energy orbitals, which have fewer nodes and hence larger overlap with the trion ground state, as we shall see below. Both the number and the intensity of the SU processes are in principle enhanced. By contrast, a centered charge on the top surface barely affects the system symmetry, which remains high ( $C_{4v}$ ), and SU processes are only slightly stronger than in the  $Q_{edge} = 0$  case.

The qualitative reasoning above can be substantiated with a CI formalism on the basis of independent particle (non-interacting) electron and hole states,<sup>31</sup> which has the additional advantage of giving intuitive insight on how Coulomb interactions affect the likelihood of SU

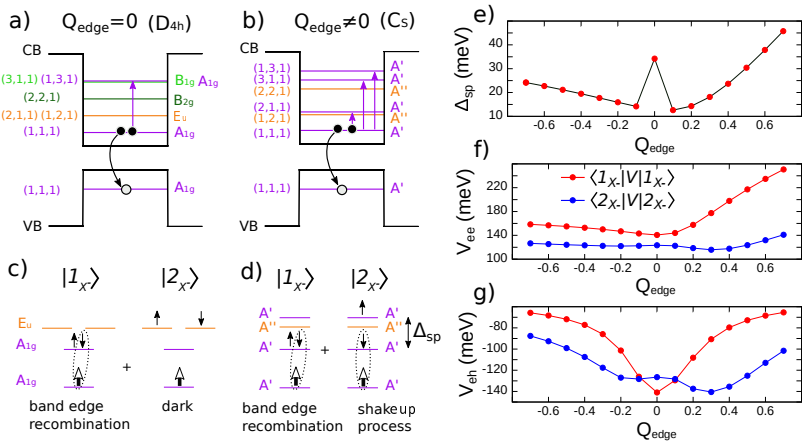


Figure 2: (a,b) Sketch of SU processes in NPLs with (a) and without (b) an edge charge. Labels on the left are  $(n_x, n_y, n_z)$  quantum numbers for the (independent particle) energy levels. Labels on the right are the corresponding irreducible representation. The surface charge lowers the point group symmetry, from  $D_{4h}$  to  $C_s$ , lifting degeneracies and enabling new channels for SU transitions (vertical arrows). (c,d) Two main configurations  $|m_{X^-}\rangle$  in the CI expansion of  $|GS_{X^-}\rangle$ , with and without edge charge. Thin (thick) arrowheads denote electron (hole) spin. Only when  $Q_{\text{edge}} \neq 0$  a SU process is expected. (e) Energy splitting between  $|1_{X^-}\rangle$  and  $|2_{X^-}\rangle$  at an independent particle level. (f) average value of electron-electron repulsion and (g) electron-hole attraction in configurations  $|1_{X^-}\rangle$  and  $|2_{X^-}\rangle$ .

processes. We consider that the transition rate from the trion ground state  $|GS_{X-}\rangle$  to an electron spin-orbital  $|f_e\rangle$ , is proportional to:<sup>40</sup>

$$P_{GS \rightarrow f} = \left| \langle f_e | \hat{P} | GS_{X-} \rangle \right|^2. \quad (1)$$

$\hat{P}$  is the dipolar transition operator,  $\hat{P} = \sum_{i_e, i_h} \langle i_e | i_h \rangle e_{i_e} h_{i_h}$ , where  $e_{i_e}$  and  $h_{i_h}$  are annihilation operators for independent electron and hole spin-orbitals  $|i_e\rangle$  and  $|i_h\rangle$ , respectively. We describe the trion ground state with a CI expansion,

$$|GS_{X-}\rangle = \sum_m c_m |m_{X-}\rangle, \quad (2)$$

where  $|m_{X-}\rangle$  is a trion configuration:  $|m_{X-}\rangle = e_{r_e}^\dagger e_{s_e}^\dagger |0\rangle_e h_{t_h}^\dagger |0\rangle_h$ , with  $e_{r_e}^\dagger$  and  $h_{t_h}^\dagger$  creator operators,  $|0\rangle_e$  and  $|0\rangle_h$  the vacuum occupation vectors of electron and hole, and  $c_m$  the coefficient in the expansion. Inserting  $\hat{P}$  and  $|GS_{X-}\rangle$  into Equation (1), one obtains:

$$P_{GS \rightarrow f} = \left| \sum_m c_m (\langle r_e | t_h \rangle \delta_{f_e s_e} - \langle s_e | t_h \rangle \delta_{f_e r_e}) \right|^2. \quad (3)$$

In SU processes,  $|f_e\rangle$  is an excited spin-orbital. It then follows from Equation (3) that such a transition will only take place if  $|GS_{X-}\rangle$  contains at least one configuration  $|m_{X-}\rangle$  in the CI expansion where one electron is in the excited spin-orbital and the other electron has finite overlap with the hole ground state ( $|s_e\rangle = |f_e\rangle$  and  $\langle r_e | t_h \rangle \neq 0$  or  $|r_e\rangle = |f_e\rangle$  and  $\langle s_e | t_h \rangle \neq 0$ ). The larger the weight of this configuration,  $|c_m|^2$ , the more likely the SU process. It is worth noting that in the strong confinement limit, the trion ground state is well described by a single configuration where all carriers are in the lowest-energy spin-orbitals (configuration  $|1_{X-}\rangle$  in Fig. 2c and 2d). That is,  $c_1 \approx 1$  and  $c_m \approx 0$  for  $m > 1$ . SU transitions are then forbidden, which is why SU peaks are rarely reported in nanocrystals. On the contrary, in systems where Coulomb interaction energies exceed quantum confinement energies, the CI expansion contains mono- and biexcitations of electrons. SU processes are then enabled. Colloidal

NPLs constitute an ideal system at this regard, because they combine weak confinement in the lateral direction with strong Coulomb interactions.<sup>41,42</sup> Hereafter, we refer to this condition ( $c_m \neq 0$  for  $m > 1$ ) as Coulomb admixture.

The role of Coulomb admixture and symmetry breaking in activating SU processes can be illustrated, in the simplest approximation, by considering the two lowest-energy configurations of the trion ground state,

$$|GS_{X^-}\rangle \approx c_1|1_{X^-}\rangle + c_2|2_{X^-}\rangle. \quad (4)$$

In Fig. 2c and 2d we depict such configurations in the absence and presence of an edge charge, respectively. These can be expected to be the two most important configurations in the full CI expansion. Notice that the two configurations must have the same symmetry, for Coulomb interaction to couple them. Because the lowest-energy configuration,  $|1_{X^-}\rangle$ , is always totally symmetric, so must be  $|2_{X^-}\rangle$ . Thus, when  $Q_{edge} = 0$  ( $D_{4h}$  group), the electronic configuration of  $|1_{X^-}\rangle$  is  $[A_{1g}^2]_e [A_{1g}]_h$ , and that of  $|2_{X^-}\rangle$  is  $[E_u^2]_e [A_{1g}]_h$ . The recombination of the  $E_u$  electrons with the hole, which stays in a  $A_{1g}$  orbital, is then symmetry forbidden ( $\langle r_e | t_h \rangle = \langle s_e | t_h \rangle = 0$  in Eq. (3)). By contrast, when  $Q_{edge} \neq 0$  ( $C_s$  group),  $|2_{X^-}\rangle$  is formed by a monoexcitation where one electron is placed in the  $(n_x, n_y, n_z) = (2, 1, 1)$  orbital, which also has  $A'$  symmetry, resulting in an electronic configuration  $[A' A']_e [A']_h$  (see Fig.2d). The hole can then recombine with the ground orbital electron, as both have  $A'$  symmetry ( $\langle r_e | t_h \rangle \neq 0$  or  $\langle s_e | t_h \rangle \neq 0$  in Eq. (3)) and leave the excited electron as the final state. This constitutes a SU process. Because both SU and fundamental transitions rely on the recombination of the same electron-hole pair (same overlap integral, e.g.  $\langle r_e | t_h \rangle$ ), the ratio between SU and fundamental radiative rates can be approximated as:

$$\frac{P_{GS \rightarrow (2,1,1)_e}}{P_{GS \rightarrow (1,1,1)_e}} \approx \frac{|c_2|^2}{|c_1|^2}. \quad (5)$$

i.e. it is set exclusively by the degree of Coulomb admixture.

One can guess the requirements that maximize  $|c_2|^2$  by looking which conditions favor energetically  $|2_{X-}\rangle$  over  $|1_{X-}\rangle$ . These include: (i) small energy splitting between the two configurations, at an independent particle level,  $\Delta_{sp}$  in Fig. 2d, (ii) weaker electron-electron repulsion ( $V_{ee}$ ) and (iii) stronger electron-hole attraction ( $V_{eh}$ ) in  $|2_{X-}\rangle$  as compared to  $|1_{X-}\rangle$ . Figures 2e-g show that these conditions are met for moderately attractive (positive) charges ( $Q_{edge} \sim 0.3 - 0.4$ ). When the off-centered charge is switched on,  $\Delta_{sp}$  rapidly decreases (see Fig. 2e) because the symmetry descent turns one of the  $E_u$  ( $p$ -like) electron orbitals into a  $A'$  ( $s$ -like) one. However, the surface charge brings about electrostatic confinement and hence  $\Delta_{sp}$  increases again soon after. As for inter-electron repulsion,  $\langle 1_{X-} | V_{ee} | 1_{X-} \rangle$  increases more rapidly than  $\langle 2_{X-} | V_{ee} | 2_{X-} \rangle$  (see Fig. 2f) because the former involves placing the two electrons in identical orbitals, while the latter does not. Last,  $\langle 1_{X-} | V_{eh} | 1_{X-} \rangle$  is rapidly quenched (see Fig. 2g) because it involves the ground orbitals of electron and hole  $-(1, 1, 1)_e$  and  $(1, 1, 1)_h$ , which dissociate rapidly under an external charge.  $\langle 2_{X-} | V_{eh} | 2_{X-} \rangle$  stays strong up to  $Q_{edge} \sim 0.3$  because it involves the  $(2, 1, 1)_e$  orbital, which is spatially more extended and then keeps significant overlap with the  $(1, 1, 1)_h$  hole. Figs. 2e-f further evidence that  $Q_{edge} > 0.3 - 0.4$  is inconvenient for SU processes, because the electrostatic potential increases lateral quantum confinement ( $\Delta_{sp}$  increases) and because the electrons and hole in configuration  $|2_{X-}\rangle$  are eventually dissociated as well ( $\langle 2_{X-} | V_{eh} | 2_{X-} \rangle$  is quenched in Fig. 2g).

Many of the above observations can be visualized by analyzing the evolution of charge densities and wave functions under  $Q_{edge}$ . In Figure 3 we show the two-electron (first row) and one-hole (second row) charge densities of  $|GS_{X-}\rangle$ , obtained from the CI calculations of Fig. 1. The wave functions of the two lowest electron orbitals which can constitute configuration  $|2_{X-}\rangle$ ,  $-(n_x, n_y, n_z)_e = (1, 1, 1)_e$  and  $(2, 1, 1)_e$  are also plotted (bottom rows). At  $Q_{edge} \approx 0$ , the two orbitals are quasi-orthogonal. As a result, Coulomb interaction cannot couple configurations  $|1_{X-}\rangle$  and  $|2_{X-}\rangle$ , so that  $c_2 \approx 0$ . This is why the two-electron charge density closely resembles the  $(1, 1, 1)_e$  orbital. SU processes are not expected in this case.

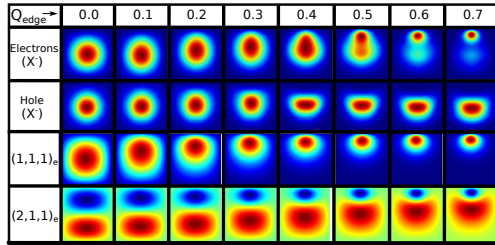


Figure 3: In-plane charge density of the two electrons and hole in the  $X^-$  ground state (top rows), and wave functions of the two lowest electron orbitals with  $A'$  symmetry (bottom rows), as a function of the edge charge magnitude. The edge charge is located on the top edge, in this view. The strongest SU peak corresponds to  $Q_{edge} \approx 0.4$ , when the  $X^-$  electron charge density reveals a clear contribution from  $(2, 1, 1)_e$ , and the hole is not yet fully dissociated from electrons.

At  $Q_{edge} \approx 0.4$ , symmetry lowering and energetic considerations enable efficient Coulomb coupling. The oval shape of the two-electron charge density reflects a significant contribution from  $(2, 1, 1)_e$  to  $|GS_{X^-}\rangle$  (i.e.  $|c_2| > 0$ ). At the same time, the electron  $(1, 1, 1)_e$  orbital and the hole ground state have sizable overlap. This is an optimal situation for the appearance for the transition  $P_{GS \rightarrow (2,1,1)_e}$  to show up as a SU process, according to Equation (3). Further increasing  $Q_{edge}$  separates the  $(2, 1, 1)_e$  electron orbital from the hole. Coulomb attraction is then weaker, making  $c_2$  and consequently  $P_{GS \rightarrow (2,1,1)_e}$  small again.

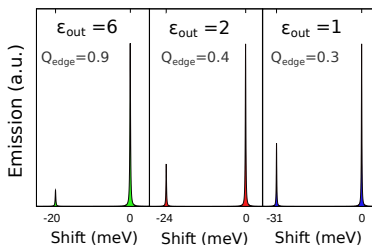


Figure 4: Normalized  $X^-$  emission as a function of the environment dielectric constant. With increasing dielectric contrast, the SU peak increases and becomes more redshifted. For every value of  $\epsilon_{out}$ , the value of  $Q_{edge}$  that maximizes SU transitions is shown. In all cases,  $\epsilon_{in} = 6$ .

We have argued above that strong Coulomb admixture of configurations facilitates the appearance of SU processes. A distinct feature of colloidal NPLs when compared to epitaxial quantum wells is the presence of a pronounced dielectric contrast with the organic

ligands surrounding the NPL, which enhances Coulomb interactions by effectively reducing the system dielectric screening.<sup>36,41,43</sup> To study the influence of this phenomenon over SU transitions, in Figure 4 we compare the trion emission spectrum for different values of the environment dielectric constant  $\epsilon_{out}$ , while fixing that of the NPL to the high-frequency CdSe value,  $\epsilon_{in} = 6$ . For the sake of comparison, the emission spectrum is normalized so that the band edge peak has the same intensity in all cases. Also, we have selected the value of  $Q_{edge}$  that maximizes the relative size of the SU peak in each case. Because  $\epsilon_{out}$  screens the surface charge electrostatic field, larger  $Q_{edge}$  values are needed when  $\epsilon_{out}$  increases. The figure evidences that lowering  $\epsilon_{out}$  increases the SU peak height and energetic redshift. For typical ligands of CdSe NPLs (e.g. oleic acid),  $\epsilon_{out} \sim 2$ .<sup>36,44</sup> We then conclude that dielectric confinement makes SU processes in colloidal NPLs more conspicuous.

## Core/shell NPLs

We next consider heterostructured core/shell NPLs. The first case under study are CdSe/CdS NPLs.<sup>12,13,17,45</sup> The NPLs have the same CdSe core as in the previous section and 6 ML thick CdS shells on top and bottom (see inset in Figure 5a). In general, the behavior of SU replicas is found to be analogous to that of core-only NPLs. An off-centered acceptor impurity is needed to yield sizable SU replicas, with an optimal value of  $Q_{edge}$  maximizing the relative size of the SU peak.

Figure 5a shows the emission spectrum of  $X^-$  for the optimal  $Q_{edge}$  value, in CdSe/CdS NPLs (green line) and CdSe core-only NPLs (black, dashed line). One can see that the SU replica of the CdSe/CdS structure is again significant (11% of the main transition), but less pronounced than in the core-only structure (26%). The smaller SU replica in the core/shell structures is a robust result, which holds for different shell thicknesses and surface charge locations. It is a consequence of the weaker Coulomb interactions. The electron leakage into the CdS shell reduces electron-electron repulsions and electron-hole attractions. The quenching of dielectric confinement by the CdS shell, which pushes organic ligands far from

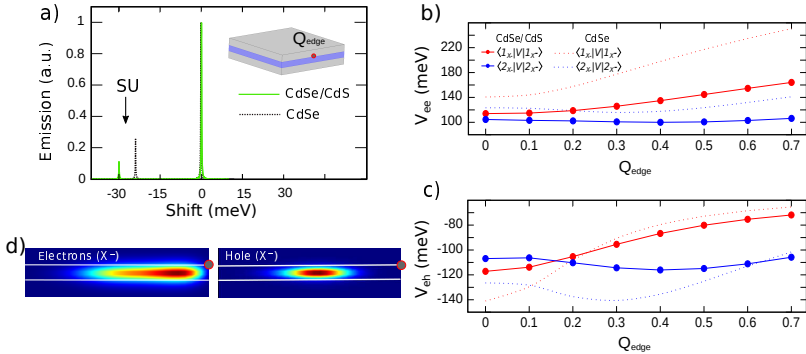


Figure 5: (a) Normalized  $X^-$  emission spectrum in a CdSe/CdS NPL with 6 ML-thick shell (solid line), compared to that of a core-only CdSe NPL (dotted line). The spectra are centered at the energy of the band edge.  $Q_{edge} = 0.6$  (0.4) is used for the CdSe/CdS NPL (core-only NPL), to maximize the relative height of SU lines. The SU peak for the core/shell system is smaller than for core-only NPLs. (b,c) Average Coulomb integrals of  $|GS_{X^-}\rangle$  configurations  $|1_{X^-}\rangle$  and  $|2_{X^-}\rangle$ : (b) electron-electron repulsion, (c) electron-hole attraction. Solid (dotted) lines are used for core/shell (core-only) NPLs. The interactions are weaker in the core/shell structure. (d) Charge densities of electrons (left) and hole (right) for the trion ground state in the CdSe/CdS NPL at  $Q_{edge} = 0.6$ . The electron stays in the vicinity of the core, despite the shallow band offset.

the core, further contributes to the weakening. This observation is reflected in Figs. 5b and 5c, which show that Coulomb interactions (especially  $V_{ee}$ ) are weakened in core/shell NPLs (solid lines) as compared to core-only NPLs (dotted lines). Configuration  $|2_{X^-}\rangle$  is then less stabilized with respect to  $|1_{X^-}\rangle$ , which implies smaller  $|c_2|$  coefficient in the CI expansion.

Figure 5d compares the charge density of the two electrons (left) and hole (right) in  $|GS_{X^-}\rangle$ . The trion electrons are found to stay in the vicinity of the core, rather than delocalizing all over the structure, to benefit from interaction with the hole. This is consistent with the observed behavior of CdSe/CdS NPLs being similar to that of core-only structures, albeit with weakened Coulomb interactions due to the lessened confinement.

Understanding the conditions which promote SU processes allows us to devise structures where their impact would be maximal. In Fig. 6 we consider a core/shell NPL with the same dimensions as before, but CdSe/CdTe composition. The NPL is chosen to be charged with a positive trion ( $X^+$ ), since the heavier mass of holes should favor Coulomb admixture as



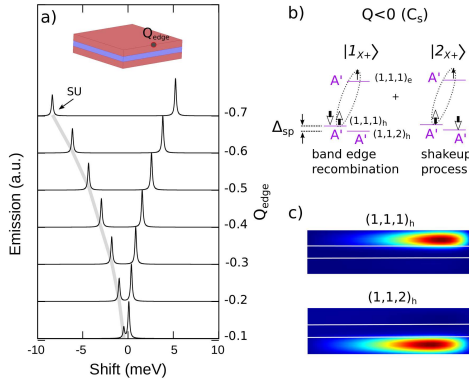


Figure 6: (a) Normalized  $X^+$  emission spectrum in a CdSe/CdTe NPL with 6 ML thick shells, as a function of the lateral charge strength. The shaded line is a guide to the eye. SU peaks and fundamental transition have comparable intensities. (b) Two main  $|GS_{X^+}\rangle$  configurations in the CI expansion in the presence of a charge. The weight of  $|2_{X^+}\rangle$  is comparable to that of  $|1_{X^+}\rangle$  in this system, which explains the high SU peaks in (a). (c) Wave function of  $(1, 1, 1)_h$  and  $(1, 1, 2)_h$  hole orbitals under  $Q_{edge} = -0.5$ . The states have the same symmetry but localize on opposite sides of the core to stay orthogonal.

compared to electrons. Because of the type-II band alignment, the electron stays in the CdSe core and the holes in the CdTe region, as observed in related core/crown structures.<sup>15,16</sup> In the absence of external charges, the two first hole orbitals are  $(1, 1, 1)_h$  and  $(1, 1, 2)_h$ , i.e. the symmetric ( $A_{1g}$ ) and antisymmetric ( $A_{1u}$ ) solutions of the double well potential, respectively, which are almost degenerate because tunneling across the core is negligible (i.e.  $\Delta_{sp} \rightarrow 0$ ). Switching on a negative surface charge,  $Q_{edge} < 0$ , lifts the inversion symmetry so that both orbitals acquire  $A'$  symmetry and can be Coulomb coupled. The admixture between configurations  $|1_{X^+}\rangle$  and  $|2_{X^+}\rangle$ , depicted in Fig. 6b, is then very strong. In the presence of the charge, the two hole orbitals tend to localize on opposite shell sides to remain orthogonal, as shown in Fig. 6c. This implies that configuration  $|1_{X^+}\rangle$ , which has two holes in the same orbital, has much stronger repulsion than configuration  $|2_{X^+}\rangle$ , which distributes the two electrons on opposite sides of the core. This makes  $\langle 1_{X^+} | V_{hh} | 1_{X^+} \rangle \gg \langle 2_{X^+} | V_{hh} | 2_{X^+} \rangle$ . Altogether, the small  $\Delta_{sp}$  value and the large difference in hole-hole repulsion explain the strong admixture between configurations  $|1_{X^+}\rangle$  and  $|2_{X^+}\rangle$ . As shown in Fig. 6a, this gives

rise to SU peaks whose magnitude is almost as large as that of the fundamental transition (72% for  $Q_{edge} = -0.5$ ).

It is worth noting that trions in type-II NPLs, having stronger repulsions than attractions, are susceptible of displaying a sizable SU peak even in the absence of trap charges. We noticed this behavior in earlier simulations of rectangular shaped ( $D_{2h}$  symmetry) core/crown CdSe/CdTe NPLs.<sup>32</sup>

## Discussion

Our simulations show that SU processes can be expected for trions in core-only and core/shell NPLs, if off-centered charges are present. We discuss here the potential relationship of this finding with experiments in the literature and practical implications.

### Relationship with experiments

In core-only CdSe NPLs, the low temperature photoluminescence is thought to arise from subpopulations of excitons and negative trions.<sup>24,33,46</sup> Very recently, Antolinez and co-workers have reported that the  $X^-$  emission shows a distinct peak or a shoulder (depending on the film thickness) redshifted from the trion band edge transition. The redshift is  $\sim 19$  meV and the relative height 15 – 25% that of the main peak.<sup>24</sup> They speculated that the origin could be a SU process of the kind we study. Our calculations support the feasibility of this interpretation. Figure 1a shows excellent agreement with the experimental measurements, both in energy and relative intensity of the SU peak, assuming a lateral charge with  $Q_{edge} = 0.3 - 0.4$ , which gives a redshift of 19 – 25 meV and a relative height of 15 – 23 %.

The presence of acceptor charges in CdSe NPLs likely originates when the hole of a photoexcited electron-hole pair is trapped by a surface defect. The next electron-hole pair generated in the NPL joins the residual electron to form  $X^-$ , while the trapped hole exerts a screened electrostatic potential.<sup>22,38,47</sup> The coexistence of  $X^-$  and trapped surface charges in

CdSe NPLs is backed up by studies reporting correlation between surface-to-volume ratio, laser irradiation time and trion emission intensity.<sup>46</sup> A plausible location for surface charges are the lateral sidewalls of the NPL (as in Fig. 1b). This possibility is suggested by studies showing that Z-type ligand desorption –and hence surface traps– in CdSe NPLs is more frequent on these facets,<sup>48</sup> and by the fact that CdSe/CdS core/crown NPLs generally improve the photoluminescence quantum yield as compared to core-only structures, despite having larger surfaces on top and bottom.<sup>14</sup> Because off-centered charges are needed to originate SU peaks, lateral charges are candidates to trigger such processes.

In core/shell CdSe/CdS NPLs, SU processes have been also proposed as the origin of multi-peaked fluorescence emission –and hence broadened line width–.<sup>23</sup> Our simulations in Fig. 5a confirm one can indeed expect a sizable SU peak in such structures. We note that earlier experimental studies had so far interpreted the line width broadening as a result of either SU processes<sup>23</sup> or of surface defects.<sup>12</sup> By showing that the second effect is a prerequisite for the first one, our study helps to reconcile both interpretations. Nonetheless, two remarkable disagreements are observed between our simulations and Ref.<sup>23</sup> measurements. First, the experiments show from 2 to 4 emission peaks, which are interpreted as the  $X^-$  fundamental transition plus up to three redshifted, SU peaks. In our calculations, however, we fail to see more than one significant SU replica. Second, the highest-energy peak in the experiment is never the brightest one. This is inconsistent with our results and with earlier studies on epitaxial quantum wells and dots, where the higher-energy peak corresponds to the fundamental transition, which is the most likely recombination channel.<sup>25–29</sup>

Tentatively, one may suspect that a large number of SU peaks in core/shell CdSe/CdS NPLs could be connected with the thick CdS shell (12 ML in Ref.<sup>23</sup>), which makes surface defects more likely than in core-only structures. A significant presence of defects in these structures has been hinted by studies showing that the long radiative lifetime is not due to electron delocalization but to the influence of impurities.<sup>13</sup> However, Coulomb interactions are weaker than in core-only structures (Fig. 5c,d), where only one SU peak has been mea-

sured.<sup>24</sup> It is then not surprising that, despite investigating different charge locations (Figs. S3, S6 and S7 in SI), conduction band-offset values (Fig. S4) and shell thicknesses (Fig.S5), we see at most one significant SU satellite. Deviations from the squared core shape, despite lowering the symmetry, do not change this result either (see Fig.S8).

Regarding the relative intensity of the peaks, as mentioned in the previous section, the highest-energy one (fundamental transition) is proportional to the weight of configuration  $|1_{X^-}\rangle$  in the CI expansion,  $|c_1|^2$ , while subsequent (SU) peaks would be proportional to  $|c_2|^2$ ,  $|c_3|^2$ , ... Configuration  $|1_{X^-}\rangle$  (all carriers in the ground orbital, Fig. 2c) is nodeless and hence naturally expected to be the dominant one, so the highest-energy peak is also the brightest one. We have not observed SU peaks exceeding the fundamental transition height despite considering different charge locations and shell thicknesses (see SI). Even in CdSe/CdTe NPLs, which constitute a limit case, SU peaks never exceed the height of the main transition, see Fig. 6a.

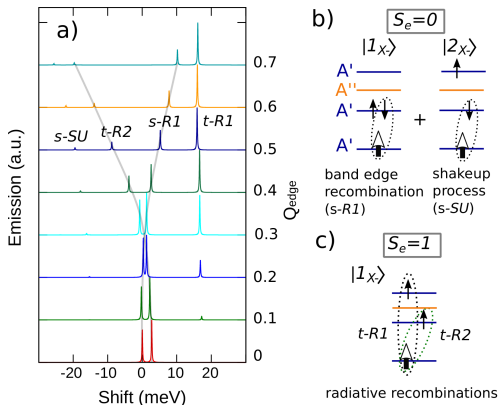


Figure 7: (a) Normalized  $X^-$  emission spectrum in a CdSe/CdS NPL, as a function of the lateral charge strength. An electron spin relaxation bottleneck is imposed, so that emission comes from the lowest singlet ( $S_e = 0$ , ground state) and triplet ( $S_e = 1$ ) states. Shaded lines are guides to the eyes. (b-c) Sketches showing the relevant electron-hole recombination channels of singlet and triplet states. (b) The singlet can give rise to one fully radiative ( $s-R1$ ) plus one SU transition ( $s-SU$ ). (c) The triplet can give rise to two fully radiative transitions,  $t-R1$  and  $t-R2$ .

We conclude from our simulations that SU lines may be present in the spectra of CdSe/CdS

NPLs, but they are unlikely to explain all the features observed in Ref.<sup>23</sup> As an alternative interpretation for the experiments, a multi-peaked emission spectrum could result from stacking of colloidal NPLs,<sup>49</sup> which leads to electronic coupling through dielectric confinement.<sup>50</sup> However, the time-dependent spectral shifts observed by Antolinez *et al.* suggest that all peaks arise from the same NPL, and significant stacking was not expected in the experiment samples.<sup>23</sup> We thus propose a different interpretation. Namely, simultaneous emission from the  $X^-$  ground state, with singlet electron spin ( $S_e = 0$ ), and a metastable excited state with triplet electron spin ( $S_e = 1$ ). The decay from the triplet to the singlet state is slowed down by spin selection rules, as phonons are spinless. This could allow simultaneous occupation of the two states even if the energy splitting exceeds thermal energy.

To illustrate this point, in Figure 7a we show the calculated emission of  $X^-$  assuming equipopulation of  $S_e = 0$  and  $S_e = 1$  trion states. One can see that the number of sizable peaks in the spectrum ranges from two to four, depending on the strength of surface charge,  $Q_{edge}$ . The origin of these peaks is summarized in the sketches of Fig. 7b and 7c. The singlet (Fig. 7b) can give rise to a fully radiative transition ( $s-R1$ ) and a SU transition ( $s-SU$ ), as described in the previous sections. In turn, the triplet (Fig. 7c) can give rise to two fully radiative transitions ( $t-R1$  and  $t-R2$ ), depending on which electron recombines with the hole.  $t-R2$  is readily visible at  $Q_{edge} = 0$ , but  $t-R1$  requires recombining the hole with an excited electron, a process which is again activated when the surface charge lifts symmetry restrictions. However, unlike in SU processes, the two triplet transitions come from the main configuration of the trion CI expansion. Therefore, their intensity can be comparable to that of the band edge transition,  $s-SU$ , even if Coulomb admixture is weak. The triplet transitions are built on both sides of  $s-SU$ , with inter-peak energy splittings up to few tens of meV. The relative sizes of the peaks will be further modulated in realistic situations by a finite triplet-singlet decay rate. This relaxation channel would possibly reduce the relative population of  $S_e = 1$ , and hence the intensity of  $t-R1$ .

Altogether, the number of peaks, the magnitude of the energy splitting between the peaks

and the flexible intensities provide a framework to explain the multi-peaked photoluminescence of Ref.<sup>23</sup> Several other aspects of this proposal are consistent with the experiments. For example, because all peaks in Fig. 7a arise from the same NPL, they will experience simultaneous spectral shifts when surface impurities migrate.<sup>23</sup> Also, the hot trion emission is expected to vanish when the impurities are removed, as *t-R1* becomes deactivated and *t-R1* almost merges with the singlet emission, *s-R1*, see Fig. 7a for  $Q_{edge} = 0$ . This agrees with the experimental observation that the line shape evolves from asymmetric to symmetric as temperature increases.<sup>12</sup>

The fact that triplet emission is observed in CdSe/CdS NPLs, but not in CdSe ones, may be explained from the strong spin-spin interaction of resident carriers and surface dangling bonds in the latter case,<sup>51</sup> which should speed up spin relaxation through flip/flop processes. This mechanism is expected to be inhibited in core/shell structures, because  $X^-$  carriers stay far from the surface, as shown in Fig. 5d. On the other hand, the triplet trion is expected to have fine structure through electron-hole exchange interaction,<sup>52</sup> which may not fit the mono-exponential photoluminescence decay reported in Ref.<sup>23</sup> Further experiments are needed, e.g. on polarisation of the different peaks under external fields<sup>33,53</sup> or magnetic dispersion<sup>31</sup> to confirm the different spin of the emissive states in CdSe/CdS NPLs.

The observation of metastable triplet trion photoluminescence has been previously reported in epitaxial quantum wells<sup>27,54</sup> and dots,<sup>53</sup> and more recently in transition metal chalcogenide monolayers.<sup>55</sup> To our knowledge, however, its presence in colloidal nanostructures has not been confirmed.

## Control of SU processes

Inasmuch as SU processes can be responsible for the line width broadening NPLs, their suppression is desirable to improve color purity in optical applications. It has been suggested that this job could be achieved by increasing quantum confinement, reducing either lateral dimensions or shell thickness –the latter would favor electrostatic confinement.<sup>23</sup> Both

strategies have the drawback of introducing size dispersion in ensemble luminescence. From our theoretical analysis, we confirm that reducing Coulomb admixture would minimize SU processes, but this can be achieved by weakening Coulomb interactions instead of increasing quantum confinement. For example, reducing dielectric confinement or using thinner cores to enhance the quasi-type-II character should contribute to this goal. Obviously, this approach would have the drawback of reducing the band edge recombination rate as well.

Alternatively, since our study shows that trap charges are ultimately responsible for SU processes, experimental routes to suppress SU processes could be directed to control of traps. Appropriate choice of surface ligands,<sup>48</sup> electrochemical potentials<sup>56</sup> and interface alloying<sup>19,20</sup> could contribute to this end.

Because we find surface charges on lateral sidewalls particularly suited to induce SU processes, the growth of core/crown heterostructures is expected to reduce their influence by keeping the outer rim away from the photogenerated carriers. This suggestion seems to agree with experimental observations by Kelestemur and co-workers, indicating that core/crown/shell CdSe/CdS NPLs have more symmetric emission behavior than core/shell ones at cryogenic temperatures,<sup>57</sup> This can be understood as a consequence of the suppression of SU processes in the low-energy tail of the emission band. It is also consistent with recent single-particle studies showing that the line width in CdTe/CdSe core/crown NPLs is set by LO phonon replica of neutral excitons, rather than SU peaks of trions.<sup>32</sup>

Should the role of metastable triplet states be confirmed in CdSe/CdS NPLs, strategies to control the line width should rather focus on enhancing the interaction of confined carriers with surface spins<sup>51</sup> or intrinsic spin-orbit interaction,<sup>58</sup> to shorten their lifetime. Replacing trion by neutral exciton emission through thermal dissociation,<sup>59</sup> is yet another possibility to avoid SU and high spin peaks.

Thus, our calculations propose a wealth of experiments targeted at material design to tune quantum and dielectric confinement, and exciton-surface/interface interactions, and set suitable temperature ranges to control SU/triplet emission.

## Conclusions

We have shown that SU processes in colloidal NPLs are enabled by severe Coulomb admixture –which results from strong Coulomb interactions and weak lateral confinement– and the presence of off-centered electrostatic traps, which suppress the protection against Auger processes provided by symmetry conservation. Surface charges on lateral sidewalls seem particularly efficient to this end.

Under typical experimental conditions, core-only and core/shell NPLs are susceptible of showing a SU peak with oscillator strength 0.1-0.3 times that of the band edge transition. This is at least one order magnitude larger than in epitaxial quantum wells. The SU peak is redshifted from the band edge peak by up to few tens of meV, thus providing a source of line width broadening.

These results are in excellent agreement with recent experimental findings in CdSe NPLs<sup>24</sup> in terms of number of emission peaks, energy splitting and relative intensity, but only partially so with those of core/shell CdSe/CdS NPLs.<sup>23</sup> Experiments in the latter structure are however in line with an alternative interpretation involving simultaneous participation from trion singlet and metastable triplet states.

Strategies to narrow the line width of NPLs through suppression of SU processes should aim at controlling charge traps or Coulomb admixture.

## Methods

Calculations are carried within k-p-continuum elastic theory framework. Independent electron and hole states are calculated with single-band Hamiltonians including core/shell strain and self-energy potential terms. Model details and material parameters are given in Ref.<sup>45</sup> Ligand induced strain<sup>60,61</sup> cannot be quantified with our continuum model, but its effect on the line width broadening is expected to arise from incomplete passivation,<sup>60</sup> resulting in surface traps. We include such traps as point charges. Point charge electrostatic potentials



and Coulomb integrals for CI matrix elements, including dielectric mismatch effects, are calculated solving Poisson Equation with Comsol 4.2. The CI basis set is formed by all possible combinations of the first 22 single-electron and 22 single-hole spin-orbitals. For  $X^-$ , these are combined to form configurations  $|m_{X^-}\rangle$  as the Hartree product of one hole spin-orbital with a two-electron Slater determinant.

### Supporting Information

This material is available free of charge via the internet at <http://pubs.acs.org>.

Additional calculations on the influence of the trion sign, surface charge location, conduction band offset and NPL core shape over the formation of SU processes.

## Acknowledgement

The authors acknowledge support from MICINN project CTQ2017-83781-P. We are grateful to I. Moreels, A. Achtstein and F. Rabouw for useful discussions.

## References

- (1) Lhuillier, E.; Pedetti, S.; Ithurria, S.; Nadal, B.; Heuclin, H.; Dubertret, B. Two-dimensional colloidal metal chalcogenides semiconductors: synthesis, spectroscopy, and applications. *Accounts of Chemical Research* **2015**, *48*, 22–30.
- (2) Min, Y.; Im, E.; Hwang, G.-T.; Kim, J.-W.; Ahn, C.-W.; Choi, J.-J.; Hahn, B.-D.; Choi, J.-H.; Yoon, W.-H.; Park, D.-S., et al. Heterostructures in two-dimensional colloidal metal chalcogenides: Synthetic fundamentals and applications. *Nano Research* **2019**, 1–20.
- (3) Diroll, B. T. Colloidal quantum wells for optoelectronic devices. *Journal of Materials Chemistry C* **2020**, *8*, 10628–10640.

- (4) Sharma, M.; Delikanli, S.; Demir, H. V. Two-Dimensional CdSe-Based Nanoplatelets: Their Heterostructures, Doping, Photophysical Properties, and Applications. *Proceedings of the IEEE* **2019**, *108*, 655–675.
- (5) Feldmann, J.; Peter, G.; Göbel, E.; Dawson, P.; Moore, K.; Foxon, C.; Elliott, R. Linewidth dependence of radiative exciton lifetimes in quantum wells. *Physical Review Letters* **1987**, *59*, 2337.
- (6) Planelles, J.; Achtstein, A. W.; Scott, R.; Owschimikow, N.; Woggon, U.; Climente, J. I. Tuning intraband and interband transition rates via excitonic correlation in low-dimensional semiconductors. *ACS Photonics* **2018**, *5*, 3680–3688.
- (7) Ithurria, S.; Tessier, M.; Mahler, B.; Lobo, R.; Dubertret, B.; Efros, A. L. Colloidal nanoplatelets with two-dimensional electronic structure. *Nature Materials* **2011**, *10*, 936–941.
- (8) Riedinger, A.; Ott, F. D.; Mule, A.; Mazzotti, S.; Knüsel, P. N.; Kress, S. J.; Prins, F.; Erwin, S. C.; Norris, D. J. An intrinsic growth instability in isotropic materials leads to quasi-two-dimensional nanoplatelets. *Nature Materials* **2017**, *16*, 743–748.
- (9) Christodoulou, S.; Climente, J. I.; Planelles, J.; Brescia, R.; Prato, M.; Martín-García, B.; Khan, A. H.; Moreels, I. Chloride-induced thickness control in CdSe nanoplatelets. *Nano letters* **2018**, *18*, 6248–6254.
- (10) Bhandari, G. B.; Subedi, K.; He, Y.; Jiang, Z.; Leopold, M.; Reilly, N.; Lu, H. P.; Zayak, A. T.; Sun, L. Thickness-controlled synthesis of colloidal PbS nanosheets and their thickness-dependent energy gaps. *Chemistry of Materials* **2014**, *26*, 5433–5436.
- (11) Tessier, M. D.; Javaux, C.; Maksimovic, I.; Loriette, V.; Dubertret, B. Spectroscopy of single CdSe nanoplatelets. *ACS nano* **2012**, *6*, 6751–6758.

- (12) Tessier, M.; Mahler, B.; Nadal, B.; Heuclin, H.; Pedetti, S.; Dubertret, B. Spectroscopy of colloidal semiconductor core/shell nanoplatelets with high quantum yield. *Nano letters* **2013**, *13*, 3321–3328.
- (13) Achtstein, A. W.; Marquardt, O.; Scott, R.; Ibrahim, M.; Riedl, T.; Prudnikau, A. V.; Antanovich, A.; Owschimikow, N.; Lindner, J. K.; Artemyev, M., et al. Impact of Shell Growth on Recombination Dynamics and Exciton–Phonon Interaction in CdSe–CdS Core–Shell Nanoplatelets. *ACS nano* **2018**, *12*, 9476–9483.
- (14) Tessier, M. D.; Spinicelli, P.; Dupont, D.; Patriarche, G.; Ithurria, S.; Dubertret, B. Efficient exciton concentrators built from colloidal core/crown CdSe/CdS semiconductor nanoplatelets. *Nano letters* **2014**, *14*, 207–213.
- (15) Antanovich, A.; Prudnikau, A.; Melnikau, D.; Rakovich, Y. P.; Chuvilin, A.; Woggon, U.; Achtstein, A. W.; Artemyev, M. Colloidal synthesis and optical properties of type-II CdSe–CdTe and inverted CdTe–CdSe core–wing heteronanoplatelets. *Nanoscale* **2015**, *7*, 8084–8092.
- (16) Kelestemur, Y.; Olutas, M.; Delikanli, S.; Guzelturk, B.; Akgul, M. Z.; Demir, H. V. Type-II colloidal quantum wells: CdSe/CdTe core/crown heteronanoplatelets. *The Journal of Physical Chemistry C* **2015**, *119*, 2177–2185.
- (17) Polovitsyn, A.; Dang, Z.; Movilla, J. L.; Martín-García, B.; Khan, A. H.; Bertrand, G. H.; Brescia, R.; Moreels, I. Synthesis of air-stable CdSe/ZnS core–shell nanoplatelets with tunable emission wavelength. *Chem. Mater.* **2017**, *29*, 5671–5680.
- (18) Saidzhonov, B.; Kozlovsky, V.; Zaytsev, V.; Vasiliev, R. Ultrathin CdSe/CdS and CdSe/ZnS core-shell nanoplatelets: The impact of the shell material on the structure and optical properties. *Journal of Luminescence* **2019**, *209*, 170–178.
- (19) Rossinelli, A. A.; Rojo, H.; Mule, A. S.; Aellen, M.; Cocina, A.; De Leo, E.; Schäublin, R.; Norris, D. J. Compositional Grading for Efficient and Narrowband Emis-

- sion in CdSe-Based Core/Shell Nanoplatelets. *Chemistry of Materials* **2019**, *31*, 9567–9578.
- (20) Kelestemur, Y.; Shynkarenko, Y.; Anni, M.; Yakunin, S.; De Giorgi, M. L.; Kovalenko, M. V. Colloidal CdSe Quantum Wells with Graded Shell Composition for Low-Threshold Amplified Spontaneous Emission and Highly Efficient Electroluminescence. *ACS nano* **2019**, *13*, 13899–13909.
- (21) Yadav, S.; Singh, A.; Thulasidharan, L.; Sapra, S. Surface decides the photoluminescence of colloidal CdSe nanoplatelets based core/shell heterostructures. *The Journal of Physical Chemistry C* **2018**, *122*, 820–829.
- (22) Rabouw, F. T.; van der Bok, J. C.; Spinicelli, P.; Mahler, B.; Nasilowski, M.; Pedetti, S.; Dubertret, B.; Vanmaekelbergh, D. Temporary charge carrier separation dominates the photoluminescence decay dynamics of colloidal CdSe nanoplatelets. *Nano Letters* **2016**, *16*, 2047–2053.
- (23) Antolinez, F. V.; Rabouw, F. T.; Rossinelli, A. A.; Cui, J.; Norris, D. J. Observation of Electron Shakeup in CdSe/CdS Core/Shell Nanoplatelets. *Nano Lett.* **2019**, *19*, 8495–8502.
- (24) Antolinez, F. V.; Rabouw, F. T.; Rossinelli, A. A.; Keitel, R. C.; Cocina, A.; Becker, M. A.; Norris, D. J. Trion Emission Dominates the Low-Temperature Photoluminescence of CdSe Nanoplatelets. *Nano Letters* **2020**, *20*, 5814–5820.
- (25) Nash, K.; Skolnick, M.; Saker, M.; Bass, S. Many body shakeup in quantum well luminescence spectra. *Physical Review Letters* **1993**, *70*, 3115.
- (26) Finkelstein, G.; Shtrikman, H.; Bar-Joseph, I. Shakeup processes in the recombination spectra of negatively charged excitons. *Physical Review B* **1996**, *53*, 12593.

- (27) Bryja, L.; Wójs, A.; Misiewicz, J.; Potemski, M.; Reuter, D.; Wieck, A. Magneto-optical probing of weak disorder in a two-dimensional hole gas. *Physical Review B* **2007**, *75*, 035308.
- (28) Dzyubenko, A. Shake-up processes in a low-density two-dimensional electron gas: Spin-dependent transitions to higher hole Landau levels. *Physical Review B* **2004**, *69*, 115332.
- (29) Paskov, P.; Holtz, P.-O.; Wongmanerod, S.; Monemar, B.; Garcia, J.; Schoenfeld, W.; Petroff, P. M. Auger processes in InAs self-assembled quantum dots. *Physica E: Low-dimensional Systems and Nanostructures* **2000**, *6*, 440–443.
- (30) Hawrylak, P. Resonant magnetoexcitons and the fermi-edge singularity in a magnetic field. *Physical Review B* **1991**, *44*, 11236.
- (31) Löbl, M. C.; Spinnler, C.; Javadi, A.; Zhai, L.; Nguyen, G. N.; Ritzmann, J.; Midolo, L.; Lodahl, P.; Wieck, A. D.; Ludwig, A., et al. Radiative Auger process in the single-photon limit. *Nature Nanotechnology* **2020**, *15*, 558–562.
- (32) Steinmetz, V. et al. Emission State Structure and Linewidth Broadening Mechanisms in Type-II CdSe/CdTe Core-Crown Nanoplatelets: A Combined Theoretical - Single Nanocrystal Optical Study. *The Journal of Physical Chemistry C* **2020**, *124*, 17352–17363.
- (33) Shornikova, E. V.; Yakovlev, D. R.; Biadala, L.; Crooker, S. A.; Belykh, V. V.; Kochiev, M. V.; Kuntzmann, A.; Nasilowski, M.; Dubertret, B.; Bayer, M. Negatively charged excitons in CdSe nanoplatelets. *Nano Letters* **2020**, *20*, 1370–1377.
- (34) Shornikova, E. V.; Biadala, L.; Yakovlev, D. R.; Feng, D.; Sapega, V. F.; Flipo, N.; Golovatenko, A. A.; Semina, M. A.; Rodina, A. V.; Mitioglu, A. A., et al. Electron and hole g-factors and spin dynamics of negatively charged excitons in CdSe/CdS colloidal nanoplatelets with thick shells. *Nano letters* **2018**, *18*, 373–380.

- (35) Adachi, S. *Handbook on Physical Properties of Semiconductors, vol.3*; Kluwer Academics, 2004.
- (36) Achtstein, A. W.; Schliwa, A.; Prudnikau, A.; Hardzei, M.; Artemyev, M. V.; Thomsen, C.; Woggon, U. Electronic structure and exciton–phonon interaction in two-dimensional colloidal CdSe nanosheets. *Nano Lett.* **2012**, *12*, 3151–3157.
- (37) Beyler, A. P.; Marshall, L. F.; Cui, J.; Brokmann, X.; Bawendi, M. G. Direct observation of rapid discrete spectral dynamics in single colloidal CdSe–CdS core-shell quantum dots. *Physical Review Letters* **2013**, *111*, 177401.
- (38) Califano, M.; Franceschetti, A.; Zunger, A. Temperature Dependence of Excitonic Radiative Decay in CdSe Quantum Dots: The Role of Surface Hole Traps. *Nano Letters* **2005**, *5*, 2360–2364.
- (39) Drijvers, E.; De Roo, J.; Martins, J. C.; Infante, I.; Hens, Z. Ligand displacement exposes binding site heterogeneity on CdSe nanocrystal surfaces. *Chemistry of Materials* **2018**, *30*, 1178–1186.
- (40) Jacak, L.; Hawrylak, P.; Wojs, A. *Quantum Dots*; Springer, 1998.
- (41) Rajadell, F.; Climente, J. I.; Planelles, J. Excitons in core-only, core-shell and core-crown CdSe nanoplatelets: Interplay between in-plane electron-hole correlation, spatial confinement, and dielectric confinement. *Phys. Rev. B* **2017**, *96*, 035307.
- (42) Richter, M. Nanoplatelets as material system between strong confinement and weak confinement. *Phys. Rev. Mater.* **2017**, *1*, 016001.
- (43) Benchamekh, R.; Gippius, N. A.; J., E.; Nestoklon, M. O.; Jancu, J.-M.; Ithurria, S.; Dubertret, B.; Efros, A. L.; P., V. Tight-Binding Calculations of Image-Charge Effects in Colloidal Nanoscale Platelets of CdSe. *Phys. Rev. B: Condens. Matter Mater. Phys.* **2014**, *89*, 035307.

- (44) Even, J.; Pedesseau, L.; Kepenekian, M. Electronic surface states and dielectric self-energy profiles in colloidal nanoscale platelets of CdSe. *Physical Chemistry Chemical Physics* **2014**, *16*, 25182–25190.
- (45) Llusar, J.; Planelles, J.; Climente, J. I. Strain in Lattice-Mismatched CdSe-Based Core/Shell Nanoplatelets. *The Journal of Physical Chemistry C* **2019**, *123*, 21299–21306.
- (46) Yu, J.; Zhang, C.; Pang, G.; Sun, X. W.; Chen, R. Effect of Lateral Size and Surface Passivation on the Near-Band-Edge Excitonic Emission from Quasi-Two-Dimensional CdSe Nanoplatelets. *ACS applied materials & interfaces* **2019**, *11*, 41821–41827.
- (47) Feng, D.; Yakovlev, D. R.; Pavlov, V. V.; Rodina, A. V.; Shornikova, E. V.; Mund, J.; Bayer, M. Dynamic evolution from negative to positive photocharging in colloidal CdS quantum dots. *Nano Letters* **2017**, *17*, 2844–2851.
- (48) Leemans, J.; Singh, S.; Li, C.; Ten Brinck, S.; Bals, S.; Infante, I.; Moreels, I.; Hens, Z. Near-Edge Ligand Stripping and Robust Radiative Exciton Recombination in CdSe/CdS Core/Crown Nanoplatelets. *The Journal of Physical Chemistry Letters* **2020**, *11*, 3339–3344.
- (49) Diroll, B. T.; Cho, W.; Coropceanu, I.; Harvey, S. M.; Brumberg, A.; Holtgrewe, N.; Crooker, S. A.; Wasielewski, M. R.; Prakapenka, V. B.; Talapin, D. V., et al. Semiconductor nanoplatelet excimers. *Nano letters* **2018**, *18*, 6948–6953.
- (50) Movilla, J. L.; Planelles, J.; Climente, J. I. Dielectric Confinement Enables Molecular Coupling in Stacked Colloidal Nanoplatelets. *J. Phys. Chem. Lett.* **2020**, *11*, 3294–3300.
- (51) Shornikova, E. V.; Golovatenko, A. A.; Yakovlev, D. R.; Rodina, A. V.; Biadala, L.; Qiang, G.; Kuntzmann, A.; Nasilowski, M.; Dubertret, B.; Polovitsyn, A., et al. Surface spin magnetism controls the polarized exciton emission from CdSe nanoplatelets. *Nature Nanotechnology* **2020**, *15*, 277–282.

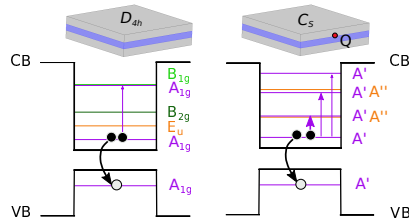
- (52) Ware, M.; Stinaff, E.; Gammon, D.; Doty, M.; Bracker, A.; Gershoni, D.; Korenev, V.; Bădescu, Ș.; Lyanda-Geller, Y.; Reinecke, T. Polarized fine structure in the photoluminescence excitation spectrum of a negatively charged quantum dot. *Physical Review Letters* **2005**, *95*, 177403.
- (53) Jovanov, V.; Kapfinger, S.; Bichler, M.; Abstreiter, G.; Finley, J. Direct observation of metastable hot trions in an individual quantum dot. *Physical Review B* **2011**, *84*, 235321.
- (54) Shields, A.; Osborne, J.; Simmons, M.; Pepper, M.; Ritchie, D. Magneto-optical spectroscopy of positively charged excitons in GaAs quantum wells. *Physical Review B* **1995**, *52*, R5523.
- (55) Vaclavkova, D.; Wyzula, J.; Nogajewski, K.; Bartos, M.; Slobodeniuk, A.; Faugeras, C.; Potemski, M.; Molas, M. Singlet and triplet trions in WS<sub>2</sub> monolayer encapsulated in hexagonal boron nitride. *Nanotechnology* **2018**, *29*, 325705.
- (56) Galland, C.; Ghosh, Y.; Steinbrück, A.; Sykora, M.; Hollingsworth, J. A.; Klimov, V. I.; Htoon, H. Two types of luminescence blinking revealed by spectroelectrochemistry of single quantum dots. *Nature* **2011**, *479*, 203–207.
- (57) Kelestemur, Y.; Guzelturk, B.; Erdem, O.; Olutas, M.; Gungor, K.; Demir, H. V. Platelet-in-Box Colloidal Quantum Wells: CdSe/CdS@ CdS Core/Crown@ Shell Heteronanoplatelets. *Advanced Functional Materials* **2016**, *26*, 3570–3579.
- (58) Tadjine, A.; Niquet, Y.-M.; Delerue, C. Universal behavior of electron g-factors in semiconductor nanostructures. *Physical Review B* **2017**, *95*, 235437.
- (59) Ayari, S.; Quick, M. T.; Owschimikow, N.; Christodoulou, S.; Bertrand, G. H.; Artemyev, M.; Moreels, I.; Woggon, U.; Jaziri, S.; Achtstein, A. W. Tuning trion binding energy and oscillator strength in a laterally finite 2D system: CdSe nanoplatelets as a model system for trion properties. *Nanoscale* **2020**, *12*, 14448.



- (60) Antanovich, A.; Achtstein, A.; Matsukovich, A.; Prudnikau, A.; Bhaskar, P.; Gurin, V.; Molinari, M.; Artemyev, M. A strain-induced exciton transition energy shift in CdSe nanoplatelets: the impact of an organic ligand shell. *Nanoscale* **2017**, *9*, 18042–18053.
- (61) Diroll, B. T. Ligand-Dependent Tuning of Interband and Intersubband Transitions of Colloidal CdSe Nanoplatelets. *Chemistry of Materials* **2020**, *32*, 5916–5923.

## For Table of Contents Use Only

Table of contents for manuscript “Nature and Control of Shakeup Processes in Colloidal Nanoplatelets”, by Jordi Llusar and Juan I. Climente.



Schematic of radiative Auger (shakeup) process in nanoplatelets (NPLs). Point symmetry largely protects the NPL from such process (left picture), but the presence of charge impurities lowers the symmetry and hence activates shakeup processes (right picture).

# Supporting Information for “Nature and Control of Shakeup Processes in Colloidal Nanoplatelets”

Jordi Llusar and Juan I. Climente\*

*Departament de Química Física i Analítica, Universitat Jaume I, E-12080, Castelló de la Plana, Spain*

E-mail: [climente@uji.es](mailto:climente@uji.es)

## **Abstract**

12 pages including 8 figures.

## Additional calculations

We present here additional calculations for further understanding of SU processes.

### Convergence of CI calculations

Configuration Interaction (CI) calculations on the basis of independent particle (or Hartree-Fock) orbitals provide an excellent description of repulsions in few- and many-fermion systems.<sup>1,2</sup> However, large basis sets are needed to describe strong attractions,<sup>3,4</sup> which are certainly present in colloidal NPLs<sup>5</sup> and are involved in a correct description of SU processes.

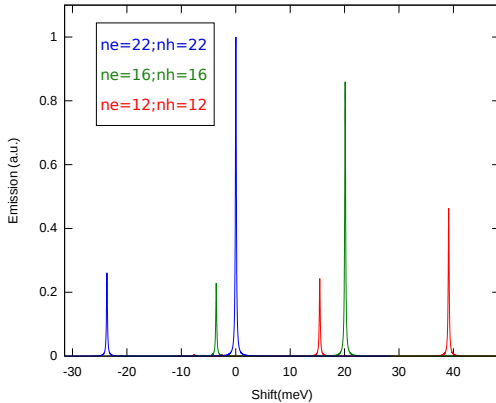


Figure S1:  $X^-$  emission spectrum for  $Q_{edge} = 0.4$  (see main text). Zero energy is set for the fundamental transition with  $ne = nh = 22$ .  $ne$  and  $nh$  are the number of single-electron and single-hole spin-orbitals, respectively, used to build the CI basis sets.

In Fig. S1 we compare the  $X^-$  emission spectrum calculated for CdSe NPLs –same dimensions as in main text– using different basis sizes. The basis is formed by all possible combinations of the first  $ne$  ( $nh$ ) independent particle spin-orbital states of electrons (holes). With increasing basis dimensions, the band edge transition peak red-shifts and gains intensity, which reveals an improved description of electron-hole correlation. The intensity of the SU peak height and its red-shift with respect to the band edge transition are however less sensitive to the basis dimensions. It follows from the figure that quantitative assessment on

the ratio of fundamental vs SU peak heights requires large basis sets. In the main text we use  $ne = nh = 22$ . By comparing with smaller values of  $ne/nh$  in the figure, it is clear that for this value –which involves very time-consuming computations– the ratio is reaching saturation. This validates the order of ratios provided in the main text. For the calculations in this Supporting Information, however, we may resort to  $ne = nh = 12$ , which overestimates the relative height of SU peaks, but suffices to provide qualitative assessment.

## Positive trion behaviour

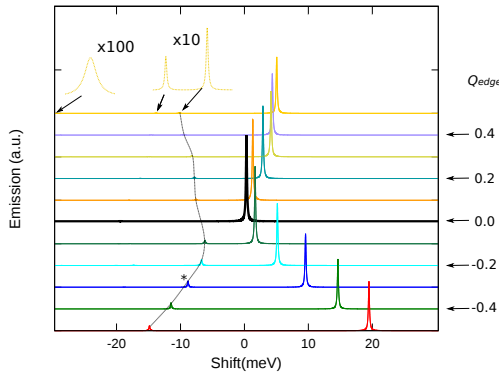


Figure S2:  $X^+$  normalized spectrum emission for different charge intensities. The arrows are pointing to SU satellites (dotted lines are guides to the eyes). The highest SU peak ( $Q_{edge} = -0.3$ ) is marked with a star. The origin of energies is set at the band edge recombination peak. The insets correspond to  $Q_{edge} = 0.5$  amplified SU peaks.

In the main text, we have mostly considered the case of negative trions. We show here that the same behavior holds for positive ones. To illustrate this point, we choose the case of the core-only NPL with an edge charge, equivalent to Fig.1d of the main text. Figure S2 shows that the presence of SU peaks in the emission spectrum is again strongly dependent on the value of the surface charge. For  $Q_{edge} = 0$ , no SU peak is observed. For repulsive ( $Q_{edge} > 0$ ) charges, SU are formed but very small in magnitude. The highest SU peaks are formed for weakly bound donor charges ( $Q_{edge} < 0$ ), which attract the holes of  $X^+$ , marked with a star in the figure. As in the  $X^-$  case, if the attractive charge further increases it

starts dissociating the trion. Consequently, SU peaks are quenched again. Notice however energy splittings for  $X^+$  (Fig. S2) are smaller than for  $X^-$  (Fig. 1d in the main text). This is expected from the heavier masses of holes.

## Effect of charge impurity location

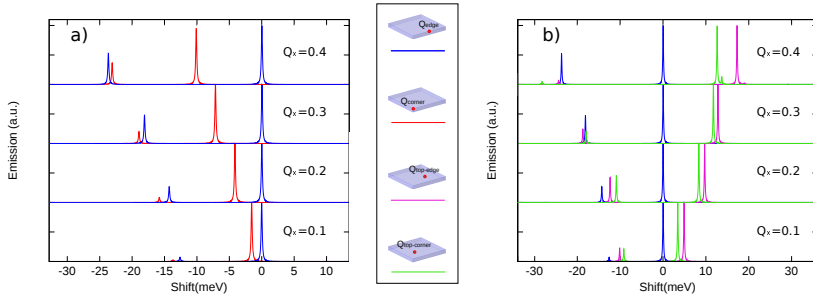


Figure S3:  $X^-$  emission spectra for different locations of surface charges. The spectra are normalized with respect to the energy and intensity of the  $Q_{edge}$  fundamental transition. (a) Edge-located vs. corner-located impurity. Blue and red lines stand for edge and corner, respectively. (b) Edge-located vs. edge-top-located vs. corner-top-located. Blue, green and pink lines stand for edge, top-corner and top-edge, respectively.  $ne = nh = 12$ .

In the main text we present the representative cases of a surface charge centered on top of the NPL ( $Q_{top}$ ), and that of a charge on the edge of lateral sidewall ( $Q_{edge}$ ). In Figure S3 we compare with different locations. One can see that the effect of a charge located in the corner, red line in Fig. S3a, provides similar SU peaks to that of the edge charge, blue line in the figure, both in energy and intensity. We recall that these traps seem to be particularly likely according to recent studies on ligand desorption.<sup>6,7</sup> Off-centered charges on top and bottom surfaces are studied in Fig. S3b. They give rise to SU peaks of similar height to that of  $Q_{edge}$ , although they reach the optimal charge value sooner than  $Q_{edge}$  ( $Q_{top-edge} \sim Q_{top-corner} \approx 0.2$  versus  $Q_{edge} = 0.4$ ), because they lie closer to the center of the NPL, where photogenerated carriers tend to localize.

## Effect of conduction band offset in CdSe/CdS NPLs

The value of the CdSe/CdS conduction band offset (CBO) has been a subject of debate in nanocrystal heterostructures.<sup>8-10</sup> We used, along our main text, an upper-bound unstrained value of 0.48 eV,<sup>8</sup> which is partly reduced by compressive strain in the core.<sup>10</sup> Here we explore the scenario where we use a lower-bound<sup>9</sup> value as well, to see the possible effect of enhancing electron delocalization over the CdS shell. Figure S4 compares the two cases. Lowering the CBO gives rise to slightly weaker electron-electron repulsion ( $V_{ee}$ ) and electron-hole attraction ( $V_{eh}$ ), however the differences are very small. One can then expect similar role of SU processes as in the main text.

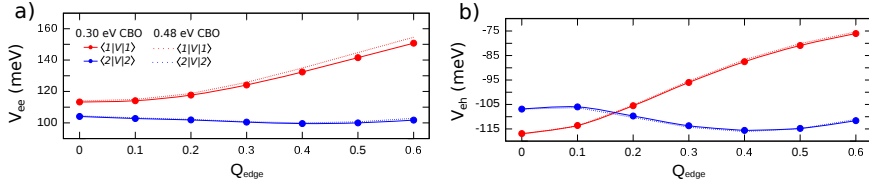


Figure S4: (a,b) Average Coulomb integrals for  $Q_{edge} = 0.6$ : (a) electron-electron repulsion and (b) electron-hole attraction for every CBO.  $ne = nh = 22$

## Effect of shell thickness in CdSe/CdS NPLs

Along the main text, core/shell NPLs under study had a shell thickness of 6ML on each side of the core. The experiments of Antolinez et al.<sup>11</sup> however used thicker shells (12 ML). In this section we compare qualitatively the response in the two cases using a moderate basis set ( $ne = nh = 12$ ), which permits addressing the experimental dimensions without the computational burden of the large basis set (for 12 ML thickness, the extended CI computation is beyond our current resources).

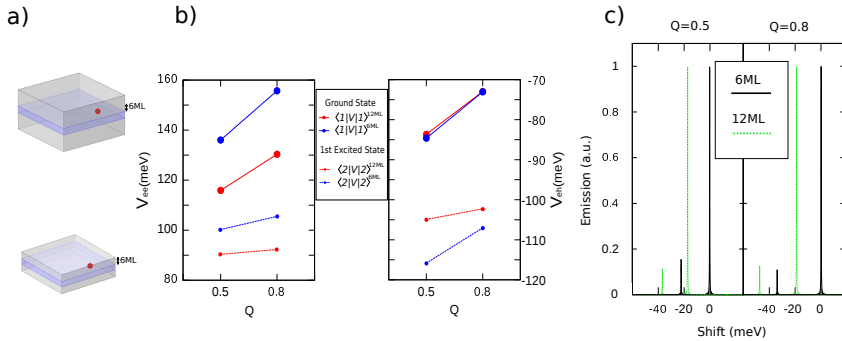


Figure S5: (a) Sketch of the NPLs we are comparing: 12ML shell (top) and 6ML (bottom). The charge is located at same coordinates. (b,c) Coulomb interactions: (b) repulsions e-e and (c) attractions e-h for  $Q = 0.5$  and  $Q = 0.8$ . (d,e) Normalized emission spectra of 6ML vs 12ML: (d)  $Q = 0.5$  and (e)  $Q = 0.8$ ;  $Q = 0$  is centred at band edge recombination energy for 6ML in both cases.  $ne = nh = 12$

If we focus on the charge location in both systems, Fig. S5a, one may expect similar behaviour. The main difference, as can be seen in Fig. S5b (left panel) occurs for repulsive electron-electron interactions, which are slightly weaker for thick shells. This is a consequence of the larger electron delocalization, which translates into smaller  $|c_2|$  coefficients in the CI expansion (see main text) and hence slightly smaller SU satellite, as observed in Fig. S5c.



## Effect of inserting multiple impurities in CdSe/CdS

We consider here the possibility that two surface traps, instead of one, are acting as electrostatic impurities in CdSe/CdS NPLs. Since there is a general preference of forming defects in the heterostructure interfaces – because of lattice mismatch<sup>10,12</sup> – and on lateral facets – where ligand desorption is more likely to happen<sup>6</sup>–, we choose the charges to be located as shown in Fig. S6a. The presence of two charges, combined with the weak in-plane confinement, easily dissociates the trion by driving one electron to each surface impurity. This can be seen in the charge densities of Fig. S6b. The number of visible SU peaks, however, remains one (see Fig. S6c). In the case of strong surface charges ( $Q = 1.0$ ), the trion triplet (discussed in the main text) becomes so close in energy to the singlet ground state that it shows up in the spectrum at 4 K, see right panel in Fig. S6c.

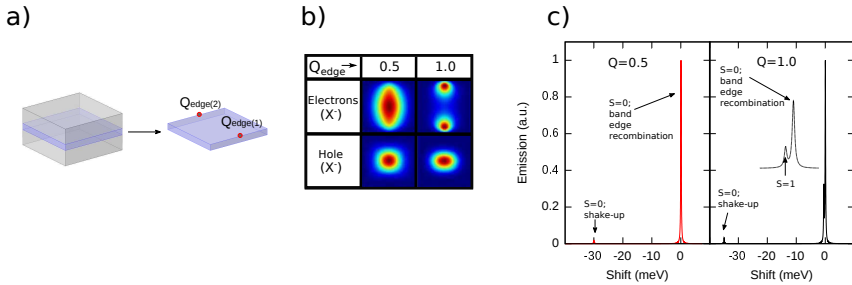


Figure S6: (a) Schematic of a CdSe/CdS NPL with 2 charges on edges intersecting interface and sidewall facet.  $Q_{edge(1)} = Q_{edge(2)} = Q_{edge}$ . The NPL shell is 12 ML thick. (b) In-plane electrons and hole charge densities for the  $X^-$  singlet ( $S = 0$ ) ground state at  $Q = 0.5$  and  $Q = 1.0$ ; (c) Normalized emission spectra at  $Q = 0.5$  (left) and  $Q = 1.0$  (right).  $ne = nh = 12$ .

If we further increase the charge  $Q$  (e.g. by assuming double point charges on each side of the NPL, see Fig. S7a), additional peaks start showing up in the emission spectrum, which is shown in Fig. S7g. The sketches in Fig. S7d-f assign each peak to a corresponding recombination process. Two transitions come from the  $X^-$  singlet ground state, namely its band edge ( $s-R1$ ) and first SU ( $s-SU$ ) recombinations. The other transitions are fully radiative recombinations arising from the triplet state,  $t-R1$  and  $t-R2$ . The picture is analogous to

that proposed in the Discussion section of the main text to explain the multi-peaked emission of ref.,<sup>11</sup> but in this case the triplet state is thermally occupied at 4 K, so there is no need to assume slow spin relaxation. The top panel in Fig S7g qualitatively resembles the clusters of four peaks often observed by Antolinez and co-workers in their photoluminescence measurements,<sup>11</sup> although the inter-peak energy splittings here are one order of magnitude smaller. As mentioned in the main text, assuming the triplet state is metastable even if it is beyond  $kT$  from the singlet ground state, and varying trapped charge location, it may be possible to retrieve the experimental spectra.

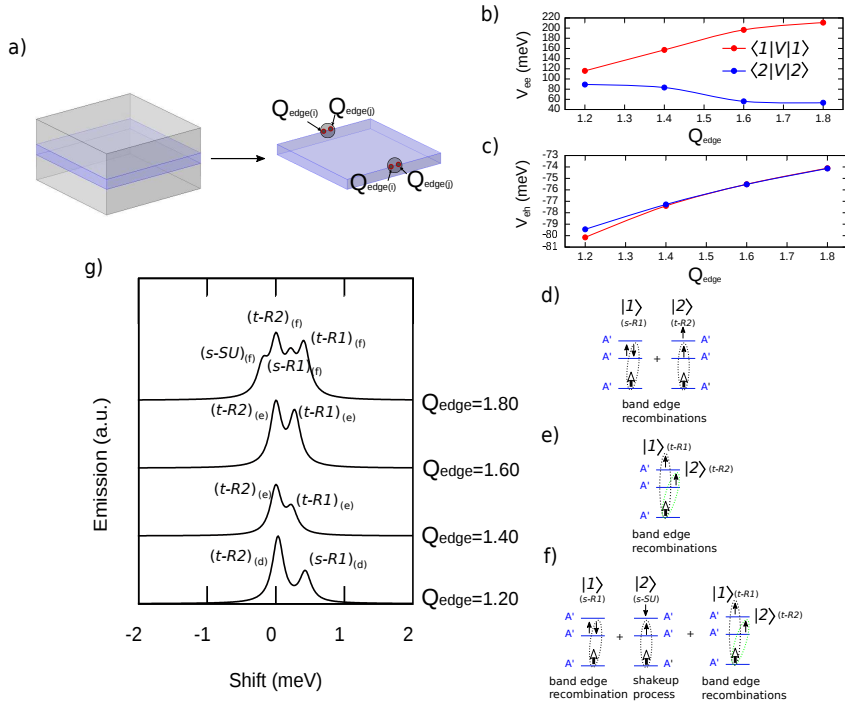


Figure S7: (a) Schematic of a CdSe/CdS NPL with 2 double charges on edges intersecting interface and sidewall facet. (b,c) Coulomb interactions: (b) electron-electron repulsion and (c) electron-hole attraction for configurations  $|1\rangle$  and  $|2\rangle$ . (d-f) Recombination processes involved in each transition. (g) Normalized emission spectrum. The energy origin is set at the position of the brightest peak,  $t-R2$ .  $Q_{edge}$  is the net charge on each edge (times the fundamental electron charge).  $ne = nh = 12$ .

## Effect of lateral shape

In the main text we study NPLs with squared geometry because we model the NPLs of ref.<sup>11</sup> experiments. Since symmetry lowering opens channels for SU processes, we wish to study if usual shape deviations –towards rectangular geometry– prompt additional SU lines. In Fig. S8 we compare the calculated emission spectrum for squared and rectangular CdSe/CdS NPLs. In the absence of surface charges, Figs. S8a and S8b, none of the two structures displays SU peaks. The reason is that symmetry lowering does not suffice to yield SU peaks. As shown in Fig. 2f,g of the main text, one also needs to enhance repulsion between the two excess carriers and reduce attraction with the opposite charge carrier to stimulate Coulomb admixture with  $|2_{\chi^-}\rangle$  for the trion ground state. This was observed for example in type-II, rectangular shaped, core/crown CdSe/CdTe NPLs.<sup>13</sup> It can be achieved in type-I and quasi-type-II NPLs with trap charges, as they lower the symmetry and partly dissociate the trion. Figs. S8c and S8d show that the presence of a lateral charge gives rise to a sizable SU peak in both squared and rectangular NPLs. In the case of the rectangular NPL, the SU peak is relatively smaller than in the squared one because of the stronger lateral confinement, which reduces Coulomb admixture. Figure S8 shows that deviations from perfect square geometry in core/shell CdSe/CdS NPLs do not induce additional SU peaks, thus reinforcing the belief that additional factors –other than SU processes– are needed to explain the observation of 3-4 emission peaks in ref.<sup>11</sup> experiments.

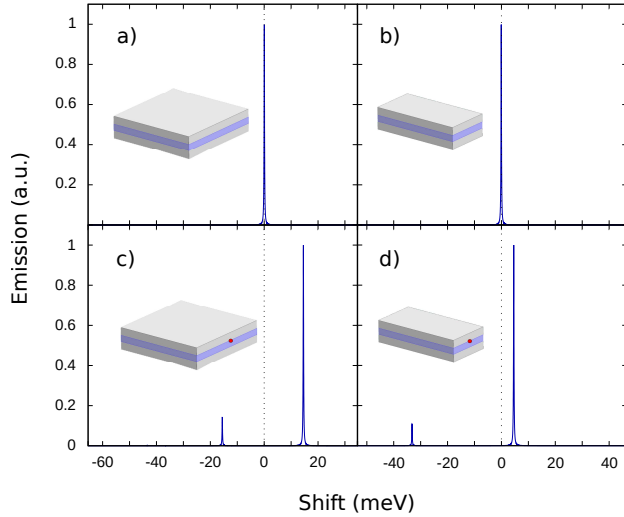


Figure S8: Normalized emission spectrum of  $X^-$  in squared (a,c) and rectangular (b,d) CdSe/CdS NPLs. (a,b) show the spectra for  $Q_{edge} = 0.0$  (no surface charge), (c,d) for  $Q_{edge} = 0.6$ . Squared (rectangular) NPLs have  $20 \times 20 \text{ nm}^2$  ( $20 \times 10 \text{ nm}^2$ ) in-plane dimensions. The energy origin is set at the position of the brightest peak of the uncharged NPL.  $ne = nh = 12$ .

## References

- (1) Jacak, L.; Hawrylak, P.; Wojs, A. Quantum Dots. *Springer* **1998**
- (2) Rontani, M.; Cavazzoni, C.; Bellucci, D.; Goldoni, G. Full configuration interaction approach to the few-electron problem in artificial atoms. *J. Chem. Phys.* **2006**, *124*, 124102.
- (3) Rontani, M.; Eriksson, G.; Åberg, S.; Reimann, S. On the renormalization of contact interactions for the configuration-interaction method in two-dimensions. *J. Phys. B* **2017**, *50*, 065301.
- (4) Shumway, J.; Franceschetti, A.; Zunger, A. Correlation versus mean-field contributions to excitons, multiexcitons, and charging energies in semiconductor quantum dots, *Phys. Rev. B* **2001**, *63*, 155316.
- (5) Rajadell, F.; Climente, J.I.; Planelles, J. Excitons in core-only, core-shell and core-

- crown CdSe nanoplatelets: Interplay between in-plane electron-hole correlation, spatial confinement, and dielectric confinement. *Phys. Rev. B* **2017**, *96*, 035307.
- (6) Leemans, J.; Singh, S.; Li, C.; Ten Brinck, S.; Bals, S.; Infante, I.; Moreels, I.; Hens, Z. Near-Edge Ligand Stripping and Robust Radiative Exciton Recombination in CdSe/CdS Core/Crown Nanoplatelets. *J. Phys. Chem. Lett.* **2020**, *11*, 3339-3344.
  - (7) Drijvers, Emile; De Roo, Jonathan; Martins, Jose C.; Infante, Ivan; Hens, Zeger, Ligand displacement exposes binding site heterogeneity on CdSe nanocrystal surfaces, *Chemistry of Materials* **2018**, *30*, 1178-1186.
  - (8) Wei, S.H.; Zhang S.B.; Zunger, A. First-principles calculation of band offsets, optical bowings, and defects in CdS, CdSe, CdTe, and their alloys. *J. Appl. Phys.* **2000**, *87*, 1304.
  - (9) Steiner, D.; Dorfs, D.; Banin, U.; Della Sala, F.; Manna, L.; Millo, O. Determination of Band Offsets in Heterostructured Colloidal Nanorods Using Scanning Tunneling Spectroscopy *Nano Lett.* **2008**, *8*, 2954-2958.
  - (10) Llusar, J.; Planelles, J.; Climente, J.I. Strain in Lattice-Mismatched CdSe-Based Core/Shell Nanoplatelets. *J. Phys. Chem. C* **2019**, *123*, 21299-21306.
  - (11) Antolinez F.V.; Rabouw F.T.; Rossinelli A.A.; Cui J., Norris D.J. Observation of Electron Shakeup in CdSe/CdS Core/Shell Nanoplatelets. *Nano Lett.* **2019**, *19*, 8495-8502.
  - (12) Li, Q.; Wu, K.; Chen, J.; Chen, Z.; McBride, J.R.; Lian, T. Size-Independent Exciton Localization Efficiency in Colloidal CdSe/CdS Core/Crown Nanosheet Type-I Heterostructures. *ACS Nano* **2016**, *10*, 3843-3851.
  - (13) Steinmetz, V.; Climente, J. I.; Pandya, R.; Planelles, J.; Margaiilan, F.; Puttisong, Y.; Marion, D.; Ithurria, S.; Sharma, A.; Lakhwani, G.; Legrand, L.; Bernardot, F.; Testelin, C.; Chamarro, M.; Chin, A.; Rao, A.; Barisien, T. Emission State

Structure and Linewidth Broadening Mechanisms in Type-II CdSe/CdTe Core-Crown Nanoplatelets: A Combined Theoretical - Single Nanocrystal Optical Study, *The Journal of Physical Chemistry C*, **2020**, *124*, 17352–17363.

## 2.3 Highly Charged Excitons and Biexcitons in Nanoplatelets

### ”Highly Charged Excitons and Biexcitons in Type-II Core/Crown Colloidal Nanoplatelets.”

Jordi Llusar and Juan I. Climente.

*J. Phys. Chem. C* **2022** *126* (16), 7152-7157

DOI: <https://doi.org/10.1021/acs.jpcc.2c00827>

#### **Abstract:**

The optoelectronic properties of type-II CdSe/CdTe colloidal nanoplatelets (NPLs) charged with neutral excitons ( $X^0$ ) have been intensively investigated in the last years. Motivated by the recent experimental progress, here we use effective mass simulations to study the effect of charging core/crown NPLs with a few extra electrons or holes. Emission spectra are calculated for charged excitons ( $X^n$ , with  $n = 2$  to  $n = -3$ ) and biexcitons ( $XX$ ). The strong Coulomb interactions within the platelet lead to a number of remarkable properties. For excitons, varying the number of excess charges gives rise to band gap red- and blue-shifts spanning over 100 meV and widely tunable oscillator strength. For biexcitons, the binding energy can be tuned from nearly nonbonding to strongly antibonding ( $\sim 40$  meV) by modulating the core/crown area ratio. We conclude that the number of excess carriers injected into type-II NPLs is a versatile degree of freedom to modulate the optoelectronic properties.

# **Highly charged excitons and biexcitons in type-II core/crown colloidal nanoplatelets**

Jordi Llusar and Juan I. Climente\*

*Departament de Química Física i Analítica, Universitat Jaume I, E-12080, Castelló de la  
Plana, Spain*

E-mail: [climente@uji.es](mailto:climente@uji.es)



## Abstract

The optoelectronic properties of type-II CdSe/CdTe colloidal nanoplatelets charged with neutral excitons ( $X^0$ ) have been intensively investigated in the last years. Motivated by recent experimental progress, here we use effective mass simulations to study the effect of charging core/crown nanoplatelets with a few extra electrons or holes. Emission spectra are calculated for charged excitons ( $X^n$ , with  $n = 2$  to  $n = -3$ ) and biexcitons ( $XX$ ). The strong Coulomb interactions within the platelet lead to a number of remarkable properties. For excitons, varying the number of excess charges gives rise to band gap red- and blue-shifts spanning over 100 meV, and widely tunable oscillator strength. For biexcitons, the binding energy can be tuned from nearly non-bonding to strongly antibonding ( $\sim 40$  meV) by modulating the core/crown area ratio. We conclude that the number of excess carriers injected in type-II nanoplatelets is a versatile degree of freedom to modulate the optoelectronic properties.

## Introduction

Colloidal nanocrystal heterostructures with type-II (staggered) band alignment, are of interest for the development of optoelectronic applications where controllable spatial separation of electrons and holes is advantageous.<sup>1,2</sup> CdSe/CdTe core-crown nanoplatelets (NPLs) are a prominent example of such structures.<sup>3-5</sup> In these systems, a rectangular CdSe core with a thickness of few atomic monolayers is laterally surrounded by a CdTe crown. Because of the type-II band alignment, photoexcited electron-hole pairs split in such a way that electrons accumulate in the CdSe core while holes do so in the peripheral CdTe crown.<sup>3-6</sup> The strong dielectric confinement of colloidal NPLs, set by the low polarizability of the capping ligands, provides sizable electron-hole attractions across the interface, hence preserving excitonic interactions.<sup>4,7,8</sup> With appropriate engineering, these structures are of interest for light harvesting, sub-band gap emission and infrared detection, fluorescence up-conversion and low-threshold lasing.<sup>1,2,9-12</sup>

To date, the majority of studies about CdSe/CdTe NPLs have focused on spectral and dynamic properties of neutral excitons ( $X^0$ ).<sup>3-6,8,10,11,13,14</sup> However, electron-hole separation in type-II nanocrystals is known to suppress Auger processes,<sup>15-17</sup> which may prompt the formation of long lived trions and biexciton species in photoexcited NPLs.<sup>18</sup> In addition, progress in electrochemical charging of heteronanocrystals has recently reached deterministic and stable control of the number of confined carriers in individual particles.<sup>19</sup> This technique produces multiply charged excitons, where a few excess carriers interact with the photoexcited electron-hole pair, while largely preserving the intrinsic behavior of the semiconductor. Charge control through doping is also advancing in this direction.<sup>20-22</sup> In this context, investigating the effect of discrete charging on the electronic structure and the ensuing optical properties of CdSe/CdTe NPLs is in order.

Early experimental studies in type-II quantum dot core/shell nanocrystals reported significant blue-shifts (20-200 meV) of the photoluminescence peak when switching from single excitons to multiexcitons or charged excitons.<sup>15,23-25</sup> Similar findings have been reported in other type-II and quasi-type-II heterostructures, such as nanorods,<sup>1</sup> tetrapods,<sup>26</sup> dot-in-rods<sup>27</sup> and rod-in-rods.<sup>28</sup> The origin of these shifts is connected with the Coulomb interactions between the recombining exciton and the spectator charges. The latter introduce Coulomb repulsions, which –owing to the spatial separation of electrons and holes– are not compensated by attractions. Because the initial state of the optical transition has more carriers (and hence more repulsions) than the final one, the transition energy increases.<sup>15,29,30</sup>

The question arises of whether type-II core/crown NPLs behave similarly. The answer is not straightforward, because NPLs have characteristic attributes that must be considered. Unlike in quantum dots, the anisotropic shape and large (but finite) in-plane dimensions of NPLs place them in an intermediate confinement regime.<sup>31,32</sup> Carriers of the same sign may then separate over large distances to minimize repulsions. Also, attractive interactions across the CdSe/CdTe interface are stimulated by dielectric confinement.<sup>4,7,8</sup> It is then unclear if Coulomb repulsions will still prevail. In this work, we address these questions by means of

computational simulations.

We use the same effective mass Hamiltonians which successfully described the emission features of neutral excitons in single CdSe/CdTe NPLs,<sup>8</sup> but now extended to the case of charged excitons ( $X^n$ , where  $n$  is the number of excess carriers, with  $n$  ranging from two extra holes,  $n = 2$ , to three extra electrons,  $n = -3$ ) and that of biexcitons ( $XX$ ). A full configuration interaction (CI) method is used to account for few-body interactions including correlation effects. We find that, as a result of the interplay between spatial and dielectric confinements, the emission spectra of typical CdSe/CdTe NPLs display a marked dependence on the number of spectator charges in terms of energy, oscillator strength and bandwidth. Some of the effects we predict are: (i) blue- and red-shifts of the band edge transition in an energy range over 100 meV around that of the neutral excitons, well beyond the typical shifts obtained by varying lateral confinement; (ii) the formation of multiple peaks at low temperature, which define the electronically limited bandwidth of these systems and can be exploited for multicolor emission; and (iii) enhanced leakage of electrons outside the core when repulsions exceed the conduction band offset, which translates into a boost of the interband recombination rate, and may be useful e.g. for the design of optical charge sensors.

## Methods

Calculations are carried within k-p theory framework. Non-interacting (single-particle) electron and hole states are calculated with single-band Hamiltonians including core/crown lattice mismatch strain in a continuum elastic model<sup>8</sup> and self-energy corrections to account for the dielectric mismatch.<sup>33</sup> Low temperature band gaps of CdSe (1.76 eV) and CdTe (1.6 eV) are taken from Ref. 34 and the rest of material parameters from Ref. 35.

Many-body eigenstates and eigenenergies are calculated within a full CI method, using *CItool* codes.<sup>36</sup> Coulomb integrals for the CI matrix elements, including the enhancement

coming from dielectric confinement, are calculated solving the Poisson equation with Comsol 4.2. The CI basis set for CdSe/CdS NPLs is formed by all possible combinations of the first 20 independent-electron and 24 independent-hole spin-orbitals. Charged exciton and biexciton configurations are then defined by all possible Hartree products between the few-electron and few-hole Slater determinants, consistent with spin and symmetry requirements. Optical spectra are calculated within the dipole approximation,<sup>37</sup> assuming Lorentzian bands with linewidth of 1 meV.

## Results

We consider core/crown NPLs with typical dimensions.<sup>3</sup> The thickness is 4.5 atomic monolayers. A crown of fixed lateral dimensions  $20 \times 30 \text{ nm}^2$  is taken, and the core size is  $10 \times 20 \text{ nm}^2$ . Figure 1a shows the calculated emission spectrum at a temperature  $T = 20 \text{ K}$ , for different excitonic complexes.  $X^0$  stands for a neutral exciton (one interacting electron-hole pair). When extra charges are introduced in the system,  $X^{n\pm}$  complexes are formed, where  $n$  is the number of charges (positive or negative) added to the neutral exciton. As can be seen in the figure, varying the number of charges in the NPL has a substantial effect on the optical spectrum. Negatively charged excitons become increasingly blue-shifted, while positively charged excitons are red-shifted instead. In both cases, charging leads to multi-peaked emission.

The energetic shift between  $X^{2+}$  and  $X^{3-}$ , over 100 meV, is of considerable magnitude. It is larger than the spectral shifts one can obtain in colloidal NPLs by modifying the weak lateral confinement (few tens of meV).<sup>38,39</sup> It is also much larger than typical shifts observed upon charging type-I NPLs.<sup>40-42</sup> The origin is connected with the unbalanced repulsive and attractive Coulomb interactions in type-II NPL. To gain semiquantitative understanding, we compare the relative strength of attractions and repulsions for each excitonic complex. We

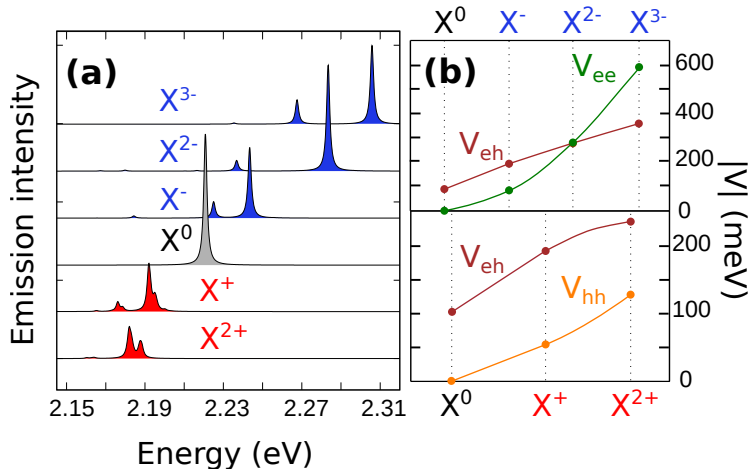


Figure 1: (a) Emission spectrum of neutral and charged excitons in a CdSe/CdTe NPL. (b) Corresponding mean value of Coulomb attractions and repulsions. Coulomb terms are depicted in absolute value. The spectra are simulated at 20 K. The core area is  $10 \times 20 \text{ nm}^2$

calculate the expectation value of the terms contributing to the total energy of  $X^{n\pm}$  :

$$\langle E_{tot} \rangle = \langle E_e \rangle + \langle E_h \rangle + \langle V_{eh} \rangle + \langle V_{ee} \rangle + \langle V_{hh} \rangle. \quad (1)$$

Here  $E_{tot}$  is the total energy of the  $X^{n\pm}$  ground state,  $E_e$  ( $E_h$ ) is the sum of the energies of the non-interacting electrons (holes) forming the complex,  $V_{eh}$  is the sum of the attractions between electron-hole pairs and  $V_{ee}$  ( $V_{hh}$ ) that of the electron-electron (hole-hole) repulsions. Figure 1b compares the absolute value of repulsions and attractions for  $X^{n-}$  (top panel) and  $X^{n+}$  (bottom panel). In both cases, the attractions  $\langle V_{eh} \rangle$  increase (in absolute value) with the number of carriers, because the electron finds more holes to interact with (or vice-versa) across the CdSe/CdTe interface. The repulsions show however contrasting behaviors for electrons and holes.  $\langle V_{ee} \rangle$  shows a rapid –superlinear– increase, reflecting the strong electron-electron interactions within the CdSe core, and leads to repulsions surpassing attractions in  $X^{n-}$ . By contrast, holes are localized in the CdTe crown, with a large core separating the two symmetric sides. This yields relatively weak repulsions,  $\langle V_{hh} \rangle$ , which remain smaller than

attractions. In short, in  $X^{n-}$  repulsions prevail over attractions, while in  $X^{n+}$  the opposite holds. This is directly connected to the blue-shift (red-shift) observed in Fig. 1a. It follows from Fig. 1 that, in spite of the weak lateral confinement, Coulomb interactions permit using the number of extra charges injected in type-II NPLs as a tool for broad and reversible tuning of the emission wave lengths around the value set by the NPL thickness. The same finding holds at room temperature, see Fig. S1. It is worth noting that the blueshift of the excitonic peak in the presence of excess electrons is partly reminiscent of the dynamical screening reported in highly doped semiconductors,<sup>43</sup> albeit in the few-particle limit.

As for the multi-peaked emission of charged species in Fig. 1a, it arises from transitions involving not only the band edge states, but also high-spin states at low energy,<sup>8</sup> with small satellites further arising from shake-up processes.<sup>44,45</sup> These peaks set the electronic limit of the bandwidth (which is greater for charged excitons than for  $X^0$ ) and might be of interest for multi-color emission.<sup>46</sup> A detailed spectral assignment of the trion states ( $X^-$  and  $X^+$ ) is provided in the SI, Figs. S2 and S3.

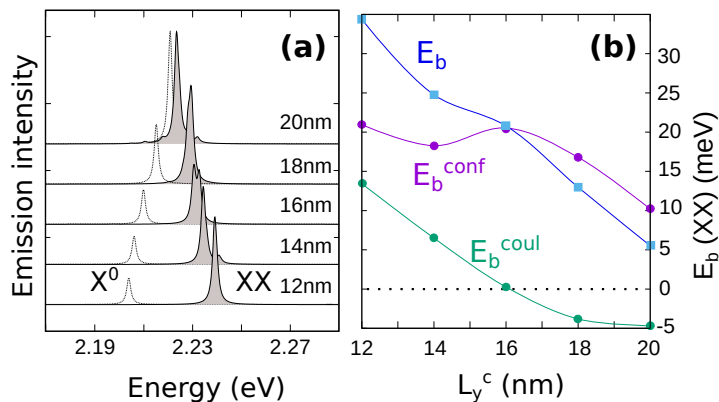


Figure 2: (a) Comparison between the emission spectrum of biexcitons and excitons for different core lengths,  $L_y^c$ . (b) Corresponding biexciton binding energy, along with its kinetic and Coulomb contributions (see text). The spectra are simulated at 20 K. The core width is 10 nm.

We next move to the study of biexcitons. In Fig. 2a we compare  $X^0$  and  $XX$  emission spectra for NPLs with variable core dimensions. The core width is fixed at 10 nm, but

the length ( $L_y^c$ ) is varied. By increasing  $L_y^c$ , the shift between  $X^0$  and  $XX$  peaks evolves from strongly antibonding ( $\sim 40$  meV blue-shift,  $L_y^c = 12$  nm). to nearly non-bonding character ( $\sim 5$  meV,  $L_y^c = 20$  nm). The tunability of the spectral shift holds at room temperature as well, see Fig. S4. This magnitude is similar to that reported for type-II core/shell nanocrystals,<sup>29</sup> but here it is achieved within the weak confinement regime, which permits keeping associated physical phenomena, such as reduced Auger relaxation<sup>47</sup> and giant oscillator strength effect.<sup>7,48</sup>

The physical origin of the shift is different from that of nanocrystals, as we explain next. In both cases the emission peak is mainly related to the band edge transition (see Fig. S5 for a detailed spectral assignment of the  $XX$  emission band). Thus, the spectral shift between  $XX$  and  $X^0$  corresponds to the biexciton binding energy,  $E_b(XX) = E_{tot}(XX) - 2E_{tot}(X)$  (here positive sign means unbound biexciton). Using expectation values, Eq. (1),  $E_b(XX)$  can be decomposed as:

$$\langle E_b(XX) \rangle = \langle E^{coul} \rangle + \langle E^{conf} \rangle. \quad (2)$$

Here,

$$E^{coul} = V_{eh}(XX) + V_{ee}(XX) + V_{hh}(XX) - 2V_{eh}(X^0) \quad (3)$$

is the Coulomb contribution, associated to changes in the relative strength of Coulomb interactions. In turn,

$$E^{conf} = (E_e(XX) - 2E_e(X^0)) + (E_h(XX) - 2E_h(X^0)) \quad (4)$$

is the spatial confinement contribution to the binding energy, associated to changes in the energy of occupied single-particle spin-orbitals. In strongly confined quantum dots and nanocrystals, the energy spacing between consecutive orbitals exceeds Coulomb repulsions. Then, both  $XX$  and  $X^0$  have electrons (holes) in the  $1S_e$  ( $1S_h$ ) orbital, which gives  $E^{conf} \approx 0$ . The biexciton shift is thus well explained from changes in  $E^{coul}$  alone.<sup>29,49</sup> However, NPLs are in a strongly correlated regime. Coulomb repulsions (of the order of  $\sim 100$  meV, see

Fig. 1b) exceed the spacing between consecutive orbitals ( $\sim 10$  meV<sup>8</sup>). This promotes the occupation of excited orbitals to minimize repulsions, making  $E^{conf}$  significant. As a matter of fact, Fig. 2b shows that  $E^{conf}$  is the dominant term in  $E_b(XX)$ . With increasing  $L_y^c$  values, repulsions in the core decrease, and so does  $E^{coul}$ . However, at  $L_y^c = 16$  nm, when  $E^{coul} \approx 0$  (attractions equal repulsions), the biexciton is unbound,  $E_b(XX) \approx 20$  meV, This is because confinement terms,  $E^{conf}$ , are still important.

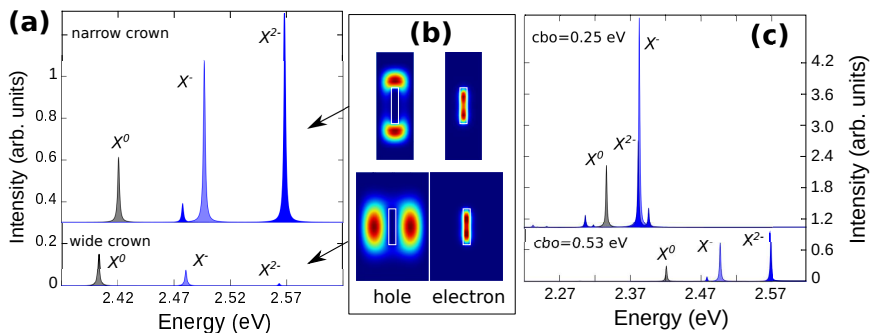


Figure 3: (a) Emission spectrum of  $X^0$ ,  $X^-$  and  $X^{2-}$  for NPLs with wide ( $20 \times 30$  nm<sup>2</sup>) and narrow ( $10 \times 30$  nm<sup>2</sup>) crown. (b) Corresponding hole (left) and two-electron (right) charge densities for  $X^-$ . (c) Emission spectrum of the narrow crown NPL, now comparing conduction band offset 0.53 eV (as in CdSe/CdTe) with 0.25 eV (as in CdSe/CdSe<sub>0.5</sub>Te<sub>0.5</sub>). The spectra are simulated at 4K and are offset vertically for clarity.

We have so far shown the potential of Coulomb repulsions to modulate the emission energy of charged excitons and biexcitons in type-II NPLs. The last question we address is whether a similar modulation can be achieved on the emission rate. In type-I NPLs, trions ( $X^\pm$ ) have smaller oscillator strength than  $X^0$ ,<sup>40</sup> because the giant oscillator strength effect is diluted.<sup>42</sup> In Fig. 1a, however, no major change is observed between  $X^0$  and  $X^{n\pm}$ , which suggests that in type-II NPLs the reduced electron-hole overlap gives rise to a distinct behavior. In what follows, we show that substantial modulation of the oscillator strength can be obtained if one uses a proper structural design, in which Coulomb interactions are exploited to force a transition from type-II to quasi-type-II localization of charged excitons. To illustrate this effect, we consider two NPLs with the same core ( $2 \times 10$  nm<sup>2</sup>) but different



crown dimensions:  $20 \times 30 \text{ nm}^2$  vs  $10 \times 30 \text{ nm}^2$ . Fig. 3a compares the resulting emission spectrum for  $X^0$ ,  $X^-$  and  $X^{2-}$  in both NPLs. Clearly, the narrow-crown NPL shows a gradual enhancement of the intensity as the number of electrons increases, which is not observed in the wide-crown NPL. The different response is related to the localization of holes in each crown. As shown in Fig. 3b, in a wide crown the hole charge density exhibits transversal localization, while in a narrow crown lateral confinement favors longitudinal localization. In turn, the electron charge density is similar in both geometries. When the number of electrons increases, Coulomb repulsions stretch the electron density along the longitudinal axis of the core (see e.g. electron charge density of  $X^-$  in Fig. 3b, which shows the electrons are off-centered). This enhances leakage into the crown, which results in stronger electron-hole overlap –and hence greater emission intensity– in the narrow crown configuration only.

Further enhancement of the intensity can be obtained by reducing the conduction band offset, e.g. by using alloyed (CdSeTe) crowns.<sup>46,50</sup> To estimate the magnitude of this effect, in Fig. 3c we compare the emission of the narrow CdSe/CdTe NPL to that of the same NPL with halved conduction band-offset (close to that of CdSe<sub>0.5</sub>Te<sub>0.5</sub>). One can see that in the latter case, a greater increase of the emission intensity is obtained when the number of electrons increases (cf.  $X^0$  and  $X^-$ ). This is because electron-electron repulsions find it easier to overcome the crown potential barrier, and increase the leakage outside the core.

All in all, Fig. 3 evidences that the emission intensity of CdSe/CdTe NPLs can be modulated through the number of injected electrons in the core. With appropriate structural design, Coulomb interactions make excitonic species gradually reduce their indirect character. Electron-electron repulsions play an important role to this regard by prompting electron delocalization outside the core, but it is worth noting that so do electron-hole attractions (see Fig. S6). This carrier-sensitive optical response could be interesting for ratiometric probing of charges in the NPL.

## Conclusions

In conclusion, we have shown that the number of carriers confined in type-II colloidal NPLs is a versatile tool to control the electronic structure. Coulomb repulsions can prevail over attractions in spite of the weak lateral confinement in these systems. As a result, we predict that the emission spectra of typical CdSe/CdTe NPLs display a marked dependence on the number of spectator charges in terms of energy, oscillator strength and homogeneous bandwidth. The emission peak is red-shifted when charging with extra holes, but blue-shifted instead when charging with electrons or another exciton. The dimensions of the core and the crown can be used to tailor the magnitude of these effects efficiently. This behavior extends the photophysics of type-II quantum dot nanocrystals to NPLs, while preserving the advantages of quasi-2D systems.

### Supporting Information

This material is available free of charge via the internet at <http://pubs.acs.org>.

Additional calculations on emission spectra at high temperature, spectral assignments for trions and biexciton, and effect of electron-hole attraction on the emission of CdSe/CdTe NPLs are given.

## Acknowledgement

The authors acknowledge support from MICINN CTQ2017-83781-P and UJI-B2021-06 projects.

We are grateful to Iwan Moreels, Thierry Barisien and Josep Planelles for discussions.

## References

- (1) Lo, S. S.; Mirkovic, T.; Chuang, C.-H.; Burda, C.; Scholes, G. D. Emergent properties resulting from type-II band alignment in semiconductor nanoheterostructures. *Advanced Materials* **2011**, *23*, 180–197.

- (2) Dorfs, D.; Franzl, T.; Osovsky, R.; Brumer, M.; Lifshitz, E.; Klar, T. A.; Eychmüller, A. Type-I and type-II nanoscale heterostructures based on CdTe nanocrystals: a comparative study. *Small* **2008**, *4*, 1148–1152.
- (3) Pedetti, S.; Ithurria, S.; Heuclin, H.; Patriarche, G.; Dubertret, B. Type-II CdSe/CdTe core/crown semiconductor nanoplatelets. *Journal of the American Chemical Society* **2014**, *136*, 16430–16438.
- (4) Antanovich, A.; Prudnikau, A.; Melnikau, D.; Rakovich, Y. P.; Chuvilin, A.; Woggon, U.; Achtstein, A. W.; Artemyev, M. Colloidal synthesis and optical properties of type-II CdSe–CdTe and inverted CdTe–CdSe core–wing heteronoplatelets. *Nanoscale* **2015**, *7*, 8084–8092.
- (5) Kelestemur, Y.; Olutas, M.; Delikanli, S.; Guzelturk, B.; Akgul, M. Z.; Demir, H. V. Type-II colloidal quantum wells: CdSe/CdTe core/crown heteronoplatelets. *The Journal of Physical Chemistry C* **2015**, *119*, 2177–2185.
- (6) Wu, K.; Li, Q.; Jia, Y.; McBride, J. R.; Xie, Z.-x.; Lian, T. Efficient and ultrafast formation of long-lived charge-transfer exciton state in atomically thin cadmium selenide/cadmium telluride type-II heteronanosheets. *ACS nano* **2015**, *9*, 961–968.
- (7) Scott, R.; Kickhöfel, S.; Schoeps, O.; Antanovich, A.; Prudnikau, A.; Chuvilin, A.; Woggon, U.; Artemyev, M.; Achtstein, A. W. Temperature dependent radiative and non-radiative recombination dynamics in CdSe–CdTe and CdTe–CdSe type II heteronoplatelets. *Physical Chemistry Chemical Physics* **2016**, *18*, 3197–3203.
- (8) Steinmetz, V.; Climente, J. I.; Pandya, R.; Planelles, J.; Margailan, F.; Puttison, Y.; Dufour, M.; Ithurria, S.; Sharma, A.; Lakhwani, G. et al. Emission State Structure and Linewidth Broadening Mechanisms in Type-II CdSe/CdTe Core-Crown Nanoplatelets: A Combined Theoretical - Single Nanocrystal Optical Study. *The Journal of Physical Chemistry C* **2020**, *124*, 17352–17363.

- (9) Min, Y.; Im, E.; Hwang, G.-T.; Kim, J.-W.; Ahn, C.-W.; Choi, J.-J.; Hahn, B.-D.; Choi, J.-H.; Yoon, W.-H.; Park, D.-S. et al. Heterostructures in two-dimensional colloidal metal chalcogenides: Synthetic fundamentals and applications. *Nano Research* **2019**, *12*, 1750–1769.
- (10) Li, Q.; Zhou, B.; McBride, J. R.; Lian, T. Efficient diffusive transport of hot and cold excitons in colloidal type II CdSe/CdTe core/crown nanoplatelet heterostructures. *ACS Energy Letters* **2017**, *2*, 174–181.
- (11) Khan, A. H.; Bertrand, G. H.; Teitelboim, A.; Sekhar M, C.; Polovitsyn, A.; Brescia, R.; Planelles, J.; Climente, J. I.; Oron, D.; Moreels, I. CdSe/CdS/CdTe Core/Barrier/Crown Nanoplatelets: Synthesis, Optoelectronic Properties, and Multiphoton Fluorescence Upconversion. *ACS nano* **2020**, *14*, 4206–4215.
- (12) Li, Q.; Xu, Z.; McBride, J. R.; Lian, T. Low threshold multiexciton optical gain in colloidal CdSe/CdTe Core/Crown type-II nanoplatelet heterostructures. *ACS nano* **2017**, *11*, 2545–2553.
- (13) Pandya, R.; Chen, R. Y.; Cheminal, A.; Dufour, M.; Richter, J. M.; Thomas, T. H.; Ahmed, S.; Sadhanala, A.; Booker, E. P.; Divitini, G. et al. Exciton–Phonon Interactions Govern Charge-Transfer-State Dynamics in CdSe/CdTe Two-Dimensional Colloidal Heterostructures. *Journal of the American Chemical Society* **2018**, *140*, 14097–14111.
- (14) Pandya, R.; Steinmetz, V.; Puttison, Y.; Dufour, M.; Chen, W. M.; Chen, R. Y.; Barisien, T.; Sharma, A.; Lakhwani, G.; Mitioglu, A. et al. Fine Structure and Spin Dynamics of Linearly Polarized Indirect Excitons in Two-Dimensional CdSe/CdTe Colloidal Heterostructures. *ACS nano* **2019**, *13*, 10140–10153.
- (15) Oron, D.; Kazes, M.; Banin, U. Multiexcitons in type-II colloidal semiconductor quantum dots. *Physical Review B* **2007**, *75*, 035330.

- (16) Climente, J. I.; Movilla, J. L.; Planelles, J. Auger recombination suppression in nanocrystals with asymmetric electron–hole confinement. *Small* **2012**, *8*, 754–759.
- (17) Philbin, J. P.; Rabani, E. Auger recombination lifetime scaling for type I and quasi-type II core/shell quantum dots. *The journal of physical chemistry letters* **2020**, *11*, 5132–5138.
- (18) Wang, J.-h.; Liang, G.-j.; Wu, K.-f. Long-lived single Excitons, Trions, and Biexcitons in CdSe/CdTe type-II colloidal quantum Wells. *Chinese Journal of Chemical Physics* **2017**, *30*, 649–656.
- (19) Morozov, S.; Pensa, E. L.; Khan, A. H.; Polovitsyn, A.; Cortés, E.; Maier, S. A.; Vezzoli, S.; Moreels, I.; Sapienza, R. Electrical control of single-photon emission in highly charged individual colloidal quantum dots. *Science advances* **2020**, *6*, eabb1821.
- (20) Capitani, C.; Pinchetti, V.; Gariano, G.; Santiago-González, B.; Santambrogio, C.; Campione, M.; Prato, M.; Brescia, R.; Camellini, A.; Bellato, F. et al. Quantized Electronic Doping towards Atomically Controlled “Charge-Engineered” Semiconductor Nanocrystals. *Nano letters* **2019**, *19*, 1307–1317.
- (21) Dutta, A.; Medda, A.; Patra, A. Recent Advances and Perspectives on Colloidal Semiconductor Nanoplatelets for Optoelectronic Applications. *The Journal of Physical Chemistry C* **2020**, *125*, 20–30.
- (22) Diroll, B. T.; Cho, W.; Coropceanu, I.; Harvey, S. M.; Brumberg, A.; Holtgrewe, N.; Crooker, S. A.; Wasielewski, M. R.; Prakapenka, V. B.; Talapin, D. V. et al. Semiconductor nanoplatelet excimers. *Nano letters* **2018**, *18*, 6948–6953.
- (23) Bang, J.; Chon, B.; Won, N.; Nam, J.; Joo, T.; Kim, S. Spectral switching of type-II quantum dots by charging. *The Journal of Physical Chemistry C* **2009**, *113*, 6320–6323.

- (24) Qin, W.; Guyot-Sionnest, P. Evidence for the role of holes in blinking: Negative and oxidized CdSe/CdS dots. *ACS nano* **2012**, *6*, 9125–9132.
- (25) Ivanov, S.; Achermann, M. Spectral and dynamic properties of excitons and biexcitons in type-II semiconductor nanocrystals. *Acs Nano* **2010**, *4*, 5994–6000.
- (26) Golinskaya, A. D.; Smirnov, A. M.; Kozlova, M. V.; Zharkova, E. V.; Vasiliev, R. B.; Mantsevich, V. N.; Dneprovskii, V. S. Tunable blue-shift of the charge-transfer photoluminescence in tetrapod-shaped CdTe/CdSe nanocrystals. *Results in Physics* **2021**, *27*, 104488.
- (27) Saba, M.; Minniberger, S.; Quochi, F.; Roither, J.; Marceddu, M.; Gocalinska, A.; Kovalenko, M. V.; Talapin, D. V.; Heiss, W.; Mura, A. et al. Exciton–exciton interaction and optical gain in colloidal CdSe/CdS dot/rod nanocrystals. *Advanced Materials* **2009**, *21*, 4942–4946.
- (28) Christodoulou, S.; Rajadell, F.; Casu, A.; Vaccaro, G.; Grim, J. Q.; Genovese, A.; Manna, L.; Climente, J. I.; Meinardi, F.; Raino, G. et al. Band structure engineering via piezoelectric fields in strained anisotropic CdSe/CdS nanocrystals. *Nature communications* **2015**, *6*, 1–8.
- (29) Piryatinski, A.; Ivanov, S. A.; Tretiak, S.; Klimov, V. I. Effect of quantum and dielectric confinement on the exciton–exciton interaction energy in type II core/shell semiconductor nanocrystals. *Nano letters* **2007**, *7*, 108–115.
- (30) Tyrrell, E.; Smith, J. Effective mass modeling of excitons in type-II quantum dot heterostructures. *Physical Review B* **2011**, *84*, 165328.
- (31) Rajadell, F.; Climente, J. I.; Planelles, J. Excitons in core-only, core-shell and core-crown CdSe nanoplatelets: Interplay between in-plane electron-hole correlation, spatial confinement, and dielectric confinement. *Phys. Rev. B* **2017**, *96*, 035307.

- (32) Richter, M. Nanoplatelets as material system between strong confinement and weak confinement. *Phys. Rev. Mater.* **2017**, *1*, 016001.
- (33) Movilla, J. L.; Planelles, J.; Climente, J. I. Dielectric Confinement Enables Molecular Coupling in Stacked Colloidal Nanoplatelets. *J. Phys. Chem. Lett.* **2020**, *11*, 3294–3300.
- (34) Adachi, S. *Handbook on Physical Properties of Semiconductors, vol.3*; Kluwer Academics, 2004.
- (35) Llusar, J.; Planelles, J.; Climente, J. I. Strain in Lattice-Mismatched CdSe-Based Core/Shell Nanoplatelets. *The Journal of Physical Chemistry C* **2019**, *123*, 21299–21306.
- (36) Bertoni, A. CIttool. <https://github.com/andreabertoni/citool>, 2011; [Online; accessed 4-May-2021].
- (37) Jacak, L.; Hawrylak, P.; Wojs, A. *Quantum Dots*; Springer, 1998.
- (38) Bertrand, G. H.; Polovitsyn, A.; Christodoulou, S.; Khan, A. H.; Moreels, I. Shape control of zincblende CdSe nanoplatelets. *Chemical Communications* **2016**, *52*, 11975–11978.
- (39) Di Giacomo, A.; Rodà, C.; Khan, A. H.; Moreels, I. Colloidal Synthesis of Laterally Confined Blue-Emitting 3.5 Monolayer CdSe Nanoplatelets. *Chemistry of Materials* **2020**, *32*, 9260–9267.
- (40) Ayari, S.; Quick, M. T.; Owschimikow, N.; Christodoulou, S.; Bertrand, G. H.; Artemyev, M.; Moreels, I.; Woggon, U.; Jaziri, S.; Achtstein, A. W. Tuning trion binding energy and oscillator strength in a laterally finite 2D system: CdSe nanoplatelets as a model system for trion properties. *Nanoscale* **2020**, *12*, 14448–14458.
- (41) Peng, L.; Otten, M.; Hazarika, A.; Coropceanu, I.; Cygorek, M.; Wiederrecht, G. P.;

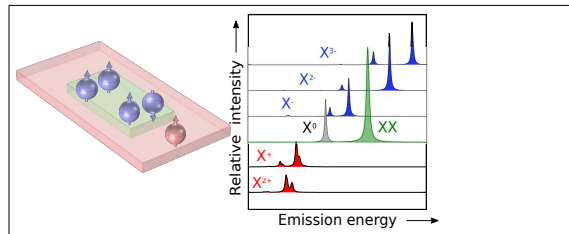
- Hawrylak, P.; Talapin, D. V.; Ma, X. Bright trion emission from semiconductor nanoplatelets. *Physical Review Materials* **2020**, *4*, 056006.
- (42) Macías-Pinilla, D. F.; Planelles, J.; Mora-Seró, I.; Climente, J. I. Comparison between trion and exciton electronic properties in CdSe and PbS nanoplatelets. 2021.
- (43) Gao, S.; Liang, Y.; Spataru, C. D.; Yang, L. Dynamical excitonic effects in doped two-dimensional semiconductors. *Nano letters* **2016**, *16*, 5568–5573.
- (44) Antolinez, F. V.; Rabouw, F. T.; Rossinelli, A. A.; Cui, J.; Norris, D. J. Observation of Electron Shakeup in CdSe/CdS Core/Shell Nanoplatelets. *Nano Lett.* **2019**, *19*, 8495–8502.
- (45) Llusar, J.; Climente, J. I. Nature and Control of Shakeup Processes in Colloidal Nanoplatelets. *ACS Photonics* **2020**, *7*, 3086–3095.
- (46) Dufour, M.; Steinmetz, V.; Izquierdo, E.; Pons, T.; Lequeux, N.; Lhuillier, E.; Legrand, L.; Chamarro, M.; Barisien, T.; Ithurria, S. Engineering bicolor emission in 2d core/crown cdse/cdse1-x te x nanoplatelet heterostructures using band-offset tuning. *The Journal of Physical Chemistry C* **2017**, *121*, 24816–24823.
- (47) Kunneman, L. T.; Tessier, M. D.; Heuclin, H.; Dubertret, B.; Aulin, Y. V.; Grozema, F. C.; Schins, J. M.; Siebbeles, L. D. Bimolecular Auger recombination of electron–hole pairs in two-dimensional CdSe and CdSe/CdZnS core/shell nanoplatelets. *The Journal of Physical Chemistry Letters* **2013**, *4*, 3574–3578.
- (48) Planelles, J.; Achtstein, A. W.; Scott, R.; Owschimikow, N.; Woggon, U.; Climente, J. I. Tuning intraband and interband transition rates via excitonic correlation in low-dimensional semiconductors. *ACS Photonics* **2018**, *5*, 3680–3688.
- (49) Dalgarno, P. A.; Smith, J. M.; McFarlane, J.; Gerardot, B. D.; Karrai, K.; Badolato, A.; Petroff, P. M.; Warburton, R. J. Coulomb interactions in single charged self-assembled



quantum dots: Radiative lifetime and recombination energy. *Physical Review B* **2008**, *77*, 245311.

- (50) Kelestemur, Y.; Guzel Turk, B.; Erdem, O.; Olutas, M.; Erdem, T.; Usanmaz, C. F.; Gungor, K.; Demir, H. V. CdSe/CdSe<sub>1-x</sub>Te<sub>x</sub> Core/Crown Heteronanostructures: Tuning the Excitonic Properties without Changing the Thickness. *The Journal of Physical Chemistry C* **2017**, *121*, 4650–4658.

# Graphical TOC Entry



# **Supporting Information for “Highly Charged Excitons and Biexcitons in Type-II Core/Crown Colloidal Nanoplatelets”**

Jordi Llusar and Juan I. Climente\*

*Departament de Química Física i Analítica, Universitat Jaume I, E-12080, Castelló de la  
Plana, Spain*

E-mail: [climente@uji.es](mailto:climente@uji.es)

## Additional calculations

### Charged excitons

As we have already seen in Fig. 1 of the main text, at low temperature ( $T = 20$  K) Coulomb interactions make  $X^{n-}$  systems blueshift ( $n = 1 - 3$ ) and  $X^{n+}$  systems redshift ( $n = 1 - 2$ ). As shown in Fig. S1, at room temperature the same trend holds, but because there are more populated states, a richer multi-peaked emission spectrum is obtained.

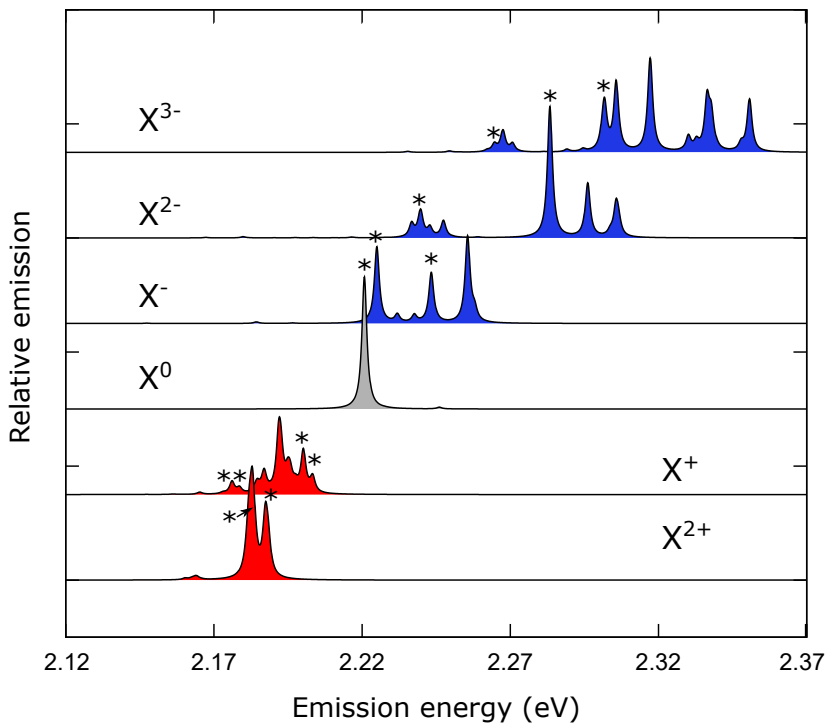


Figure S1: Emission spectrum of neutral and charged excitons in a CdSe/CdTe NPL. We set  $L_y^c = 20$  nm. The spectra are simulated at room temperature, 300K. Stars stand for peaks visible at 20K.

For  $X^{n+}$  systems at 300K, the range of emitting energies one can achieve does not vary much with relation to that at 20K. However, for  $X^{n-}$  the emission energies can become significantly higher (cf.  $X^{3-}$  in Fig. S1 and in Fig.4). This is a result of the thermal occupation of excited states.

To gain insight into the optical spectra of charged excitons, we study in detail the spectral assignment in the case of trions,  $X^-$  and  $X^+$ . These species are frequently observed in type-I NPLs<sup>1-3</sup> and have been reported in CdSe/CdTe core/crown NPLs as well.<sup>4</sup> We have analyzed which transitions are more relevant and characterized the main electronic configurations –or combination of configurations– involved in each case. Fig. S2 corresponds to a negative trion,  $X^-$ . Fig. S2a shows the energy of the initial ( $X^-$ , top of the figure) and final (single electron, bottom of the figure) states involved in the recombination of the trion. From the negative trion dispersion energy  $E_{X^-}$ , it is easy to see that high-spin states get closer to the low-spin ones as  $L_y^c$  increases. This trend leads to a higher number of thermally occupied states with increasing  $L_y^c$ , which translate into a higher number of allowed transitions, see Fig. S2c and the associated peaks in the emission spectrum, Fig. S2b. Notice that the band edge transition (labeled as ① in Fig. S2c) is still the most intense peak in the spectrum at 50K. Additional transitions arise from shake-up processes<sup>5-7</sup> of the ground state (transition ②), and transitions arising from the first electron spin triplet state, which can reach two different final states (transitions ③ and ④). Fig. S2d shows the main electronic configurations involved in the transitions ① to ④, with ellipsoids highlighting the recombining electron-hole pair. The configurations rely on the non-interacting electron and hole states, which we label with the corresponding irreducible representation in the  $D_{2h}$  point group (see e.g. Fig. 4 of Ref. 8 for details).

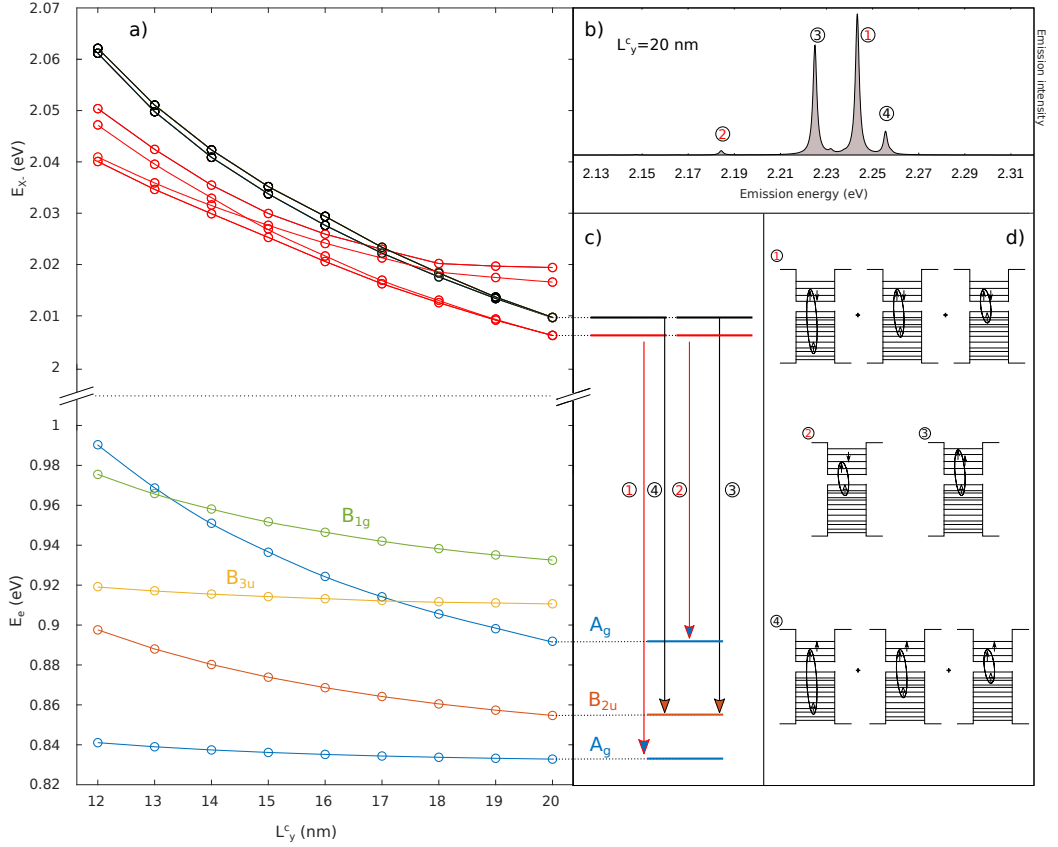


Figure S2: (a) Dispersion energy for  $X^-$  (above dotted line) and for single-particle electron (below dotted line). (b) Negative trion emission spectrum for  $L_y^c = 20$  nm. (c) Transitions involved in (b). (d) Main configurations referred to in (c) and (b). Red and black lines stand for singlet and triplet electron spin states. Single-particle state colors denote different irreducible representations. The spectrum is simulated at 50 K.

A detailed assignment for  $X^+$  is given in Fig. S3. In this case, the assignment is more involved because the density of states is higher, since holes are heavier than electrons. Also, the initial state has nearly degenerate singlet and triplet hole spin states, described with black and red lines in Fig. S3a (top), and the final hole states have two-fold degeneracy (e.g.  $A_g$  and  $B_{2u}$  levels in Fig. S3d). Both the degeneracy of  $X^+$  and single hole states arise from the double-box formed by the crown in the presence of a core, which acts as a barrier for holes. The higher density of states when  $L_y^c$  increases has an important influence of the

number of thermally occupied states participating in the emission spectrum. For this reason, the emission spectrum of  $L_y^c = 12$  nm and  $L_y^c = 20$  nm is visibly different.

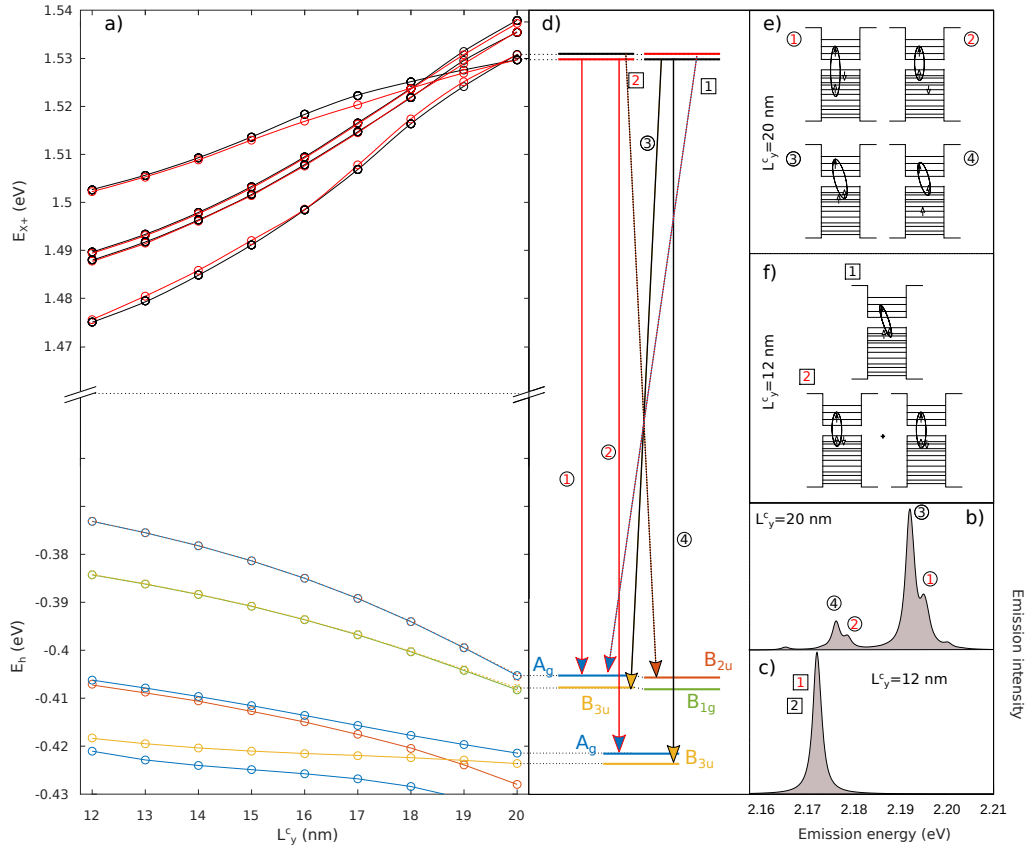


Figure S3: (a) Dispersion energy for  $X^+$  (above dotted line) and for single-particle hole (below dotted line). Positive trion emission spectrum for (b)  $L_y^c = 20$  nm and (c)  $L_y^c = 12$  nm. (d) Transitions involved in (b) –solid lines– and (c) –dotted lines–. (e) Main configurations for  $L_y^c = 20$  nm and (f) same for  $L_y^c = 12$  nm. Red and black lines stand for singlet and triplet hole spin, respectively. Single-particle states colors denote different irreducible representations. The spectrum is simulated at 20 K.

## Biexcitons

Figure 2a in the main text compares the emission spectra of excitons and biexcitons as a function of the core size at 20K. Fig. S4 shows that the main conclusions hold at room temperature: the biexciton remains blueshifted by tens of meV for small and mid-sized cores, but emits close to the neutral exciton for large cores ( $L_y^c = 20$  nm). The higher temperature enables emission from excited states of the biexciton, which explains the larger number of peaks in Fig. S4.

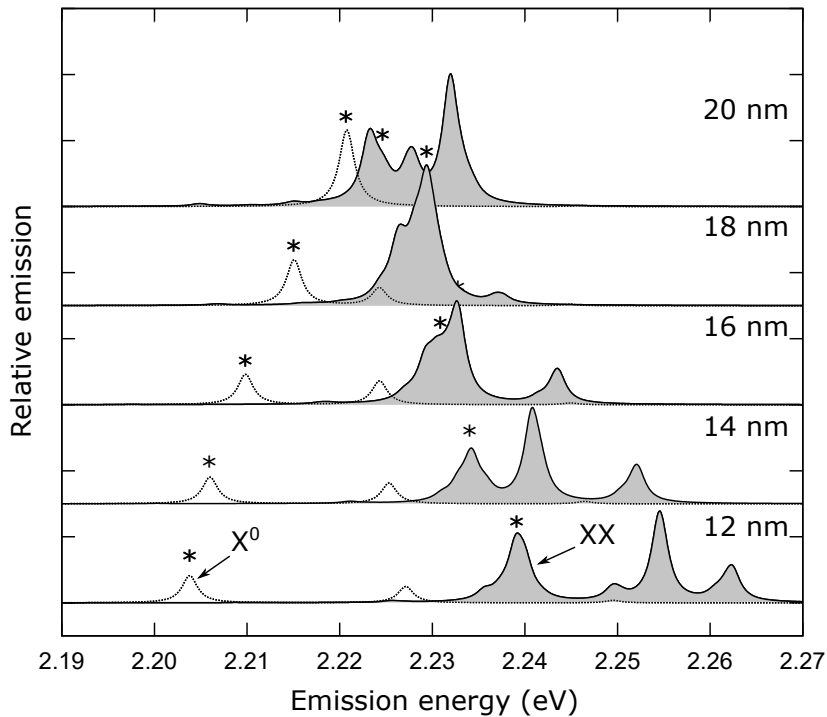


Figure S4: Comparison between the emission spectrum of biexcitons and excitons as a function of the core length. The spectra are simulated at room temperature, 300K. Stars stand for peaks visible at 20K.



Transition assignments for the biexciton emission at  $T = 20\text{K}$  can be found in Fig. S5. Unlike in the case of charged excitons, here most of the emission intensity comes from the band edge transition.

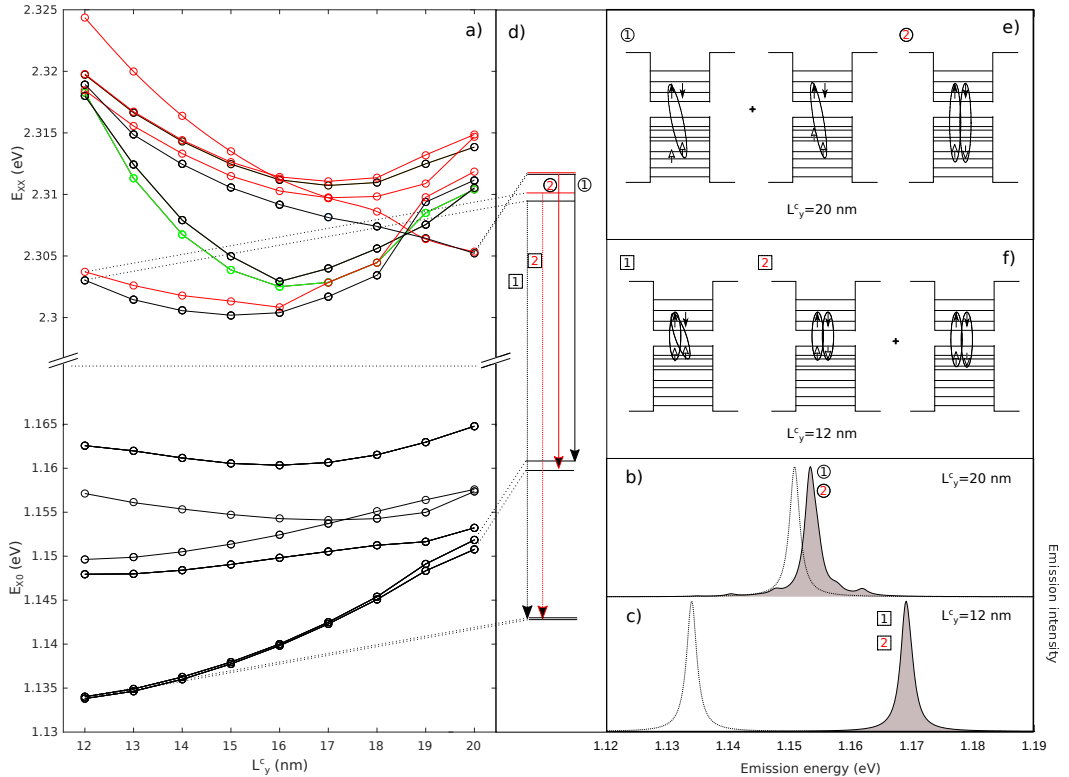


Figure S5: (a) Dispersion energies for biexcitons (top) and excitons (bottom). Emission spectra simulated at 20K for (b)  $L_y^c = 20$  nm and (c)  $L_y^c = 12$  nm. (d) Transitions involved in (b) –solid lines– and (c) –dotted lines–. (e) Main configurations for  $L_y^c = 20$  nm and (f) same for  $L_y^c = 12$  nm. Red, black and green lines stand for different total spin of the biexciton,  $S_{XX} = 0, 1$  and  $2$ , respectively.

## Role of Coulomb attraction on the transition towards quasi-type-II NPL

In addition to electron-electron repulsions, electron-hole attractions play an important role in the transition towards quasi-type-II system. In Fig. S6a and b we show the  $X^0$  and  $X^-$

charge densities along the  $y$  (long) axis for a narrow crown CdSe/CdTe NPL like that of Fig. 3 in the main text. Red lines correspond to a standard calculation, while blue lines represent a situation in which we deliberately quench electron-hole multiplying such Coulomb integrals by a factor of 0.1. Clearly, the electron (solid line) and hole (dashed line) reduce the overlap substantially. In the emission spectrum, Fig. S6c, this translates into weaker intensity.

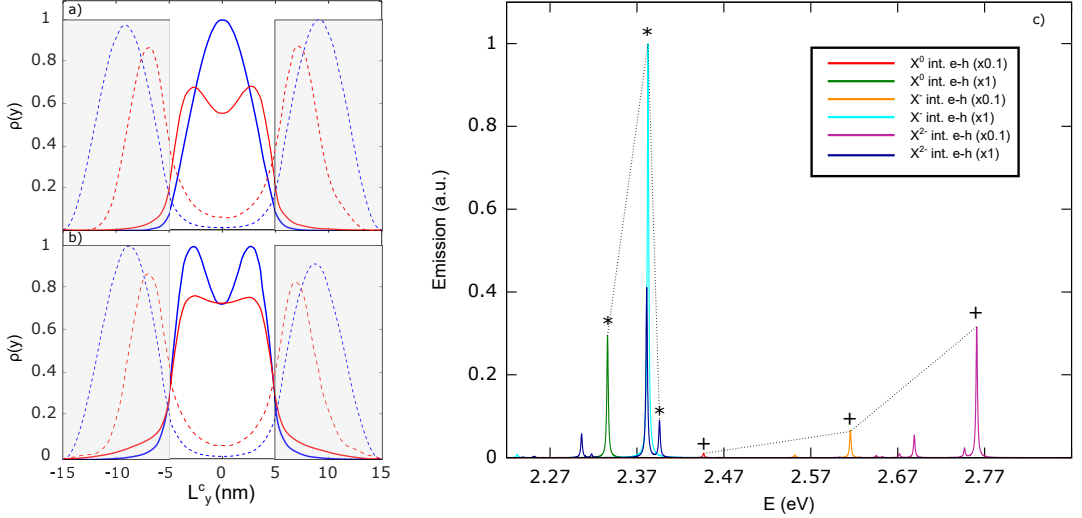


Figure S6: Charge density of (a)  $X^0$  and (b)  $X^-$  along the  $y$  axis of the NPL. Red and blue lines stand for normal and quenched electron-hole interactions, respectively. Solid and dashed lines represent electron and hole charge density, respectively. (c) Emission spectrum of  $X^0$ ,  $X^-$  and  $X^{2-}$  with standard ((x1) e-h interaction) and quenched ((x0.1) e-h interaction) Coulomb attractions. The conduction band offset is set at 0.25eV and  $T = 4$  K.

## References

- (1) Shornikova, E. V.; Yakovlev, D. R.; Biadala, L.; Crooker, S. A.; Belykh, V. V.; Kochiev, M. V.; Kuntzmann, A.; Nasilowski, M.; Dubertret, B.; Bayer, M. Negatively Charged Excitons in CdSe Nanoplatelets. *Nano Lett.* **2020**, *20*, 1370–1377.
- (2) Ayari, S.; Quick, M. T.; Owschimikow, N.; Christodoulou, S.; Bertrand, G. H.; Artemyev, M.; Moreels, I.; Woggon, U.; Jaziri, S.; Achtstein, A. W. Tuning Trion Binding

Energy and Oscillator Strength in a Laterally Finite 2D System: CdSe Nanoplatelets as a Model System for Trion Properties. *Nanoscale* **2020**, *12*, 14448–14458.

- (3) Peng, L.; Otten, M.; Hazarika, A.; Coropceanu, I.; Cygorek, M.; Wiederrecht, G. P.; Hawrylak, P.; Talapin, D. V.; Ma, X. Bright Trion Emission From Semiconductor Nanoplatelets. *Phys. Rev. Mater.* **2020**, *4*, 056006.
- (4) Wang, J.-H.; Liang, G.-J.; Wu, K.-F. Long-Lived Single Excitons, Trions, and Biexcitons in CdSe/CdTe Type-II Colloidal Quantum Wells. *Chin. J. Chem. Phys.* **2017**, *30*, 649–656.
- (5) Löbl, M. C.; Spinnler, C.; Javadi, A.; Zhai, L.; Nguyen, G. N.; Ritzmann, J.; Midolo, L.; Lodahl, P.; Wieck, A. D.; Ludwig, A. et al. Radiative Auger Process in the Single-Photon Limit. *Nat. Nanotechnol.* **2020**, *15*, 558–562.
- (6) Antolinez, F. V.; Rabouw, F. T.; Rossinelli, A. A.; Cui, J.; Norris, D. J. Observation of Electron Shakeup in CdSe/CdS Core/Shell Nanoplatelets. *Nano Lett.* **2019**, *19*, 8495–8502.
- (7) Llusar, J.; Climente, J. I. Nature and Control of Shakeup Processes in Colloidal Nanoplatelets. *ACS Photonics* **2020**, *7*, 3086–3095.
- (8) Steinmetz, V.; Climente, J. I.; Pandya, R.; Planelles, J.; Margailan, F.; Puttisong, Y.; Dufour, M.; Ithurria, S.; Sharma, A.; Lakhwani, G. et al. Emission State Structure and Linewidth Broadening Mechanisms in Type-II CdSe/CdTe Core-Crown Nanoplatelets: A Combined Theoretical - Single Nanocrystal Optical Study. *J. Phys. Chem. C* **2020**, *124*, 17352–17363.

## 2.4 Shell Filling and Spontaneous Magnetism in Nanoplatelets

”Shell Filling and Paramagnetism in Few Electron Colloidal Nanoplatelets.”

Jordi Llusar and Juan I. Climente.

*Phys. Rev. Lett.* **2022** XX (XX), XXXX-XXXX

DOI: <https://doi.org/10.1021/acs.jpcc.2c00827>

### Abstract:

Colloidal semiconductor nanoplatelets are excellent optical emitters, which combine a quasi-2D structure with strong in-plane Coulomb interactions. Here we go beyond the photoexcitation regime and investigate theoretically the effect of charging nanoplatelets with a few interacting fermions (electrons or holes). This introduces severe Coulomb repulsions in the system, enhanced by the inherent dielectric confinement. We predict strong electronic correlations and electron-electron exchange energies (over 20 meV) in type-I (CdSe/CdS) and type-II (CdSe/CdTe) nanoplatelets, which give rise to characteristic physical phenomena. These include shell filling spectra deviating from the Aufbau principle, large addition energies which permit deterministic control of the number of charges at room temperature and paramagnetic electron spin configuration activated at cryogenic temperatures.

# Shell Filling and Paramagnetism in Few Electron Colloidal Nanoplatelets

Jordi Llusar<sup>1</sup> and Juan I. Climente<sup>1</sup>

<sup>1</sup>*Departament de Química Física i Analítica, Universitat Jaume I, E-12080, Castelló de la Plana, Spain*

(Dated: March 18, 2022)

Colloidal semiconductor nanoplatelets are excellent optical emitters, which combine a quasi-2D structure with strong in-plane Coulomb interactions. Here we go beyond the photoexcitation regime and investigate theoretically the effect of charging nanoplatelets with a few interacting fermions (electrons or holes). This introduces severe Coulomb repulsions in the system, enhanced by the inherent dielectric confinement. We predict strong electronic correlations and electron-electron exchange energies (over 20 meV) in type-I (CdSe/CdS) and type-II (CdSe/CdTe) nanoplatelets, which give rise to characteristic physical phenomena. These include shell filling spectra deviating from the Aufbau principle, large addition energies which permit deterministic control of the number of charges at room temperature and paramagnetic electron spin configuration activated at cryogenic temperatures.

The number of excess carriers (electrons or holes) confined in semiconductor quantum dots is analogous to the charge number of ions in chemistry. Because changes in this number are expected to modify the electronic properties, experiments in the early years of quantum dots struggled to control it. Orbital shell filling was subsequently demonstrated in gated[1], self-assembled[2–4], carbon nanotube[5] and graphene[6] quantum dots. In colloidal nanocrystal quantum dots, orbital shell filling of conduction and valence bands was pursued using different approaches such as scanning tunneling spectroscopy[7], direct or remote doping[8] and electrochemical injection.[9] The placement of resident charges in the nanocrystals translated into substantial changes of the transport and optical properties, including lower threshold optical gain[10] and large electrochromic shifts,[11, 12] which are of interest for lasing and sensing applications, respectively.

Recently, progress in electrochemical charge injection has reached deterministic and stable control of the number of confined carriers in individual nanocrystals.[13] Charge control through doping (with impurities or surrounding molecules) is advancing in this direction,[14–16] and scanning tunneling spectroscopy[7, 17, 18] in the shell-filling regime can be expected to do so as well. These achievements open path for a precise analysis of the shell structure, potentially unveiling few-body charge and spin interaction effects at a level so far restricted to fully solid state systems. In nanocrystal quantum dots, quantum confinement energies usually prevail over Coulomb interaction energies.[19] This is a similar situation to that of epitaxial quantum dots. One can then expect orbital shell filling to be simply understood from the dot geometry, following Hund and Aufbau rules, with many-body interactions acting as a perturbation.[1, 2, 20, 21] A different scenario can however be foreseen for nanoplatelets (NPLs). These are often considered the colloidal analogous of epitaxial quantum wells, albeit with finite and controllable lateral confinement, the possibility to develop in-plane

(core/crown) heterostructures and a strong dielectric confinement imposed by the organic ligands.[22]

The flexible design and outstanding optical properties of colloidal NPLs have triggered intensive research over the last years aiming at applications in optoelectronic devices.[15, 23–26] Much of the interest follows from the strong attraction between photogenerated electron-hole pairs, enhanced by the quasi-2D geometry and the dielectric confinement, which prompt large binding energies (150-250 meV) and fast radiative recombination rates through the so-called giant oscillator strength effect.[22, 27–30] One should however note that the same factors that favor strong electron-hole attraction, favor strong electron-electron or hole-hole repulsion too. In NPLs with injected carriers, these interactions ( $\sim 100$  meV) largely exceed the small energy spacings between states of non-interacting particles, which are set by the weak lateral confinement ( $\sim 10$  meV). The resulting shell structure can then be expected to display non-trivial many-body phenomena.[3, 4, 31] Possible implications of an electronic structure shaped by strong repulsive correlations include the buildup of intrinsic ferromagnetism and exotic spin states.[31–33]

In order to investigate these effects, we study CdSe-based NPLs of current interest. Specifically, we model CdSe/CdS and CdSe/CdTe core/crown heterostructures,[22] see schematics in Figures 1a and 1d, respectively. Similar behavior can be expected for core-only and core/shell NPLs, but the crown passivates lateral facets, which are prone to formation of traps,[34] and the use of shells gradually quenches dielectric confinement, which is needed to reach the strong correlation regime we report.

To visualize the role of Coulomb repulsions we will conjugate two competing degrees of freedom: the number of confined carriers and the quantum confinement strength. Thus, we take a fixed crown (lateral dimensions  $20 \times 30$  nm<sup>2</sup>), and change the core size (lateral dimensions  $10 \times L_y^c$  nm<sup>2</sup>, where  $L_y^c = 12 - 20$  nm is the length of the core). The NPL thickness is 4.5 monolayers. These are typical

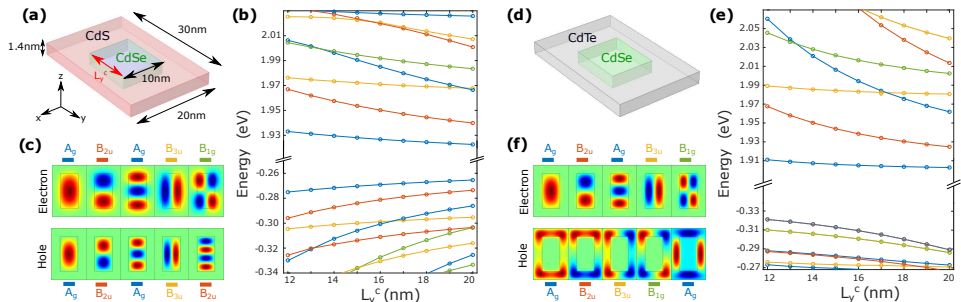


FIG. 1: (a) Schematic of the CdSe/CdS NPLs under study. (b) Non-interacting electron (top) and hole (bottom) energy levels as a function of the core length. (c) Wave functions of the lowest electron (highest hole) energy levels for  $L_y^c = 20$  nm. (d-f): same but for CdSe/CdTe NPLs. The NPLs have the same dimensions as for CdSe/CdS. All energies are referred to the top of the CdSe valence band. The colors of the lines in (b), (c), (e) and (f) denote the irreducible representation of the level (within the  $D_{2h}$  point group).

values for this kind of structure.[35]

It is convenient to start by analyzing the energy structure of non-interacting electrons and holes, which we calculate using effective mass Hamiltonians, including strain and dielectric mismatch terms (see Supporting Information, SI). In CdSe/CdS NPLs, the first electron and hole states localize in the core (Fig. 1c), but in CdSe/CdTe NPLs the hole moves towards the crown (Fig. 1f), as expected from the type-I vs type-II band alignment. The energy dependence on the core length is similar for all particles localized within it. For instance, Fig. 1b shows that increasing  $L_y^c$  in CdSe/CdS NPLs has little influence on the electron or hole ground state energy ( $A_g$  symmetry) because the lateral confinement is already weak. However, some of the excited states (those with nodes along the  $y$  axis) are more sensitive to the confinement relaxation and lower their energy more, see e.g. the first excited state ( $B_{2u}$  symmetry). The same happens for electrons in CdSe/CdTe NPLs, as can be seen in Fig. 1e (top part). This is an indication that the NPL core is not yet in the quantum well limit,[18] and hence the density of states can be increased by making it larger. The smaller interlevel energy spacings will translate into stronger electronic correlation effects, as we shall show below.

For holes in CdSe/CdTe, the behavior is different because increasing the core size reduces the space left in the crown. This unstabilizes the energy levels for large  $L_y^c$  values. It is also worth noting that the top-most levels of the valence band are formed by nearly degenerate pairs of states ( $A_g$  and  $B_{2u}$ ,  $B_{3u}$  and  $B_{1g}$ ). This is because the core constitutes a potential barrier which separates the crown into two symmetric sides. The pairs of levels are the symmetric and antisymmetric solutions of the double box system. The top-most hole states have little kinetic energy, so that tunneling is weak and the two solutions are quasi degenerate.[36] This is a diatomic-like system,

where characteristic interactions –different from those of quantum dots– can be expected.

We are now in a position to study the orbital shell filling of the NPLs. To this end, we calculate the addition energy (the analogous of electron affinity in real atoms) spectrum for the two first conduction and valence band shells (i.e. up to 4 electrons or 4 holes). The addition energy is the energy required to insert one additional charge into the nanostructure:[1]

$$\Delta = \mu(N+1) - \mu(N) = E(N+1) - 2E(N) + E(N-1). \quad (1)$$

where  $\mu(N)$  and  $E(N)$  are the chemical potential and ground state energy for  $N$  carriers (electrons or holes).  $E(N)$  values are extracted from full configuration interaction (CI) calculations on the basis of the single-particle spin-orbitals (see SI).

Fig. 2a shows the addition energies one would expect for non-interacting electrons in a core with  $L_y^c = 20$  nm. In this case, a simple orbital shell filling sequence is observed. Odd numbers of electrons ( $N_e$ ) involve half-filled (open) shell. Because we are neglecting Coulomb interactions so far, introducing an extra electron in these cases requires no additional energy,  $\Delta = 0$  meV. By contrast, even numbers of electrons involve closed shells. Introducing an extra electron requires providing the energy to access the next excited orbital, which is set by the lateral quantum confinement or in other words, it is due to the inter-level spacing separation observed in Fig. 1b,e. This results in  $\Delta \approx 20$  meV.

Upon inclusion of Coulomb interactions, major changes take place in the electron addition spectrum. Fig. 2b show the spectrum in the absence of dielectric confinement (assuming the outer medium has the same dielectric constant as the NPL,  $\epsilon_{out} = \epsilon_{in}$ ). This situation can be expected in NPLs with thick shells and is reminiscent of epitaxial quantum dots. Open shells have now addition energies  $\Delta = 25 - 30$  meV, which give

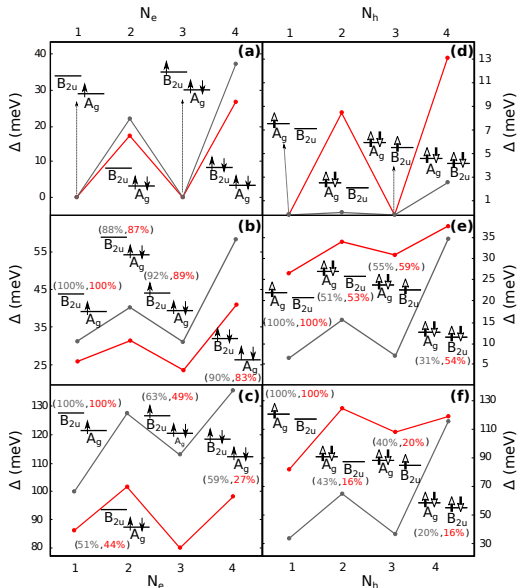


FIG. 2: Addition energy spectra as a function of the number of carriers for CdSe/CdS (red line) and CdSe/CdTe (gray line) in a NPL with  $L_y^c = 20$  nm. (a) Non-interacting electrons. (b) Interacting electrons neglecting dielectric confinement ( $\epsilon_{out} = \epsilon_{in}$ ). (c) Interacting electrons including dielectric confinement ( $\epsilon_{out} = 2$ ). (d-f) Same for holes. The insets show the dominant electronic configuration along with its weight in the CI expansion (red value for CdSe/CdS, gray one for CdSe/CdTe).

a direct measure of the electron-electron repulsions one needs to overcome in order to place an extra electron in the same orbital. Closed shells are still more stable than open ones, but Coulomb repulsions are less severe when the extra electron is placed in a different (orthogonal) orbital. Consequently, the sawtooth structure in Fig. 2b is less pronounced than one would expect from quantum confinement alone (Fig. 2a). When dielectric confinement is added ( $\epsilon_{out} < \epsilon_{in}$ ), which provides a realistic description of NPLs with no shell, Coulomb repulsions are greatly enhanced (roughly tripled), yielding  $\Delta$  values over 80 meV, see Fig. 2c. It is worth noting that the  $\Delta$  shift between non-interacting and interacting cases is not constant against the number of carriers (see Fig. S1 in the SI). This is a first indication that we are beyond the perturbative Coulomb regime, and electronic correlations play a significant role. The latter effect is particularly remarkable in CdSe/CdS NPLs with cores under  $L_y^c = 15$  nm, where anomalous shell filling spectra can be observed, with closed shell configurations being less stable than open ones, see Fig. S2.

For holes, the impact of Coulomb interactions is also drastic. Holes in CdSe/CdS NPLs behave much like elec-

trons in spite of the heavier masses, see red line in Fig. 2d-f. Holes in CdSe/CdTe behave differently instead because they are localized in the crown, see gray lines in the figure. In a non-interacting picture, Fig. 2d,  $\Delta \approx 0$  meV for a number of holes  $N_h = 1 - 3$ , but  $\Delta = 2.8$  meV for  $N_h = 4$ . This reflects the valence band electronic structure analyzed in Fig. 1f. The top-most hole orbitals ( $A_g$  and  $B_{2u}$ ) are quasi degenerate. Together with the spin degree of freedom, this gives a four-fold quasi-degenerate ground state. Then, adding extra holes requires very little energy except for the closed shell,  $N_h = 4$ . However, when repulsions are taken into account (Figs. 2e,f), all addition energies shift up and a peak emerges for  $N_h = 2$ . The latter is because two holes feel comfortable sitting on opposite sides of the crown, but adding a third hole necessarily implies stronger repulsions.

The insets in Fig. 2 show, for each  $N_e$  or  $N_h$  value, the electronic configuration which is expected to dominate from the Aufbau principle of atoms, i.e. assuming that independent-particle spin-orbitals are filled sequentially. For interacting particles, the percentage gives the weight of such a configuration within the CI expansion. In the absence of dielectric mismatch, Figs. 2b,e, this is indeed the dominant configuration (weights over 50%). This is especially true for electrons, while holes are in a regime of stronger correlations, consistent with earlier studies on epitaxial quantum dots.[3, 4, 31] Upon inclusion of dielectric mismatch, however, correlations become even stronger, which is manifested as weights below 50% in Figs. 2c,f. That is, the configuration expected from the Aufbau principle is no longer the dominant one, and it misses most of the electronic structure details.

It is concluded from Fig. 2 that Coulomb repulsions play a dominant role in shaping the electronic structure and addition energy spectrum of electrons and holes in NPLs. This is so in spite of the large in-plane dimensions, which in principle allow fermions to localize far from each other to minimize interactions (as in incipient Wigner crystals[37]). An important practical consequence is that, owing to dielectric confinement, all  $\Delta$  values exceed thermal energy at room temperature. This implies that electrochemical charging of NPLs[38] is susceptible of being conducted electron-by-electron (or hole-by-hole), thus enabling deterministic control of the number of charges in spite of the weak lateral confinement. The same conclusion holds for different core dimensions (Fig.S2).

The results so far also reveal that electrons in CdSe cores can experience severe correlations, because Coulomb repulsions are up to one order of magnitude larger than the interlevel energy spacing set by lateral confinement ( $\sim 100$  meV against  $\sim 10$  meV for  $L_y^c = 20$  nm). These are potentially suitable conditions for the formation of magnetic phases.[39, 40] Confirming such a point is of significant interest, since ear-

lier manifestations of magnetic phases in colloidal NPLs were restricted to doping[24, 41–44] and surface-induced paramagnetism.[45] The development of intrinsic magnetism would open up new scenarios for spintronic and magnetic devices.

To explore this possibility, in Fig. 3 we plot the energy difference between low and high spin states of few-electron ( $N_e = 2 - 4$ ) CdSe/CdS NPLs and the associated expectation values of the total spin quantum number (similar results hold for CdSe/CdTe, Fig. S3). Fig. 3a shows the energy splitting between the  $N_e = 2$  ground state (singlet,  $S_e = 0$ ) and the first excited state (triplet,  $S_e = 1$ ). Clearly, as the core size increases, the triplet approaches the singlet ground state. There are two reasons for this. One is the weakening of lateral confinement, which selectively relaxes the first excited orbital ( $B_{2u}$ ,  $p_y$ -like) but not the lowest one ( $A_g$ ,  $s$ -like), as discussed before in Fig. 1. The other reason is that strong Coulomb repulsions imply large Coulomb exchange energies as well, which stabilize triplets as compared to singlets. Fig. 3a compares the triplet energy for two non-interacting (dotted line) and two interacting (solid line with black circles) electrons. The energy decrease for non-interacting electrons is merely due to the weakened confinement, while that of the interacting case further benefits from exchange energies as large as 20–30 meV. Consequently, for two interacting electrons, the  $S_e = 1$  state is only 8 meV away from the  $S_e = 0$  ground state when  $L_y^c = 12$  nm, and is nearly degenerate when  $L_y^c = 20$  nm. It follows that thermal occupation of high spin states is feasible at room temperature or even earlier. This is evidenced by Fig. 3b. With increasing temperature, the total spin  $\langle S_e \rangle$  rapidly departs from  $\langle S_e \rangle = 0$  (pure singlet), which is the value one would obtain in strongly confined nanocrystals, and reaches  $\langle S_e \rangle \approx 3/4$ , which implies equal population of singlet and triplet states. For large cores ( $L_y^c = 20$  nm), this is achieved at temperatures under 50 K. The practical implication is that paramagnetic response must be expected except at temperatures  $T \rightarrow 0$  K.

The ground state of a  $N_e = 2$  system in the absence of external magnetic fields or spin-orbit interaction is always spin-singlet.[40] In Fig. 3c,d we explore whether this situation can be reversed for  $N_e = 3 - 4$  NPLs, and high-spin ground states show up. For the geometries we address the answer is negative (at  $T = 0$  K the spin is low). but again high-spin states are occupied at room temperature. In fact, for  $N_e = 4$  and 300K we obtain  $\langle S_e \rangle > 3/4$ , see Fig. 3d. That is, thermal population of triplet states exceeds that of singlet ones. The reason is that more than one triplet state becomes reachable at room temperature, see Fig. S3.

Solid and dashed lines in Fig. 3 refer to estimates including and excluding dielectric confinement. It is clear from the comparison that the spin momenta are higher when the inhomogeneous dielectric screening is taken into

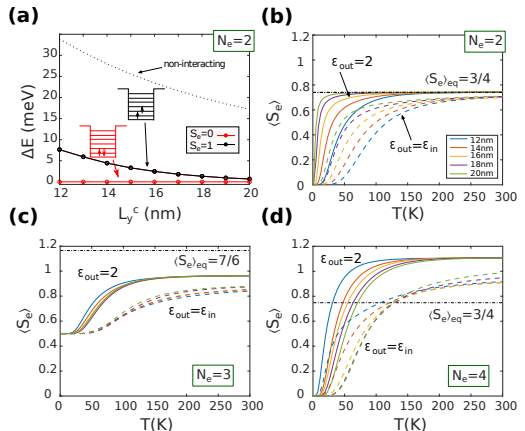


FIG. 3: (a) Energy splitting between ground state (singlet) and the first excited state (triplet) for two electrons in CdSe/CdS NPL with varying core length. The insets illustrate the main electronic configuration for each state. The dashed line in (a) represents the triplet state of two non-interacting electrons, for comparison. (b-d): expectation value of total electron spin as a function of the temperature for different core lengths, with two (b), three (c) and four (d) electrons.  $\langle S_e \rangle_{eq}$  is the value for equal number of low and high spin states populated. Solid (dashed) lines are used for calculations including (excluding) dielectric confinement.

account, which is a reflection of the greater Coulomb exchange energies.

We conclude from Fig. 3 that the large Coulomb exchange energy and the weak lateral confinement of colloidal NPLs enable the occupation of high spin states from cryogenic temperatures, which should provide few-electron NPLs with paramagnetic behavior in most practical instances.

In summary, we have shown that the number of fermions (electrons or holes) confined in colloidal NPLs sparks profound changes on the electronic structure. The strong Coulomb repulsions and the weak lateral confinement of NPLs combine to yield a regime of strong electronic correlations, producing non-trivial physical effects. These include (i) violations of the Aufbau principle; (ii) addition energies over 30 meV, which imply the feasibility of charging NPLs carrier-by-carrier at room temperature despite the weak lateral confinement; (iii) thermal occupation of high-spin states, enabled by the strong Coulomb exchange energies (20–35 meV), which implies that magnetic interactions with external fields or dopants will be greatly enhanced in multi-electron and multi-hole systems.

The authors acknowledge support from MICINN CTQ2017-83781-P and UJI-B2021-06 projects. We are grateful to Josep Planelles, Iwan Moreels, Thierry Barisien, Louis Biadala and Nemanja Peric for discus-



sions.

- 
- [1] S. Tarucha, D. Austing, T. Honda, R. Van der Hage, and L. P. Kouwenhoven, *Physical Review Letters* **77**, 3613 (1996).
- [2] H. Drexler, D. Leonard, W. Hansen, J. Kotthaus, and P. Petroff, *Physical Review Letters* **73**, 2252 (1994).
- [3] D. Reuter, P. Kailuweit, A. Wieck, U. Zeitler, O. Wibbelhoff, C. Meier, A. Lorke, and J. Maan, *Physical review letters* **94**, 026808 (2005).
- [4] M. Ediger, G. Bester, A. Badolato, P. Petroff, K. Karrai, A. Zunger, and R. Warburton, *Nature Physics* **3**, 774 (2007).
- [5] H. I. Jørgensen, K. Grove-Rasmussen, K.-Y. Wang, A. Blackburn, K. Flensberg, P. Lindelof, and D. Williams, *Nature Physics* **4**, 536 (2008).
- [6] J. Güttinger, T. Frey, C. Stampfer, T. Ihn, and K. Ensslin, *Physical review letters* **105**, 116801 (2010).
- [7] E. Bakkers, Z. Hens, A. Zunger, A. Franceschetti, L. Kouwenhoven, L. Gurevich, and D. Vanmaekelbergh, *Nano Letters* **1**, 551 (2001).
- [8] D. J. Norris, A. L. Efros, and S. C. Erwin, *Science* **319**, 1776 (2008).
- [9] P. Guyot-Sionnest, *Microchimica Acta* **160**, 309 (2008).
- [10] K. Wu, Y.-S. Park, J. Lim, and V. I. Klimov, *Nature Nanotechnology* **12**, 1140 (2017).
- [11] C. Wang, M. Shim, and P. Guyot-Sionnest, *Science* **291**, 2390 (2001).
- [12] S. Brovelli, W. K. Bae, C. Galland, U. Giovannela, F. Meinardi, and V. I. Klimov, *Nano letters* **14**, 486 (2014).
- [13] S. Morozov, E. L. Pensa, A. H. Khan, A. Polovitsyn, E. Cortés, S. A. Maier, S. Vezzoli, I. Moreels, and R. Sapienza, *Science advances* **6**, eabb1821 (2020).
- [14] C. Capitani, V. Pinchetti, G. Gariano, B. Santiago-González, C. Santambrogio, M. Campione, M. Prato, R. Brescia, A. Camellini, F. Bellato, *et al.*, *Nano letters* **19**, 1307 (2019).
- [15] A. Dutta, A. Medda, and A. Patra, *The Journal of Physical Chemistry C* (2020).
- [16] B. T. Diroll, W. Cho, I. Coropceanu, S. M. Harvey, A. Brumberg, N. Holtgrewe, S. A. Crooker, M. R. Wasielewski, V. B. Prakapenka, D. V. Talapin, *et al.*, *Nano letters* **18**, 6948 (2018).
- [17] D. Katz, O. Millo, S.-H. Kan, and U. Banin, *Applied Physics Letters* **79**, 117 (2001).
- [18] N. Peric, Y. Lambert, S. Singh, A. H. Khan, N. A. Franchina Vergel, D. Deresmes, M. Berthe, Z. Hens, I. Moreels, C. Delerue, *et al.*, *Nano Letters* **21**, 1702 (2021).
- [19] A. Piryatinski, S. A. Ivanov, S. Tretiak, and V. I. Klimov, *Nano letters* **7**, 108 (2007).
- [20] S. Nagaraja, P. Matagne, V.-Y. Thean, J.-P. Leburton, Y.-H. Kim, and R. M. Martin, *Physical Review B* **56**, 15752 (1997).
- [21] R. Warburton, B. T. Miller, C. Dürr, C. Bödefeld, K. Karrai, J. Kotthaus, G. Medeiros-Ribeiro, P. Petroff, and S. Huant, *Physical Review B* **58**, 16221 (1998).
- [22] M. Nasilowski, B. Mahler, E. Lhuillier, S. Ithurria, and B. Dubertret, *Chemical reviews* **116**, 10934 (2016).
- [23] B. T. Diroll, *Journal of Materials Chemistry C* **8**, 10628 (2020).
- [24] M. Sharma, S. Delikanli, and H. V. Demir, *Proceedings of the IEEE* **108**, 655 (2019).
- [25] Y. Min, E. Im, G.-T. Hwang, J.-W. Kim, C.-W. Ahn, J.-J. Choi, B.-D. Hahn, J.-H. Choi, W.-H. Yoon, D.-S. Park, *et al.*, *Nano Research* **12**, 1750 (2019).
- [26] B. Vasić, S. Aškračić, M. M. Jakovljević, and M. Artemyev, *Applied Surface Science* **513**, 145822 (2020).
- [27] A. W. Achtstein, A. Schliwa, A. Prudnikau, M. Hardzei, M. V. Artemyev, C. Thomsen, and U. Woggon, *Nano Lett.* **12**, 3151 (2012).
- [28] F. Rajadell, J. I. Climente, and J. Planelles, *Phys. Rev. B* **96**, 035307 (2017).
- [29] A. Naeem, F. Masia, S. Christodoulou, I. Moreels, P. Borri, and W. Langbein, *Physical Review B* **91**, 121302 (2015).
- [30] S. J. Zelewski, K. C. Nawrot, A. Zak, M. Gladysiewicz, M. Nyk, and R. Kudrawiec, *The journal of physical chemistry letters* **10**, 3459 (2019).
- [31] L. He, G. Bester, and A. Zunger, *Physical review letters* **95**, 246804 (2005).
- [32] H. Tasaki, *Physics and mathematics of quantum many-body systems* (Springer, 2020).
- [33] C. P. García, V. Pellegrini, A. Pinczuk, M. Rontani, G. Goldoni, E. Molinari, B. S. Dennis, L. N. Pfeiffer, and K. W. West, *Physical review letters* **95**, 266806 (2005).
- [34] J. Leemans, S. Singh, C. Li, S. Ten Brinck, S. Bals, I. Infante, I. Moreels, and Z. Hens, *The Journal of Physical Chemistry Letters* **11**, 3339 (2020).
- [35] S. Pedetti, S. Ithurria, H. Heuclin, G. Patriarche, and B. Dubertret, *Journal of the American Chemical Society* **136**, 16430 (2014).
- [36] V. Steinmetz, J. I. Climente, R. Pandya, J. Planelles, F. Margailan, Y. Puttisong, M. Dufour, S. Ithurria, A. Sharma, G. Lakhwani, L. Legrand, F. Bernardot, C. Testelin, M. Chamarro, A. Chin, A. Rao, and T. Barisien, *The Journal of Physical Chemistry C* **124**, 17352 (2020).
- [37] V. Goldman, M. Santos, M. Shayegan, and J. Cunningham, *Physical review letters* **65**, 2189 (1990).
- [38] B. T. Diroll, M. Chen, I. Coropceanu, K. R. Williams, D. V. Talapin, P. Guyot-Sionnest, and R. D. Schaller, *Nature Communications* **10**, 1 (2019).
- [39] H. Tasaki, *Physics and mathematics of quantum many-body systems* (Springer, 2020).
- [40] D. C. Mattis, *The theory of magnetism I: Statics and Dynamics*, Vol. 17 (Springer Science & Business Media, 2012).
- [41] E. V. Shornikova, D. R. Yakovlev, D. O. Tolmachev, V. Y. Ivanov, I. V. Kalitukha, V. F. Sapega, D. Kudlacik, Y. G. Kusrayev, A. A. Golovatenko, S. Shend्रे, *et al.*, *ACS nano* **14**, 9032 (2020).
- [42] A. H. Davis, E. Hofman, K. Chen, Z.-J. Li, A. Khamrang, H. Zamani, J. M. Franck, M. M. Maye, R. W. Meulenbergh, and W. Zheng, *Chemistry of Materials* **31**, 2516 (2019).
- [43] L. Dai, C. Strelow, T. Kipp, A. Mews, I. Benkenstein, D. Eifer, T. H. Vuong, J. Rabeah, J. McGettrick, R. Lesyuk, *et al.*, *Chemistry of Materials* (2020).
- [44] A. Najafi, M. Sharma, S. Delikanli, A. Bhattacharya, J. R. Murphy, J. Pientka, A. Sharma, A. P. Quinn, O. Erdem, S. Kattel, *et al.*, *The Journal of Physical Chemistry Letters* **12**, 2892 (2021).

- [45] E. V. Shornikova, A. A. Golovatenko, D. R. Yakovlev, A. V. Rodina, L. Biadala, G. Qiang, A. Kuntzmann, M. Nasilowski, B. Dubertret, A. Polovitsyn, *et al.*, *Nature nanotechnology* **15**, 277 (2020).

# Supporting Information for “Shell Filling and Paramagnetism in Few Electron Colloidal Nanoplatelets”

Jordi Llusar and Juan I. Climente\*

*Departament de Química Física i Analítica, Universitat Jaume I, E-12080, Castelló de la  
Plana, Spain*

E-mail: [climente@uji.es](mailto:climente@uji.es)

## Theoretical model

Calculations are carried within the k·p theory framework. The Hamiltonian for  $N$  interacting particles (electrons or holes) reads:

$$\hat{H}_N = \sum_{i=1}^N \hat{h}_i + \frac{1}{2} \sum_{i,j \neq i}^N V_c(\mathbf{r}_i, \mathbf{r}_j), \quad (1)$$

where  $V_c$  terms account for repulsive Coulomb interactions, and  $\hat{h}_i$  is a single-particle, single-band Hamiltonian for conduction electrons ( $i = e$ ) or valence band heavy holes ( $i = h$ ):

$$\hat{h}_i = \sum_{\alpha=x,y,z} \left( \frac{\hat{p}_\alpha^2}{2m_{i,\alpha}} + V_i(\mathbf{r}_i) \right). \quad (2)$$

In this equation,  $\hat{p}_\alpha$  are the components of the 3-dimensional momentum operator,  $m_{i,\alpha}$  those of the effective mass (anisotropic for holes), and  $V_i$  is a single-particle potential that can admit different kind of terms within it. In our calculations, the  $V_i$  term was spanned as:

$$V_i = V_i^{conf} + V_i^{strain} + V_i^{self}, \quad (3)$$

where  $V_i^{conf}$ ,  $V_i^{strain}$  and  $V_i^{self}$  stand for the spatial confining potential, strain deformation potential and self-energy interaction potential, respectively.  $V_i^{conf}$  is defined by the band offset between the core and the crown or surrounding materials. It is taken to be zero inside the core, a value defined by the (bulk) band offset in the crown (see Table. 1 below) and 2.5 eV in the outer matrix (representing insulating organic ligands).  $V_i^{strain}$  is taken as the diagonal term of the deformation potential in k·p Hamiltonians, see Ref. 1 for details.  $V_i^{self}$  is described within the image charge method for infinite quantum wells,<sup>2</sup> as lateral dielectric confinement is comparatively much weaker in NPLs owing to the large shape anisotropy.

Coulomb interaction terms,  $V_c(\mathbf{r}_i)$ , are calculated by integrating the Poisson equation within an inhomogeneous dielectric environment, using Comsol Multiphysics 4.2. Many-body eigenstates and eigenenergies are then calculated within a full CI method,<sup>3</sup> exploiting

permutation and spin  $S_z$  symmetries, using *CItool* codes.<sup>4</sup> The CI basis set is formed by all possible combinations of the first 20 independent-electron and 24 independent-hole spin-orbitals

Regarding material parameters, low temperature band gaps of CdSe (1.76 eV) and CdTe (1.6 eV) and band offsets potentials (Table 1) are taken from Ref. 5. The NPL relative dielectric constant is set to  $\varepsilon_{in} = 10$  and that of the outer medium (if dielectric mismatch is considered) to  $\varepsilon_{out} = 2$ . These are reasonable values for Cd chalcogenide NPLs and typical ligands, which reproduce well experimentally observed trion binding energies, to name an example.<sup>6</sup> The rest of parameters are given in the supporting information of Ref. 1. We note that the value of the conduction band offset for CdSe/CdS is sometimes considered to be uncertain, with some studies suggesting it could be negligible.<sup>7</sup> If we used a lower band offset than 0.24 eV in our simulations, the situation would be essentially equivalent to that of a CdSe/CdS NPL with a somewhat larger core, so the same conclusions would hold.

Table 1: CdSe/CdS and CdSe/CdTe band offset values.

Band Offsets (eV)	
Conduction Band Offset (CBO)	
CdSe/CdS	CdSe/CdTe
0.24	0.53
Valence Band Offset (VBO)	
CdSe/CdS	CdSe/CdTe
0.48	-0.69

Thermal occupation is simulated by the Fermi-Dirac thermal population distribution on the stationary states. The spin for equal population of high and low spins is obtained as  $\langle S_e \rangle_{eq} = \frac{M^l S^l + M^h S^h}{M^l + M^h}$  where  $S^l$  ( $S^h$ ) is the spin of the low (high) spin states that can be formed with  $N$  electrons (e.g.  $S = 0$  and  $S = 1$  for  $N = 2$ ), and  $M^{i=l,h}$  the corresponding spin multiplicities.

# Additional calculations

## Addition energies and spin of few fermion systems

In Fig. S1 we plot the difference between the addition energies of interacting and non-interacting carriers, as inferred from Fig.2 of the main text. In a perturbative scheme, where electron-electron (or hole-hole) Coulomb integrals were approximately constant for different values of  $N_e$  ( $N_h$ ), the repulsive terms in  $\Delta$  would compensate (see Eq. 1 of the main text) and one would expect a roughly constant value of the figure. It is quite clear from the figure, however, that this is not the case.

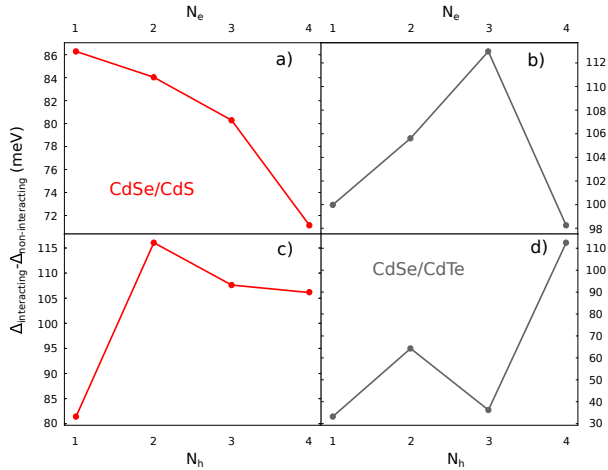


Figure S1: Difference between addition energy spectra of interacting and non-interacting particles in NPLs with  $L_y^c = 20$  nm. (a) Electrons in CdSe/CdS NPLs. (b) Electrons in CdSe/CdTe NPLs. (c) Holes in CdSe/CdS NPLs. (d) Holes in CdSe/CdTe NPLs. The interacting case is that including dielectric mismatch (Fig.2c and 2f in the main text).

For electrons in CdSe/CdS nanoplatelets (panel a), the difference decreases monotonically as  $N_e$  increases. This suggests electrons are leaking outside the core to reduce repulsions (even if the single-particle orbitals in Fig.1b of the main text would suggest more electrons can fit inside the core). For electrons in CdSe/CdTe (panel b) and for holes in both materials (panels c and d), the changes are non-monotonic, because the confinement potential (band

offset) is more rigid, and the interplay between correlation and lateral confinement becomes more complicated.

In general, the figure evidences changes of 15 meV for electrons, and much more for holes (over 100 meV for the CdSe/CdTe core-crown platelets). This variation is a hint of the strong electronic correlations taking place in the system (about 15% of the total addition energy). In the case of holes in CdSe/CdTe, the differences also reflect the non-simple (diatomic-like) confinement potential.

The addition energies presented in Fig. 2 of the manuscript correspond to NPLs with a  $L_y^c = 20$  nm core. Fig. S2 shows that electron and hole addition energies greater than room temperature thermal energy are also obtained for smaller core sizes (notice that in our model smaller cores imply larger crowns).

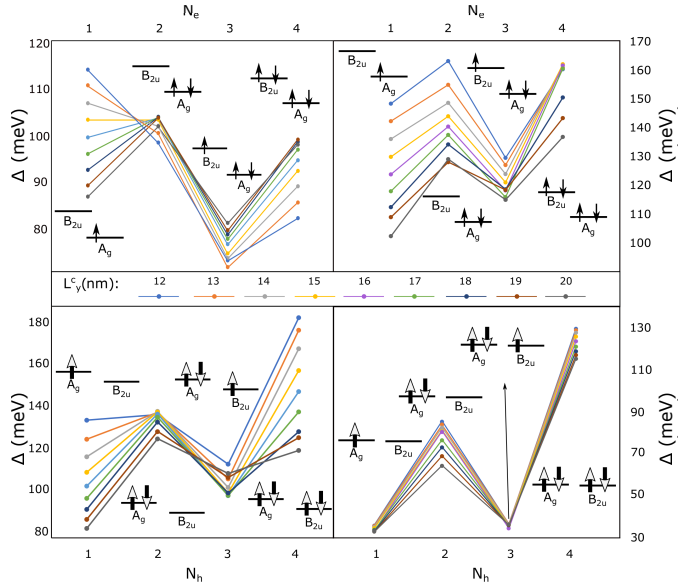


Figure S2: Addition energy spectra as a function of the number of carriers for interacting electrons (top row) and interacting holes (bottom row) in CdSe/CdS NPLs (left column) and CdSe/CdTe NPLs (right column) with different core lengths,  $L_y^c$ .

A shell structure, with maxima at even number of electrons (closed shells) is preserved

in most instances. A relevant exception takes place for electrons in CdSe/CdS NPLs with  $L_y^c < 15$  nm. In such a case,  $N_e = 2$  does not reflect a local maximum in  $\Delta$ . That is, the closed shell configuration ( $N_e = 2$ ) is less stable than the open shell one ( $N_e = 1$ ). The reason is that, for small enough cores, the lowest single electron orbital is localized in CdSe, but Coulomb repulsions are strong enough as to overcome the band offset and push the second electron into excited orbitals, which are delocalized all over the CdSe/CdS heterostructure. This is a Coulomb-blockade effect.

Fig. S3 shows that thermal occupation of high spin states can be obtained not only in few-electron CdSe/CdS NPLs (Fig. 3 of the main text) but also in CdSe/CdTe NPLs.

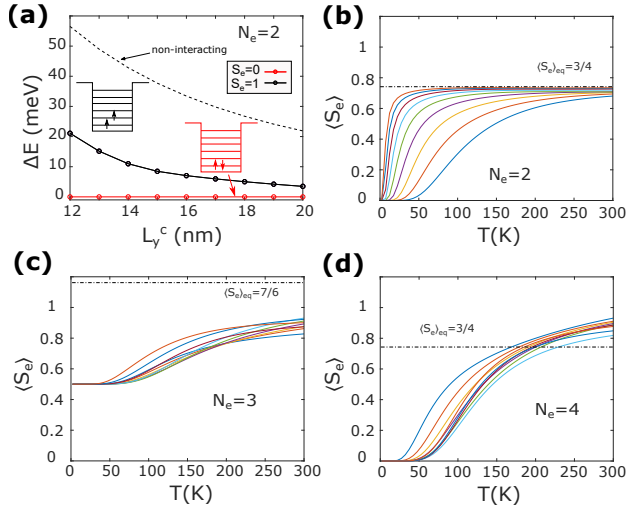


Figure S3: Same as Fig. 3 of the main text, but for CdSe/CdTe NPLs.

Fig. S4 represents the  $N_e = 3$  and  $N_e = 4$  energy levels for CdSe/CdS and CdSe/CdTe NPLs, as a function of the core size. The ground state corresponds to the lowest possible spin in all cases, but high spin states are generally available at temperatures under  $\sim 24$  meV (room temperature thermal energy). For  $N_e = 4$ , spin triplet states (black lines) within such an energy range outnumber spin singlet ones (red lines). The higher density of states in CdSe/CdS, as compared to CdSe/CdTe, is due to the low conduction band offset.



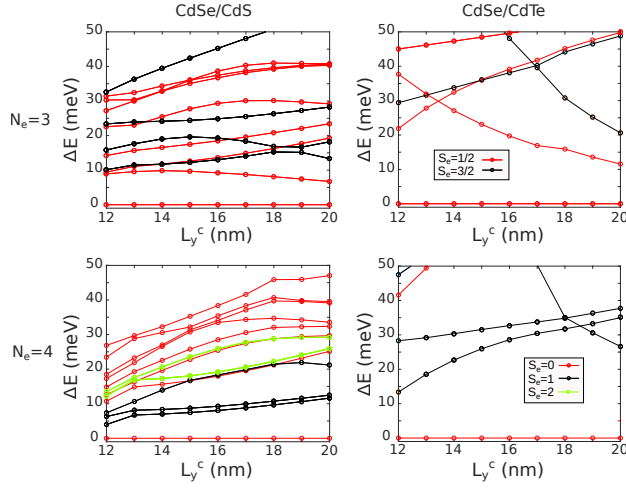


Figure S4: Energy levels as a function of the core length for three and four interacting electrons in CdSe/CdS (left) and CdSe/CdTe (right). Different lines denote different total electron spin. All energies are referred to the ground state for a given core length,  $L_y^c$ .

One can note in Fig. S4 that, contrary to the case of  $N_e = 2$  electrons (Fig.3 in the main text), high spin states for  $N_e = 3$  and  $N_e = 4$  do not get closer to the ground state with increasing core length,  $L_y^c$ . The reason is that for  $N_e = 2$ , the ground state is a singlet with two paired electrons. The triplet state requires occupying an excited orbital, and the larger the length of the core, the closer this orbital is – see Fig. 3(a) –. For  $N_e = 3$  and  $N_e = 4$ , however, the excited orbital is already occupied in the ground state, so the influence of confinement is less straightforward. This difference explains the opposite trends of  $\langle S_e \rangle$  in Fig.3 of the main text: it increases with  $L_y^c$  when  $N_e = 2$ , but it does not when  $N_e = 3$  or  $N_e = 4$ .

## References

- (1) Llusar, J.; Planelles, J.; Climente, J. I. Strain in Lattice-Mismatched CdSe-Based Core/Shell Nanoplatelets. *The Journal of Physical Chemistry C* **2019**, *123*, 21299–21306.

- (2) Kumagai, M.; Takagahara, T. Excitonic and Nonlinear-Optical Properties of Dielectric Quantum-Well Structures. *Phys. Rev. B.* **1989**, *40*, 12359–12381.
- (3) Llusar, J.; Climente, J. I. Nature and Control of Shakeup Processes in Colloidal Nanoplatelets. *ACS Photonics* **2020**, *7*, 3086–3095.
- (4) Bertoni, A. CItool. <https://github.com/andreabertoni/citool>, 2011; [Online; accessed 4-May-2021].
- (5) Adachi, S. *Handbook on Physical Properties of Semiconductors, vol.3*; Kluwer Academics, 2004.
- (6) Macias-Pinilla, D. F.; Planelles, J.; Mora-Seró, I.; Climente, J. I. Comparison between trion and exciton electronic properties in CdSe and PbS nanoplatelets. *The Journal of Physical Chemistry C* **2021**, *125*, 15614–15622.
- (7) Eshet, H.; Grünwald, M.; Rabani, E. The electronic structure of CdSe/CdS core/shell seeded nanorods: type-I or quasi-type-II? *Nano letters* **2013**, *13*, 5880–5885.

## 2.5 Changing Symmetries in Nanoplatelets

### ”Changing Spin and Orbital Ground State Symmetries in Colloidal Nanoplatelets with Magnetic Fields.”

Jordi Llusar and Juan I. Climente.

*Phys. Status Solidi B* **2022**, 2200081

DOI: <https://doi.org/10.1002/pssb.202200081>

#### **Abstract:**

The symmetry of the electronic ground state is of paramount importance in determining the magnetic, optical, and electrical properties of semiconductor nanostructures. Here, it is shown theoretically that nontrivial spin and orbital symmetries can be induced in colloidal nanoplatelets (NPLs) by applying out-of-plane magnetic fields. Two scenarios are presented. The first one deals with two electrons confined inside a platelet. Here, the strong electron–electron exchange interaction reduces the interlevel energy spacing set by lateral quantum confinement. As a result, relatively weak magnetic fields suffice to induce a singlet-to-triplet spin transition. The second one deals with type-II core/crown NPLs. Here, the crown has doubly connected topology, akin to that of quantum rings. As a result, the energy levels of carriers within it undergo Aharonov–Bohm (AB) oscillations. This implies changes in the ground state orbital symmetry, which switch the exciton and trion optical activity from bright to dark.

Check the original paper through this ”Shareable link”: <https://onlinelibrary.wiley.com/share/N5T7FJ7GM3JVBKM4FMMK?target=10.1002/pssb.202200081>

# Changing Spin and Orbital Ground State Symmetries in Colloidal Nanoplatelets with Magnetic Fields

Jordi Llusar Juan I. Climente\*

Mr. J. Llusar, Prof. J.I. Climente  
 Universitat Jaume I, E-12080, Castelló de la Plana, Spain  
 Email Address: climente@uji.es

Keywords: *nanoplatelet, heterostructure, magnetism, bright exciton, dark exciton, charged exciton, Aharonov-Bohm effect*

The symmetry of the electronic ground state is of paramount importance in determining the magnetic, optical and electrical properties of semiconductor nanostructures. Here it is shown theoretically that non-trivial spin and orbital symmetries can be induced in colloidal nanoplatelets by applying out-of-plane magnetic fields. Two scenarios are presented. The first one deals with two electrons confined inside a platelet. Here, the strong electron-electron exchange interaction reduces the interlevel energy spacing set by lateral quantum confinement. As a result, relatively weak magnetic fields suffice to induce a singlet-to-triplet spin transition. The second one deals with type-II core/crown nanoplatelets. Here, the crown has doubly-connected topology, akin to that of quantum rings. As a result, the energy levels of carriers within it undergo Aharonov-Bohm oscillations. This implies changes in the ground state orbital symmetry, which switch the exciton and trion optical activity from bright to dark.

## 1 Introduction

Changing the electronic ground state symmetry has a major effect on the physical response of semiconductor nanostructures. In all-solid systems, this has sparked a large number of works applying external electrical and magnetic fields in order to achieve reversible ground state transitions.[1, 2, 3, 4, 5, 6] In colloidal nanocrystals, however, studies are mostly restricted to the use of magnetic fields in order to modify the exciton fine structure. Exciton spin triplet (dark) and spin singlet (bright) states are hybridized or reversed in energy under such fields, which has a significant impact on the optical activity.[7, 8, 9, 10, 11]

Alternative strategies to manipulate the ground state have been largely prevented by the strong quantum confinement in such structures, which usually places the first excited state several tens of meV above the ground state. This magnitude vastly exceeds the range of energetic modifications that can be induced even by high magnetic fields (up to a few meV for 30 T, when relying on Zeeman splitting).[12, 13]

The advent of colloidal nanoplatelets (NPLs) in metal-chalcogenide and halide perovskite materials[14, 15] may be a turning point to this regard. NPLs are slab-like nanocrystals which combine a strongly confined direction (with a thickness of a few atomic monolayers only) and weak lateral confinement in the other two dimensions (from few nm to tens of nm).[14, 15, 16, 17] In a typical CdSe NPL with a lateral side of 30 nm, the energy spacing between ground and first excited state of an independent conduction band electron reduces down to  $\sim 10$  meV.[18, 19, 20] In addition, the large lateral dimensions enable sizable diamagnetic shifts when the field is applied perpendicular to the NPL plane. Under these conditions, strategies can be devised to induce a crossing of the ground and first excited state using magnetic field strengths attainable in conventional laboratories. In this work we propose two such strategies, and use effective mass calculations to assess on their viability.

The first strategy consists in replacing single-electron by few-electron systems. It has been recently shown that dielectric confinement in colloidal NPLs, which arises from the weak polarizability of the ligands surrounding the NPL, gives rise to large electron-electron exchange energies, which in turn favor high spin configurations.[20] Here we consider the paradigmatic case of two electrons. In the absence of external fields, the ground state is a spin singlet, with two electrons of anti-parallel spin occupying the lowest orbital. The strong exchange interaction drives the first excited state, which is a spin triplet with one electron in the first excited orbital, close to the singlet ground state. For CdSe NPLs with usual dimensions, we estimate the splitting to be less than 1 meV. It is then possible to induce a singlet-to-triplet

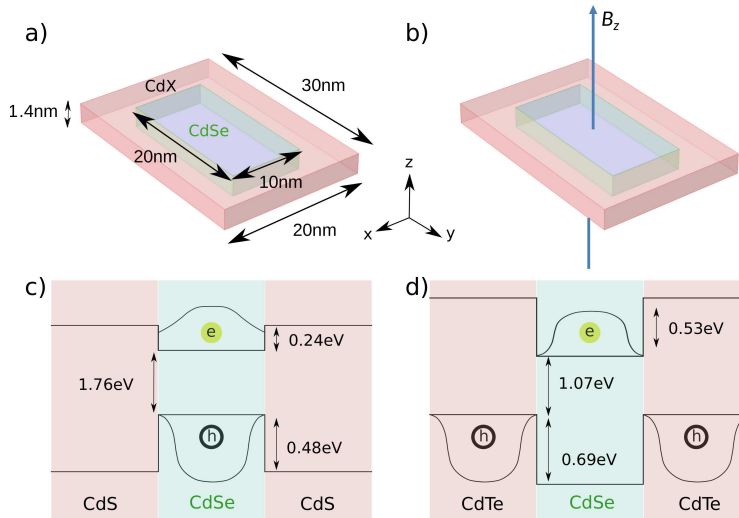


Figure 1: (a) Schematic of the CdSe/CdX NPLs under study, with X=S,Te. (b) Direction of the external magnetic field. (c,d) Band offset profiles for CdSe/CdS (c) and CdSe/CdTe (d) along the long axis of the NPL. The spatial localization of conduction band electrons and valence band holes is plotted for each case.

transition mediated by Zeeman splitting at low values of the magnetic field. The controlled, reversible change in the spin symmetry of the ground state is of interest for the development of spintronics and spin-based qubits for quantum information processing.[4, 21, 22, 23]

The second strategy deals with excitons in core/crown NPLs. These are heterostructures in which a seed NPL is laterally surrounded by a different material, forming a crown around the core NPL.[14, 15] Because the crown has doubly connected (toroidal) topology, carriers confined within are liable of displaying phenomena related to the Aharonov-Bohm (AB) effect in the presence of external magnetic fields.[2, 24] For illustration purposes, we consider the case of CdSe/CdTe core/crown NPLs.[18, 25] This is a type-II heterostructure, where electrons localize in the CdSe core and holes in the CdTe crown. Upon inclusion of a magnetic field perpendicular to the NPL plane, the hole energy levels undergo AB oscillations, while the electron ones do not. As a result, at moderate values of the magnetic field, the electron and hole ground states present different orbital symmetries and their overlap vanishes. This gives rise to a sudden decrease in the radiative recombination rate of the band edge exciton. This phenomenon, known as the “optical Aharonov-Bohm effect” was originally proposed for epitaxial quantum rings[26] and soon after observed in epitaxial type-II ZnSe/ZnTe quantum dots.[27] We predict that the same phenomenon should take place in colloidal CdSe/CdTe NPLs.

## 2 Results and Discussion

To exemplify the strategies we propose, we simulate core/crown NPLs made of either CdSe/CdS or CdSe/CdTe, and typical experimental dimensions, see schematic in Figure 1a. The resulting behavior can be however extrapolated to many other related colloidal nanostructures. A homogeneous, external magnetic field ( $B_z$ ) is applied transversal to the NPL plane (Faraday configuration), see Fig. 1b. The energy gaps and band-offsets of CdSe/CdS and CdSe/CdTe NPLs are shown in Figure 1c,d, respectively. Notice that the former is a type-I structure, with electrons and holes localizing in the CdSe core, but the latter is a type-II structure, with holes localizing in the CdTe crown.

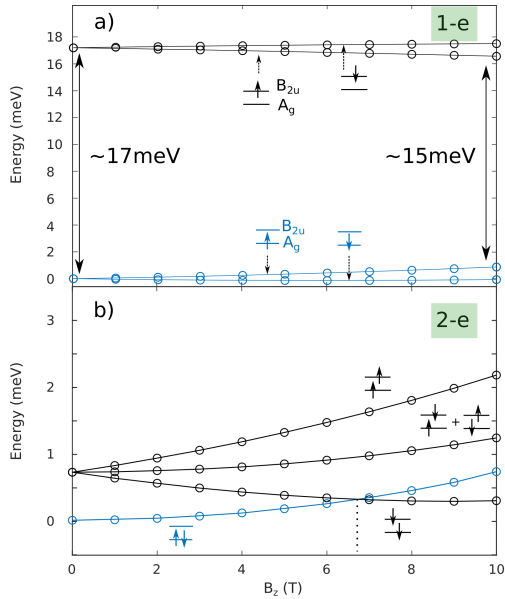


Figure 2: Electron energy levels as a function of the external magnetic field in the CdSe/CdS NPL. Blue (black) circled lines: ground (excited) state at  $B_z = 0$  T. (a) 1-electron system. (b) 2-electron system. The dotted vertical line in (b) points out the singlet-triplet ground state crossing. All energies are referred to the ground state at  $B_z = 0$  T. The insets show the dominant electronic configurations.

## 2.1 Singlet-triplet reversal

Let us begin with a type-I (CdSe/CdS) NPL. As shown in Figure 2a, when a single conduction band electron is confined in the NPL, the two first orbitals ( $A_g$  and  $B_{2u}$  symmetry in the  $D_{2h}$  group) are split by 17 meV at zero external field. Switching on  $B_z$  splits the spin sublevels, but the Zeeman energy at 10 T is of 2 meV only. No ground state crossing can then be expected except at overwhelming values of the field. This is in sharp contrast with the case of two electrons, shown in Figure 2b. When a second electron is injected into the NPL, the strong exchange interaction—stimulated by dielectric confinement—largely compensates for the extra kinetic energy of the excited orbital, and a triplet state forms very close to the singlet ground state at zero field.[20] For the system under study, we estimate 1 meV separation at  $B_z = 0$  T, see Figure 2b. This energy splitting is similar to that observed in the exciton fine structure of CdSe NPLs,[9] and it opens venue for magnetic manipulation of the ground state symmetry. The two-electron triplet (total spin  $S = 1$ ) couples to  $B_z$  via the Zeeman term, but the singlet (total spin  $S = 0$ ) does not. As a result, a singlet-to-triplet ground state crossing takes place at  $B_z = 6.7$  T, see Figure 2b.

It is worth noting that magnetic saturation reported in Fig. 2b is feasible in two-electron NPLs, but not in negatively charged excitons (trions,  $X^-$ ). In the latter case, the ground state (which contains a two-electron singlet) remains well below the excited state (with a two-electron triplet). For the structure under study, the splitting we calculate is 26 meV. The reason is that in  $X^-$  the two electrons are no longer confined by the lateral sides of the NPL, but rather by the Coulomb potential exerted by the hole. This leads to a small effective Bohr radii.[28, 29]

Consequently, electrons are no longer in the strong correlation regime and their exchange interaction cannot compensate for kinetic energies.

We conclude from this section that magnetic fields can be used to change the spin symmetry of the few-electron ground state in colloidal NPLs. One should however avoid charging schemes based on optical excitations, which produce electron-hole pairs, and rely on electron-only (or hole-only) injection schemes,

such as doping[30], electrochemical injection[31, 32] or scanning tunneling spectroscopy in the shell filling regime.[33]

While the singlet-to-triplet reversal scheme we report can be expected to hold for type-I NPLs of different materials, provided lateral confinement is weak enough, the choice of a core/crown structure as in our simulation improves the passivation of the lateral sides, which are prone to labile ligand binding.[34] Avoiding exposed facets seems convenient in highly charged nanocrystals to avoid surface reduction reactions.[35] Also, we note that spin-orbit terms, which are neglected in our model, could turn the singlet-triplet crossings we report into anticrossings,[36, 37], but for conduction band electrons in nanocrystals these are minor corrections.[8]

## 2.2 Aharonov-Bohm effect

As mentioned before, nanostructures with doubly connected topology experience AB phenomena.[24] The Peierls phase of the carriers in such structures is modified by the flux of magnetic field piercing the structure even if they are not in contact with the field itself. Oscillations of the energy levels result, which can yield alternating orbital symmetries of the ground state.[38]

AB effects have been reported in epitaxial and lithographic quantum rings.[2, 39, 40, 41] In colloidal systems, quantum rings have been recently synthesized as well.[42, 43] However, their electronic structure is often affected by trap states on facets inaccessible to ligands.[44] In comparison, core/crown NPLs present arguably improved surface passivation.[18, 34] We thus consider the latter nanostructure for our study of AB effects. For clarity of the orbital effects we wish to present here, spin Zeeman splitting is disregarded in this section (i.e. we set g-factors to zero).

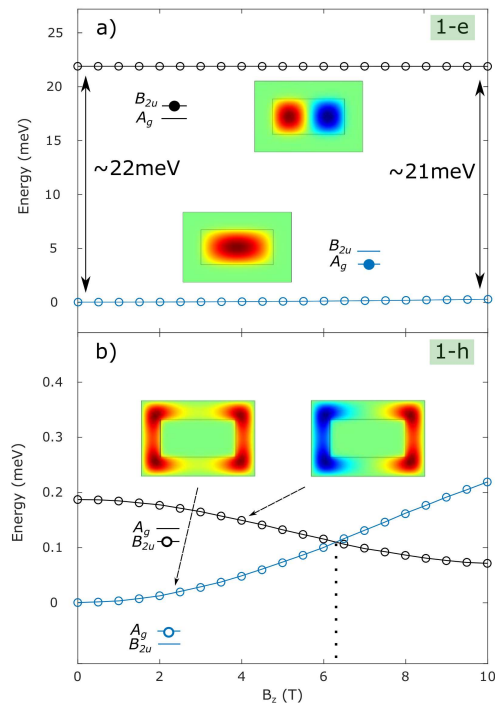


Figure 3: (a) Electron and (b) hole energy levels as a function of the external magnetic field in the CdSe/CdTe NPL. The dotted vertical line in (b) points out the  $A_g$ - $B_{2u}$  ground state crossing. The insets in (a) and (b) represent, respectively, the electron and hole wave functions at  $B_z = 0$  T.

We study a type-II CdSe/CdTe NPL, like that in Figure 1a. Electrons and holes perceive the magnetic

field differently since they occupy different spatial regions, see Figure 1d. Because electrons are confined in the CdSe core, the single-electron spectrum –shown in Figure 3a– is very similar to that in CdSe/CdS NPLs –Figure 2a–, with no remarkable effect of  $B_z$  (recall we have removed Zeeman splittings). On the contrary, holes are confined in the crown. Consequently, the single-hole spectrum –shown in Figure 3b– displays a few characteristic features. At zero field, two orbitals ( $A_g$  and  $B_{2u}$ ) with similar energy are observed. They correspond to the even and odd solutions of the double quantum box formed by the crown on each side of the core (see insets). The splitting between the two states is set by the hole tunneling energy between the two sides. When  $B_z$  is switched on, the  $A_g$  orbital exhibits a quadratic (diamagnetic) shift, proportional to the size of inner core.[45] In turn, the  $B_{2u}$  orbital is stabilized by the linear-in- $B_z$  term. At 7 T, the  $B_{2u}$  state stabilizes below  $A_g$ . This is an AB oscillation, which enables a change of the ground state orbital symmetry. As we shall see next, this swapping is not only present in single-hole systems, but also in excitonic complexes. Hence, it greatly affects the optical properties of the NPL.

### 2.2.1 Excitons: Optical Aharonov-Bohm effect

For excitons, the motion of electrons and holes is correlated through Coulomb interactions, which we include in our effective mass model through a Configuration Interaction (CI) method. In a type-II structure like the CdSe/CdTe NPLs we consider, however, excitonic correlations are moderate. As a result, the exciton behavior is reminiscent of that of independent electrons and holes studied above. As shown in Figure 4a, the exciton ground state changes symmetry at  $B_z = 7$  T. This crossing is closely connected to the change in hole orbital symmetry reported in Fig. 3b, which is actually reflected in the main configurations of the CI expansion (see insets in Fig. 4a).

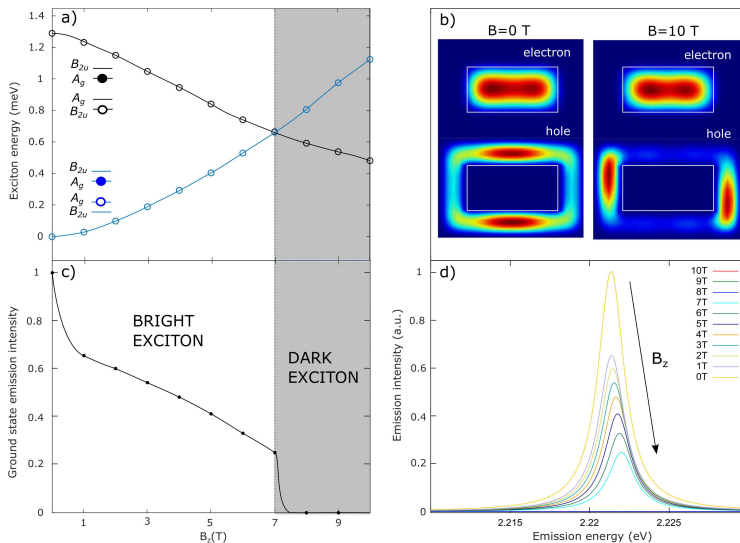


Figure 4: (a) Exciton energy as a function of the magnetic field in the CdSe/CdTe NPL. The insets illustrate the main exciton configuration in the CI expansion. (b) Electron and hole charge density of the exciton ground state before and after the crossing. (c) Integrated ground state emission intensity at temperature  $T = 0.1$  K, as a function of the magnetic field. (d) Same but energy-resolved. Blue (black) circled lines in (a) represent ground (first excited) state at  $B_z = 0$  T. Gray regions in (a) and (c) highlight the domain of the dark exciton ground state.

The change in the exciton orbital symmetry gives rise to a remarkable change in the optical response. At low magnetic fields, electron and hole orbitals forming the exciton ground state have the same symmetry ( $A_g$ ). Their recombination probability, which is proportional to the electron-hole overlap integral, is then finite. This is consistent with experiments, which measured sizable emission despite the type-II band alignment.[25, 18, 46] Nonetheless, when the magnetic field exceeds 7 T, the crossing of the ground



state translates into an abrupt increase of the electron-hole separation (compare the charge densities at  $B_z = 0$  and 10 T in Figure 4b) and, what is more important, the electron and hole start having different symmetries ( $A_g$  and  $B_{2u}$  respectively). As a consequence, the overlap integral vanishes and the transition becomes forbidden. This is reflected as a sudden drop of the emission intensity beyond 7 T in Figures 4c and d. The formation of a dark exciton induced by the AB oscillations of one of constituent carriers is the so-called optical AB effect.[26]

### 2.2.2 Trions: Breakdown of the optical Aharonov-Bohm effect

There are experimental evidences that CdSe-based NPLs are prone to developing surface defects, which give rise to trions –instead of neutral excitons– upon photoexcitation.[49, 28, 50, 51] To account for this possibility, we extend the study of AB effects to negative trions. Figure 5 shows the energy and emission spectrum of a trion under a field  $B_z$ . Similar to the case of the neutral exciton, an AB oscillation takes place at  $B_z \sim 6.3$  T, which changes the hole symmetry in the ground state. It is worth noting, however, that this no longer translates into an abrupt decrease of the emission intensity down to zero (see Fig. 5b and c). That is, the optical AB effect no longer holds strictly.

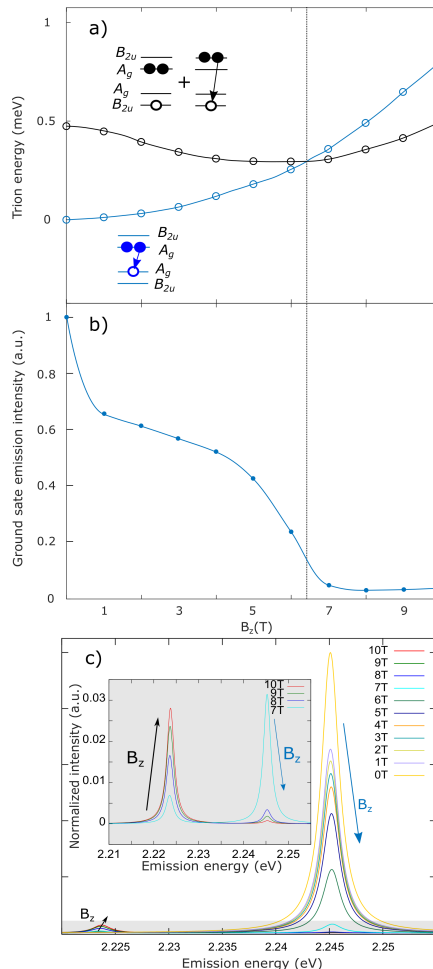


Figure 5: Same as Fig. 5 but for a negative trion. The insets in (a) show the dominant configurations of the trion states, and the arrows show the radiative recombination path.

The different optical response of the negative trion as compared to the neutral exciton is because the two-electron wave function is no longer orthogonal to that of the hole. To minimize repulsions, the electrons occupy not only the lowest ( $A_g$ ) orbitals, but also excited ( $B_{2u}$ ) ones. This is illustrated in the insets of Figure 5a, which show the dominant configurations of the CI expansion. Before the ground state crossing, the  $A_g$  hole can recombine with  $A_g$  electrons (blue inset). After the crossing, the hole switches to  $B_{2u}$  symmetry but it is still able to recombine with one of the two  $B_{2u}$  electrons (black inset). In the latter case, because the final state involves one electron in an excited orbital, the transition shows up as a redshifted peak, see Figure 5c. When  $B_z$  increases beyond 6.3 T, the redshifted peak becomes increasingly important, as shown in the inset of Fig. 5c. In short, for trions AB oscillations still take place, and reduced emission is predicted after the ground state crossing, but the symmetry selection rule responsible for the optical AB effect is no longer strict, owing to electron-electron correlation.

We infer from sections 2.2.1 and 2.2.2 that the use of magnetic fields in type-II colloidal nanostructures with doubly-connected topology, such as core/crown CdSe/CdTe NPLs, is susceptible of producing AB phenomena. The experimental observation of such effects may be challenging though. Recent studies of the low-temperature emission of core/crown CdSe/CdTe NPLs under magnetic fields reveal broad band edge exciton transitions, as well as a significant contribution of the spin Zeeman splitting.[47] Fine energetic effects like the AB oscillation we report in Figs. 4 and 5 will then be likely masked. The use of narrower crowns -to separate hole states energetically- and wider cores -to reduce the  $B_z$  field needed for AB oscillations[45]- as compared to the typical CdSe/CdTe NPL dimensions we study here, may improve the observability of the effects we predict. A practical implementation of the optical AB effect would be of interest for optical applications, such as exciton storage.[48]

### 3 Conclusions

We have presented two strategies to switch spin and orbital symmetries in the ground state of colloidal NPLs by means of external magnetic fields.

(i) In NPLs charged with a few fermions, the strong Coulomb exchange interaction places high spin states energetically close to low spin ones. We then predict that  $B_z$  values of a few T should suffice to induce magnetic saturation, mediated by the large Zeeman splitting of high spin states. As an example, we simulated the two electrons in a type-I CdSe/CdS NPL, where a singlet-to-triplet ground state transition is observed at  $B_z \sim 7$  T.

(ii) In core/crown NPLs charged with excitons, we argue that carriers confined in the crown are liable of experiencing AB effects. As an example, we studied case of type-II CdSe/CdTe NPLs and showed that the hole undergoes AB oscillations at moderate magnetic fields (few T). For neutral excitons, this gives rise to the optical AB effect, whereby the exciton ground state switches from bright to dark mediated by orbital selection rules. For negative trions, we observed AB oscillations are still present but electron-electron correlations soften the optical AB effect.

Effective mass calculations including 3D spatial confinement, Coulomb interactions and dielectric mismatch effects show that such transitions are feasible in colloidal NPLs with realistic dimensions and field values.

### 4 Methods

We used single-band k-p Hamiltonians to describe non-interacting electron and hole states, with core/crown strain modeled within the continuum elastic theory.[18, 53] Self-energy terms arising from the dielectric mismatch between the nanoplatelet and the organic phase are included.[54] The axial magnetic field  $B_z$  is modeled using the symmetric gauge for the potential vector,  $\vec{A} = \frac{1}{2}(-yB_z, xB_z, 0)$ , within the minimal coupling scheme  $\vec{p} \rightarrow \vec{\pi} = \vec{p} - q_{e,h}\vec{A}$ , where  $\vec{p}$  is the momentum operator and  $q_{e,h}$  is the electron or hole charges.[55]

Interacting, few-body (few-electron or excitonic) states and eigenenergies are calculated within a full CI method on the basis of independent particle states[51], exploiting permutation and spin  $S_z$  symmetries, using *CItool* codes.[56] The CI basis set for two electrons in CdSe/CdS NPLs was constructed from all possible combinations of the first 16 independent-electron spin-orbitals, while that for excitons and trions in CdSe/CdTe NPLs used 16 electron and 20 hole spin-orbitals. Coulomb integrals, including the enhancement coming from dielectric confinement, were calculated solving the Poisson equation with Comsol 4.2.

All optical spectra are calculated within the dipole approximation,[57] assuming Lorentzian bands with linewidth of 1 meV and temperature  $T = 0.1$  K. We used the material parameters from ref [20], except for g-factors ( $g_e(\text{CdSe}) = 1.62$ ) which were taken from ref [49].

### **Conflict of interest**

The authors declare no financial nor commercial conflict of interest.

### **Acknowledgements**

The authors acknowledge support from MICINN project CTQ2017-83781-P and project UJI-B2021-06.

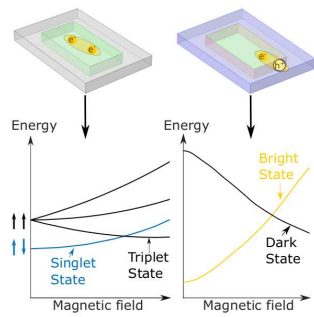
## References

- [1] T. Chakraborty, *Quantum Dots: A Survey of the Properties of Artificial Atoms*, Elsevier, **1999**.
- [2] V. M. Fomin, *Physics of Quantum Rings*, Springer, **2014**.
- [3] K. Müller, G. Reithmaier, E. C. Clark, V. Jovanov, M. Bichler, H. J. Krenner, M. Betz, G. Abstreiter, J. J. Finley, *Phys. Rev. B* **2011**, *84*, 081302.
- [4] S. Sasaki, T. Fujisawa, T. Hayashi, Y. Hirayama, *Phys. Rev. Lett.* **2005**, *95*, 056803.
- [5] L. Gaudreau, G. Granger, A. Kam, G. C. Aers, S. A. Studenikin, P. Zawadzki, M. Pioro-Ladrière, Z. R. Wasilewski, A. S. Sachrajda, *Nature Phys* **2012**, *8*, 54.
- [6] M. Bayer, O. Stern, A. Kuther, A. Forchel, *Phys. Rev. B* **2000**, *61*, 7273.
- [7] Al. L. Efros, M. Rosen, M. Kuno, M. Nirmal, D. J. Norris, and M. Bawendi, *Phys. Rev. B* **1996**, *54*, 4843.
- [8] A. V. Rodina, A. A. Golovatenko, E.V. Shornikova, D. R. Yakovlev, *Phys. Solid State* **2018**, *60*, 1537.
- [9] E. V. Shornikova, L. Biadala, D.R. Yakovlev, V.F. Sapega, Y.G. Kusrayev, A.A. Mitioglu, M.V. Ballottin, P.C.M Christianen, V.V. Belykh, M.V. Kochiev, N.N. Sibeldin, A.A. Golovatenko, A.V. Rodina, N.A. Gippius, A. Kuntzmann, Y. Jiang, M. Nasilowski, B. Dubertret, M. Bayer, *Nanoscale* **2018**, *10*, 646.
- [10] M. Fu, P. Tamarat, H. Huang, J. Even, A. L. Rogach, B. Lounis, *Nano Lett.* **2017**, *17*, 2895.
- [11] A. Brodu, M. V. Ballottin, J. Buhot, E. J. van Harten, D. Dupont, A. La Porta, P. T. Prins, M. D. Tessier, M. A. M. Versteegh, V. Zwiller, S. Bals, Z. Hens, F. T. Rabouw, P. C. M. Christianen, C. de Mello Donega, and D. Vanmaekelbergh, *ACS Photonics* **2018**, *5*, 3353.
- [12] A. Granados del Águila, G. Pettinari, E. Groeneveld, C. de Mello Donegá, D. Vanmaekelbergh, J. C. Maan, and P. C. M. Christianen, *J. Phys. Chem. C* **2017**, *121*, 23693.
- [13] L. Turyanska, J. H. Blokland, U. Elfurawi, O. Makarovsky, P. C. M. Christianen, and A. Patanè, *Phys. Rev. B* **2010**, *82*, 193302.
- [14] M. Nasilowski, B. Mahler, E. Lhuillier, S. Ithurria, B. Dubertret, *Chem. Rev.* **2016**, *116*, 10934.
- [15] C. Otero-Martínez, J. Ye, J. Sung, I. Pastoriza-Santos, J. Pérez-Juste, Z. Xia, A. Rao, R. L. Z. Hoyer, L. Polavarapu, *Adv. Mater.* **2021**, *n/a*, 2107105.
- [16] G. H. V. Bertrand, A. Polovitsyn, S. Christodoulou, A. H. Khan, I. Moreels, *Chem. Commun.* **2016**, *52*, 11975.
- [17] A. W. Achtstein, R. Scott, S. Kickhöfel, S. T. Jagsch, S. Christodoulou, G. H. V. Bertrand, A. V. Prudnikau, A. Antanovich, M. Artemyev, I. Moreels, A. Schliwa, U. Woggon, *Phys. Rev. Lett.* **2016**, *116*, 116802.
- [18] V. Steinmetz, J.I. Climente, R. Pandya, J. Planelles, F. Margaillan, Y. Puttisong, M. Dufour, S. Ithurria, A. Sharma, G. Lakhwani, L. Legrand, F. Bernardot, C. Testelin, M. Chamarro, A. Chin, A. Rao, T. Barisien, *J. Phys. Chem. C* **2020**, *124*, 17352.
- [19] S. Bose, Z. Song, W. J. Fan, D. H. Zhang. *J. Appl. Phys.* **2016**, *119*, 143107.
- [20] J. Llusar, J.I. Climente, Charging of colloidal nanoplatelets: effect of Coulomb repulsion on spin and optoelectronic properties, (Preprint) arXiv:2105.14825, v1, submitted: May **2021**.

- [21] C. Barthel, D. J. Reilly, C. M. Marcus, M. P. Hanson, A. C. Gossard, *Phys. Rev. Lett.* **2009**, *103*, 160503.
- [22] K. M. Weiss, J. Miguel-Sanchez, J. M. Elzerman, *Sci. Rep* **2013**, *3*, 3121.
- [23] R. Hanson, L. P. Kouwenhoven, J. R. Petta, S. Tarucha, L. M. K. Vandersypen, *Rev. Mod. Phys.* **2007**, *79*, 1217.
- [24] Y. Aharonov, D. Bohm, *Phys. Rev.* **1959**, *115*, 485.
- [25] S. Pedetti, S. Ithurria, H. Heuclin, G. Patriarche, B. Dubertret, *J. Am. Chem. Soc* **2014**, *136*, 16430.
- [26] A.O. Govorov, S.E. Ulloa, K. Karrai, R..J. Warburton, *Phys. Rev. B* **2002**, *66*, 081309.
- [27] I. R. Sellers, V. R. Whiteside, I. L. Kuskovsky, A. O. Govorov, B. D. McCombe, *Phys. Rev. Lett.* **2008**, *100*, 136405.
- [28] S. Ayari, M. T. Quick, N. Owschimikow, S. Christodoulou, G. H. V. Bertrand, M. Artemyev, I. Moreels, U. Woggon, S. Jaziri, A. W. Achtstein, *Nanoscale* **2020**, *12*, 14448.
- [29] D. F. Macias-Pinilla, J. Planelles, I. Mora-Seró, J. I. Climente, *J. Phys. Chem. C* **2021**, *125*, 15614.
- [30] D. J. Norris, A. L. Efros, S.C. Erwin, *Science* **2008**, *319*, 1776.
- [31] P. Guyot-Sionnest, *Mikrochim Acta* **2008**, *160*, 309.
- [32] S. Morozov, E. L. Pensa, A. H. Khan, A. Polovitsyn, E. Cortés, S. A. Maier, S. Vezzoli, I. Moreels, R. Sapienza, *Sci. Adv* **2020**, *6*, eabb1821.
- [33] E. P. A. M. Bakkers, Z. Hens, A. Zunger, A. Franceschetti, L. P. Kouwenhoven, L. Gurevich, D. Vanmaekelbergh, *Nano Lett.* **2001**, *1*, 551.
- [34] E. Drijvers, J. De Roo, J. C. Martins, I. Infante, Z. Hens, *Chem. Mater.* **2018**, *30*, 1178.
- [35] I. du Fossé, S. Lal, A. N. Hossaini, I. Infante, A. J. Houtepen, *J. Phys. Chem. C* **2021**, *125*, 23968.
- [36] M. Florescu, P. Hawrylak, *Phys. Rev. B* **2006**, *73*, 045304.
- [37] J. I. Climente, A. Bertoni, G. Goldoni, M. Rontani, E. Molinari, *Phys. Rev. B* **2007**, *75*, 081303.
- [38] J. Planelles, J.I. Climente, J.L. Movilla, Aharonov-Bohm effect for pedestrian, (Preprint) arXiv:cond-mat/0506691v1, v1, submitted: Jun **2005**.
- [39] A. Fuhrer, S. Lüscher, T. Ihn, T. Heinzel, K. Ensslin, W. Wegscheider, M. Bichler, *Nature* **2001**, *413*, 822.
- [40] M. Bayer, M. Korkusinski, P. Hawrylak, T. Gutbrod, M. Michel, A. Forchel, *Phys Rev Lett.* **2003**, *18*, 186801.
- [41] J. I. Climente, J. Planelles, and W. Jaskólski, *Phys. Rev. B* **2003**, *68*, 075307.
- [42] I. Fedin, D.V. Talapin, *J. Am. Chem. Soc.* **2016**, *138*, 9771.
- [43] B. B. V. Salzmann, J. F. Vliem, D. N. Maaskant, L. C. Post, C. Li, S. Bals, D. Vanmaekelbergh, *Chem. Mater.* **2021**, *33*, 6853.
- [44] J. Xiao, Y. Liu, V. Steinmetz, M. Çağlar, J. Mc Hugh, T. Baikie, N. Gauriot, M. Nguyen, E. Ruggeri, Z. Andaji-Garmaroudi, S. D. Stranks, L. Legrand, T. Barisien, R. H. Friend, N. C. Greenham, A. Rao, R. Pandya, *ACSNano* **2020**, *14*, 14740.
- [45] J. I. Climente, J. Planelles, and J. L. Movilla, *Phys. Rev. B* **2004**, *70*, 081301.

- [46] R. Scott, S. Kickhöfel, O. Schoeps, A. Antanovich, A. Prudnikau, A. Chuvin, U. Woggon, M. Artemyev, A. W. Achtstein, *Phys. Chem. Chem. Phys.* **2016**, *18*, 3197.
- [47] R. Pandya, V. Steinmetz, Y. Puttison, M. Dufour, W. M. Chen, R. Y. S. Chen, T. Barisien, A. Sharma, G. Lakhwani, A. Mitioglu, P. C. M. Christianen, L. Legrand, F. Bernardot, C. Testelin, A. W. Chin, S. Ithurria, M. Chamarro, A. Rao, *ACS Nano* **2019**, *13*, 10140.
- [48] J. I. Climente, J. Planelles, *Appl. Phys. Lett.* **2014**, *104*, 193101.
- [49] E.V. Shornikova, D.R. Yakovlev, L. Biadala, S.A. Crooker, V.V. Belykh, M.V. Kochiev, A. Kuntzmann, M. Nasilowski, B. Dubertret, M. Bayer, *Nano Lett.* **2020**, *20*, 1370.
- [50] F.V. Antolinez, F.T. Rabouw, A.A. Rossinelli, J. Cui, D.J. Norris, *Nano Lett.* **2019**, *19*, 8495.
- [51] J. Llusar, J.I. Climente, *ACS Photonics* **2020**, *7*, 3086.
- [52] R. Pandya, R. Y. S. Chen, A. Cheminal, M. Dufour, J. M. Richter, T. H. Thomas, S. Ahmed, A. Sadhanala, E. P. Booker, G. Divitini, F. Deschler, N. C. Greenham, S. Ithurria, A. Rao, *J. Am. Chem. Soc.* **2018**, *140*, 14097.
- [53] J. Llusar, J. Planelles, J. I. Climente, *J. Phys. Chem. C* **2019**, *123*, 21299.
- [54] J.L. Movilla, J. Planelles, J.I. Climente, *J. Phys. Chem. Lett.* **2020**, *11*, 3294.
- [55] J. Planelles and J. I. Climente, *J. Phys.: Condens. Matter*, **2013**, *25*, 485801.
- [56] A. Bertoni, CIttool, <https://github.com/andreabertoni/citool>, accessed: Oct, **2021**.
- [57] L. Jacak, P. Hawrylak, A. Wojs, *Quantum Dots*, Springer, **1998**.

## Table of Contents



Spin and orbital ground state transitions induced by moderate external magnetic fields. Left: a singlet-to-triplet spin reversal in a type-I nanoplatelet charged with two electrons. Right: an Aharonov-Bohm oscillation in an optically charged type-II nanoplatelet, switching the excitonic ground state from bright to dark.

# Chapter 3

## Conclusions

Metal chalcogenide colloidal NPLs are quasi-2D nanostructures with excellent synthetic control along out-of-plane and in-plane dimensions, a strong dielectric confinement, and the possibility of growing radially heterostructures. These features have converted these NPLs into a distinct nanostructure worthy of being studied. In this Ph.D. thesis, we have developed and employed theoretical models built on  $k \cdot p$  theory to investigate a variety of properties of interest in NPLs. The dependence of the electronic structure on several design parameters (dimensions, composition) and physical factors present in these systems (strain, impurities, dielectric mismatch, and external fields) has been analysed. We have provided interpretations for a number of spectroscopic observations in the literature and put forward predictions for further expansion of the functionalities.

In Chapter 2 § 2.1 we investigated the elastic properties in heterostructured NPLs. Specifically, we studied the internal strain that undergoes CdSe-based CS NPLs. We found that (i) strain influences CS NPLs up to 5 nm away from the edges of their finite lateral sides; (ii) the coupled strain-momentum terms provide a non-negligible energetic shift of a few tens of meV, in contrast with that seen in epitaxial quantum wells. This is ascribed to the extremely thin thickness present in NPLs; (iii) tunnelling is the primary source of PL redshift in CS NPLs upon shell growth [140], however, the energetic influence of strain can amplify or reduce this redshift; (iv) contrary to some hypothesis in experiments, [195] CdSe/ZnS remain type-I even in the presence of an asymmetric shell coating; (v) the usual redshift observed when coating CdSe NPLs with a CdS shell [140] can be reverted by growing yet another shell of ZnS. The compressive strain propagates throughout the entire NPL producing a net blueshift instead.

The above observations provide the first rationalization of the impact of lattice-mismatch strain on the electronic structure of hetero-NPLs. Having understood their role, one can envisage new architectures where strain becomes the dominant factor that affects excitonic properties. The ternary CdSe/CdS/ZnS is one



such case. Ternary structures have actually started to attract attention in recent years. [196, 197]

In Chapters 2, §§ 2.2 to 2.4 we explored how a variety of electrostatic phenomena affect the optical properties and electronic structure of NPLs.

In § 2.2, we analysed from a theoretical perspective the possible role of SU processes in determining the homogeneous linewidth of CS NPLs, as suggested by recent photoluminescence experiments, showing multi-peaked PL spectra of individual NPLs at low temperature. [160, 163] We verified that NPLs indeed gather the conditions that maximize the likelihood of these processes, where the intensity can be 1 order of magnitude higher than in epitaxial quantum wells. [198] That is, they present, in CdSe CO NPLs and in CdSe/CdS CS NPLs, a SU peak with an oscillator strengths of  $0.3\times$  and  $0.1\times$ , respectively, that of the band-edge transition. This confirms that the satellite peak observed in CdSe NPLs [160] can be ascribed to SU processes. Nevertheless, SU processes are expected to vanish rapidly upon shell growth because Coulomb interactions eventually become quenched. This occurs because carriers are placed far from the organic medium in growing a shell, and thus this yields a weak dielectric confinement. Then, this renders the interpretation of reference [163] unlikely to explain the multi-peaked spectra they observe. We propose an alternative interpretation in which the different peaks arise from states with different spins. This implies that spin selection rules forbid phonon-mediated decay in NPLs, hence enabling emission from metastable states.

In § 2.3, it is shown that in type-II colloidal NPLs the number of confined carriers can be used as a realistic degree of freedom to control their electronic structure and modulate their optics. Coulomb repulsions, which are usually overlooked because most studies are focused on neutral excitons ( $X^0$ ) and the weak lateral confinement present in NPLs, result more relevant than attractions. By proper conjugation of Coulomb repulsions (through the number of carriers injected electrochemically), the emission spectrum experiences chromic shifts over 100 meV, which is well above those attained with lateral confinement. Moreover, through appropriate control of the core/crown dimensions, the biexciton binding energies can be modulated from non-binding ( $\sim 5$  meV blueshift) to strongly anti-binding ( $\sim 40$  meV). This implies that type-II NPLs offer the same spectral tunability as strongly confined quantum dots [129], while keeping the natural advantages of quasi-2D systems.

In § 2.4, we extended the study on the effect of Coulomb repulsions to type-I NPLs. Here, we focused on the (hitherto unexplored) case of few-interacting fermions (electrons or holes). We observed that the combination of weak lateral confinement and strong dielectric confinement leads to the strongest electronic correlations reported in colloidal nanocrystals. A number of non-trivial physical effects follow, such as: (i) violations of the Aufbau principle when filling spin-

orbital shells with electrons or holes; (ii) addition energies over 30 meV - in spite of the weak lateral confinement - which imply it is feasible to charge NPLs carrier by carrier even at room temperature; and (iii) thermal occupation of high-spin states, enabled by strong Coulomb exchange energies (20 – 35 meV), which lead to paramagnetic behaviour readily from cryogenic temperatures.

Then, from §§ 2.2 to 2.4 it is concluded that electrostatic interactions, play a key role in tuning emission energy lines, intensity peaks, oscillator strength, or linewidth broadening of carriers confined in NPLs.

In Chapter 2 § 2.5, we investigated whether the application of external magnetic fields is susceptible to inducing ground state transitions in NPLs. Reversible field-induced transitions have been studied in different semiconductor nanostructures [5, 199, 200, 201, 202, 203], but the application in colloidal nanocrystals has been hindered by strong confinement, which generally leads to large inter-level spacings. Here, we show that the situation is different in NPLs due to weak lateral confinement and strong exchange interactions. Two strategies were proposed to illustrate this fact: (i) The ground state spin can be switched from low to high angular momentum in few-electron systems under axial magnetic fields. This is because the (Coulomb exchange-induced) proximity of high- and low-spin states can be overcome by the Zeeman splitting; (ii) in type-II CC NPLs one can take advantage of the AB effect that experience those carriers confined in the crown. It is shown how both excitons and negative trions exhibit AB oscillations. The former gives rise to the optical AB effect, whereby the exciton ground state switches sharply from bright to dark through orbital selection rules, while the latter, because of electron-electron correlations, leads to a softened optical AB effect.

Thus, NPLs under the effect of an external magnetic field could provide promising features by combining the possibility of growing heterostructures laterally with the strong Coulomb interactions present in many-body systems.

In conclusion, in this Ph.D. project it has been found that the extreme dielectric confinement is a dominating physical factor, which enhances both attractive and repulsive Coulomb interactions to a level rarely seen in all-solid systems. In combination with strain and external fields, it provides interpretations for several optical phenomena reported in the literature. The knowledge gained on the electronic structure allowed us to propose new paradigms to further exploit NPL functionalities.

# Bibliography

- [1] A. I. Ekimov and A. A. Onushchenko. Quantum Size Effect in Three-Dimensional Microscopic Semiconductor Crystals. *SPIE Milestone Series*, 180:3–5, 2005.
- [2] S. Link and M. A. El-Sayed. Size and Temperature Dependence of the Plasmon Absorption of Colloidal Gold Nanoparticles. *J. Phys. Chem. B*, 103(21):4212–4217, 1999.
- [3] A. L. Efros. Interband Absorption of Light in Semiconductor Sphere. *Sov. Phys. Semicond.*, 16:772, 1982.
- [4] L. Brus. Electronic Wave Functions in Semiconductor Clusters: Experiment and Theory. *J. Phys. Chem.*, 90(12):2555–2560, 1986.
- [5] T. Chakraborty. *Quantum Dots: A Survey of the Properties of Artificial Atoms*. Elsevier Science, 1999.
- [6] Y. Yin and A. Alivisatos. Colloidal Nanocrystal Synthesis and the Organic–Inorganic Interface. *Nature*, 437:664–670, 2005.
- [7] A. Pimpale. Excitonic Radiative Recombination of Electrons and Holes in Semiconductors. *J. Opt. Soc. Am. B*, 3(1):36–40, Jan 1986.
- [8] A. P. Alivisatos. Perspectives on the Physical Chemistry of Semiconductor Nanocrystals. *J. Phys. Chem.*, 100(31):13226–13239, 1996.
- [9] E. Groeneveld, C. Delerue, G. Allan, Y.-M. Niquet, and C. de Mello Donegá. Size Dependence of the Exciton Transitions in Colloidal CdTe Quantum Dots. *J. Phys. Chem. C*, 116(43):23160–23167, 2012.
- [10] R. Koole, E. Groeneveld, D. Vanmaekelbergh, A. Meijerink, and C. de Mello Donegá. *Size Effects on Semiconductor Nanoparticles*. Springer, 2014.
- [11] G. Bastard. *Wave Mechanics Applied to Semiconductor Heterostructures*. Monographies de physique. Wiley, 1988.

- [12] A. L. Efros and L. E. Brus. Nanocrystal Quantum Dots: From Discovery to Modern Development. *ACS Nano*, 15(4):6192–6210, 2021. PMID: 33830732.
- [13] M. Nasilowski, B. Mahler, E. Lhuillier, S. Ithurria, and B. Dubertret. Two-Dimensional Colloidal Nanocrystals. *Chem. Rev.*, 116(18):10934–10982, 2016. PMID: 27434678.
- [14] F. T. Rabouw and C. de Mello Donegá. Excited-State Dynamics in Colloidal Semiconductor Nanocrystals. *Top. Curr. Chem.*, 374:58, 2016.
- [15] C. Galland, S. Brovelli, W. K. Bae, L. A. Padilha, F. Meinardi, and V. I. Klimov. Dynamic Hole Blockade Yields Two-Color Quantum and Classical Light from Dot-in-Bulk Nanocrystals. *Nano Lett.*, 13(1):321–328, 2013. PMID: 23252581.
- [16] I. Tanghe, J. Llusar, I. Climente J, A. Barker, G. Paternò, F. Scotognella, A. Polovitsyn, A. H. Khan, Z. Hens, D. Van Thourhout, P. Geiregat, and I. Moreels. Role of Thermally Occupied Hole States in Room-Temperature Broadband Gain in CdSe/CdS Giant-Shell Nanocrystals. *ACS Photonics*, X:XX, 2022.
- [17] Y. Shi, H. Li, and L.-J. Li. Recent Advances in Controlled Synthesis of Two-Dimensional Transition Metal Dichalcogenides via Vapour Deposition Techniques. *Chem. Soc. Rev.*, 44:2744–2756, 2015.
- [18] M. de la Mata, X. Zhou, F. Furtmayr, J. Teubert, S. Gradečak, M. Eickhoff, A. Fontcuberta i Morral, and J. Arbiol. A Review of MBE Grown 0D, 1D and 2D Quantum Structures in a Nanowire. *J. Mater. Chem. C*, 1:4300–4312, 2013.
- [19] C. Tabor, W. Qian, and M. A. El-Sayed. Dependence of the Threshold Energy of Femtosecond Laser Ejection of Gold Nanoprisms from Quartz Substrates on the Nanoparticle Environment. *J. Phys. Chem. C*, 111(25):8934–8941, 2007.
- [20] J. Chen, Q. Ma, X.-J. Wu, L. Li, J. Liu, and H. Zhang. Wet-Chemical Synthesis and Applications of Semiconductor Nanomaterial-Based Epitaxial Heterostructures. *Nano-Micro Lett.*, 11(86):2150–5551, 2019.
- [21] Z. M. Wang. *Self-Assembled Quantum Dots*, volume 1. Springer Science & Business Media, 2007.
- [22] D. Bimberg, M. Grundmann, and N. N. Ledentsov. *Quantum Dot Heterostructures*. John Wiley & Sons, 1999.
- [23] L. E. Brus, Al. L. Efros, and T. Itoh. The Spectroscopy of Isolated and Assembled Semiconductor Nanocrystals. *J. Lumin.*, 70:1–484, 1996.

- [24] A. L. Rogach. *Semiconductor Nanocrystal Quantum Dots*. Springer, 2008.
- [25] V. I. Klimov. *Nanocrystal Quantum Dots*. CRC press, 2017.
- [26] M. Bayer. Bridging Two Worlds: Colloidal versus Epitaxial Quantum Dots. *Ann. Phys.*, 531(6):1900039, 2019.
- [27] Y. Shirasaki, G. J. Supran, M. G. Bawendi, and V. Bulović. Emergence of Colloidal Quantum-Dot Light-Emitting Technologies. *Nat. Photonics*, 7:13–23, 2013.
- [28] A. M. Smith and S. Nie. Semiconductor Nanocrystals: Structure, Properties, and Band Gap Engineering. *Acc. Chem. Res.*, 43(2):190–200, 2010. PMID: 19827808.
- [29] C. B. Murray, D. J. Norris, and M. G. Bawendi. Synthesis and Characterization of Nearly Monodisperse CdE (E = Sulfur, Selenium, Tellurium) Semiconductor Nanocrystallites. *J. Am. Chem. Soc.*, 115(19):8706–8715, 1993.
- [30] I. Ramiro, O. Özdemir, S. Christodoulou, S. Gupta, M. Dalmases, I. Torre, and G. Konstantatos. Mid- and Long-Wave Infrared Optoelectronics via Intraband Transitions in PbS Colloidal Quantum Dots. *Nano Lett.*, 20(2):1003–1008, 2020. PMID: 31934762.
- [31] S. Y. Bang, Y.-H. Suh, X.-B. Fan, D.-W. Shin, S. Lee, H. W. Choi, T. H. Lee, J. Yang, S. Zhan, W. Harden-Charters, C. Samarakoon, L. G. Occhipinti, S. D. Han, S.-M. Jung, and J. M. Kim. Technology Progress on Quantum Dot Light-Emitting Diodes for Next-Generation Displays. *Nanoscale Horiz.*, 6:68–77, 2021.
- [32] Z. Luo, J. Manders, and J. Yurek. Television’s Quantum Dots Will Be the Next Darling of TV Manufacturers. *IEEE Spectr.*, 55(3):28–53, 2018.
- [33] F. Baletto and R. Ferrando. Structural Properties of Nanoclusters: Energetic, Thermodynamic, and Kinetic Effects. *Rev. Mod. Phys.*, 77:371–423, May 2005.
- [34] C. de Mello Donegá. Synthesis and Properties of Colloidal Heteronanocrystals. *Chem. Soc. Rev.*, 40:1512–1546, 2011.
- [35] M. A. Boles, D. Ling, T. Hyeon, and D. V. Talapin. The Surface Science of Nanocrystals. *Nat. Mater.*, 15:141–153, 2016.
- [36] S. J. Lim, A. Schleife, and A. M. Smith. Optical Determination of Crystal Phase in Semiconductor Nanocrystals. *Nat. Commun.*, 8:14849, 2017.

- [37] Z. A. Peng and X. Peng. Nearly Monodisperse and Shape-Controlled CdSe Nanocrystals via Alternative Routes: Nucleation and Growth. *J. Am. Chem. Soc.*, 124(13):3343–3353, 2002. PMID: 11916419.
- [38] S. Kumar and T. Nann. Shape Control of II-VI Semiconductor Nanomaterials. *Small*, 2(3):316–329, 2013.
- [39] C. Xia, N. Winckelmans, P. T. Prins, S. Bals, H. C. Gerritsen, and C. de Mello Donegá. Near-Infrared-Emitting CuInS<sub>2</sub>/ZnS Dot-in-Rod Colloidal Heteronanorods by Seeded Growth. *J. Am. Chem. Soc.*, 140(17):5755–5763, 2018. PMID: 29569443.
- [40] C. Bouet, B. Mahler, B. Nadal, B. Abecassis, M. D. Tessier, S. Ithurria, X. Xu, and B. Dubertret. Two-Dimensional Growth of CdSe Nanocrystals, from Nanoplatelets to Nanosheets. *Chem. Mater.*, 25(4):639–645, 2013.
- [41] E. Lhuillier, S. Pedetti, S. Ithurria, B. Nadal, H. Heuclin, and B. Dubertret. Two-Dimensional Colloidal Metal Chalcogenides Semiconductors: Synthesis, Spectroscopy, and Applications. *Acc. Chem. Res.*, 48(1):22–30, 2015. PMID: 25554861.
- [42] M. J. Kelly and R. J. Nicholas. The Physics of Quantum Well Structures. *Rep. Prog. Phys.*, 48(12):1699–1741, dec 1985.
- [43] G. H. V. Bertrand, A. Polovitsyn, S. Christodoulou, A. H. Khan, and I. Moreels. Shape Control of Zincblende CdSe Nanoplatelets. *Chem. Commun.*, 52:11975–11978, 2016.
- [44] B. T. Diroll. Colloidal Quantum Wells for Optoelectronic Devices. *J. Mater. Chem. C*, 8:10628–10640, 2020.
- [45] S. Ithurria, M. D. Tessier, B. Mahler, R. P. S. M. Lobo, B. Dubertret, and Al. L. Efros. Colloidal Nanoplatelets With Two-Dimensional Electronic Structure. *Nat. Mater.*, 10:936–941, 2011.
- [46] N. Peric, Y. Lambert, S. Singh, A. H. Khan, V. Franchina, A. Nathali, D. Deresmes, M. Berthe, Z. Hens, I. Moreels, C. Delerue, B. Grandidier, and L. Biadala. Van Hove Singularities and Trap States in Two-Dimensional CdSe Nanoplatelets. *Nano Lett.*, 21(4):1702–1708, 2021. PMID: 33544602.
- [47] F. Rajadell, J. I. Climente, and J. Planelles. Excitons in Core-Only, Core-Shell and Core-Crown CdSe Nanoplatelets: Interplay Between In-Plane Electron-Hole Correlation, Spatial Confinement, and Dielectric Confinement. *Phys. Rev. B*, 96:035307, Jul 2017.
- [48] J. Q. Grim, S. Christodoulou, F. Di Stasio, R. Krahne, R. Cingolani, L. Manna, and I. Moreels. Continuous-Wave Biexciton Lasing at Room Temperature Using Solution-Processed Quantum Wells. *Nat. Nanotechnol.*, 9:891–895, 2014.

- [49] R. Benchamekh, N. A. Gippius, J. Even, M. O. Nestoklon, J.-M. Jancu, S. Ithurria, B. Dubertret, Al. L. Efros, and P. Voisin. Tight-Binding Calculations of Image-Charge Effects in Colloidal Nanoscale Platelets of CdSe. *Phys. Rev. B*, 89:035307, Jan 2014.
- [50] M. D. Tessier, P. Spinicelli, D. Dupont, G. Patriarche, S. Ithurria, and B. Dubertret. Efficient Exciton Concentrators Built from Colloidal Core/Crown CdSe/CdS Semiconductor Nanoplatelets. *Nano Lett.*, 14(1):207–213, 2014. PMID: 24328730.
- [51] A. Prudnikau, A. Chuvilin, and M. Artemyev. CdSe–CdS Nanoheteroplatelets with Efficient Photoexcitation of Central CdSe Region through Epitaxially Grown CdS Wings. *J. Am. Chem. Soc.*, 135(39):14476–14479, 2013. PMID: 24047284.
- [52] S. Pedetti, S. Ithurria, H. Heuclin, G. Patriarche, and B. Dubertret. Type-II CdSe/CdTe Core/Crown Semiconductor Nanoplatelets. *J. Am. Chem. Soc.*, 136(46):16430–16438, 2014. PMID: 25338215.
- [53] Y. Kelestemur, M. Olutas, S. Delikanli, B. Guzelturk, M. Z. Akgul, and H. V. Demir. Type-II Colloidal Quantum Wells: CdSe/CdTe Core/Crown Heteronanoplatelets. *J. Phys. Chem. C*, 119(4):2177–2185, 2015.
- [54] S. Ithurria, G. Bousquet, and B. Dubertret. Continuous Transition from 3D to 1D Confinement Observed during the Formation of CdSe Nanoplatelets. *J. Am. Chem. Soc.*, 133(9):3070–3077, 2011. PMID: 21323349.
- [55] M. D. Tessier, C. Javaux, I. Maksimovic, V. Loriette, and B. Dubertret. Spectroscopy of Single CdSe Nanoplatelets. *ACS Nano*, 6(8):6751–6758, 2012. PMID: 22783952.
- [56] C. E. Rowland, I. Fedin, H. Zhang, S. K. Gray, A. O. Govorov, D. V. Talapin, and R. D. Schaller. Picosecond Energy Transfer and Multiexciton Transfer Outpaces Auger Recombination in Binary CdSe Nanoplatelet Solids. *Nat. Mater.*, 14:484–489, 2015.
- [57] S. A. Crooker, J. A. Hollingsworth, S. Tretiak, and V. I. Klimov. Spectrally Resolved Dynamics of Energy Transfer in Quantum-Dot Assemblies: Towards Engineered Energy Flows in Artificial Materials. *Phys. Rev. Lett.*, 89:186802, Oct 2002.
- [58] J. Llusar. Chemistry in Two-Dimensional World, 2017.
- [59] J. Planelles, A. W. Achtstein, R. Scott, N. Owschimikow, U. Woggon, and J. I. Climente. Tuning Intraband and Interband Transition Rates via Excitonic Correlation in Low-Dimensional Semiconductors. *ACS Photonics*, 5(9):3680–3688, 2018.

- [60] P. Geiregat, C. Rodá, I. Tanghe, S. Singh, A. O. Govorov, A. Di Giacomo, D. Lebrun, G. Grimaldi, J. Maes, D. Van Thourhout, I. Moreels, A. J. Houtepen, and Z. Hens. Localization-Limited Exciton Oscillator Strength in Colloidal CdSe Nanoplatelets Revealed by the Optically Induced Stark Effect. *Light Sci. Appl.*, 10:112, 2021.
- [61] M. Pelton. Carrier Dynamics, Optical Gain, and Lasing with Colloidal Quantum Wells. *J. Phys. Chem. C*, 122(20):10659–10674, 2018.
- [62] C. She, I. Fedin, D. S. Dolzhenkov, A. Demortière, R. D. Schaller, M. Pelton, and D. V. Talapin. Low-Threshold Stimulated Emission Using Colloidal Quantum Wells. *Nano Lett.*, 14(5):2772–2777, 2014. PMID: 24773282.
- [63] B. Guzelturk, Y. Kelestemur, M. Olutas, S. Delikanli, and H. V. Demir. Amplified Spontaneous Emission and Lasing in Colloidal Nanoplatelets. *ACS Nano*, 8(7):6599–6605, 2014. PMID: 24882737.
- [64] S. Ithurria and B. Dubertret. Quasi 2D Colloidal CdSe Platelets With Thicknesses Controlled at the Atomic Level. *J. Am. Chem. Soc.*, 130(49):16504–16505, 2008.
- [65] P. Reiss, M. Protiere, and L. Li. Core/Shell Semiconductor Nanocrystals. *Small*, 5(2):154–168, 2009.
- [66] S. Yadav, A. Singh, L. Thulasidharan, and S. Sapra. Surface Decides the Photoluminescence of Colloidal CdSe Nanoplatelets Based Core/Shell Heterostructures. *J. Phys. Chem. C*, 122(1):820–829, 2018.
- [67] E. Lhuillier, S. Pedetti, S. Ithurria, H. Heuclin, B. Nadal, A. Robin, G. Patriarche, N. Lequeux, and B. Dubertret. Electrolyte-Gated Field Effect Transistor to Probe the Surface Defects and Morphology in Films of Thick CdSe Colloidal Nanoplatelets. *ACS Nano*, 8(4):3813–3820, 2014. PMID: 24601578.
- [68] B. Mahler, B. Nadal, C. Bouet, G. Patriarche, and B. Dubertret. Core/Shell Colloidal Semiconductor Nanoplatelets. *J. Am. Chem. Soc.*, 134(45):18591–18598, 2012.
- [69] M. A. Hines and P. Guyot-Sionnest. Synthesis and Characterization of Strongly Luminescing ZnS-Capped CdSe Nanocrystals. *J. Phys. Chem.*, 100(2):468–471, 1996.
- [70] B. O Dabbousi, J. Rodriguez-Viejo, F. V. Mikulec, J. R. Heine, H. Mattoussi, R. Ober, K. F. Jensen, and M. G. Bawendi. (CdSe) ZnS Core-Shell Quantum Dots: Synthesis and Characterization of a Size Series of Highly Luminescent Nanocrystallites. *J. Phys. Chem. B*, 101(46):9463–9475, 1997.



- [71] X. Peng, M. C. Schlamp, A. V. Kadavanich, and A. P. Alivisatos. Epitaxial Growth of Highly Luminescent CdSe/CdS Core/Shell Nanocrystals With Photostability and Electronic Accessibility. *J. Am. Chem. Soc.*, 119(30):7019–7029, 1997.
- [72] J. McBride, J. Treadway, L. C. Feldman, S. J. Pennycook, and S. J. Rosenthal. Epitaxial Growth of Highly Luminescent CdSe/CdS Core/Shell Nanocrystals With Photostability and Electronic Accessibility. *Nano Lett.*, 6(7):1496–1501, 2006.
- [73] M. Achermann, M. A. Petruska, S. A. Crooker, and V. I. Klimov. Picosecond Energy Transfer in Quantum Dot Langmuir–Blodgett Nanoassemblies. *J. Phys. Chem. B*, 107(50):13782–13787, 2003.
- [74] T. Franzl, D. S. Koktysh, T. A. Klar, A. L. Rogach, and J. Feldmann. Fast Energy Transfer in Layer-By-Layer Assembled CdTe Nanocrystal Bilayers. *Appl. Phys. Lett.*, 84:2904, 2004.
- [75] C. de Mello Donegá and R. Koole. Size Dependence of the Spontaneous Emission Rate and Absorption Cross Section of CdSe and CdTe Quantum Dots. *J. Phys. Chem. C*, 113(16):6511–6520, 2009.
- [76] H. Jeong and S. K. Shin. Optical Properties of Colloidal Semiconductor Quantum Dots in Dielectric Media: A Natural Potential Well Approach. *Chem. Phys. Lett.*, 692:333–339, 2018.
- [77] A. Brumberg, S. M. Harvey, J. P. Philbin, B. T. Diroll, B. Lee, S. A. Crooker, M. R. Wasielewski, E. Rabani, and R. D. Schaller. Determination of the In-Plane Exciton Radius in 2D CdSe Nanoplatelets via Magneto-Optical Spectroscopy. *ACS Nano*, 13(8):8589–8596, 2019. PMID: 31251582.
- [78] J. Shumway, A. Franceschetti, and A. Zunger. Correlation Versus Mean-Field Contributions to Excitons, Multiexcitons, and Charging Energies in Semiconductor Quantum Dots. *Phys. Rev. B*, 63:155316, Mar 2001.
- [79] Q. Li and T. Lian. Exciton Spatial Coherence and Optical Gain in Colloidal Two-Dimensional Cadmium Chalcogenide Nanoplatelets. *Acc. Chem. Res.*, 52(9):2684–2693, 2019. PMID: 31433164.
- [80] A. W. Achtstein, A. Schliwa, A. Prudnikau, M. Hardzei, M. V. Artemyev, C. Thomsen, and U. Woggon. Electronic Structure and Exciton–Phonon Interaction in Two-Dimensional Colloidal CdSe Nanosheets. *Nano Lett.*, 12(6):3151–3157, 2012. PMID: 22625408.
- [81] M. Achermann, J. A. Hollingsworth, and V. I. Klimov. Multiexcitons Confined Within a Subexcitonic Volume: Spectroscopic and Dynamical Signatures of Neutral and Charged Biexcitons in Ultrasmall Semiconductor Nanocrystals. *Phys. Rev. B*, 68:245302, Dec 2003.

- [82] B. Patton, W. Langbein, and U. Woggon. Trion, Biexciton, and Exciton Dynamics in Single Self-Assembled CdSe Quantum Dots. *Phys. Rev. B*, 68:125316, Sep 2003.
- [83] S. M. Kim, H. S. Yang, M. G. Ha, E. D. Jeong, and K. S. Hong. Quantum Yields and Time-Resolved Spectroscopy in CdSe and CdSe/ZnS Nanocrystals. *J. Korean Phys. Soc.*, 56(12):467–471, 2010.
- [84] M. Califano, A. Franceschetti, and A. Zunger. Temperature Dependence of Excitonic Radiative Decay in CdSe Quantum Dots: The Role of Surface Hole Traps. *Nano Lett.*, 5(12):2360–2364, 2005.
- [85] K. Gong, Y. Zeng, and D. F. Kelley. Extinction Coefficients, Oscillator Strengths, and Radiative Lifetimes of CdSe, CdTe, and CdTe/CdSe Nanocrystals. *J. Phys. Chem. C*, 117(39):20268–20279, 2013.
- [86] C. A. Leatherdale, W.-K. Woo, F. V. Mikulec, and M. G. Bawendi. On the Absorption Cross Section of CdSe Nanocrystal Quantum Dots. *J. Phys. Chem. B*, 106(31):7619–7622, 2002.
- [87] A. Yeltik, S. Delikanli, M. Olutas, Y. Kelestemur, B. Guzelturk, and H. V. Demir. Experimental Determination of the Absorption Cross-Section and Molar Extinction Coefficient of Colloidal CdSe Nanoplatelets. *J. Phys. Chem. C*, 119(47):26768–26775, 2015.
- [88] A. A. Mikhailovsky, A. V. Malko, J. A. Hollingsworth, M. G. Bawendi, and V. I. Klimov. Multiparticle Interactions and Stimulated Emission in Chemically Synthesized Quantum Dots. *Appl. Phys. Lett.*, 80(13):2380–2382, 2002.
- [89] M. D. Tessier, B. Mahler, B. Nadal, H. Heuclin, S. Pedetti, and B. Dubertret. Spectroscopy of Colloidal Semiconductor Core/Shell Nanoplatelets With High Quantum Yield. *Nano Lett.*, 13(7):3321–3328, 2013.
- [90] S. Ithurria and D. V. Talapin. Colloidal Atomic Layer Deposition (c-ALD) using Self-Limiting Reactions at Nanocrystal Surface Coupled to Phase Transfer between Polar and Nonpolar Media. *J. Am. Chem. Soc.*, 134(45):18585–18590, 2012. PMID: 23061923.
- [91] M. Sharma, S. Delikanli, and H. V. Demir. Two-Dimensional CdSe-Based Nanoplatelets: Their Heterostructures, Doping, Photophysical Properties, and Applications. *Proc. IEEE*, 108(5):655–675, 2019.
- [92] V. Steinmetz, J. I. Climente, R. Pandya, J. Planelles, F. Margailan, Y. Puttisong, M. Dufour, S. Ithurria, A. Sharma, G. Lakhwani, L. Legrand, F. Bernardot, C. Testelin, M. Chamarro, A. W. Chin, A. Rao, and T. Barisien. Emission State Structure and Linewidth Broadening

- Mechanisms in Type-II CdSe/CdTe Core-Crown Nanoplatelets: A Combined Theoretical–Single Nanocrystal Optical Study. *J. Phys. Chem. C*, 124(31):17352–17363, 2020.
- [93] D. V. Talapin, J.-S. Lee, M. V. Kovalenko, and E. V. Shevchenko. Prospects of Colloidal Nanocrystals for Electronic and Optoelectronic Applications. *Chem. Rev.*, 110(1):389–458, 2010.
- [94] Y. Altintas, U. Quliyeva, K. Gungor, O. Erdem, Y. Kelestemur, E. Mutlugun, M. V. Kovalenko, and H. V. Demir. Highly Stable, Near-Unity Efficiency Atomically Flat Semiconductor Nanocrystals of CdSe/ZnS Hetero-Nanoplatelets Enabled by ZnS-Shell Hot-Injection Growth. *Small*, 15(8):1804854, 2019.
- [95] A. A. Rossinelli, A. Riedinger, P. Marqués-Gallego, P. N. Knüsel, F. V. Antolinez, and D. J. Norris. High-Temperature Growth of Thick-Shell CdSe/CdS Core/Shell Nanoplatelets. *Chem. Comm.*, 53(71):9938–9941, 2017.
- [96] M. İzmir, A. Sharma, S. Shendre, E. G. Durmusoglu, V. K. Sharma, F. Shabani, H. D. Baruj, S. Delikanli, M. Sharma, and H. V. Demir. Blue-Emitting CdSe Nanoplatelets Enabled by Sulfur-Alloyed Heterostructures for Light-Emitting Diodes with Low Turn-On Voltage. *ACS Appl. Nano Mater.*, 2021.
- [97] S.-H. Wei and A. Zunger. Calculated Natural Band Offsets of All II–VI and III–V Semiconductors: Chemical Trends and the Role of Cation d Orbitals. *Appl. Phys. Lett.*, 72(16):2011–2013, 1998.
- [98] A. V. Antanovich, A. V. Prudnikau, D. Melnikau, Y. P. Rakovich, A. Chuvilin, U. Woggon, A. W. Achtstein, and M. V. Artemyev. Colloidal Synthesis and Optical Properties of Type-II CdSe–CdTe and Inverted CdTe–CdSe Core–Wing Heteronanoplatelets. *Nanoscale*, 7(17):8084–8092, 2015.
- [99] Y. Kelestemur, Y. Shynkarenko, M. Anni, S. Yakunin, M. L. De Giorgi, and M. V. Kovalenko. Colloidal CdSe Quantum Wells with Graded Shell Composition for Low-Threshold Amplified Spontaneous Emission and Highly Efficient Electroluminescence. *ACS Nano*, 13(12):13899–13909, 2019.
- [100] R. Scott, J. Heckmann, A. V. Prudnikau, A. Antanovich, A. Mikhailov, N. Owschimikow, M. Artemyev, J. I. Climente, U. Woggon, N. B. Grosse, and A. W. Achtstein. Directed Emission of CdSe Nanoplatelets Originating From Strongly Anisotropic 2D Electronic Structure. *Nat. Nanotechnol.*, 12(12):1155–1160, 2017.
- [101] M. Lorenzon, S. Christodoulou, G. Vaccaro, J. Pedrini, F. Meinardi, I. Moreels, and S. Brovelli. Reversed Oxygen Sensing Using Colloidal Quan-

- tum Wells Towards Highly Emissive Photoresponsive Varnishes. *Nat. Commun.*, 6(1):1–9, 2015.
- [102] B. Jin, P. Huang, Q. Zhang, X. Zhou, X. Zhang, L. Li, J. Su, H. Li, and T. Zhai. Self-Limited Epitaxial Growth of Ultrathin Nonlayered CdS Flakes for High-Performance Photodetectors. *Adv. Funct. Mater.*, 28(20):1800181, 2018.
- [103] X. Wang, X. He, H. Zhu, L. Sun, W. Fu, X. Wang, L. C. Hoong, H. Wang, Q. Zeng, W. Zhao, J. Wei, Z. Jin, Z. Shen, J. Liu, T. Zhang, and Z. Liu. Subatomic Deformation Driven by Vertical Piezoelectricity From CdS Ultrathin Films. *Sci. Adv.*, 2(7):e1600209, 2016.
- [104] J. Even, L. Pedesseau, and M. Kepenekian. Electronic Surface States and Dielectric Self-Energy Profiles in Colloidal Nanoscale Platelets of CdSe. *Phys. Chem. Chem. Phys.*, 16(45):25182–25190, 2014.
- [105] Y. Zhang, H. Zhang, D. Chen, C.-J. Sun, Y. Ren, J. Jiang, L. Wang, Z. Li, and X. Peng. Engineering of Exciton Spatial Distribution in CdS Nanoplatelets. *Nano Lett.*, 21(12):5201–5208, 2021.
- [106] I. B. Amara, H. Boustanji, and S. Jaziri. Tuning Optoelectronic Response of Lateral Core-Alloyed Crown Nanoplatelets: Type-II CdSe–CdSe<sub>1-x</sub>Te<sub>x</sub>. *J. Condens. Matter Phys.*, 33(46):465301, 2021.
- [107] K. A. Nguyen, R. Pachter, and P. N. Day. Theoretical Analysis of Structures and Electronic Spectra of Molecular Colloidal Cadmium Sulfide Clusters and Nanoplatelets. *J. Chem. Phys.*, 155(9):094302, 2021.
- [108] A. Szemjonov, T. Pauporté, S. Ithurria, N. Lequeux, B. Dubertret, I. Ciofini, and F. Labat. Ligand-Stabilized CdSe Nanoplatelet Hybrid Structures With Tailored Geometric and Electronic Properties. New Insights From Theory. *RSC Adv.*, 4(99):55980–55989, 2014.
- [109] Q. Zhou, Y. Cho, S. Yang, E. A. Weiss, T. C. Berkelbach, and P. Darancet. Large Band Edge Tunability in Colloidal Nanoplatelets. *Nano Lett.*, 19(10):7124–7129, 2019.
- [110] A. R. Greenwood, S. Mazzotti, D. J. Norris, and G. Galli. Determining the Structure–Property Relationships of Quasi-Two-Dimensional Semiconductor Nanoplatelets. *J. Phys. Chem. C*, 125(8):4820–4827, 2021.
- [111] P. Yu and M. Cardona. *Fundamentals of Semiconductors: Physics and Materials Properties*. Springer Science & Business Media, 2010.
- [112] S. Bose, Z. Song, W. J. Fan, and D. H. Zhang. Effect of Lateral Size and Thickness on the Electronic Structure and Optical Properties of Quasi Two-Dimensional CdSe and CdS Nanoplatelets. *J. Appl. Phys.*, 119(14):143107, 2016.

- [113] S. Bose, S. Shendre, Z. Song, V. K. Sharma, D. H. Zhang, C. Dang, W. Fan, and H. V. Demir. Temperature-Dependent Optoelectronic Properties of Quasi-2D Colloidal Cadmium Selenide Nanoplatelets. *Nanoscale*, 9(19):6595–6605, 2017.
- [114] J. F. Specht, R. Scott, M. C. Castro, S. Christodoulou, G. H. V. Bertrand, A. V. Prudnikau, A. Antanovich, L. D. A. Siebbeles, N. Owschimikow, I. Moreels, M. Artemyev, U. Woggon, A. W. Achtstein, and M. Richter. Size-Dependent Exciton Substructure in CdSe Nanoplatelets and Its Relation to Photoluminescence Dynamics. *Nanoscale*, 11(25):12230–12241, 2019.
- [115] R. B. Vasiliev, A. I. Lebedev, E. P. Lazareva, N. N. Shlenskaya, V. B. Zaytsev, A. G. Vitukhnovsky, Y. Yao, and K. Sakoda. High-Energy Exciton Transitions in Quasi-Two-Dimensional Cadmium Chalcogenide Nanoplatelets. *Phys. Rev. B*, 95(16):165414, 2017.
- [116] S. Ayari, M. T. Quick, N. Owschimikow, S. Christodoulou, G. H. V. Bertrand, M. Artemyev, I. Moreels, U. Woggon, S. Jaziri, and A. W. Achtstein. Tuning Trion Binding Energy and Oscillator Strength in a Laterally Finite 2D System: CdSe Nanoplatelets as a Model System for Trion Properties. *Nanoscale*, 12(27):14448–14458, 2020.
- [117] J. Planelles and J. I. Climente. A Simple Variational Quantum Monte Carlo-Effective Mass Approach for Excitons and Trions in Quantum Dots. *Comput. Phys. Commun.*, 261:107782, 2021.
- [118] F. Bloch. Über die Quantenmechanik der Elektronen in Kristallgittern. *Z. Phys*, 52(7):555–600, 1929.
- [119] S. Tomić and N. Vukmirović. Quantum dots. *Handbook of Optoelectronic Device Modeling and Simulation*, pages 419–448, 2017.
- [120] S. Bandyopadhyay. *Physics of Nanostructured Solid State Devices*. Springer Science & Business Media, 2012.
- [121] J. P. Loehr. *Physics of Strained Quantum Well Lasers*. Springer Science & Business Media, 1997.
- [122] S. L. Chuang. *Physics of Photonic Devices*. John Wiley & Sons, 2012.
- [123] Al. L. Efros and M. Rosen. Quantum Size Level Structure of Narrow-Gap Semiconductor Nanocrystals: Effect of Band Coupling. *Phys. Rev. B*, 58:7120–7135, Sep 1998.
- [124] J. Planelles, J. I. Climente, F. Rajadell, M. F. Doty, A. S. Bracker, and D. Gammon. Effect of Strain and Variable Mass on the Formation of Antibonding Hole Ground States in InAs Quantum Dot Molecules. *Phy. Rev. B*, 82(15):155307, October 2010.

- [125] C. Segarra, J. I. Climente, and J. Planelles. Valence Band Mixing of Cubic GaN/AlN Quantum Dots. *J. Condens. Matter Phys.*, 24(11):115801, 2012.
- [126] F. Rajadell, J. I. Climente, and J. Planelles. Large Hole Spin Anticrossings in InAs/GaAs Double Quantum Dots. *Appl. Phys. Lett.*, 103(13):132105, 2013.
- [127] C. Segarra, J. I. Climente, A. Polovitsyn, F. Rajadell, I. Moreels, and J. Planelles. Piezoelectric Control of the Exciton Wave Function in Colloidal CdSe/CdS Nanocrystals. *J. Phys. Chem. Lett.*, 7(12):2182–2188, 2016. PMID: 27225599.
- [128] S. Christodoulou, F. Rajadell, A. Casu, G. Vaccaro, J. Q. Grim, A. Genovese, L. Manna, J. I. Climente, F. Meinardi, G. Raino, et al. Band Structure Engineering via Piezoelectric Fields in Strained Anisotropic CdSe/CdS Nanocrystals. *Nat. Commun.*, 6(1):1–8, 2015.
- [129] A. Piryatinski, S. A. Ivanov, S. Tretiak, and V. I. Klimov. Effect of Quantum and Dielectric Confinement on the Exciton–Exciton Interaction Energy in Type II Core/Shell Semiconductor Nanocrystals. *Nano Lett.*, 7(1):108–115, 2007. PMID: 17212448.
- [130] N. Vukmirović and S. Tomić. Plane wave methodology for single quantum dot electronic structure calculations. *J. Appl. Phys.*, 103(10):103718, 2008.
- [131] J. Planelles. Simple Correlated Wave-Function for Excitons in 0D, Quasi-1D and Quasi-2D Quantum Dots. *Theor. Chem. Acc.*, 136:81, 2017.
- [132] S. Singh, R. Tomar, S. Ten Brinck, J. De Roo, P. Geiregat, J. C. Martins, I. Infante, and Z. Hens. Colloidal CdSe Nanoplatelets, a Model for Surface Chemistry/Optoelectronic Property Relations in Semiconductor Nanocrystals. *J. Am. Chem. Soc.*, 140(41):13292–13300, 2018.
- [133] A. Antanovich, A. W. Achtstein, A. Matsukovich, A. Prudnikau, P. Bhaskar, V. Gurin, M. Molinari, and M. Artemyev. A Strain-Induced Exciton Transition Energy Shift in CdSe Nanoplatelets: The Impact of an Organic Ligand Shell. *Nanoscale*, 9:18042–18053, 2017.
- [134] B. T. Diroll. Ligand-Dependent Tuning of Interband and Intersubband Transitions of Colloidal CdSe Nanoplatelets. *Chem. Mater.*, 32(13):5916–5923, 2020.
- [135] A. M. Smith, A. M. Mohs, and S. Nie. Tuning the Optical and Electronic Properties of Colloidal Nanocrystals by Lattice Strain. *Nat. Nanotechnol.*, 4(1):56–63, 2009.

- [136] Q. Martinet, J. Baronnier, A. Girard, T. Albaret, L. Saviot, A. Mermet, B. Abecassis, J. Margueritat, and B. Mahler. Ligand-Dependent Nano-Mechanical Properties of CdSe Nanoplatelets: Calibrating Nanobalances for Ligand Affinity Monitoring. *Nanoscale*, 13:8639–8647, 2021.
- [137] R. B. Vasiliev, M. S. Sokolikova, A. G. Vitukhnovskii, S. A. Ambrozevich, A. S. Selyukov, and V. S. Lebedev. Optics of Colloidal Quantum-Confined CdSe Nanoscrolls. *IEEE J. Quantum Electron.*, 45(9):853, 2015.
- [138] E. M. Hutter, E. Bladt, B. Goris, F. Pietra, J. C. Van Der Bok, M. P. Boneschanscher, C. de Mello Donega, S. Bals, and D. Vanmaekelbergh. Conformal and Atomic Characterization of Ultrathin CdSe Platelets With a Helical Shape. *Nano Lett.*, 14(11):6257–6262, 2014.
- [139] J. Llusar, J. Planelles, and J. I. Climente. Strain in Lattice-Mismatched CdSe-Based Core/Shell Nanoplatelets. *J. Phys. Chem. C*, 123(34):21299–21306, 2019.
- [140] A. Polovitsyn, Z. Dang, J. L. Movilla, B. Martín-García, A. H. Khan, G. H. V. Bertrand, R. Brescia, and I. Moreels. Synthesis of Air-Stable CdSe/ZnS Core–Shell Nanoplatelets With Tunable Emission Wavelength. *Chem. Mater.*, 29(13):5671–5680, 2017.
- [141] R.M. Kolbas, N.G. Anderson, W.D. Laidig, Y. Sin, Y.C. Lo, K.Y. Hsieh, and Y.J. Yang. Strained-Layer InGaAs-GaAs-AlGaAs Photopumped and Current Injection Lasers. *IEEE J. Quantum Electron.*, 24(8):1605–1613, 1988.
- [142] H. K. Choi and C. A. Wang. InGaAs/AlGaAs Strained Single Quantum Well Diode Lasers With Extremely Low Threshold Current Density and High Efficiency. *Appl. Phys. Lett.*, 57(4):321–323, 1990.
- [143] S. Masi, C. Echeverría-Arrondo, K. M. M. Salim, T. T. Ngo, P. F. Mendez, E. López-Fraguas, D. F. Macias-Pinilla, J. Planelles, J. I. Climente, and I. Mora-Sero. Chemi-Structural Stabilization of Formamidinium Lead Iodide Perovskite by Using Embedded Quantum Dots. *ACS Energy Lett.*, 5(2):418–427, 2020.
- [144] U. W. Pohl. *Epitaxy of Semiconductors*. Springer, 2020.
- [145] F. Rajadell, M. Royo, and J. Planelles. Strain in Free Standing CdSe/CdS Core-Shell Nanorods. *J. Appl. Phys.*, 111(1):014303, 2012.
- [146] K. Gawarecki and M. Zieliński. Importance of Second-Order Deformation Potentials in Modeling of InAs/GaAs Nanostructures. *Phys. Rev. B*, 100(15):155409, 2019.

- [147] A. W. Achtstein, O. Marquardt, R. Scott, M. Ibrahim, T. Riedl, A. V. Prudnikau, A. Antanovich, N. Owschimikow, J. K. N. Lindner, M. Artemyev, and U. Woggon. Impact of Shell Growth on Recombination Dynamics and Exciton–Phonon Interaction in CdSe–CdS Core–Shell Nanoplatelets. *ACS Nano*, 12(9):9476–9483, 2018. PMID: 30192515.
- [148] L. E. Brus. Electron–Electron and Electron–Hole Interactions in Small Semiconductor Crystallites: The Size Dependence of the Lowest Excited Electronic State. *J. Chem. Phys.*, 80(9):4403–4409, 1984.
- [149] J. L. Movilla. *Confinamiento Nanoscópico en Estructuras Semiconductoras Cero-Dimensionales*. PhD thesis, Universitat Jaume I, 2007.
- [150] M. Royo, J. I. Climente, J. L. Movilla, and J. Planelles. Dielectric Confinement of Excitons in Type-I and Type-II Semiconductor Nanorods. *J. Condens. Matter Phys.*, 23(1):015301, 2010.
- [151] B. Ji, E. Rabani, A. L. Efros, R. Vaxenburg, O. Ashkenazi, D. Azulay, U. Banin, and O. Millo. Dielectric Confinement and Excitonic Effects in Two-Dimensional Nanoplatelets. *ACS Nano*, 14(7):8257–8265, 2020.
- [152] S. Adachi. *Handbook on Physical Properties of Semiconductors*. Springer Science & Business Media, 2004.
- [153] J. D. Jackson. *Classical Electrodynamics*. Wiley, 2012.
- [154] R. P. Feynman, R. B. Leighton, and M. Sands. *The Feynman Lectures on Physics, Vol. II: The New Millennium Edition: Mainly Electromagnetism and Matter*. The Feynman Lectures on Physics. Basic Books, 2011.
- [155] D. J. Griffiths, P. D. J. Griffiths, and R. College. *Introduction to Electrodynamics*. Prentice Hall, 1999.
- [156] M. Kumagai and T. Takagahara. Excitonic and Nonlinear-Optical Properties of Dielectric Quantum-Well Structures. *Phys. Rev. B*, 40(18):12359, 1989.
- [157] A. W. Achtstein, R. Scott, S. Kickhöfel, S. T. Jagsch, S. Christodoulou, G. H. V. Bertrand, A. V. Prudnikau, A. Antanovich, M. Artemyev, I. Moreels, et al. p-State Luminescence in CdSe Nanoplatelets: Role of Lateral Confinement and a Longitudinal Optical Phonon Bottleneck. *Phys. Rev. Lett.*, 116(11):116802, 2016.
- [158] J. Llusar and J. I. Climente. Nature and Control of Shakeup Processes in Colloidal Nanoplatelets. *ACS Photonics*, 7(11):3086–3095, 2020.
- [159] E. V. Shornikova, D. R. Yakovlev, L. Biadala, S. A. Crooker, V. V. Belykh, M. V. Kochiev, A. Kuntzmann, M. Nasilowski, B. Dubertret, and



- M. Bayer. Negatively Charged Excitons in CdSe Nanoplatelets. *Nano Lett.*, 20(2):1370–1377, 2020.
- [160] F. V Antolinez, F. T. Rabouw, A. A. Rossinelli, R. C. Keitel, A. Cocina, M. A. Becker, and D. J. Norris. Trion Emission Dominates the Low-Temperature Photoluminescence of CdSe Nanoplatelets. *Nano Lett.*, 20(8):5814–5820, 2020.
- [161] M. D. Tessier, L. Biadala, C. Bouet, S. Ithurria, B. Abecassis, and B. Dubertret. Phonon Line Emission Revealed by Self-Assembly of Colloidal Nanoplatelets. *ACS Nano*, 7(4):3332–3340, 2013.
- [162] B. T. Diroll, W. Cho, I. Coropceanu, S. M. Harvey, A. Brumberg, N. Holtgrewe, S. A. Crooker, M. R. Wasielewski, V. B. Prakapenka, D. V. Talapin, et al. Semiconductor Nanoplatelet Excimers. *Nano Lett.*, 18(11):6948–6953, 2018.
- [163] F. V. Antolinez, F. T. Rabouw, A. A. Rossinelli, J. Cui, and D. J. Norris. Observation of Electron Shakeup in CdSe/CdS Core/Shell Nanoplatelets. *Nano Lett.*, 19(12):8495–8502, 2019.
- [164] K. J. Karki, J. R. Widom, J. Seibt, I. Moody, M. C. Lonergan, T. Pullerits, and A. H. Marcus. Coherent Two-Dimensional Photocurrent Spectroscopy in a PbS Quantum Dot Photocell. *Nat. Commun.*, 5(1):1–7, 2014.
- [165] L. Peng, X. Ma, H. Zhu, O. Chen, and W. Wang. Influence of Local Structures on the Energy Transfer Efficiencies of Quantum-Dot Films. *Phys. Rev. B*, 102:035437, Jul 2020.
- [166] L. Peng, W. Cho, X. Zhang, D. Talapin, and X. Ma. Observation of Biexciton Emission From Single Semiconductor Nanoplatelets. *Phys. Rev. Mater.*, 5:L051601, May 2021.
- [167] M. Zavelani-Rossi, M. G. Lupo, F. Tassone, L. Manna, and G. Lanzani. Suppression of Biexciton Auger Recombination in CdSe/CdS Dot/Rods: Role of the Electronic Structure in the Carrier Dynamics. *Nano Lett.*, 10(8):3142–3150, 2010. PMID: 20698629.
- [168] M. R. Golobostanfard and H. Abdizadeh. Tandem Structured Quantum Dot/Rod Sensitized Solar Cell Based on Solvothermal Synthesized Cdse Quantum Dots and Rods. *J. Power Sources*, 256:102–109, 2014.
- [169] S. Morozov, E. L. Pensa, A. H. Khan, A. Polovitsyn, E. Cortés, S. A. Maier, S. Vezzoli, I. Moreels, and R. Sapienza. Electrical Control of Single-Photon Emission in Highly Charged Individual Colloidal Quantum Dots. *Sci. Adv.*, 6(38):eabb1821, 2020.

- [170] M. Saba, S. Minniberger, F. Quochi, J. Roither, M. Marceddu, A. Gocalinska, M. V. Kovalenko, D. V. Talapin, W. Heiss, A. Mura, et al. Exciton–Exciton Interaction and Optical Gain in Colloidal CdSe/CdS Dot/Rod Nanocrystals. *Adv. Mater.*, 21(48):4942–4946, 2009.
- [171] S. S. Lo, T. Mirkovic, C. H. Chuang, C. Burda, and G. D. Scholes. Emergent Properties Resulting from Type-II Band Alignment in Semiconductor Nanoheterostructures. *Adv. Mater.*, 23, 2011.
- [172] A. D. Golinskaya, A. M. Smirnov, M. V. Kozlova, E. V. Zharkova, R. B. Vasiliev, V. N. Mantsevich, and V. S. Dneprovskii. Tunable Blue-Shift of the Charge-Transfer Photoluminescence in Tetrapod-Shaped CdTe/CdSe Nanocrystals. *Results Phys.*, 27:104488, 2021.
- [173] Al. L. Efros, M. Rosen, M. Kuno, M. Nirmal, D. J. Norris, and M. Bawendi. Band-Edge Exciton in Quantum Dots of Semiconductors With a Degenerate Valence Band: Dark and Bright Exciton States. *Phys. Rev. B*, 54:4843–4856, Aug 1996.
- [174] K. Leung, S. Pokrant, and K. B. Whaley. Exciton Fine Structure in CdSe Nanoclusters. *Phys. Rev. B*, 57:12291–12301, May 1998.
- [175] A. Franceschetti, H. Fu, L. W. Wang, and A. Zunger. Many-Body Pseudopotential Theory of Excitons in InP and CdSe Quantum Dots. *Phys. Rev. B*, 60(3):1819, 1999.
- [176] A. Shabaev and Al. L. Efros. 1D Exciton Spectroscopy of Semiconductor Nanorods. *Nano Lett.*, 4(10):1821–1825, 2004.
- [177] A. V. Rodina, A. A. Golovatenko, E. V. Shornikova, and D. R. Yakovlev. Spin Physics of Excitons in Colloidal Nanocrystals. *Phys. Solid State*, 60(8):1537–1553, 2018.
- [178] E. V. Shornikova, L. Biadala, D. R. Yakovlev, V. F. Sapega, Y. G. Kusrayev, A. A. Mitioglu, M. V. Ballottin, P. C. M. Christianen, V. V. Belykh, M. V. Kochiev, et al. Addressing the Exciton Fine Structure in Colloidal Nanocrystals: The Case of CdSe Nanoplatelets. *Nanoscale*, 10(2):646–656, 2018.
- [179] M. Fu, P. Tamarat, H. Huang, J. Even, A. L. Rogach, and Brahim L. Neutral and Charged Exciton Fine Structure in Single Lead Halide Perovskite Nanocrystals Revealed by Magneto-optical Spectroscopy. *Nano Lett.*, 17(5):2895–2901, 2017. PMID: 28240910.
- [180] A. Brodu, M. V. Ballottin, J. Buhot, E. J. Van Harten, D. Dupont, A. La Porta, P. T. Prins, M. D. Tessier, M. A. M. Versteegh, V. Zwiller, et al. Exciton Fine Structure and Lattice Dynamics in InP/ZnSe Core/Shell Quantum Dots. *ACS Photonics*, 5(8):3353–3362, 2018.

- [181] J. I. Climente, J. Planelles, and F. Rajadell. Energy Structure and Far-Infrared Spectroscopy of Two Electrons in a Self-Assembled Quantum Ring. *J. Condens. Matter Phys.*, 17(10):1573–1582, feb 2005.
- [182] I. R. Sellers, V. R. Whiteside, I. L. Kuskovsky, A. O. Govorov, and B. D. McCombe. Aharonov-Bohm Excitons at Elevated Temperatures in Type-II ZnTe/ZnSe Quantum Dots. *Phys. Rev. Lett.*, 100:136405, Apr 2008.
- [183] Y. Aharonov and D. Bohm. Significance of Electromagnetic Potentials in the Quantum Theory. *Phys. Rev.*, 115:485–491, Aug 1959.
- [184] J. Planelles, J. I. Climente, and J. L. Movilla. Aharonov-Bohm Effect for Pedestrian, 2005.
- [185] A. O. Govorov, S. E. Ulloa, K. Karrai, and R. J. Warburton. Polarized Excitons in Nanorings and the Optical Aharonov-Bohm Effect. *Phys. Rev. B*, 66:081309, Aug 2002.
- [186] R. W. Meulenberg, J. R. I. Lee, S. K. McCall, K. M. Hanif, D. Haskel, J. C. Lang, L. J. Terminello, and T. van Buuren. Evidence for Ligand-Induced Paramagnetism in CdSe Quantum Dots. *J. Am. Chem. Soc.*, 131(20):6888–6889, 2009. PMID: 19415891.
- [187] S. Neeleshwar, C. L. Chen, C. B. Tsai, Y. Y. Chen, C. C. Chen, S. G. Shyu, and M. S. Seehra. Size-Dependent Properties of CdSe Quantum Dots. *Phys. Rev. B*, 71:201307, May 2005.
- [188] M. P. Lima, L. Cabral, E. Margapoti, S. Mahapatra, J. L. F. Da Silva, F. Hartmann, S. Höfling, G. E. Marques, and V. Lopez-Richard. Defect-Induced Magnetism in II-VI Quantum Dots. *Phys. Rev. B*, 99:014424, Jan 2019.
- [189] A. Saha and R. Viswanatha. Magnetism at the Interface of Magnetic Oxide and Nonmagnetic Semiconductor Quantum Dots. *ACS Nano*, 11(3):3347–3354, 2017. PMID: 28260377.
- [190] J. Llusar and J. I. Climente. Highly Charged Excitons and Biexcitons in Type-II Core/Crown Colloidal Nanoplatelets. *J. Phys. Chem. C*, 126(16):7152–7157, 2022.
- [191] E. V. Shornikova, A. A. Golovatenko, D. R. Yakovlev, A. V. Rodina, L. Bidada, G. Qiang, A. Kuntzmann, M. Nasilowski, B. Dubertret, A. Polovitsyn, et al. Surface Spin Magnetism Controls the Polarized Exciton Emission From CdSe Nanoplatelets. *Nat. Nanotechnol.*, 15(4):277–282, 2020.
- [192] A. Najafi, M. Sharma, S. Delikanli, A. Bhattacharya, J. R. Murphy, J. Pientka, A. Sharma, A. P Quinn, O. Erdem, S. Kattel, et al. Light-Induced Paramagnetism in Colloidal Ag<sup>+</sup>-Doped CdSe Nanoplatelets. *J. Phys. Chem. Lett.*, 12(11):2892–2899, 2021.

- [193] E. V. Shornikova, D. R. Yakovlev, D. O. Tolmachev, V. Y. Ivanov, I. V. Kalitukha, V. F. Sapega, D. Kudlacik, Y. G. Kusrayev, A. A. Golovatenko, S. Shendre, S. Delikanli, H. V. Demir, and M. Bayer. Magneto-Optics of Excitons Interacting with Magnetic Ions in CdSe/CdMnS Colloidal Nanoplatelets. *ACS Nano*, 14(7):9032–9041, 2020. PMID: 32585089.
- [194] J. Planelles and J. I. Climente. Magnetic Field Implementation in Multiband k-p Hamiltonians of Holes in Semiconductor Heterostructures. *J. Condens. Matter Phys.*, 25(48):485801, oct 2013.
- [195] S. Luo, M. Kazes, H. Lin, and D. Oron. Strain-Induced Type II Band Alignment Control in CdSe Nanoplatelet/ZnS-Sensitized Solar Cells. *J. Phys. Chem. C*, 121(21):11136–11143, 2017.
- [196] S. Shendre, S. Delikanli, M. Li, D. Dede, Z. Pan, S. T. Ha, Y. H. Fu, P. L. Hernández-Martínez, J. Yu, O. Erdem, A. I. Kuznetsov, C. Dang, T. C. Sum, and H. V. Demir. Ultrahigh-Efficiency Aqueous Flat Nanocrystals of CdSe/CdS@Cd<sub>1-x</sub>Zn<sub>x</sub>S Colloidal Core/Crown@Alloyed-Shell Quantum Wells. *Nanoscale*, 11:301–310, 2019.
- [197] A. H. Khan, G. H. V. Bertrand, A. Teitelboim, M. Chandrasekhar, A. Polovitsyn, R. Brescia, J. Planelles, J. I. Climente, D. Oron, and I. Moreels. CdSe/CdS/CdTe Core/Barrier/Crown Nanoplatelets: Synthesis, Optoelectronic Properties, and Multiphoton Fluorescence Upconversion. *ACS Nano*, 14(4):4206–4215, 2020.
- [198] K. J. Nash, M. S. Skolnick, M. K. Saker, and S. J. Bass. Many Body Shakeup in Quantum Well Luminescence Spectra. *Phys. Rev. Lett.*, 70:3115–3118, May 1993.
- [199] V. M. Fomin. *Physics of Quantum Rings*. Springer Science & Business Media, 2013.
- [200] K. Müller, G. Reithmaier, E. C. Clark, V. Jovanov, M. Bichler, H. J. Krenner, M. Betz, G. Abstreiter, and J. J. Finley. Excited State Quantum Couplings and Optical Switching of an Artificial Molecule. *Phys. Rev. B*, 84:081302, Aug 2011.
- [201] S. Sasaki, T. Fujisawa, T. Hayashi, and Y. Hirayama. Electrical Pump-and-Probe Study of Spin Singlet-Triplet Relaxation in a Quantum Dot. *Phys. Rev. Lett.*, 95:056803, Jul 2005.
- [202] L. Gaudreau, G. Granger, A. Kam, G. C. Aers, S. A. Studenikin, P. Zawadzki, M. Pioro-Ladrière, Z. R. Wasilewski, and A. S. Sachrajda. Coherent Control of Three-Spin States in a Triple Quantum Dot. *Nature*, 8:54–58, 2012.

- [203] M. Bayer, O. Stern, A. Kuther, and A. Forchel. Spectroscopic Study of Dark Excitons In  $\text{In}_x\text{Ga}_{1-x}\text{As}$  Self-Assembled Quantum Dots by a Magnetic-Field-Induced Symmetry Breaking. *Phys. Rev. B*, 61:7273–7276, Mar 2000.

# Appendices

# A Coauthors Authorization



Castelló de la Plana, 2 May 2022

I, **Josep Planelles**, hereby authorise **Jordi Llusar** to include the publications listed below in his/her doctoral thesis. In addition, I waive the right to use those articles as part of any other doctoral thesis.

List of articles:

- Jordi Llusar, Josep Planelles, and Juan I. Clemente, J. Phys. Chem. C 2019, 123, 34, 21299–21306, DOI: <https://doi.org/10.1021/acs.jpcc.9b06577>

Signed, **JOSEP HILARI PLANELLES FUSTER**  
Firmado digitalmente por JOSEP HILARI PLANELLES FUSTER  
Número de reconocimiento (RN):  
com=JOSEP HILARI PLANELLES FUSTER  
uicpNumber=100037316  
parentName=JOSEP HILARI PLANELLES FUSTER, com=CUCADANOS, ser=ACCV, c=ES  
Fecha: 2022.05.02 11:02:19 +02'00'

*In accordance with article 28 of the Regulations on doctoral studies of the Universitat Jaume I in Castelló, regulated by RD 99/2011, at the Universitat Jaume I (Approved by the Governing Council at its meeting no. 8/2020 held on 2 October 2020):*

"(...)

*4. In the case of joint publications, all the co-authors must explicitly state their approval that the doctoral student presented the work as part of her/his thesis and the express waiver of presenting this same work as part of another doctoral thesis. This authorisation must be attached as documentation when the evaluation of the thesis begins."*

Castelló de la Plana, 2 May 2022

I, **Juan I. Climente**, hereby authorise **Jordi Llusar** to include the publications listed below in his/her doctoral thesis. In addition, I waive the right to use those articles as part of any other doctoral thesis.

List of articles:

- Jordi Llusar, Josep Planelles, and Juan I. Climente, J. Phys. Chem. C 2019, 123, 34, 21299–21306, DOI: <https://doi.org/10.1021/acs.jpcc.9b06577>
- Jordi Llusar and Juan I. Climente, ACS Photonics 2020, 7, 11, 3086–3095, DOI: <https://doi.org/10.1021/acsphotonics.0c01160>
- Jordi Llusar and Juan I. Climente, Phys Status Solidi B 2022, 2200081, DOI: <https://doi.org/10.1002/pssb.202200081>
- Jordi Llusar and Juan I. Climente, J. Phys. Chem. C 2022, 126, 16, 7152–7157, DOI: <https://doi.org/10.1021/acs.jpcc.2c00827>
- Jordi Llusar and Juan I. Climente, Shell Filling and Paramagnetism in Few Electron Colloidal Nanoplatelets. (under review)

Signed,

Firmado por JUAN IGNACIO  
CLIMENTE PLASENCIA -  
NIF:44795725M el día  
06/05/2022 con un certificado  
emitido por ACCVCA-120

*In accordance with article 28 of the Regulations on doctoral studies of the Universitat Jaume I in Castelló, regulated by RD 99/2011, at the Universitat Jaume I (Approved by the Governing Council at its meeting no. 8/2020 held on 2 October 2020):*

"(...)

*4. In the case of joint publications, all the co-authors must explicitly state their approval that the doctoral student presented the work as part of her/his thesis and the express waiver of presenting this same work as part of another doctoral thesis. This authorisation must be attached as documentation when the evaluation of the thesis begins."*



## B Training Activities

### Participation in Conferences:





- Strain in Lattice-Mismatched CdSe-Based Core/Shell Nanoplatelets. Jordi Llusar, Josep Planelles, and Juan I. Climente. SPRING MEETING 2019 IUMRS-ICAM International Conference on Advanced Materials (E-MRS), May 2019, Nice-France (Poster).
- Strain in Lattice-Mismatched CdSe-Based Core/Shell Nanoplatelets. Jordi Llusar and Juan I. Climente. NanoGe Fall Meeting 19 (Fundació Scito), November 2019, Berlin-Germany (Poster).
- Control of Shake-Up Lines in Colloidal NPLs. Jordi Llusar and Juan I. Climente. Shape-Controlled Nanocrystals: Synthesis, Characterization Methods and Applications (Fundació Scito), May 2020, online (Poster).
- Nature and Control of Shakeup Processes in Colloidal Nanoplatelets. Jordi Llusar and Juan I. Climente. Internet Conference for Quantum Dots (Fundació Scito), July 2020, online (Poster).
- Nature and Control of Shakeup Processes in Colloidal Nanoplatelets. Jordi Llusar and Juan I. Climente. Internet NanoGe Conference on Nanocrystals (Fundació Scito), June 2021, online (Oral Contribution).
- Coulomb Repulsions as a Means of Modulating Electronic and Optical Properties of Colloidal Nanoplatelets. Jordi Llusar, David F. Macias-Pinilla, Josep Planelles, Juan I. Climente. SPRING MEETING 2022 Semiconductor Nanostructures Towards Opto-Electronic and Photonic Device Applications VIII (E-MRS), June 2022, online (Oral Contribution)

### Participation in Accredited Courses:

- Programming for Everybody (Getting Started with Python). Jordi Llusar. University of Michigan (Coursera), December 2021, online. <https://coursera.org/verify/AQPZ5T2UXQ5M>
- Python Data Structures. Jordi Llusar. University of Michigan (Coursera), December 2021, online. <https://coursera.org/verify/96SURC22296G>
- Scientific article writing workshop for sustainability journals' and scientific research methodologies for sustainability studies. Jordi Llusar. Escola de Doctorat de la Universitat Jaume I, Nov 2018, online.

## C Curriculum Vitae

## CONTACT

 jordi.llusar@uji.es  
 0000-0002-4947-5192  
 Jordi Llusar Camarellles  
 +34 722 768 822

## SKILLS

Microsoft Office	14 yrs
Mathematica	10 yrs
Group Theory	7 yrs
COMSOL Multiphysics	4 yrs
MATLAB	4 yrs
Linux	4 yrs
Gnuplot	4 yrs
Inkscape	4 yrs
Python	1 yrs

# JORDI LLUSAR CAMARELLES

Research Scholar - Sciences: Physical Chemistry

## EDUCATION

**Ph. D. - Sciences: Physical Chemistry** 2018 - 2022  
Universitat Jaume I (UJI) - Castelló de la Plana, Com. Val. (Spain)

**M. S. - Advanced Physics** 2017 - 2018  
Universitat de València (UV) - València, Com. Val (Spain)

**B. S. - Chemistry** 2012 - 2017  
Universitat Jaume I (UJI) - Castelló de la Plana, Com. Val. (Spain)

## PUBLICATIONS

**Strain in Lattice-Mismatched CdSe-Based Core/Shell Nanoplatelets** Q2  
*J. Phys. Chem. C* **2019** *123* (34), 21299-21306

(DOI: <https://doi.org/10.1021/acs.jpcc.9b06577>)

Jordi Llusar, Josep Planelles, and Juan I. Climente

**Nature and Control of Shakeup Processes in Colloidal Nanoplatelets** Q1  
*ACS Photonics* **2020** *7* (11), 3086-3095

(DOI: <https://doi.org/10.1021/acsp Photonics.0c01160>)

Jordi Llusar and Juan I. Climente

**Changing Spin and Orbital Ground State Symmetries in Colloidal Nanoplatelets with Magnetic Fields** Q3  
*Phys. Status Solidi B* **2022**, 2200081

(DOI: <https://doi.org/10.1002/pssb.202200081>)

Jordi Llusar and Juan I. Climente

**Highly Charged Excitons and Biexcitons in Type-II Core/Crown Colloidal Nanoplatelets** Q2  
*J. Phys. Chem. C* **2022** *126* (16), 7152-7157

(DOI: <https://doi.org/10.1021/acs.jpcc.2c00827>)

Jordi Llusar and Juan I. Climente

# ACHIEVEMENTS

## First Certificate in English (FCE)

**160 out of 190 score**

A certificate issued by Cambridge English Language Assessment to prove English language proficiency (B2).

## Programming for Everybody (Getting Started with Python)

**96.60%**

A certificate issued by Coursera to prove basic understanding of Python. Verification Link: <https://coursera.org/verify/AQPZ5T2UXQ5M>

## Python Data Structures

**98.40%**

A certificate issued by Coursera to prove further understanding of Python. Verification Link: <https://coursera.org/verify/96SURC22296G>

## Shell Filling and Paramagnetism in Few Electron Colloidal Nanoplatelets Journal Name 2022, XX

QX

(DOI: <https://doi.org/XX>)

Jordi Llusar and Juan I. Climente

## Role of Thermally Occupied Hole States in Room-Temperature Broadband Gain in CdSe/CdS Giant-Shell Nanocrystals Journal Name 2022, XX

QX

(DOI: <https://doi.org/XX>)

Ivo Tanghe, **Jordi Llusar**, Juan I. Climente, Alex Barker, Giuseppe Paternò, Francesco Scotognella, Anatolii Polovitsyn, Ali Hossain Khan, Zeger Hens, Dries Van Thourhout, Pieter Geiregat, and Iwan Moreels

# WORKSHOPS & CONFERENCES

## Scientific article writing workshop for sustainability journals' and scientific research methodologies for sustainability studies Escola de Doctorat de la Universitat Jaume I

Nov 2018

## Strain in Lattice-Mismatched CdSe-Based Core/Shell Nanoplatelets SPRING MEETING 2019 IUMRS-ICAM (E-MRS)

May 2019

Nice-France (Poster)

## Strain in Lattice-Mismatched CdSe-Based Core/Shell Nanoplatelets NanoGe Fall Meeting 19 (Fundació Scito)

Nov 2019

Berlin-Germany (Poster)

## Control of Shake-Up Lines in Colloidal NPLs Shape-Controlled Nanocrystals: Synthesis, Characterization Methods and Applications (Fundació Scito)

May 2020

online (Poster)

## Nature and Control of Shakeup Processes in Colloidal Nanoplatelets Internet Conference for Quantum Dots (Fundació Scito)

Jul 2020

online (Poster)

## Nature and Control of Shakeup Processes in Colloidal Nanoplatelets Internet NanoGe Conference on Nanocrystals (Fundació Scito)

Jun 2021

online (Oral Contribution)

**Coulomb Repulsions as a Means of Modulating  
Electronic and Optical Properties of Colloidal  
Nanoplatelets**

**SPRING MEETING 2022 Semiconductor Nanostruc-  
tures Towards Opto-Electronic and Photonic Device  
Applications VIII (E-MRS)**

online (Oral Contribution)

